Measurement of the Polarisation of the W Boson and Application to Supersymmetry Searches at the Large Hadron Collider

Alexander Sparrow

High Energy Physics

Blackett Laboratory
Imperial College London

Thesis submitted to Imperial College London
for the degree of Doctor of Philosophy and the Diploma of Imperial College

2012

Abstract

This thesis gives an account of two analyses performed using data from the Compact Muon Solenoid experiment at the Large Hadron Collider. The first analysis measures the polarisation of W bosons with large transverse momentum using 36 pb^{-1} of data collected in 2010. The second applies similar techniques to a search for supersymmetry in events containing a single lepton, jets and missing transverse energy. This analysis utilises 1.14 fb^{-1} of data collected up to 2011. Background material related to the Standard Model, supersymmetry and the experimental apparatus are reviewed in detail.

The W polarisation measurement is performed in both the $\text{W} \longrightarrow \text{e}\nu$ and $\text{W} \longrightarrow \mu\nu$ channels. The expected effect, a large dominance of the left-handed over the right-handed helicity state, is observed with a significance of 7.8σ for the W^+ and 5.1σ for the W^- in the muon channel. Similar results are found in the electron channel and for a combined fit to both lepton channels.

The second analysis conducts a search for supersymmetry in events containing a single lepton, jets and missing transverse energy. The search employs techniques developed for the W polarisation measurement to separate supersymmetry from Standard Model backgrounds. No deviation from the Standard Model is observed. A detailed statistical interpretation is performed and used to set limits within the Constrained Minimal Supersymmetric Standard Model as well as two simplified models.

Declaration

This dissertation is the result of my own work, except where explicit reference is made to the work of others, and has not been submitted for another qualification to this or any other university.

The work presented in Chapters 6, 7 and 8 is the result of collaboration with a number of others. For completeness and necessary context, I have presented a full account of these analyses. For the W polarisation measurement, my contributions were primarily to the electron channel and the fitting procedure. For the supersymmetry search, I worked mainly on estimating the systematic uncertainties and optimising the selection cuts. I also set up the statistical procedure detailed in Appendix B.1 and performed the interpretation and validation work shown in Chapter 8. Finally, Appendix C details my service work on the SusyV2 analysis package and the Level 1 Trigger at CMS.

Alexander Sparrow

Acknowledgements

I would firstly like to thank my direct collaborators at CERN and Imperial College. To Georgia Karapostoli for all of her help and advice, particularly in helping me to get started on this work. To Markus Stoye, Jad Marrouche and Loukas Gouskos for providing so much helpful input and fixing so many of my mistakes. Finally, to Oliver Buchmüller and Paris Sphicas for their continuous oversight on both analyses and for steering the ship through so many storms.

There are many others deserving of thanks for their continuous support and advice. First and foremost to my immediate colleagues at CERN: Arlo Guneratne Bryer, Michael Cutajar, Zoe Hatherell, Martyn Jarvis, Bryn Mathias, Robin Nandi and Nick Wardle for their unending advice, good humour and inspiration. Particular thanks to John Jones for the SusyV2 code and many interesting discussions. I am also grateful to Burt Betchart and Ted Laird for their many technical contributions.

At Imperial College, I'd like to thank Costas Foudas for supervising my Masters project and for encouraging me to start a PhD in the first place. I should also like to thank my supervisor Alex Tapper, who has been immensely supportive and helpful throughout my PhD.

The last few years have been among the most enjoyable of my life. This is thanks, in no small part, to a number of great friends. Happily, several are among the colleagues already mentioned. I should like to thank the many others, in Bath, London and Geneva. In particular, to Paul Schaack for being an excellent friend, housemate and colleague. But most of all, to Kitty Liao for her tireless help and support and for putting up with me for so long.

Finally, to my family. To my two sisters, Maddie and Lydia, for so many happy times. Above all, to my parents, Pauline and Timothy, who taught me the value of education. For encouraging me to pursue my dreams and for supporting me unwaveringly at every step along the way.

Contents

List of Figures **15**

List of Tables **19**

Introduction **21**

1. The Standard Model **25**

1.1. Introduction . . . 25
1.2. Particles and Fundamental Forces . . . 26
1.3. Electroweak Gauge Theory . . . 27
1.3.1. Gauge Invariance . . . 27
1.3.2. The Principle of Least Action and Lagrangian Formalism . . . 28
1.3.3. A Real Scalar Field . . . 28
1.3.4. Symmetries . . . 29
1.3.5. Complex Scalar Fields and the Gauge Principle . . . 29
1.3.6. Yang-Mills Theory . . . 31
1.3.7. Spin and Chirality . . . 32
1.3.8. The Electroweak Theory . . . 33
1.3.9. Remaining Issues . . . 35
1.4. Electroweak Symmetry Breaking . . . 35
1.4.1. A Real Scalar Field . . . 36
1.4.2. A Complex Scalar Field and Goldstone's Theorem . . . 36
1.4.3. The Higgs Mechanism . . . 37
1.4.4. Yukawa Couplings . . . 38
1.5. Quantum Chromodynamics . . . 39
1.5.1. Quarks . . . 39
1.5.2. Colour . . . 39
1.5.3. Unique Properties . . . 40

2. Supersymmetry **41**
2.1. Limitations of the Standard Model . . . 41
2.1.1. The Hierarchy Problem . . . 42
2.1.2. Dark Matter . . . 42
2.2. Beyond the Standard Model . . . 43
2.3. Supersymmetry . . . 44
2.3.1. An Additional Symmetry . . . 44
2.3.2. Consequences . . . 45
2.3.3. R-Parity . . . 46
2.3.4. Supersymmetry Breaking . . . 47
2.4. The Minimal Supersymmetric Standard Model . . . 48
2.4.1. Particle Content . . . 48
2.4.2. Neutralinos and Charginos . . . 50
2.5. Supersymmetry Searches . . . 50
2.5.1. Supersymmetry at Colliders . . . 50

3. Theoretical Framework **53**
3.1. W Polarisation . . . 53
3.1.1. QCD at Hadron Colliders . . . 54
3.1.2. Vector Boson Production at Hadron Colliders . . . 55
3.1.3. Polarisation Effects Parallel to the Beam Line . . . 55
3.1.4. Polarisation Effects in the Transverse Plane . . . 56
3.1.5. Measuring Helicity . . . 60
3.2. Modelling New Physics . . . 64
3.2.1. The Constrained Minimal Supersymmetric Standard Model . . . 64
3.2.2. Simplified Models . . . 65
3.3. Summary . . . 69

4. The Compact Muon Solenoid Experiment at the Large Hadron Collider **71**
4.1. Introduction . . . 71
4.2. The Large Hadron Collider . . . 71
4.2.1. Accelerator Complex . . . 72
4.3. The Compact Muon Solenoid Experiment . . . 73
4.3.1. Coordinate System . . . 74
4.3.2. Silicon Tracker . . . 74
4.3.3. Electromagnetic Calorimeter . . . 76

4.3.4. Hadronic Calorimeter . . . 78
4.3.5. Muon Chambers . . . 79
4.3.6. Data Acquisition and Trigger System . . . 81
4.3.7. Computing at CMS . . . 83

5. Physics Objects 85
5.1. Introduction . . . 85
5.2. Leptons . . . 85
5.2.1. Muons . . . 85
5.2.2. Electrons . . . 87
5.3. Jets . . . 92
5.3.1. Jet Energy Corrections and Jet Energy Scale . . . 93
5.4. Missing Energy . . . 94
5.5. Particle Flow at CMS . . . 95
5.5.1. Iterative Tracking . . . 96
5.5.2. Calorimeter Clustering . . . 98
5.5.3. Building Links . . . 98
5.5.4. Particle Reconstruction . . . 99
5.5.5. Physics Performance . . . 100

6. Measurement of the Polarisation of the W Boson 103
6.1. Introduction . . . 103
6.2. Measuring the Helicity Fractions of the W Boson . . . 103
6.2.1. Generator and Simulation Level Expectations . . . 103
6.2.2. The Lepton Projection Variable . . . 104
6.2.3. Template Re-weighting Method . . . 107
6.3. Analysis Method . . . 111
6.3.1. Introduction . . . 111
6.3.2. Backgrounds . . . 112
6.3.3. Leptons . . . 113
6.3.4. Jets . . . 115
6.3.5. Kinematic Cuts . . . 115
6.3.6. Selection Requirements . . . 118
6.3.7. Triggers . . . 118
6.4. Validation in Simulation . . . 120
6.4.1. Signal and Background Expectations in Simulation . . . 121

6.5. Fitting Procedure . . . 121
6.5.1. Electroweak Backgrounds . . . 122
6.5.2. QCD and γ + jets Backgrounds . . . 123
6.5.3. Fitting $(f_{\mathrm{L}} - f_{\mathrm{R}})$ and f_0 . . . 123
6.5.4. Combined Fit . . . 124
6.6. Electron Channel . . . 124
6.6.1. QCD and γ + jets Backgrounds . . . 124
6.6.2. Kinematics . . . 125
6.6.3. Optimisation of Selection Requirements . . . 125
6.6.4. Data-Driven Background Estimation . . . 126
6.7. Systematic Uncertainties . . . 129
6.7.1. Experimental Uncertainties . . . 130
6.7.2. Theoretical Uncertainties . . . 136
6.8. Results . . . 138
6.8.1. Fit Results . . . 141
6.9. Summary . . . 146

7. Searching for Supersymmetry in the Single Lepton Final State 147
7.1. Introduction . . . 147
7.2. Distinguishing SUSY from SM Backgrounds . . . 147
7.3. Analysis Method . . . 149
7.4. Object Definitions . . . 150
7.4.1. Jets and Missing Energy . . . 151
7.4.2. Muons . . . 151
7.4.3. Electrons . . . 152
7.4.4. Resolving Ambiguities . . . 152
7.5. Analysis Selection . . . 152
7.6. Triggers and Datasets . . . 153
7.7. Control Sample . . . 156
7.8. Background Prediction . . . 157
7.8.1. Muons . . . 159
7.8.2. Electrons . . . 159
7.9. Systematic Uncertainties . . . 160
7.9.1. Control Region $L_{\mathrm{P}} > 0.3$ . . . 161
7.9.2. Monte Carlo Statistical Uncertainty . . . 162
7.9.3. Jet Energy Scale . . . 162

7.9.4. E_T^{miss} Resolution . . . 162
7.9.5. W + jets and $t\bar{t}$ Backgrounds . . . 163
7.9.6. Muon Momentum Scale . . . 163
7.9.7. W and $t\bar{t}$ Polarisation . . . 163
7.9.8. Fully Leptonic $t\bar{t}$ . . . 165
7.9.9. Parton Distribution Functions . . . 165
7.9.10. Trigger Efficiency . . . 165
7.9.11. Summary . . . 165
7.10. Results . . . 166

8. Interpretation of Search Results 171
8.1. Introduction . . . 171
8.2. Statistical Methods . . . 172
8.2.1. The Likelihood Function . . . 172
8.2.2. Profile Likelihood and Wilks' Theorem . . . 173
8.2.3. Hypothesis Testing . . . 174
8.2.4. The CL_{s} Method . . . 174
8.3. The Single Lepton Supersymmetry Search . . . 176
8.3.1. Systematic Uncertainties on Signal Efficiency . . . 176
8.3.2. Validation . . . 176
8.4. Results . . . 179
8.4.1. The CMSSM . . . 181
8.4.2. Simplified Models . . . 183
8.5. Summary . . . 190

Conclusion 191

A. Kinematics 193

B. Statistics 195
B.1. Modelling the Single Lepton Analysis . . . 195
B.1.1. Notation . . . 195
B.1.2. The Likelihood Function . . . 196
B.1.3. The Signal Yield . . . 197
B.1.4. Background Prediction . . . 197
B.1.5. Parameterising Systematic Uncertainties . . . 198
B.1.6. Nuisance Parameters . . . 200

B.1.7. Signal Contamination 201
B.1.8. Uncertainties on N_i^{control} 203
B.2. Validation Plots 203

C. Service Work **205**
C.1. SusyV2 Analysis Framework 205
C.2. The Global Calorimeter Trigger 206

D. Monte Carlo Samples **209**

E. List of Acronymns **211**

Bibliography **215**

List of Figures

2.1. Two-loop renormalisation group evolution of the inverse gauge couplings 47

2.2. SUSY decay chain leading to a single lepton final state 52

3.1. Illustration of a $p\overline{p}$ collision 54

3.2. Diagrams showing the $ug \longrightarrow W^{+}d$ subprocess 57

3.3. Diagrams showing the $u\overline{d} \longrightarrow W^{+}g$ and $g\overline{d} \longrightarrow W^{+}\overline{u}$ subprocesses. . . . 58

3.4. Illustrations of $W^{+} + 1$ jet production modes at the LHC 59

3.5. Illustration of the helicity frame 61

3.6. The polarisation fractions, f_{L}, f_{R} and f_0 as a function of P_T^{W} 64

3.7. Illustration of direct and cascade decay modes within simplified models . 67

3.8. Feynman diagrams illustrating two simplified model topologies 68

4.1. Illustration of the LHC accelerator complex 73

4.2. Illustration of the CMS detector 74

4.3. Schematic cross section through the CMS tracker 75

4.4. Diagram showing the organisation of the CMS L1T 82

5.1. Muon transverse momentum resolution 88

5.2. Diagram illustrating electron conversion rejection variables 91

5.3. Electromagnetic Calorimeter (ECAL) energy resolution 91

5.4. Electron fake rate for 95% and 80% efficiency working points 93

5.5. Total jet energy correction factor as a function of η 94

5.6. Particle Flow event display showing a hadronic jet 97

5.7. Jet energy resolution as a function of p_{T} 101

5.8. Jet angular resolution (RMS) as a function of p_{T} 101

5.9. Particle Flow E_T^{miss} energy and angular resolution in $\mathrm{t\bar{t}}$ events 102

6.1. Distribution of $\cos\theta^*$ for W^+ bosons in three bins of P_T^{W} 104

6.2. Correlation of $\cos\theta^*$ and $2L_{\mathrm{P}} - 1$ for W bosons in MC 105

6.3. Generator level W phase space distributions 110

6.4. P_T^{W} resolution in the electron channel at reconstruction-level 116

6.5. L_{P} fits after cuts $E_T^{\mathrm{miss}} > 30$ GeV and $M_{\mathrm{T}} > 30$ GeV 126

6.6. Plots illustrating the signal significance in the electron channel 127

6.7. The dependence of f_{QCD} on a combined E_T^{miss} and M_{T} cut 128

6.8. The L_{P} distribution for two sets of electron identification cuts 128

6.9. Comparison of selected and anti-selected L_{P} shapes in QCD/γ + jets MC 129

6.10. Relative change of the muon L_{P} distribution due to the JES uncertainty 131

6.11. ECAL transparency correction factors as a function of η 134

6.12. Kinematic distributions in data and MC for the electron channel 139

6.13. Kinematic distributions in data and MC for the muon channel 140

6.14. Results of the binned maximum likelihood fit - electrons 142

6.15. Results of the binned maximum likelihood fit - muons 142

6.16. Error ellipses in the $((f_{\mathrm{L}} - f_{\mathrm{R}}), f_0)$ plane for the electron channel 143

6.17. Error ellipses in the $((f_{\mathrm{L}} - f_{\mathrm{R}}), f_0)$ plane for the muon channel 143

6.18. Error ellipses in the $((f_{\mathrm{L}} - f_{\mathrm{R}}), f_0)$ plane for the combined fit 145

7.1. MC Distributions showing the L_{P} variable in the three highest S_T^{lep} bins . 149

7.2. Kinematic variables as measured in the muon control sample 158

7.3. Distribution of the L_{P} variable as measured in the muon control sample . 158

7.4. MC L_{P} shape comparison between selected and anti-selected QCD events 160

7.5. Results of fits to the QCD background shape in the electron channel . . . 161

7.6. Effect of a 15% shift in $(f_{\mathrm{L}} - f_{\mathrm{R}})$ on the electron L_{P} distribution 164

7.7. Comparison of L_{P} distributions between data and MC 168

7.8. Comparison of predicted and observed event yields in bins of S_T^{lep} 169

8.1. Illustration showing the use of the CL_{s} method 175

8.2. The negative log PL ratio as a function of μ 177

8.3. Distributions of the test statistic, q_μ 177

8.4. Signal efficiency for the muon channel in the CMSSM 179

8.5. Signal efficiency for the electron channel in the CMSSM 180

8.6. 95% confidence level exclusion plot for the CMSSM 181

8.7. Signal efficiency in the T3W simplified model 185

8.8. Limit in the T3W simplified model with M_χ set assuming $x = 0.25$ . . . 186

8.9. Limit in the T3W simplified model with M_χ set assuming $x = 0.5$ 187

8.10. Limit in the T3W simplified model with M_χ set assuming $x = 0.75$ . . . 187

8.11. Signal efficiencies for the muon channel in the T2tt simplified model . . . 188

8.12. Signal efficiencies for the electron channel in the T2tt simplified model . 189

8.13. Limit in the T2tt simplified model 190

B.1. The negative log PL ratio as a function of μ 204

B.2. Distributions of the test statistic, q_μ 204

List of Tables

2.1. Chiral supermultiplets in the MSSM 49

2.2. Gauge supermultiplets in the MSSM 49

5.1. Simple cut-based electron idenitification 92

6.1. W Polarisation fit results for a number of closure tests 111

6.2. Selection requirements for the W polarisation measurement 119

6.3. MC event yields in the electron channel of the W polarisation analysis . . 121

6.4. MC event yields in the muon channel of the W polarisation analysis . . . 122

6.5. Systematic uncertainties in the muon channel 137

6.6. Systematic uncertainties in the electron channel 137

6.7. Systematic uncertainties in the combined fit 138

6.8. Theoretical uncertainties in the W polarisation measurement 138

6.9. Summary of fit results in the W polarisation measurement 144

6.10. Summary of the W polarisation fit results for the QCD background . . . 145

6.11. Comparison of the W polarisation with theoretical predictions 146

7.1. SUSY search selection requirements 154

7.2. MC event yields in the signal region 155

7.3. MC event yields in the control region 155

7.4. Triggers used in the SUSY search analysis 156

7.5. Event yields in the muon control sample 157

7.6. Systematic uncertainties in the muon channel 166

7.7. Systematic uncertainties in the electron channel 167

7.8. Event yields in data and MC for the muon search sample 167

7.9. Event yields in the electron search sample 169

8.1. Summary of systematic uncertainties related to the signal efficiency . . . 178

B.1. Nuisance parameters included in the single lepton likelihood function . . 200

D.1. MC samples used in the W polarisation analysis 209

D.2. MC samples used in the SUSY analysis 210

Introduction

Most philosophers of science would probably agree that the process by which scientific revolutions unfold is understood either poorly or not at all. During such periods, and by some mysterious process, many of the foundational ideas within a given field are rapidly replaced or altered. Often the field that emerges is so vastly different from what went before as to be almost unrecognisable.

History is rich with examples across many scientific fields. A particularly spectacular case was the emergence of quantum mechanics in the early part of the 20th century. This instigated a seismic shift in physicists' understanding of the universe, tearing down many long-held beliefs, and bringing with it incredible progress.

In some ways, particle physics has become the victim of this great success. The quantum revolution of the 1920's led eventually to the formulation of the Standard Model (SM) of particle physics in the latter half of the 20th century. This theory has been so phenomenally successful that it has lasted, almost unchanged, for the last 30 years.

However, as is often the case in science, finding answers often yields further questions. In the second decade of the 21st century, particle physics faces a number of open questions, which seem to be unanswerable within the context of the SM; most disturbingly, the failure to combine gravity and quantum field theory in a single, unified theory. A related cause for concern has been the mounting, and at this point fairly conclusive, evidence for dark matter – a substance lacking any explanation within the SM.

It is for these reasons that many feel another revolution is long overdue. Of course, theoretical developments have continued at a rapid pace since the formulation of the SM. This has bred a zoo of colourful theories – string theory and loop quantum gravity being among the current favourites. However, without experimental results to guide theoretical progress, such theories can remain only mathematical curiosities. The crucial missing ingredient, many feel, is inspiration from the universe itself.

It is against this backdrop that the Large Hadron Collider (LHC), a next generation particle accelerator, has been constructed at the CERN particle physics laboratory near Geneva, Switzerland. Able to reach an unparalleled centre-of-mass energy of 14 TeV, hopes are high that this will open new doors to understanding the universe. Perhaps paradoxically, chief among its goals is the observation of a SM particle, the notorious Higgs boson, understood to give other particles their mass. First conceived in the 1960's, the Higgs has proved particularly elusive to experiment.

It may seem strange to hope for a radical reformation of the SM, whilst at the same time seeking to discover its last missing piece. However, this misses a crucial point about the nature of scientific discoveries – a null result is often the most disruptive. A particularly well-known example in recent history is the Michelson-Morley experiment [1]. In this case, a null result utterly debunked the prevailing theory at the time, the "luminiferous ether". This allowed special relativity to emerge as a superior theory of nature. Even if the Higgs is discovered at the LHC, as many expect it will be, measurement of its mass may provide essential insight to the shape of physics beyond the SM.

Many well-understood aspects of the SM will be tested once again at the LHC. This is important for a number of reasons. Firstly, from a purely pragmatic perspective, as a means of testing the various detectors before venturing into unknown territory. And secondly because, if history is any lesson, new physics can often appear in completely unexpected places.

The first part of the work in this thesis presents the results of just such a precision measurement – the polarisation of the W boson. Surprisingly the novelty of this measurement is not just due to the increased energy of the LHC. Rather, for reasons that will be explained, the proton-proton environment at the LHC leads to a dominance of left-handed over right-handed W bosons at large transverse momentum. This is an effect that has not been previously observed.

The tools developed for this measurement turn out to be more generally useful in searches for new physics. The second part of this thesis presents a search for a popular extension to the SM, known as Supersymmetry (SUSY). This is theoretically attractive for a number of reasons, not least that it provides a potential solution to the dark matter problem. Whilst SUSY is a fairly incremental step beyond the SM, and not the drastic paradigm shift many feel is necessary, it can be seen as a stepping-stone to further discovery. Most excitingly for the LHC, it makes solid, testable predictions in the form of a myriad of undiscovered particles. If these particles exist, they should be observed at the LHC.

The structure of this thesis is as follows. Chapter 1 begins with an introduction to the SM and an explanation of the Higgs mechanism. Chapter 2 will highlight the deficiencies of the SM and present SUSY as a possible solution. Chapter 3 introduces the theoretical background necessary for understanding the W polarisation measurement. Models of SUSY useful for interpreting experimental results will also be discussed.

Chapter 4 will introduce the LHC and the Compact Muon Solenoid (CMS) experiment – a large, general purpose detector designed for new physics searches as well as precision tests of the SM. Chapter 5 will then discuss the object reconstruction and selection requirements used for the analysis work presented in later chapters.

In Chapter 6 the W polarisation analysis will be presented. Particular attention will be paid to the electron channel of the measurement and the fitting procedure which was the focus of the author's work. Chapter 7 will then describe how this analysis was adapted to search for SUSY in events with a single lepton, jets and missing energy. Finally, Chapter 8 will take the results of this search and provide interpretation within the context of several theoretical models.

Unless indicated otherwise, "natural units" should be assumed throughout, in which $\hbar = c = 1$.

Chapter 1.

The Standard Model

1.1. Introduction

The Standard Model of particle physics is the best available theory describing the interactions of all known fundamental particles [2–10]. It is perhaps the most extensively tested of any fundamental theory of nature, having withstood the scrutiny of several decades of data-taking at a multitude of experiments. However, despite this success, there appear to be a number of major theoretical deficiencies in desperate need of attention. In this chapter, the foundations of the theory will be laid out in a concise manner. As well as being of direct relevance to the measurement described in Chapter 6, this will inform discussion of the aforementioned theoretical issues, and potential solutions, in Chapter 2.

It is important to note that, although the SM will be presented here as a complete theory, seemingly designed to match the currently observed set of fundamental particles, this is not how it came into being. The theory was built up over much of the second half of the 20th century and actually successfully predicted a number of discoveries. Perhaps the best example of this is the discovery of the W and Z bosons by the UA1 and UA2 experiments at CERN in 1983 [11, 12]. These had been theorised by Weinberg, Glashow and Salam in 1968 [6–8].

1.2. Particles and Fundamental Forces

The SM incorporates three of the four known fundamental forces, namely: electromagnetism, the weak nuclear force and the strong nuclear force. The other force, gravity, having resisted unification with the other three, is not part of the SM.

Within the SM, each fundamental force is mediated by one or more *gauge bosons*. For electromagnetism, this is the photon, for the weak force, the W^+, W^- and Z bosons. Strong interactions are mediated by a set of 8 *gluons* (g). The bosons are all vector particles with a spin of 1.

As a complete theory of the known fundamental particles, the SM must also describe the many matter particles discovered by experiment. These are the *fermions*, of which there are two varieties – leptons and quarks. The leptons, or "light particles", make up three generations. Each generation associates a relatively heavy charged lepton with a much lighter neutral partner, a *neutrino*. The charged leptons are: the electron (e), the muon (μ) and the tau lepton (τ). Each has identical charge, typically written in terms of the charge carried by a single electron, e. The corresponding neutral leptons are then referred to as the electron neutrino (ν_e), muon neutrino (ν_μ) and tau neutrino (ν_τ).

The quarks are also arranged in three generations, with two quarks occupying each. The first of each generation is referred to as an "up-type" quark and has charge $+\frac{2}{3}e$, the second "down-type" with charge $-\frac{1}{3}e$. The up-type quarks are (in order of increasing mass): up (u), charm (c) and top (t)[1]. Similarly, the respective down-type partners are: down (d), strange (s) and bottom[2] (b). In addition to electromagnetism and the weak force, quarks interact via the strong nuclear force.

Each of the fermions is associated with an anti-particle partner, with opposite charge. For the charged leptons, the charge may be indicated by a superscript, e.g. e^+, e^-, μ^+, μ^- etc. For the quarks, the anti-particles will normally be denoted $\overline{u}$, $\overline{d}$ etc. In the case of the neutrinos, being electromagnetically neutral, the question of the nature of the anti-particles is as yet unanswered. It is theoretically possible for a neutrino to be its own anti-particle, $\nu_\ell = \overline{\nu}_\ell$. This would make the neutrino a "Majorana Fermion" [13] and is an area of active experimental research [14].

The particle content and properties of the SM seem, at first glance, to be quite arbitrary. Why are there three forces? Why does the Weak sector have three bosons, and the

[1] also known as truth
[2] also known as beauty

electromagnetic only one? Some of these questions may be answered by constructing the SM as a so-called *gauge theory*. This will be explained in the next section.

1.3. Electroweak Gauge Theory

1.3.1. Gauge Invariance

The theoretical principle of gauge invariance can be seen in Maxwell's theory of electromagnetism [2]. Recall that the electric, $\vec{E}$, and magnetic, $\vec{B}$, components of the field may be written in terms of a vector potential, $\vec{A}$, and a scalar potential, V, as follows:

$$\begin{aligned} \vec{B} &= \vec{\nabla} \times \vec{A} \quad \text{and} \\ \vec{E} &= -\vec{\nabla} V - \frac{\partial \vec{A}}{\partial t}. \end{aligned}$$

It can be seen that these equations do not relate a given ($\vec{B}$, $\vec{E}$) to unique values of $\vec{A}$ and V. In particular, if the following transformations are applied simultaneously to $\vec{A}$ and V, the values of $\vec{B}$ and $\vec{E}$ will be unchanged,

$$\begin{aligned} \vec{A} &\longrightarrow \vec{A} + \vec{\nabla}\chi \quad \text{and} \\ V &\longrightarrow V - \frac{\partial \chi}{\partial t}, \end{aligned}$$

where χ is some arbitrary function of spacetime. Such transformations are known as *gauge transformations* and $\vec{B}$ and $\vec{E}$ are said to be *gauge invariant*.

If the scalar and vector potentials are rewritten in terms of a single 4-vector potential, $A^\mu = (V, \vec{A})$ and taking a 4-vector differential operator, $\partial^\mu = (\partial/\partial t, -\vec{\nabla})$, the gauge transformation takes the form

$$A^\mu \longrightarrow A^\mu - \partial^\mu \chi. \tag{1.1}$$

In this form, the Maxwell equations can be rewritten as

$$\partial_\mu F^{\mu\nu} = j^\nu_{\text{em}},$$

where $F^{\mu\nu}$ is the electromagnetic tensor, defined as

$$F^{\mu\nu} = \partial^\mu A^\nu - \partial^\nu A^\mu.$$

and j^ν_{em} is the *current*. It can be seen that $F^{\mu\nu}$ is invariant under the gauge transformation (Eqn. 1.1) and thus the Maxwell equations are gauge invariant.

1.3.2. The Principle of Least Action and Lagrangian Formalism

Before continuing, it is useful to review the Lagrangian formalism and the principle of least action. The action, S, is a quantity associated with a physical system, used to characterise its dynamics. The action can be written

$$S = \int dt L = \int d^4x \mathcal{L},$$

where L is the *Lagrangian*, and $\mathcal{L}$ the *Lagrangian density* and

$$L = \int d^3x \mathcal{L}.$$

The Lagrangian is a function of some generalised coordinates, ϕ_i, describing the dynamics of the system and their derivatives, $\partial^\mu \phi_i$. From this, the Euler-Lagrange relation can be used to derive an equation of motion for the system [4],

$$\frac{\partial \mathcal{L}}{\partial \phi_i} - \partial_\mu \left(\frac{\partial \mathcal{L}}{\partial \left(\partial_\mu \phi_i \right)} \right) = 0.$$

By writing down a suitable Lagrangian, a theory may be fully described. However, in order to perform calculation of real, measurable quantities, the theory must first be quantised. This is a complex procedure involving *renormalisation* techniques which are beyond the scope of this discussion. We shall only note that renormalisability requires a theory with dimensionality at most $[M]^4$ i.e. mass to the fourth power [4].

1.3.3. A Real Scalar Field

To see how a theory can be written in terms of a Lagrangian, we will first approach a highly simplified example, namely that of a *real scalar field*. The Lagrangian density for

such a theory may be written as follows:

$$\mathcal{L} = \frac{1}{2}\left(\partial_\mu \phi(x)\right)\left(\partial^\mu \phi(x)\right) - \frac{1}{2}m^2\phi^2(x) - \frac{\lambda}{4!}\phi^4(x). \tag{1.2}$$

The three components of this expression are known respectively as the *kinetic term*, the *mass term* and the *interaction term*. The field ϕ is a function of spacetime coordinates x representing a single kind of particle ϕ, m is the mass of the particle and λ a constant controlling the strength of the interaction between particles in the theory.

Setting $\lambda = 0$ and applying the Euler-Lagrange relations to Equation 1.2, one obtains

$$\partial^\mu \partial_\mu \phi + m^2\phi = 0.$$

This can be recognised as the Klein-Gordon equation describing the motion of a scalar particle.

1.3.4. Symmetries

It can be seen that the Lagrangian of Eqn. 1.2 is invariant under certain transformations. In particular, it has been constructed to obey the symmetry $\phi \longrightarrow -\phi$. Such symmetries are known as global symmetries of the theory – global in the sense that they are performed identically at all points in spacetime. These symmetries can be classified in terms of the mathematical theory of groups.

Noether's theorem states, that for a theory with a continuous symmetry, each generator of the symmetry group corresponds to a conserved current in the theory [15]. This elucidates many aspects of the physics of a given theory by considering only its symmetries.

1.3.5. Complex Scalar Fields and the Gauge Principle

We will now take a slightly more realistic example – that of a complex scalar field. The Lagrangian for this theory may be written as follows,

$$\mathcal{L} = \frac{1}{2}\left(\partial_\mu \phi(x)\right)\left(\partial^\mu \phi(x)\right)^* - \frac{1}{2}m^2\left|\phi(x)\right|^2 - \frac{\lambda}{4!}\left|\phi(x)\right|^4, \tag{1.3}$$

where the field ϕ is now a complex quantity. This field is seen to possess an additional symmetry,

$$\phi \longrightarrow e^{i\theta}\phi, \tag{1.4}$$

where θ is some arbitrary parameter (constant, for the moment, in spacetime). This is known as a global $U(1)$ symmetry and has a single generator - and therefore, by Noether's theorem, a single conserved current.

The transformation of Eqn. 1.4 can be extended such that the parameter θ becomes a function of the spacetime coordinate, x - a *local* symmetry transformation. The Lagrangian is then no longer invariant with respect to this transformation. The symmetry is said to be *broken*, with the Lagrangian acquiring additional terms,

$$\delta\mathcal{L} = (\partial_\mu\theta)\left[i\left(\partial^\mu\phi^*\right)\phi - i\phi^*\left(\partial^\mu\phi\right)\right] + (\partial_\mu\theta)\left(\partial^\mu\theta\right)|\phi|^2 . \tag{1.5}$$

In order to compensate for this change, we define the *covariant derivative* as follows

$$D_\mu = \partial_\mu + igB_\mu(x), \tag{1.6}$$

where B is taken to be a new four-vector field and g a constant. This operator must transform under a change of phase in such a way as to cancel the additional terms in Eqn. 1.5. The Lagrangian would then be rewritten as follows,

$$\mathcal{L} = (D_\mu\phi)\left(D^\mu\phi\right)^* - \frac{1}{2}m^2|\phi|^2 - \frac{\lambda}{4!}|\phi|^4 .$$

It can be shown that this requires the B_μ field to transform as follows

$$B_\mu \longrightarrow B'_\mu = B_\mu - \frac{1}{g}\partial_\mu\theta.$$

This is seen to be the same transformation as that applied to the electromagnetic four-vector field in Eqn. 1.1. By requiring the fields to be symmetric under a local $U(1)$ phase transformation, a new field must be introduced. This field then appears as a gauge boson in the theory – in this case an analogue of the photon. Incorporating the Maxwell equations into the Lagrangian, one arrives at Scalar Quantum Electrodynamics (SQED),

$$\mathcal{L} = -\frac{1}{4}F_{\mu\nu}F^{\mu\nu} + (D_\mu\phi)\left(D^\mu\phi\right)^* - \frac{1}{2}m^2|\phi|^2 - \frac{\lambda}{4!}|\phi|^4 . \tag{1.7}$$

The procedure which has just been outlined is an example of the *gauge principle* [5]. This might seem an interesting, but trivial result, but it turns out that all particles and interactions of the SM (see Section 1.2) can be predicted by essentially repeating this procedure with larger symmetry groups.

1.3.6. Yang-Mills Theory

We have seen how the gauge principle can be applied, within a highly simplified model, to predict the existence of gauge bosons by enforcing a local symmetry. This will now be extended to "larger" symmetry groups.

Extending the symmetry group to $SU(2)$ and replacing the single complex field ϕ by a vector of complex fields Φ [4, 5],

$$\begin{aligned} \Phi \longrightarrow \Phi' &= \exp\left(i\alpha^a(x)T^a\right)\Phi \quad \text{and} \\ D_\mu &= \partial_\mu + igA^a_\mu T^a, \end{aligned}$$

where T^a are the generators of the group $SU(2)$, $T^a = \frac{1}{2}\sigma^a$, the index $a = 1, 2, 3$ and the σ^a are the well-known Pauli matrices. The parameter $\alpha^a(x)$ is the analogue of $\theta(x)$ in Eqn. 1.4 and g is a constant. Notice that this symmetry group predicts the existence of three gauge bosons A^a_μ – matching the three weak gauge bosons: Z, W^+ and W^-. This is an example of a Yang-Mills theory [16].

An important aspect of this toy theory is related to the structure of the symmetry group $SU(2)$. In particular, the generators of this symmetry group do not commute – they are said to be *non-Abelian*. This requires the Lagrangian to be modified to maintain local gauge invariance,

$$\begin{aligned} \mathcal{L} &= -\frac{1}{4}F^a_{\mu\nu}F^{a\mu\nu} \quad \text{where} \\ F^a_{\mu\nu} &= \partial_\mu A^a_\nu - \partial_\nu A^a_\mu + gf^{abc}A^b_\mu A^c_\nu, \end{aligned}$$

and f^{abc} are known as *structure constants* of the group $SU(2)$. The additional quadratic terms in the Lagrangian lead to self interactions, just as is observed in the weak sector.

It would seem that a model based on a symmetry group $SU(2) \times U(1)$ would appear to give the correct number of degrees of freedom for a unification of the electromagnetic and weak nuclear forces. One immediate problem is the fact that the weak bosons are

known to be massive. It is not possible to introduce straightforward mass terms into the Lagrangian whilst maintaining gauge invariance. Another more subtle issue is that the W^+ and W^- would be uncharged in this picture, since the $SU(2)$ component is able to commute with the $U(1)$ part.

1.3.7. Spin and Chirality

Having arrived at a toy gauge theory bearing some similarity to the SM, it is important to introduce a concept not yet represented in the theory. The Lagrangians presented so far have worked only with scalar fields, but these are known to not represent the physical world. In reality, particles have intrinsic angular momentum or *spin*.

Fermionic degrees of freedom are represented as *spinors*. These transform in a different manner to vectors under spatial rotations. In addition, they obey a different equation of motion, known as the *Dirac Equation* [4],

$$(i\gamma^\mu \partial_\mu - m)\,\Psi = 0,$$

where Ψ is a spinor and γ^μ are known as the Dirac matrices (see e.g. [2]). The Dirac matrices obey the anti-commutation relation $\{\gamma^\mu, \gamma^\nu\} = 2g^{\mu\nu}$ where $g^{\mu\nu}$ is the spacetime metric. A suitable Lagrangian may be written as

$$\bar{\Psi}\,(i\gamma^\mu \partial_\mu - m)\,\Psi \qquad \text{where} \qquad \bar{\Psi} = \Psi^\dagger \gamma^0.$$

An important aspect of spinors is a property known as "handedness" or *chirality*. Spinors have both *left-handed* and *right-handed* components. A particle's chirality is related to its transformation properties under the Poincaré group – the symmetry group of spacetime.

Physically speaking, a right-handed particle is one whose spin is aligned with its direction of motion and a left-handed one whose spin is oppositely aligned. Note that a left-handed anti-spinor corresponds to a right handed physical particle [4].

A related, but distinct concept, is *helicity*. Helicity is the projection of a particle's spin, $\vec{S}$ onto its momentum, $\vec{p}$ [4],

$$h = \frac{\vec{S}.\vec{p}}{|\vec{p}|}.$$

In cases where the particle's spin is aligned with its momentum, it is said to have right-handed helicity. In cases where it is anti-aligned, it has left-handed helicity. For massless particles, the helicity and chirality states are equivalent, and the helicity must be non-zero. Particles with helicity, $h = \pm 1$, are said to be *transversely polarised* and $h = 0$, *longitudinally polarised*.

1.3.8. The Electroweak Theory

A striking property of the electroweak theory is the observation of parity violation by Wu et al. [17] in the β decay of Cobalt-60 atoms. The spins of the atoms were polarised by a magnetic field. The angular distribution of the β electrons was then measured. It was seen that electrons were emitted preferentially in the direction opposite to their spin. This implies that the anti-neutrino's spin is always aligned with its momentum – i.e. it is right-handed. And similarly the neutrino is always left-handed. More generally, the charged weak current couples only left-handed particles and right-handed anti-particles. Parity is thus said to be *maximally* violated. The coupling of the weak bosons has a "vector minus axial" or $(\mathrm{V} - \mathrm{A})$ form which leads to parity violation. Parity violation will be of vital importance to the analysis presented in Chapter 6.

It is not necessary for us to fully detail the electroweak sector of the SM Lagrangian. For the sake of completeness, an outline of the construction of the theory will be given. Firstly, the symmetry group chosen is $SU(2)_{\mathrm{L}} \times U(1)_{Y}$ where the subscript L indicates a coupling only to left-handed spinors. The Y refers to the fact that the $U(1)$ group here is not electromagnetism but *hypercharge*. This is essential to overcoming the issues with $SU(2) \times U(1)$ which have already been described.

The fermions themselves are placed into *isospin* doublets, coupling a charged lepton with a neutrino [5],

$$\Psi_{\mathrm{L}} = \begin{pmatrix} \nu_{\mathrm{L}} \\ \ell_{\mathrm{L}} \end{pmatrix},$$

where ν_{L} and ℓ_{L} are left-handed spinor fields representing a neutral and charged lepton respectively. The right-handed component of the charged lepton (which *does* interact electromagnetically) is incorporated as an isospin singlet,

$$\Psi_{\mathrm{R}} = \ell_{\mathrm{R}}.$$

Dividing the Lagrangian as follows,

$$\mathcal{L} = \mathcal{L}_{\text{gauge}} + \mathcal{L}_{\text{free}},$$

and writing the analogue of the tensor, $F^{\mu\nu}$, for the gauge group $SU(2)_{\text{L}} \times U(1)$, one obtains

$$\mathcal{L}_{\text{gauge}} = -\frac{1}{4} W^{a\mu\nu} W^a_{\mu\nu} - \frac{1}{4} B^{\mu\nu} B_{\mu\nu},$$

where

$$\begin{aligned} W^a_{\mu\nu} &= \partial_\mu W^a_\nu - \partial_\nu W^a_\mu + g f^{abc} W^b_\mu W^c_\nu \quad \text{and} \\ B_{\mu\nu} &= \partial_\mu B_\nu - \partial_\nu B_\mu. \end{aligned}$$

The piece of the Lagrangian for free leptons is then,

$$\mathcal{L}_{\text{leptons}} = \bar{\Psi}_{\text{L}} i\gamma^\mu D_\mu \Psi_{\text{L}} + \bar{\Psi}_{\text{R}} i\gamma^\mu D_\mu \Psi_{\text{R}}.$$

with the covariant derivative

$$D_\mu = \partial_\mu + igW^a_\mu T^a + ig' B^\mu \frac{Y}{2},$$

where $T^a = \frac{1}{2}\sigma^a$ when acting on the left-handed doublet and zero otherwise. Similarly, the hypercharge Y is -1 for the doublet and -2 for the singlet [5]. The g and g' are coupling constants.

The physical W^+ and W^- bosons are superpositions [5],

$$\text{W}^\pm{}_\mu = \frac{1}{\sqrt{2}} \left(\text{W}^1_\mu \mp \text{W}^2_\mu \right),$$

as are the photon and Z boson,

$$\begin{pmatrix} A_\mu \\ Z_\mu \end{pmatrix} = \begin{pmatrix} \cos\theta_{\text{W}} & \sin\theta_{\text{W}} \\ -\sin\theta_{\text{W}} & \cos\theta_{\text{W}} \end{pmatrix} \begin{pmatrix} B_\mu \\ W^3_\mu \end{pmatrix},$$

where θ_{W} is known as the Weinberg angle. It is related to the coupling constants g and g' by

$$\sin\theta_{\mathrm{W}} = \frac{g'}{\sqrt{g + g'^2}} \tag{1.8}$$

$$\cos\theta_{\mathrm{W}} = \frac{g}{\sqrt{g + g'^2}}. \tag{1.9}$$

The $U(1)_{\mathrm{EM}}$ symmetry describing electromagnetism is now formed from a superposition of generators in the $SU(2)$ and $U(1)_{\mathrm{Y}}$ groups. This model now includes the correct charge assignments to the gauge bosons. Parity violation in the weak sector has also been included.

1.3.9. Remaining Issues

The above model is now remarkably close to the full electroweak theory. Unfortunately, two major problems remain – both of them relating to mass. Firstly, the leptons do not yet have mass. Naively, one might be tempted to add a mass term with the following form:

$$m\bar{\Psi}_{\mathrm{L}}\Psi_{\mathrm{L}} = m(\overline{\nu}_{\mathrm{L}}\nu_L + \overline{\ell}_{\mathrm{L}}\ell_{\mathrm{L}}).$$

However, terms of this form are required to vanish. This can be seen by applying left-handed and right-handed projection operators to the spinors. The second issue relates to the mass of the gauge bosons – in particular how to generate masses for the W^+, W^- and Z bosons whilst leaving the photon massless. Both issues will be addressed in the next section.

1.4. Electroweak Symmetry Breaking

In order to give mass to the weak gauge bosons, as well as other fermions in the SM), a mechanism known as Electroweak Symmetry Breaking (EWSB) is employed [18]. This posits that, although the actual Lagrangian is invariant under a certain symmetry group, the vacuum state of the theory is not.

1.4.1. A Real Scalar Field

To illustrate EWSB, we will return to a simplified model with a single real scalar field

$$\mathcal{L} = (\partial^\mu \phi)(\partial_\mu \phi) - V(\phi),$$

where V is the potential,

$$V(\phi) = \frac{1}{2}\mu^2\phi^2 + \frac{1}{4}\lambda\phi^4.$$

The lowest energy states, ϕ_0, are spacetime independent ($\partial_\mu \phi_0 = 0$) and minimising V we find [15],

$$\phi_0\left(\mu^2 + \lambda\phi_0^2\right) = 0.$$

To ensure that the total energy is bounded below, λ should be positive. For $\mu^2 > 0$, there is one solution $\phi_0 = 0$. For $\mu^2 < 0$, there are two solutions $\phi_0^\pm = \pm\sqrt{-\mu^2/\lambda}$. Recall that the initial Lagrangian is invariant under the transformation $\phi \longrightarrow -\phi$. Given that one of the two possible vacua must be chosen, the vacuum is no longer invariant under this symmetry. Furthermore, it is possible to expand around the new vacuum (i.e. either ϕ_0^+ or ϕ_0^-), $v = \sqrt{-\mu^2/\lambda}$ and define a new field ϕ' such that

$$\phi' \equiv \phi - v.$$

The Lagrangian becomes

$$\mathcal{L} = \frac{1}{2}(\partial_\mu \phi')(\partial^\mu \phi') - \frac{1}{2}\left(\sqrt{-2\mu^2}\right)^2 \phi'^2 - \lambda v \phi'^3 - \frac{1}{4}\lambda\phi'^4,$$

which, with the addition of the ϕ^3 term, no longer respects the $\phi \longrightarrow -\phi$ symmetry.

1.4.2. A Complex Scalar Field and Goldstone's Theorem

Moving now to the case of a complex scalar field,

$$\mathcal{L} = (\partial_\mu \phi)(\partial^\mu \phi^*) - V(\phi^* \phi),$$

where the potential is written

$$V\left(\phi^*\phi\right) = \mu^2\left(\phi^*\phi\right) + \lambda\left(\phi^*\phi\right)^2,$$

the vacua are now $|\phi_0|^2 = -\mu^2/2\lambda$. The vacuum is now symmetric under a global $U(1)$ symmetry (as is the original Lagrangian). Writing

$$\phi = \frac{1}{\sqrt{2}}\left(\phi_1 + i\phi_2\right),$$

and picking a vacuum configuration $\phi_1 = v$, $\phi_2 = 0$ we can once again expand around the new vacuum. This yields the Lagrangian,

$$\mathcal{L} = \frac{1}{2}\left(\partial_\mu\phi_1'\right)\left(\partial^\mu\phi_1'\right) - \frac{1}{2}\left(-2\mu^2\right)\phi_1'^2 + \frac{1}{2}\left(\partial_\mu\phi_2'\right)\left(\partial^\mu\phi_2'\right) + (\text{interaction terms}).$$

We can now identify a massive scalar field ϕ_1 and a massless scalar field ϕ_2. This is an example of Goldstone's theorem – when an exact continuous global symmetry is broken, a massless scalar field will appear for each broken group generator [19, 20]. In this case, the original $U(1)$ symmetry of the group has been broken, resulting in a single massless Goldstone boson.

1.4.3. The Higgs Mechanism

Massless scalar Goldstone bosons are theoretically undesirable as they have not been observed by experiment. Fortunately, the Higgs mechanism [9, 10, 21] offers a solution to this problem, while also giving the necessary mass to the weak gauge bosons. This is accomplished by extending the global symmetry shown above to a local one.

Consider again the case of SQED (Eqn. 1.7). For small perturbations, the fields may be expanded around the vacuum as follows,

$$\phi = \exp\left(i\frac{\phi_2'}{v}\right)\frac{1}{\sqrt{2}}\left(\phi_1' + v\right) \approx \phi' + \frac{v}{\sqrt{2}}.$$

where

$$\phi' = \frac{1}{\sqrt{2}}\left(\phi_1' + i\phi_2'\right).$$

When substituted into the Lagrangian, this gives

$$\mathcal{L} = \frac{1}{2}\left(\partial_\mu \phi_1'\right)\left(\partial^\mu \phi_1'\right) - \frac{1}{2}\left(-2\mu^2\right){\phi_1'}^2 + \frac{1}{2}\left(\partial_\mu \phi_2'\right)\left(\partial^\mu \phi_2'\right) + (\text{interaction terms}) \\ -\frac{1}{4}F_{\mu\nu}F^{\mu\nu} + \frac{g^2 v^2}{2}A_\mu A^\mu + gvA_\mu\left(\partial^\mu \phi_2'\right). \quad (1.10)$$

Two things should be noted about the resulting Lagrangian. Firstly, that the second term implies the existence of a scalar field with mass $\sqrt{-2\mu^2}$. Secondly that the vector boson A_μ has acquired a mass, gv – due to the second-to-last term in Eqn. 1.10. The last term in Eqn. 1.10 is problematic, but can be removed by moving to the *unitary gauge* [4].

It can be seen that the Goldstone boson has been absorbed into the vector boson, adding an additional degree of freedom and causing it to acquire mass. This is the essence of the mechanism employed in the SM to give mass to the weak gauge bosons whilst leaving the photon massless. The $SU(2)_{\mathrm{L}} \times U(1)_Y$ symmetry of the SM is broken down to the $U(1)_{\mathrm{EM}}$ symmetry of electromagnetism. Goldstone bosons for each broken generator are absorbed by the W^+, W^- and Z– giving them mass. The symmetry corresponding to electromagnetism remains unbroken, and hence the photon remains massless.

It should be noted that the Higgs mechanism also predicts the existence of a massive scalar (a spin-0 particle) – the ϕ field in the Lagrangian above. This is the famous Higgs particle which has been the focus of many recent particle physics experiments – including the LHC.

1.4.4. Yukawa Couplings

It was noted in Section 1.3.9 that it is not possible to write down a straightforward mass term for the fermions in the electroweak theory. It turns out that this problem is also solved by the Higgs mechanism with the addition of a *Yukawa coupling* term to the Lagrangian [4],

$$\mathcal{L} = g\left(\bar{\Psi}_{\mathrm{L}}\phi\Psi_{\mathrm{R}} + \bar{\Psi}_{\mathrm{R}}\phi^\dagger\Psi_{\mathrm{L}}\right),$$

where ϕ is the Higgs field. When ϕ acquires a vacuum expectation value via EWSB, it can be seen that the fermion field Ψ acquires a mass-like term – with

$$m_\Psi = \frac{gv}{\sqrt{2}}.$$

It is thought that all SM fermions acquire mass in this way.

1.5. Quantum Chromodynamics

The preceding discussion has covered only the electroweak sector of the SM - leptons, electroweak gauge bosons and the Higgs particle. The strong force is incorporated within the framework of Quantum Chromodynamics (QCD) [4, 22]. Whilst this at first appears to be quite straightforward, certain properties of the strong force often make calculations considerably more difficult. Here, a brief summary of the theory will be given with further details available in [22].

1.5.1. Quarks

The quarks can be included in the SM in a similar manner to the leptons. The left-handed components of up and down type are paired into doublets,

$$Q = \begin{pmatrix} \mathrm{u_L} \\ \mathrm{d_L} \end{pmatrix}.$$

There is one such doublet for each of the three generations. The right-handed components are once again placed in a singlet representation.

The weak eigenstates of the quarks are rotated with respect to their mass eigenstates via the Cabibbo Kobayashi Maskawa matrix [23, 24]. This encodes the strength of various flavour-changing weak decays.

1.5.2. Colour

Inclusion of QCD in the SM continues in the same manner as for the electroweak force. The local gauge symmetry group is extended to include an additional product, $SU(3)_C$ where the C indicates a new conserved quantity – *colour charge*. The quarks – of which six flavours are currently known – each carry one of three colour charges. These are labelled *red*, *green* and *blue*. As before, local invariance under this transformation group requires the introduction of a covariant derivative and a set of 8 gauge bosons – the gluons.

1.5.3. Unique Properties

In the case of the weak force, it was seen that the non-Abelian generators of the $SU(2)$ group give rise to self-interactions in the gauge bosons. The same is true for the $SU(3)$ gauge group of QCD. However, in this case the situation is further complicated by the energy-scaling behaviour of the strong coupling constant.

At large energies – or equivalently, short distances – the strong coupling constant becomes relatively small [25] and perturbation theory can be used reliably. This is a phenomenon known as *asymptotic freedom* [26]. At lower energies (or long distances), the coupling constant becomes much larger. This causes the theory to become highly non-linear [27] and standard perturbation theory can no longer be used.

An additional phenomenon, not predicted by perturbation theory [28] is *confinement*. Confinement forbids the existence of free quarks, forcing them to exist only as bound states - baryons or mesons. This observation has been repeatedly confirmed by a number of experimental searches [29, p. 30].

Many additional techniques have been developed to tackle these difficulties, for instance Lattice QCD [25]. In spite of this, QCD processes are often poorly understood, particularly at low energies. This has important consequences for high energy physics experiments and will be an important consideration in subsequent chapters.

Having covered necessary material on the SM, it can be seen that the SM appears to be enormously successful in explaining the fundamental particles and forces so far observed in experiments. Seemingly, the only remaining issue is the discovery of the Higgs boson, which has not yet been observed experimentally. However, even with the Higgs boson discovered, a number of additional problems remain. These will be explored in the next chapter.

Chapter 2.

Supersymmetry

The SM describes all the known fundamental particles and interactions to an incredible degree of accuracy. What cause is there to believe that there might be physical phenomena not described by this theory? This will be the topic we now turn to.

2.1. Limitations of the Standard Model

A limitation of the SM, which is readily apparent, is that it makes no attempt to unify gravity with the other fundamental forces. From a purely experimental perspective, this is not an issue, since no experiment is able to explore gravitational effects at the quantum scale. This is unlikely to change in the foreseeable future. However, it seems clear to many theorists that a quantised theory of gravity must exist, and indeed this has been the focus of great theoretical effort over the last thirty years. Several potential theories have emerged, aiming to provide an entirely unified picture of fundamental physics; two examples being *string theory* [30] and *loop quantum gravity* [31]. Whilst proponents of these theories have been criticised for devising untestable hypotheses, it seems certain that some New Physics (NP) must be present to give a more unified physical theory.

It should be noted that the SM, as initially formulated, is unable to account for the phenomenon of *neutrino oscillation* [29] – transitions in flight between the neutrino flavour eigenstates (ν_e, ν_μ and ν_τ). Neutrino oscillation, first observed in solar and atmospheric neutrinos [32, 33], indicates that neutrinos are massive – a property not incorporated into the SM. There are a number of extensions to the SM proposed to explain this observation, the simplest of which introduces a set of right-handed neutrino fields [29].

2.1.1. The Hierarchy Problem

The *hierarchy problem* is arguably one of the strongest theoretical arguments for physics beyond the SM. This relates to the apparently huge difference between the weak mass scale, M_{weak}, and the *Planck scale* of gravity, M_{planck} – over 16 orders of magnitude. To some, it seems unthinkable that no new physics should appear in this vast range of energies [34].

As well as being aesthetically undesirable, the hierarchy problem presents a real theoretical issue for the mass of the Higgs boson. The Higgs boson mass receives quantum corrections from every particle that it couples to – directly or indirectly. These corrections have the form [34, 35],

$$\Delta {m_{\text{H}}}^2 = -\frac{|\lambda_f|^2}{8\pi^2}{\Lambda_{\text{UV}}}^2 + \ldots, \tag{2.1}$$

where λ_f is the coupling constant to a fermion f and Λ_{UV} is the momentum cut-off regulating the loop integral. All SM fermions can contribute to this correction, but it is largest for the top quark, where $\lambda_f \approx 1$. Interpreting Λ_{UV} as the scale at which new physics should appear to alter the behaviour of the theory and taking this to be the Planck scale, these corrections are found to be 30 orders of magnitude larger than the expected Higgs mass (≈ 100 GeV).

Whilst it might seem possible to just pick a small value of Λ_{UV}, this would require some form of new physics at this scale to alter the propagators in the loop as well as cutting off the loop integral. As will be seen SUSY provides a neat solution to this problem.

2.1.2. Dark Matter

The problem of dark matter is perhaps the most convincing argument, at least to experimentalists, for the existence of some physics beyond the SM. It was observed as early as 1932 [36] that galactic rotation curves appear to be at odds with those predicted from estimates of their visible mass. This seems to suggest a great deal of additional mass, or *dark matter*, is present in the galaxy, over and above that which can be inferred by direct observation. This observation is confirmed by measurements of gravitational lensing [37] and mapping of the cosmic microwave background [38]. Current observations suggest dark matter comprises about 80% [38, Table 8] of the matter content of the universe. No experimentally confirmed theory is able to explain this.

One possible explanation is that the universe is populated with massive particles that interact only via the weak force (and gravity). These Weakly Interacting Massive Particles (WIMPs) would therefore be invisible. Experiments hoping to directly detect such a particle have been underway for some time. Typically, these employ a large volume of a suitable gas or liquid, in the hope that passing WIMPs will undergo a nuclear interaction which may then be detected. Whilst some experiments have claimed discoveries, the evidence is not yet believed to be conclusive [39].

A related issue is that of *dark energy* – believed to constitute nearly three-quarters of the mass-energy content of the universe [38]. Like dark matter, this also has no basis in currently accepted theories of particle physics. Taken together, these phenomena are strong evidence of physics beyond the SM.

2.2. Beyond the Standard Model

Having provided some motivation for looking beyond the SM towards a more complete theory, one might ask what sort of new physics might be expected. An extremely large number of potential theories have been proposed. The majority of these can be categorised as follows[1]:

- a shift beyond gauge theories to an entirely new theoretical paradigm;
- an extension of the SM gauge group by an additional symmetry – either by a simple product or by embedding into some larger group or
- an extension of the symmetry group of spacetime – the Poincaré group.

Examples of the first approach have already been mentioned – string theory, loop quantum gravity and numerous others. Nothing further will be said of these except that, whilst not making predictions which are directly testable by contemporary experiments, they do, in certain cases, suggest extensions of the SM, which might fit under the second and third categories (for instance in the case of supersymmetry).

Many attempts have been made to construct a Grand Unified Theory using the second approach. The Georgi-Glashow model, for instance, embeds the SM into the $SU(5)$

[1]This list is not intended to be exhaustive but only to highlight a few popular approaches to the problem.

group [40]. This suffers from a number of problems – in particular predicting unstable protons – but is otherwise quite successful as a description of the SM.

Finally, the last kind of extension has also attracted considerable theoretical interest. Much of this was forever stymied by a so-called "no go theorem" published by Coleman and Mandula in 1967 [41]. This essentially forbids a class of extensions to the SM which attempt to combine the Poincaré group with an additional symmetry beyond just as a simple product. Put precisely [35], the Lie algebra representing the continuous symmetries of the S-matrix, containing as subalgebras the Poincaré Lie algebra and some other Lie algebra defined by generators T^a and structure constants t_c^{ab}, must be a direct sum of the two algebras i.e.

$$[T^a, P_\mu] = [T^a, M_{\mu\nu}] = 0,$$

where P_μ and $M_{\mu\nu}$ are generators representing translations and rotations/boosts in the Poincaré group. Commutativity of the generators implies that the group may be separated into a simple product of two groups.

However, one of the technical requirements of this theorem – that it applies exclusively to Lie algebras – points to a potential escape route. As will be seen, this limitation allows Supersymmetry (SUSY) to neatly sidestep the Coleman-Mandula theorem and introduce an additional, non-trivial space-time symmetry. The next section will explain how this is done and, importantly how it solves the issues introduced in Section 2.1.

2.3. Supersymmetry

2.3.1. An Additional Symmetry

The central concept of SUSY is to introduce an additional spacetime symmetry – one relating bosons and fermions [35]. At first this might seem to fall foul of the Coleman-Mandula theorem. It can be seen that this additional "supersymmetry" must be represented by an anti-commuting spinor, Q_a (where the subscript a is a spinor index). Like other spinors, this has an anti-spinor, $Q_a^\dagger$. The algebra representing this transformation is no longer a Lie Algebra, which requires commutation relations, but a *Lie superalgebra* obeying *anti-commutation* relations.

Since supersymmetric theories are not based on a Lie algebra, they do not fall under the Coleman-Mandula theorem. Instead they are bound by the Haag, Lopuszanski, Sohnius theorem [42]. This will not be stated explicitly except to say that it places restrictions on the form of the SUSY algebra. These have the schematic form [34]:

$$\begin{aligned} \left\{Q, Q^\dagger\right\} &= P^\mu \\ \{Q, Q\} &= \left\{Q^\dagger, Q^\dagger\right\} = 0 \\ [P^\mu, Q] &= \left[P^\mu, Q^\dagger\right] = 0, \end{aligned} \tag{2.2}$$

where spinor indices have been dropped.

2.3.2. Consequences

This seemingly simple addition brings with it a very rich phenomenology. Most importantly, from the point of view of experimental physics, it predicts a large number of new particles. Each particle in a supersymmetric theory is paired with another in a so-called *supermultiplet*. These particles are said to be *superpartners* of one another and are related by a SUSY transformation.

It can be shown [34], that each supermultiplet must contain an equal number of bosonic and fermionic degrees of freedom. This allows the range of possible supermultiplets to be enumerated. The simplest supermultiplet contains a spinor with two fermionic degrees of freedom. This implies that it should also contain two bosonic degrees of freedom: either as two real scalar fields or a single complex scalar field. This pairing is known as a *chiral supermultiplet*.

Consider next a supermultiplet containing a massless spin 1 boson (these have two helicity states, and thus two bosonic degrees of freedom). This must be paired with a single massless spinor with two fermionic degrees of freedom. It must also be spin-$\frac{1}{2}$ – a spin-$\frac{3}{2}$ particle would cause renormalisation problems [34]. This pairing is known as a *vector* (or *gauge*) *supermultiplet*.

SUSY therefore requires that all SM particles be placed into one of these supermultiplets. Inevitably, this requires the existence of a whole range of additional particles – each possessing a spin differing by $\frac{1}{2}$ from its SM counterpart.

In addition to having a certain theoretical elegance, this turns out to address the major problems pointed out in Section 2.1. Firstly, it provides a remedy to the hierarchy

problem. The additional superpartners also contribute to the Higgs mass corrections (see Eqn. 2.1). In fact, bosonic and fermionic loops contributing to the correction appear with opposite signs. Supersymmetry therefore causes exact cancellations of these problematic contributions – effectively fixing the hierarchy problem.

A certain class of supersymmetric theories also contain a solution to the dark matter puzzle. Such theories contain a Lightest Supersymmetric Particle (LSP) which appears to match the characteristics of a WIMP.

Finally, another aspect of SUSY theories that is often touted as an advantage, is that they allow the gauge couplings for the electromagnetic, weak and strong forces to unify at a certain energy scale. The running of the inverse couplings is shown in Figure 2.1.

2.3.3. *R*-parity

When it comes to writing down a supersymmetric Lagrangian, it is possible to write down terms which violate either Baryon (B) or Lepton number (L) conservation. Such terms are forbidden in the SM by renormalisability requirements. B or L violation would imply proton decay times much shorter than experimental lower limits. In order to prevent such terms from appearing in the Lagrangian, a new discrete symmetry is supposed, R-parity.

R-parity is often considered as a new quantum number possessed by each particle and multiplicatively conserved,

$$P_R = (-1)^{3(B-L)+2s},$$

where s is the spin of the particle. This results in an assignment of $P_R = 1$ to all SM particles, and -1 to their superpartners. To ensure this is conserved, SUSY particles may only be pair-produced from SM particles. Each of their decays must also result in an odd number of SUSY particles.

The importance of this becomes clear when one considers the lightest superpartner in the theory – the LSP. This is unable to decay to a lighter SUSY particle and thus cannot satisfy the requirements of R-parity conservation. It is therefore stable and, under certain other assumptions, a suitable candidate for the WIMP hypothesised to solve the dark matter problem.

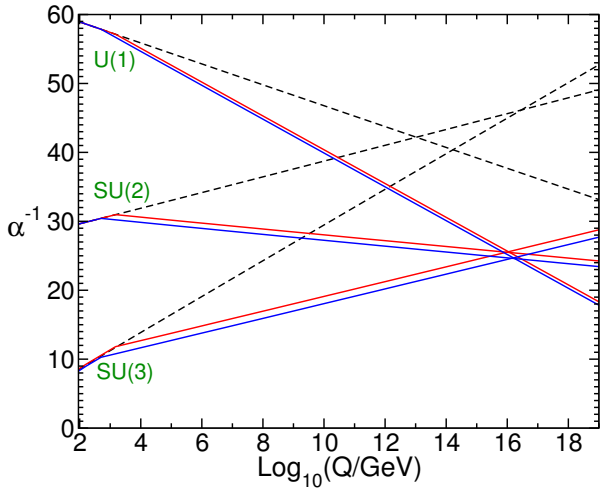

Figure 2.1.: Two-loop renormalisation group evolution of the inverse gauge couplings $\alpha_a^1(Q)$ in the SM (dashed lines) and the MSSM (solid lines). In the MSSM case, the sparticle masses are treated as a common threshold varied between 500 GeV and 1.5 TeV, and $\alpha_3(m_Z)$ is varied between 0.117 and 0.121. [34]

2.3.4. Supersymmetry Breaking

Examining the commutator in Eqn. 2.2, it is seen that the SUSY generator Q_a commutes with P^μ and hence also with $P^\mu P_\mu = m^2$. This requires superpartners to have identical mass – a prediction that is clearly at odds with experiment, since no additional superpartners have so far been observed.

If SUSY is to be a symmetry of the universe, some additional mechanism must be incorporated into the theory to explain these differing masses. Taking inspiration from EWSB, SUSY is said to be spontaneously broken. SUSY would therefore be respected by the Lagrangian but not by the vacuum. This would effectively "hide" SUSY at lower mass scales (i.e. those so far explored by experiment). There are a number of proposed mechanisms for SUSY breaking, including: Minimal Supergravity (mSUGRA) [43], Gauge-Mediated Supersymmetry Breaking (GMSB) [44] and Anomaly-Mediated Supersymmetry Breaking (AMSB) [45].

Having invoked SUSY initially as a solution to the hierarchy problem, it is desirable that the breaking of SUSY not prevent the cancellations which stabilise the Higgs mass. Terms in the Lagrangian which preserve this property are known as "soft" SUSY-breaking terms. They are required to have positive mass dimension [34]. Scenarios involving "non-soft" SUSY breaking will not be considered here.

2.4. The Minimal Supersymmetric Standard Model

The Minimal Supersymmetric Standard Model (MSSM) [46] is a minimal extension of the SM to include soft SUSY-breaking terms. Since the mechanism and dynamics of this breaking are unknown, additional parameters must be introduced into the theory. The MSSM adds 105 additional real constants to the 19 present in the SM [35, p. 186]. This proves extraordinarily problematic from the point of view of experimental SUSY searches. In Chapter 3, it will be shown how simplified models can offer a much simpler context for interpretation of results.

2.4.1. Particle Content

We shall now discuss the particle content of the MSSM, a summary of which is presented in Tables 2.1 and 2.2. The basic forms of the allowed supermultiplets were discussed in Section 2.3.2. Each fermion in the SM is placed into a chiral supermultiplet with a spin-0 *sfermion*. These are written with a tilde, e.g. $\widetilde{\mathrm{e}}_L$ for the *selectron*. Left-handed and right-handed components must lie in separate chiral supermultiplets. It is important to note that the subscripts on the sfermions indicate the chirality of the *partner fermion*. Being spin-0 bosons, the sfermions are not chiral.

Similarly the SM gauge bosons are placed into gauge supermultiplets. The corresponding superpartners are referred to generically as *gauginos* or more specifically as *Winos*, *Bino* and *gluinos*. Electroweak symmetry breaking (see Section 1.4) leads to mixing of the gauge eigenstates W^0 and B^0 to give the Z and γ. The corresponding combinations of superpartners are known as the Zino ($\widetilde{\mathrm{Z}}$) and Photino ($\widetilde{\gamma}$) respectively.

One might expect the Higgs field to be placed into a single chiral supermultiplet with a spin-$\frac{1}{2}$ superpartner. This turns out not to be possible for two reasons. Firstly, for reasons beyond the scope of this discussion, such a theory would suffer a gauge anomaly after quantisation. Secondly, the structure of the Yukawa couplings (see Section 1.4.4) actually requires two Higgs supermultiplets to give mass to up and down type quarks. The complex scalar doublets with hypercharge, $Y = \pm\frac{1}{2}$ will be referred to as H_u and H_d respectively. The weak isospin components of these are then H_u^+, H_u^0, H_d^0 and H_d^- where the superscript indicates electric charge.

The fermionic superpartners of each Higgs field, the Higgsinos, are then denoted $\widetilde{\mathrm{H}}_u$ and $\widetilde{\mathrm{H}}_d$. The physical SM Higgs is taken to be a linear combination of the neutral components H_u^0 and H_d^0.

Table 2.1.: Chiral supermultiplets in the MSSM [34]. Right-handed neutrino fields and their corresponding superpartners are not shown.

spin-0		spin-$\frac{1}{2}$	
Squarks	$\tilde{Q} = \begin{pmatrix} \widetilde{\mathrm{u}}_\mathrm{L} \\ \widetilde{\mathrm{d}}_\mathrm{L} \end{pmatrix}$	Quarks	$Q = \begin{pmatrix} \mathrm{u}_\mathrm{L} \\ \mathrm{d}_\mathrm{L} \end{pmatrix}$
	$\widetilde{\mathrm{u}}_\mathrm{R}$		u_R
	$\widetilde{\mathrm{d}}_\mathrm{R}$		d_R
Sleptons	$\tilde{L} = \begin{pmatrix} \widetilde{\nu}_\mathrm{L} \\ \widetilde{\ell}_\mathrm{L} \end{pmatrix}$	Leptons	$L = \begin{pmatrix} \nu_\mathrm{L} \\ \ell_\mathrm{L} \end{pmatrix}$
	$\widetilde{\ell}_\mathrm{R}$		ℓ_R
Higgs	$\mathrm{H}_u = \begin{pmatrix} \mathrm{H}_u^+ \\ \mathrm{H}_u^0 \end{pmatrix}$	Higgsinos	$\widetilde{\mathrm{H}}_u = \begin{pmatrix} \widetilde{\mathrm{H}}_u^+ \\ \widetilde{\mathrm{H}}_u^0 \end{pmatrix}$
	$\mathrm{H}_d = \begin{pmatrix} \mathrm{H}_d^0 \\ \mathrm{H}_d^- \end{pmatrix}$		$\widetilde{\mathrm{H}}_d = \begin{pmatrix} \widetilde{\mathrm{H}}_d^0 \\ \widetilde{\mathrm{H}}_d^- \end{pmatrix}$

Table 2.2.: Gauge supermultiplets in the MSSM

spin-$\frac{1}{2}$		spin-1	
Gluino	$\widetilde{\mathrm{g}}$	Gluon	g
Winos	$\widetilde{\mathrm{W}}^0$, $\widetilde{\mathrm{W}}^\pm$	Weak bosons	$\mathrm{W}^\pm$, W^0
Binos	$\widetilde{\mathrm{B}}^0$	B boson	B

2.4.2. Neutralinos and Charginos

EWSB leads to mixing of the charged and neutral spin-$\frac{1}{2}$ superpartners. The four mass eigenstates formed from the charged gauginos and Higgsinos are known as *charginos*. They are composed of the charged Higgsinos ($\widetilde{\mathrm{H}}_u^+$, $\widetilde{\mathrm{H}}_d^-$) and Winos ($\widetilde{\mathrm{W}^{\pm}}$). The four chargino states are denoted $\widetilde{\chi}^{\pm}{}_i$ for $i = 1, 2$. Similarly the neutral Higgsinos ($\widetilde{\mathrm{H}}_u^0$, $\widetilde{\mathrm{H}}_d^0$), Wino ($\widetilde{\mathrm{W}}^0$) and Bino ($\widetilde{\mathrm{B}}^0$) mix to give four *neutralinos*. These will be denoted $\widetilde{\chi}^0{}_i$ where $i = 1, 2, 3, 4$. The lightest of these will be denoted $\widetilde{\chi}^0$, the LSP. This is often taken to be the dark matter candidate referred to in Section 2.3.2.

2.5. Supersymmetry Searches

Since the emergence of SUSY in the 1970s, a number of particle physics experiments have undertaken dedicated searches for evidence of supersymmetric particles. These collider or fixed-target experiments have sought to produce supersymmetric particles in high-energy collisions – so far without success [47–50]. As discussed in Section 2.1.2, dedicated searches have also been performed specifically for "WIMP-like" dark matter signals. The detection experiments will not be discussed further here, except to say that they offer a highly complementary path to the discovery of dark matter [51].

In this section, the constraints set by previous SUSY searches will be summarised. This will naturally motivate discussion of the experimental signatures of SUSY particles. Finally, the signatures most relevant for searches at the LHC will be presented – in particular the single lepton channel that is the basis for the search described in Chapter 7.

2.5.1. Supersymmetry at Colliders

Useful experimental signatures of SUSY at colliders depend greatly on whether R-parity is assumed as a conserved quantity. Since, conservation of R-parity predicts the existence of a WIMP and ensures a stable proton, it is often assumed by experimental searches. R-parity violating theories are the subject of theoretical [52] and experimental work but will not be discussed further here.

As stated previously, R-parity conservation predicts the existence of a stable LSP or WIMP. Being weakly interacting, this will not be directly detected at a collider experiment but is observable as a deficit of energy in the detector – a so-called missing

energy signature. This signal forms the basis of the majority of collider SUSY searches. In addition to one or more LSPs, SUSY decays typically result in a large number of SM particles.

Whilst missing energy offers a relatively clean experimental signature, SM backgrounds with a missing energy component may be rejected by making further selection on the final state particles in an event. These backgrounds may contain genuine missing energy signal, in the form of a SM neutrino, or be the result of detector mismeasurement – a "fake" signal. Additional requirements often exploit other features of SUSY particle production. Suitable choices will depend on the dominant SUSY production processes and therefore on the nature of the colliding particles e.g. e^+e^-, $p\overline{p}$, pp. In other cases, such additional requirements may focus sensitivity on a more specific class of SUSY models.

e^+e^- Colliders

All sparticles (excluding the gluino) may be produced in tree-level processes at e^-e^+ colliders [34]. The Large Electron-Positron (LEP) experiment which ran up to centre-of-mass energies of 209 GeV has excluded all charged sparticles up to masses of approximately half this energy. If the mass splitting between a given sparticle and the LSP is assumed to be smaller, the detection efficiency becomes worse and these limits become weaker.

Take as an example the pair-production of charginos. The charginos subsequently decay to the LSP in association with either: four jets, two jets and 1 lepton, or two leptons of opposite charge [35]. Searches at LEP set a limit of $m_{\widetilde{\chi}^\pm} > 103$ GeV (or weaker if the mass difference between chargino and LSP is in the range 100 MeV $< m_{\widetilde{\chi}^\pm} - m_{\widetilde{\chi}^0_1} < 3$ GeV [34]).

Hadron Colliders

At hadron colliders, production of charginos, neutralinos, sleptons and sneutrinos is possible via electroweak processes. Production of squarks and gluinos is also possible, and has "QCD-strength" coupling [35]. At Fermilab's Tevatron accelerator, squark and gluino production were initially expected to dominate. However, once the low-mass region had been excluded, chargino and neutralino production became the focus of searches. Likewise, at the LHC, $\widetilde{q}\widetilde{q}$, $\widetilde{g}\widetilde{g}$ or $\widetilde{q}\widetilde{g}$ production are presumed to dominate.

R-parity requires that sparticles be pair produced. Each proceeds via a cascade decay to the LSP. The cascade will generally produce a number of jets and possibly leptons. This covers most typical SUSY topologies studied at hadron colliders.

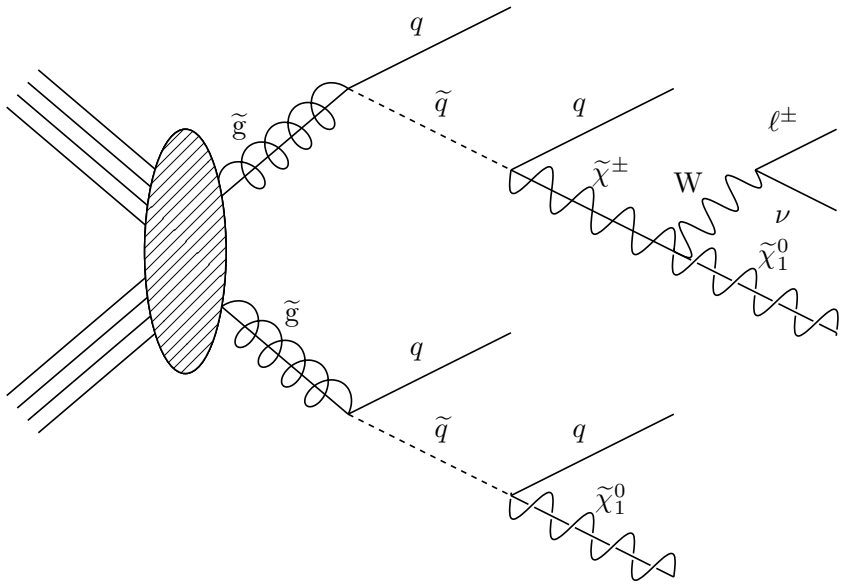

Figure 2.2.: Diagram showing a possible SUSY decay chain beginning with gluino pair-production and leading to a single lepton final state.

One such cascade decay is shown in Figure 2.2. This would be a typical cascade decay leading to a single-lepton final state. Whilst being less inclusive than the pure jets plus missing energy signature, the addition of a lepton requirement serves to significantly suppress the experimental background from QCD events [53]. With additional kinematic requirements imposed, this channel is sensitive to a range of SUSY scenarios. A search based on this final state will be presented in Chapter 7.

Chapter 3.

Theoretical Framework

The previous two chapters have given a theoretical overview of the SM and SUSY. In order to bring the predictions of these theories closer to the realm of experiment, this chapter will provide a higher-level discussion more suited to the results that will be presented later on.

A brief account of vector boson production at a hadron collider is given in Section 3.1, along with details of the polarisation of W bosons at the LHC. This motivates the measurement described in Chapter 6 and forms the framework within which the experimental results will be interpreted.

In the second part of this chapter, several models relevant to SUSY searches will be presented. These contain a relatively low-dimensional parameter space, making them convenient for the interpretation of experimental results. This will be highly relevant to Chapter 8, where the models will be used to interpret the results of the SUSY search presented in Chapter 7.

3.1. Polarisation of W Bosons

Some theoretical background relating to the SM has been presented in Chapter 1. Here, theoretical material relating to massive vector boson production at hadron colliders will be briefly summarised. Then material relating specifically to the polarisation of W bosons will be covered in detail.

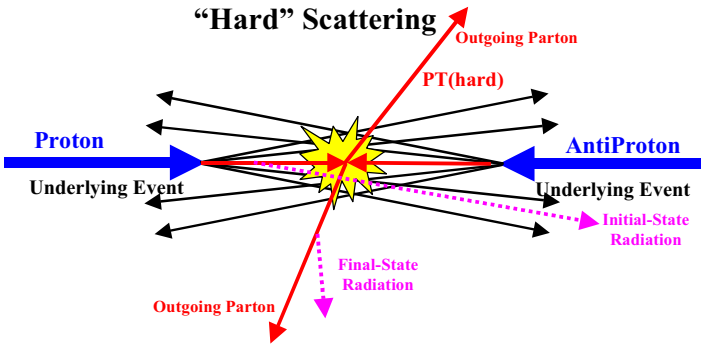

Figure 3.1.: Illustration of a $p\bar{p}$ collision in which a hard 2-2 parton scattering has occurred. The underlying event is also shown, along with initial and final state radiation [56].

3.1.1. QCD at Hadron Colliders

Before discussing vector boson production specifically, it is helpful to review the process by which particles are produced at a hadron collider. As will be discussed further in Chapter 4, beams consisting of protons or anti-protons are focussed by magnets and forced to collide. Among the many protons making up a "bunch" (approximately 100 billion at the LHC [54]), only a small fraction interact. Interactions may be further characterised as either "elastic" or "inelastic", where elastic collisions do not involve the break up of the beam particles [55]. Often the colour exchange between the partons will be "soft", and thus the outgoing particles will have relatively low transverse momentum. More rarely, a "hard" interaction will occur, giving rise to particles with large transverse momentum and jets. These are the events of interest to most LHC physics analyses.

A hard interaction will typically involve two partons from the incoming beam particles. The remaining constituents of the two beam particles make up the "beam-beam remnant" [56]. More generally, particles considered not to originate from the hard interaction are referred to as the "underlying event" [56]. This is illustrated in Figure 3.1. Because of asymptotic freedom (see Section 1.5), the hard interaction is generally well modelled using perturbative techniques. In contrast, the soft processes which contribute to the underlying event are generally more poorly understood [56]. Finally, since much of the beam-beam remnant escapes along the beamline, outside the acceptance of the detector, the energy of the underlying event is poorly measured. This provides an additional motivation for working with transverse detector-level quantities.

3.1.2. Vector Boson Production at Hadron Colliders

A detailed account of massive vector boson production at hadron colliders can be found in [22, 57, 58]. These processes are often referred to as W + jets and Z + jets – meaning production of a W or Z boson in association with jets. At hadron colliders, production proceeds predominantly via $q\overline{q}$ or qg interactions and so is strongly dependent on QCD calculations. Cross-sections can be calculated as the product of the hard scattering cross-section, evaluated in perturbative QCD, with a Parton Distribution Function (PDF).

The PDF is a probability density function giving the probability of finding a certain parton with a given fraction of the longitudinal momentum, x, as a function of the momentum transfer, Q^2. It is obtained from a fit of a parameterised model to hadronic data. Cross-section calculations for these processes may be referred to as Leading Order (LO) or Next-To-Leading Order (NLO). This indicates the precision of the calculation in terms of the expansion of the strong coupling constant, α_s [59].

These processes have been extensively studied and significant recent progress made, particularly for calculation of higher jet multiplicity observables [60, 61]. The W + jets cross-section has been calculated at NLO for up to 4 jets [62]. The discussion will now turn to aspects relevant to W + jets production and in particular the polarisation effects.

3.1.3. Polarisation Effects Parallel to the Beam Line

It is well known from straightforward helicity arguments [63] that W bosons produced along the beam axis will exhibit a 100% left-handed polarisation. This can be seen by considering the leading order partonic subprocesses,

$$\mathrm{u\overline{d}} \longrightarrow \mathrm{W}^+ \qquad \text{and} \qquad \mathrm{d\overline{u}} \longrightarrow \mathrm{W}^-.$$

Firstly, note that in the case of valence quarks, the fraction of the proton momentum carried by the quark (as determined by the PDFs) is greater than that of the anti-quark. In addition given that the LHC is a pp collider, valence anti-quarks are not present. Anti-quarks must be drawn from the sea and are therefore likely to be low momentum. Taking these two facts together, the quark is likely to have higher momentum than the anti-quark. By momentum conservation, it is expected that the W boson will be produced predominantly in the direction of the original quark. Then, given the (V − A) nature of the charged weak interaction (see Section 1.3.8), it is seen that the quark must

be left-handed. Therefore, by helicity conservation, the W will be polarised nearly 100% left-handedly along the beam axis. A small dilution will occur in instances where the anti-quark has, by chance, a larger momentum fraction than the quark.

It is worth mentioning that the situation is not identical at the Tevatron $p\overline{p}$ collider. Although the W^+ also possess a 100% left-handed polarisation along the beam-line (via similar arguments to those given above), the W^- are found to have a near 100% right-handed polarisation. This is a result of the subprocess $\overline{u}d \longrightarrow W^-$ where this time the $\overline{u}$ carries more momentum.

An effect related to the W polarisation is the so-called *charge asymmetry*. At a pp collider there are two valence u quarks for each d quark. Since, at leading order, W^+ (W^-) production is initiated by a u (d) quark, W^+ events are found to dominate over W^- [64]. The ratio of the W^+ cross-section to W^-, R, has been measured at CMS as $R = 1.43 \pm 0.04$ [65].

3.1.4. Polarisation Effects in the Transverse Plane

In the case where the W boson carries a significant transverse momentum, P_T^{W}, the situation is more complex. For the sake of this discussion we will consider cases involving only a single associated jet. Also, in order to simplify matters, one need only consider the W^+ case, as the W^- case is very similar. At leading order, three subprocesses should be considered [60],

$$\mathrm{ug} \longrightarrow \mathrm{W^+d}\ , \qquad \mathrm{u\overline{d}} \longrightarrow \mathrm{W^+g} \qquad \text{and} \qquad \mathrm{g\overline{d}} \longrightarrow \mathrm{W^+\overline{u}}. \tag{3.1}$$

For sufficiently large P_T^{W}, the soft-gluon enhancement of $\mathrm{u\overline{d}} \longrightarrow \mathrm{W^+g}$ is not so significant and the quark-gluon subprocess is found to dominate. It has been found that 70-80% of W + N jet ($N \leq 4$) production at LO is initiated by this subprocess [66].

For the quark-gluon subprocess, the s and t-channel diagrams are shown in Figure 3.2. For reference, diagrams for the subdominant processes are shown in Figure 3.3. For the s-channel ug diagram, the on-shell d quark is coupled directly to the W and therefore must be in a negative helicity state (i.e. left-handed). Assuming a positive helicity for the W boson (as depicted in Figure 3.2a), the spin along the axis formed by the W boson and d quark is $1 + \frac{1}{2} = \frac{3}{2}$. Such a configuration is not allowed for the spin-$\frac{1}{2}$ off-shell quark and thus the s-channel must lead to a 100% left-handed polarisation of the W.

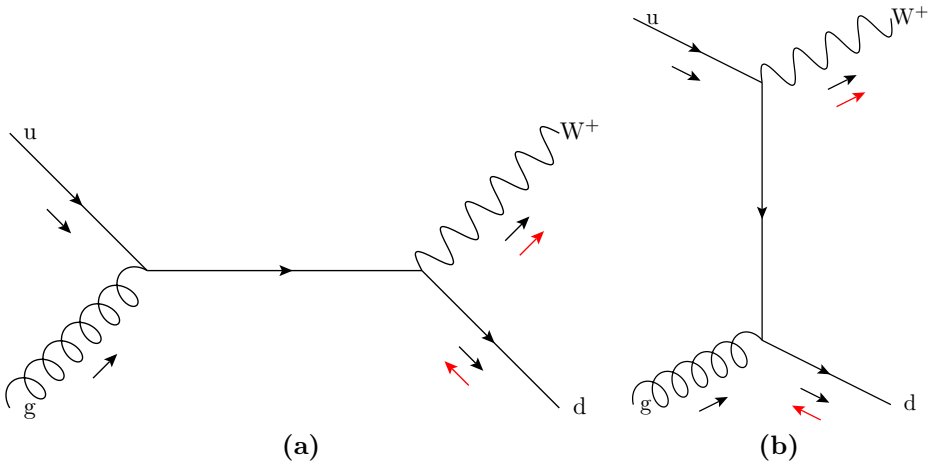

Figure 3.2.: Diagrams showing the ug $\longrightarrow$ W^+d subprocess in the (a) s and (b) t channels. The black displaced arrows indicate the particle momenta. The red arrows indicate helicity in the case of a right-handed W boson and a left-handed d quark.

In contrast, the t-channel diagram is not similarly constrained by spin arguments (since the W is not coupled directly to the quark) and thus the polarisation will not be seen. It can be shown that, for a left-handed incoming gluon, the t-channel diagram can be made to vanish [60]. Also, for a right-handed gluon, the W polarisation is not constrained, but has been shown to become predominantly right-handed at high P_T^{W}. The helicity of the outgoing W will be almost 100% correlated with that of the incoming gluon at high P_T^{W}.

Overall, due to a factor 4 difference in the size of the corresponding matrix elements, the W is expected to asymptotically approach an 80% left-handed polarisation at large P_T^{W}. The (V − A) coupling allows the decay leptons to be used as an analyser of the W polarisation. This allows the effect to be measured. Having given an overview of the physics underlying this effect, a more detailed argument will now be presented.

Writing the amplitudes of the subprocesses in Eqn. 3.1 in terms of spinor products, two distinct expressions emerge. The corresponding cross-sections are [60],

$$d\sigma_{(a)}^{\mathrm{LO}} \propto (k_{\mathrm{d}} \cdot k_{\nu})^2 \quad \text{and} \quad d\sigma_{(b)}^{\mathrm{LO}} \propto (k_{\mathrm{u}} \cdot k_{\mathrm{e}})^2, \tag{3.2}$$

where the k are Lorentz vectors representing the particle momenta. For each subprocess, the helicity configurations corresponding to (a) and (b) are shown in the upper and lower rows of Figure 3.4 respectively. The red arrows indicate particle helicity, with a

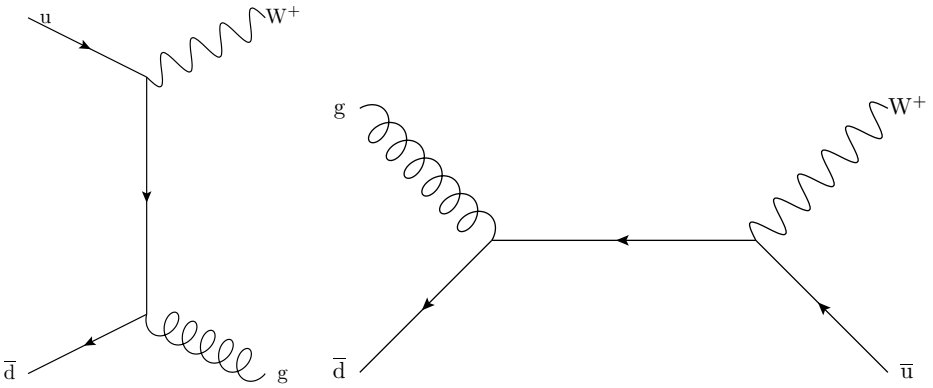

(a) $u\bar{d} \longrightarrow W^+g$ **(b)** $g\bar{d} \longrightarrow W^+\bar{u}$

Figure 3.3.: Diagrams showing the $u\bar{d} \longrightarrow W^+g$ and $g\bar{d} \longrightarrow W^+\bar{u}$ subprocesses.

double-stemmed arrow for the W polarisation. In the cases where the W boson is neither purely left-handed nor right-handed, the arrow is placed at an angle.

Starting with the subprocess $ug \longrightarrow W^+d$, the (a) expression in 3.2 correlates the axis of the d quark with the neutrino. This is shown in Figure 3.4a. The $(V - A)$ coupling requires the neutrino to have a left-handed helicity. By angular momentum conservation, the W boson must also be left-handed. The angular dependence is $(1 - \cos\tilde{\theta}^*)^2$ where $\tilde{\theta}^*$ is the angle of the charged decay lepton with respect to the W flight direction in the partonic centre-of-mass frame. In contrast, consider an identical particle configuration, but with helicities corresponding to (b). This is shown in Figure 3.4d. The e^+ direction is now correlated with the incoming beam direction. Boosting to the W rest frame, at high P_T^W, the incoming quark and gluon are nearly parallel. Thus, given a scattering angle of 90°, the u quark momentum is seen to be half that of the d quark. The angular dependence is thus $\frac{1}{4}(1 + \cos\tilde{\theta}^*)^2$, yielding a right-handed polarisation at a quarter of the rate of the left-handed component.

For the sub-dominant process $u\bar{d} \longrightarrow W^+g$, the terms in Eqn. 3.2 correlate the momenta of the decay leptons with the beam direction. The two cases are shown in Figures 3.4b and 3.4e. Although it can be seen once again that a left-handed and right-handed polarisation emerge, in this case they are found to cancel for a scattering angle of 90° and thus give no net polarisation effect. Lastly, for the subprocess $g\bar{d} \longrightarrow W^+\bar{u}$, shown in Figures 3.4c and 3.4f, the (b) contribution correlates the u quark and the e^+ direction, leading to a dominantly right-handed polarisation. However, since the PDF, $\bar{d}(x)$, is much smaller than $u(x)$, this effect is largely washed out by the dominant left-handed polarisation mode.

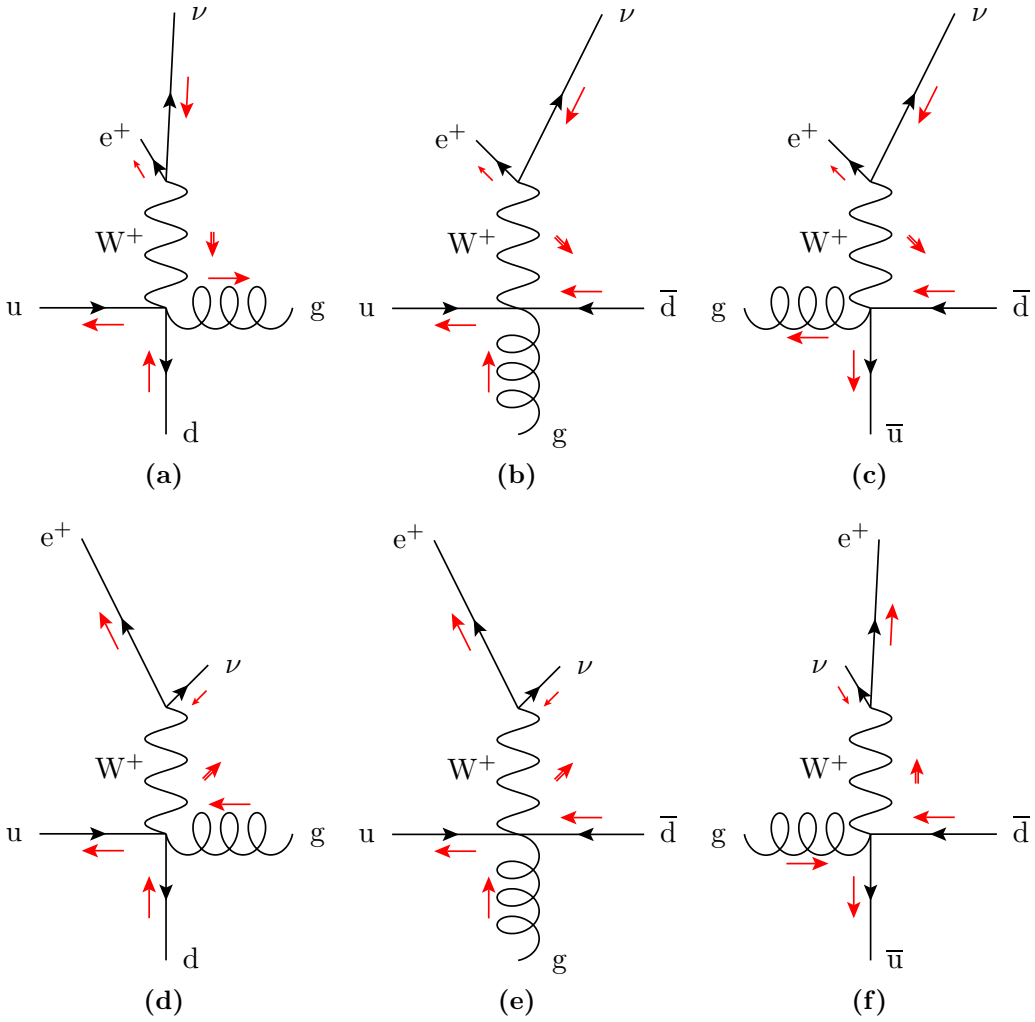

Figure 3.4.: Illustrations of $W^+ + 1$ jet production modes at the LHC. Red single-stemmed arrows represent particle helicity. Red double-stemmed arrows indicate the polarisation of the W boson. In cases where the W is not produced with a definite polarisation, the arrow is placed at an angle. The angles and sizes of the particle lines are suggestive of their momenta in the centre-of-mass frame.

It has been seen that the proton-proton environment at the LHC is expected to lead to a dominance of left-handed over right-handed helicity states for W bosons with large transverse momentum. In order to observe this effect, the helicity of W bosons must be measured. This will be discussed in the next section.

3.1.5. Measuring Helicity

The Helicity Frame

Polarisation effects may be conveniently studied within the helicity frame of the W boson. This is illustrated in Figure 3.5. The helicity frame is defined in the rest frame of the W boson, with the polarisation axis (here, the z-axis) aligned along the W line-of-flight in the lab frame. The x-axis is then chosen to lie in the plane spanned by the two colliding protons in the boson rest frame. The sense is chosen such that the angle between the axis and the nearest proton is minimised. The y-axis is then fixed to be perpendicular to these two (the coordinate system is right-handed). The polar angle, θ^*, is measured between the positive z-axis and the lepton. Likewise, the azimuthal angle, ϕ^*, is measured in the $x-y$ plane, between the positive x-axis and the lepton. For $0 < |\phi^*| < \frac{\pi}{2}$, the charged lepton will have a larger rapidity than the W boson and thus a smaller p_{T}. Alternatively, for $\frac{\pi}{2} < |\phi^*| < \pi$, the lepton will have a smaller rapidity and a larger p_{T} [67].

Quantifying Helicity

The hadronic cross-section of the W is obtained within the parton model by weighting the individual parton-level cross-sections with the respective PDFs [63],

$$\frac{d\sigma^{h_1 h_2}}{d\left(P_T^{\mathrm{W}}\right)^2 dY^{\mathrm{W}} d\Omega^*} = \sum_{ab} \int dx_1 dx_2 f_a^{h_1}\left(x_1, \mu_F^2\right) f_b^{h_2}\left(x_2, \mu_F^2\right) \frac{s d\tilde{\sigma}_{ab}}{dt du d\Omega^*}\left(x_1 P_1, x_2 P_2, \alpha_s(\mu_R^2)\right),$$

where $d\Omega^* = \sin\theta^* d\theta^* d\phi^*$, θ^* and ϕ^* are the polar and azimuthal decay angles of the leptons in the helicity frame and Y^{W} is the rapidity of the W boson. h_1 and h_2 are the interacting hadrons and the sum runs over $a, b = q, \overline{q}, \mathrm{g}$. The PDFs, $f_a^h\left(x, \mu^2\right)$, give the probability of finding a parton a with momentum fraction x in hadron h when probed at a scale μ^2. The $d\tilde{\sigma}_{ab}$ are the parton-level cross-sections for the chosen process(es). The

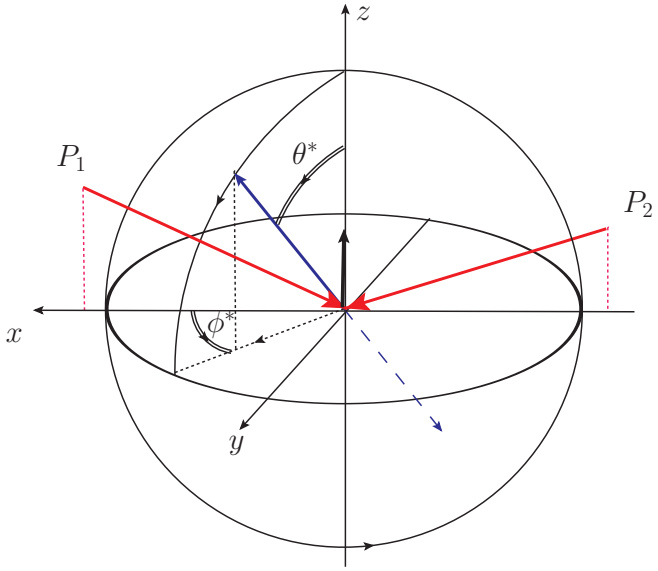

Figure 3.5.: Illustration of the helicity frame. The lines P_1 and P_2 represent the incoming protons boosted into the helicity frame. The blue line indicates the direction of the decay lepton. The azimuthal and polar angles, ϕ^* and θ^*, are also shown [60].

hadron-level Mandelstam variables are written in uppercase,

$$S = (P_1 + P_2)^2 \qquad T = (P_1 - Q)^2 \qquad U = (P_2 - Q)^2,$$

and parton-level in lowercase,

$$\begin{aligned} s &= (p_1 + p_2)^2 = x_1 x_2 S \\ t &= (p_1 - Q)^2 = x_1(T - Q^2) + Q^2 \\ u &= (p_2 - Q)^2 = x_2(U - Q^2) + Q^2, \end{aligned}$$

where

$$p_1 = x_1 P_1 \qquad p_2 = x_2 P_2.$$

The momenta of the incoming hadrons are labelled P_1 and P_2, the interacting partons, p_1 and p_2 and the W boson, Q. The cross-section can be decomposed in terms of a standard

set of angular coefficients, A_i, to give [60, 68, 69]

$$\begin{aligned}\frac{1}{\sigma}\frac{d\sigma}{d\left(\cos\theta^*\right)d\phi^*} = \frac{3}{16\pi}\big[&\left(1+\cos^2\theta^*\right)\\ &+\frac{1}{2}A_0\left(1-3\cos^2\theta^*\right)+A_1\sin 2\theta^*\cos\phi^*\\ &+\frac{1}{2}A_2\sin^2\theta^*\cos 2\phi^*+A_3\sin\theta^*\cos\phi^*\\ &+A_4\cos\theta^*+A_5\sin\theta^*\sin\phi^*\\ &+A_6\sin 2\theta^*\sin\phi^*+A_7\sin^2\theta^*\sin 2\phi^*\big],\end{aligned} \tag{3.3}$$

where σ may be any differential cross-section that does not depend on the individual lepton kinematics [60]. The A_i are ratios of the separate helicity cross-sections of the boson to its total unpolarised cross-section. They are dependent on the W boson charge, transverse momentum, P_T^{W}, and rapidity, Y^{W}. Eqn. 3.3 can be integrated over ϕ^* to give

$$\frac{d\sigma}{d(\cos\theta^*)} \propto \left(1+\cos^2\theta^*\right)+\frac{1}{2}A_0\left(1-3\cos^2\theta^*\right)+A_4\cos\theta^*. \tag{3.4}$$

Again, because of the (V − A) coupling, the W^+ (W^-) may couple only to a right-handed (left-handed) charged lepton and left-handed (right-handed) neutrino. Therefore the angular momentum state of the decay leptons is

$$\begin{aligned}\left|\ell\nu^{J,M}\right\rangle &= \left|\frac{1}{2},\pm\frac{1}{2}\right\rangle\oplus\left|\frac{1}{2},\pm\frac{1}{2}\right\rangle\\ &= \quad |1,+1\rangle \quad (\text{for } \mathrm{W}^+) \quad \text{or}\\ &\quad\ |1,-1\rangle \quad (\text{for } \mathrm{W}^-),\end{aligned}$$

where $|J,M\rangle$ represents an angular momentum state with a total angular momentum, J, and projection, M. Rotating these states through the angle θ^*, one obtains

$$\left|\ell\nu^{J,M}\right\rangle' = \sum_{M'=-J}^{M'=+J} d^J_{M,M'}\left|J,M'\right\rangle, \tag{3.5}$$

where $d^J_{M,M'}$ are elements of the Wigner d-matrix [29]. The angular momentum of a W boson in a helicity eigenstate is then $\left|\mathrm{W}^{J,M''}\right\rangle$. The matrix element for the angular

momentum coupling can be written

$$\begin{aligned}\left\langle \mathrm{W}^{J,M''} \mid \ell\nu^{J,M} \right\rangle' &\sim \sum_{M'=-J}^{M'=+J} d^J_{M,M'} \left\langle J, M'' \mid J, M' \right\rangle \\ &\sim d^J_{M,M''} \left\langle J, M'' \mid J, M'' \right\rangle \sim d^J_{M,M''}.\end{aligned}$$

The cross-section is calculated by squaring the matrix elements and summing over the helicity states (M'') of the incoming W boson. Each state is weighted by the helicity fraction $f_{M''}$,

$$\sigma(\mathrm{W} \longrightarrow \ell\nu_\ell) \sim f_0 \left|d^1_{M,0}\right|^2 + f_{-1} \left|d^1_{M,-1}\right|^2 + f_1 \left|d^1_{M,+1}\right|^2,$$

where $f_0 + f_1 + f_{-1} = 1$. Finally, using the fact that for $\mathrm{W}^\pm$, $M = \pm 1$, and replacing for the elements of the Wigner d-matrix in terms of $\cos\theta^*$ gives,

$$\sigma(\theta^*_{\ell^\pm}) = \frac{f_0}{2} \sin^2\theta^*_{\ell^\pm} + \frac{f_\mathrm{L}}{4} \left(1 \mp \cos\theta^*_{\ell^\pm}\right)^2 + \frac{f_\mathrm{R}}{4} \left(1 \pm \cos\theta^*_{\ell^\pm}\right)^2. \tag{3.6}$$

Note that the helicity fractions f_i have been relabelled to give a more intuitive interpretation as the left-handed, right-handed and longitudinal polarisation fractions. Comparing now to Eqn. 3.4, we identify

$$\begin{aligned} A_0 &\sim f_0 \quad \text{and} \\ A_4 &\sim \pm(f_\mathrm{L} - f_\mathrm{R}). \end{aligned}$$

Whilst the A_i are the more fundamental parameters from a theoretical point of view, the helicity fractions f_0, f_L and f_R will often be more convenient for experimental discussion. The other A_i parameters will not be discussed in detail, though their small effect on the measurement of A_0 and A_4 will be evaluated.

In Chapter 6, the measurement of the helicity fractions f_L, f_R and f_0 will be described. The intention of this analysis is to confirm the prediction that the left-handed mode dominates at high P_T^W, or equivalently, $(f_\mathrm{L} - f_\mathrm{R}) > 0$. In addition, it is expected that $f_\mathrm{L} > f_0$.

The evolution of the polarisation fractions with P_T^W has also been studied in simulation [60]. The evolution of f_L, f_R and f_0 is shown in Figure 3.6 for the W^+ case. The increase of $(f_\mathrm{L} - f_\mathrm{R})$ with P_T^W can be readily seen. Also, because of the equivalence theorem [70–74], the behaviour of the longitudinal polarisation mode approximates the corresponding

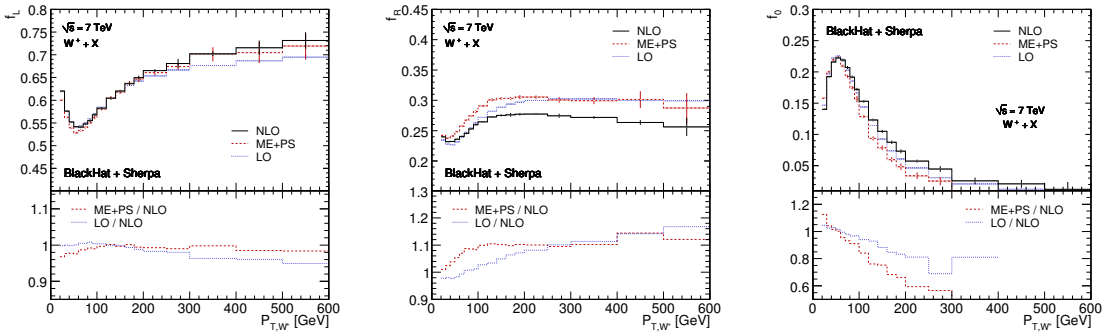

(a) f_{L} **(b)** f_{R} **(c)** f_0

Figure 3.6.: The polarisation fractions f_{L}, f_{R} and f_0 as a function of P_T^{W} for W^+ production are shown in the upper panes of Figures 3.6a, 3.6b and 3.6c respectively. Three predictions are shown: the fixed-order NLO result as a solid black line, the ME+PS result as red dashed line and the fixed-order LO result as a dotted blue line. Uncertainties are indicated by thin vertical lines. The lower pane in each plot show the ratio of each prediction with respect to the NLO prediction [60].

Goldstone boson (see Section 1.4.2) at large P_T^{W}. This explains the decrease of f_0 as P_T^{W} becomes large.

Whilst the dependence of the polarisation on P_T^{W} makes for a very interesting measurement, it was found to be infeasible with the relatively small data sample available for this analysis.

3.2. Modelling New Physics

In the following section, a number of models will be presented. All are suitable for the interpretation of the single lepton SUSY search described in Chapter 7.

3.2.1. The Constrained Minimal Supersymmetric Standard Model

It was said in Chapter 2 that the MSSM is problematic from the point of view of collider searches due to the extremely large number of parameters associated with SUSY breaking. In order to make quantitative statements about the sensitivity of a given experimental search, a more restricted theory must be considered.

One such theory that has often been used is the Constrained Minimal Supersymmetric Standard Model (CMSSM) [35]. The CMSSM is inspired by mSUGRA [75]. This proposes a gravity-mediated SUSY breaking mechanism via a hidden sector. This assumption reduces the parameter space of the MSSM to just 5 parameters, 4 of which are continuous:

- a universal trilinear scalar coupling, A_0;
- a single scalar mass, m_0;
- a single gaugino mass, $m_{\frac{1}{2}}$;
- $\tan\beta$ is the ratio of the Higgs' vacuum expectation values and
- sign(μ) where μ is the self-coupling of the Higgs field.

Whilst this proves to be a much more practical model from the point of view of experimental searches, there is no particular reason to assume that SUSY is broken in this way. The restricted parameter space of the CMSSM may disfavour a number of topologies which would appear in a larger class of SUSY theories. One example of this is that the gluino mass parameter, M_3, is related to the Bino and Wino mass parameters, M_1 and M_2, by the following approximate relation [34, p.99]:

$$M_3 : M_2 : M_1 \approx 6 : 2 : 1.$$

This relation holds near the TeV scale in models with mSUGRA or GMSB boundary conditions. However, it is not necessarily the case in more general SUSY theories.

An additional, but related difficulty is that interpretations of results within the CMSSM may not be robustly extrapolated to alternative models. As will be seen, both of these difficulties are addressed by a more generic set of SUSY-inspired models. These will be presented in the next section.

3.2.2. Simplified Models

It is often the case that theorists, having devised some theory, and made concrete phenomenological predictions from it, wish to test it against experimental data. The difficulty then arises of taking these predictions and translating them into a form where they can be compared directly with experimental results. Typically, these results will be provided in the form of one or more event yields, corresponding background predictions

and statistical and systematic uncertainties. In some (but probably not most) cases, the relevant correlations will also be included. The theorist must then take the predictions of the theory and apply experimental resolution effects to them in order to simulate the expected signal yield. Modern detectors are highly complex and require very complex simulation to precisely model all of the resolution and acceptance effects. In some cases, in particular for relatively simple kinematic quantities, a simplified parameterisation may suffice. However, detailed checks will be required to confirm that a given approximation reproduces, with adequate fidelity, the results of the full detector simulation or the actual recorded data. If it can be confirmed that this is the case, the theorist may then proceed to redo the work of the experimentalist in modelling the various statistical and systematic effects in the form of a likelihood function. Finally, they may then utilise all of these components to produce their own interpretation of the data against the chosen theory.

Clearly, this procedure is both laborious and error-prone. It was therefore proposed that the LHC experiments would provide a richer interpretation in the context of a set of *simplified models* [76]. Broadly speaking, a simplified model is an effective theory, chosen to characterise a particular phenomenological scenario present within one or more NP models. Free parameters which have little effect on the physics (at least at small integrated luminosities) are integrated out, leaving only those with a greater effect on the physics. By constructing a number of these models, the full space of possible physical signatures arising in much more complicated theories may be spanned. This collection of models is sometimes referred to as a Simplified Model Spectrum (SMS)

Although the concept of a simplified model is quite general, the discussion here will now focus on those inspired by SUSY or "SUSY-like" theories, and more specifically those giving rise to single lepton final states.

Dark Matter Models

As discussed in Chapter 2, a highly desirable prediction of certain supersymmetric theories is the existence of a stable, weakly-interacting particle or WIMP. This is a dark matter candidate with a striking experimental signature at collider experiments – a large missing energy component. Since these topologies are largely inspired by R-parity conserving SUSY, similar terminology and notation will be used to refer to their particle content. This should not be taken to suggest that these topologies are exclusive to SUSY type theories.

The topologies considered here may be split into two categories. The first begins with pair-production of a neutral, coloured object – the gluino in the case of SUSY. The second is initiated by production of a charged, coloured object – the squark of SUSY . As for the CMSSM, if suitably light, these are expected to be produced most abundantly at the LHC.

In either case, the squark or gluino-type particle then decays, either directly to an LSP or via some intermediate particles (comparable to the heavy electroweakinos of SUSY) – a cascade decay.

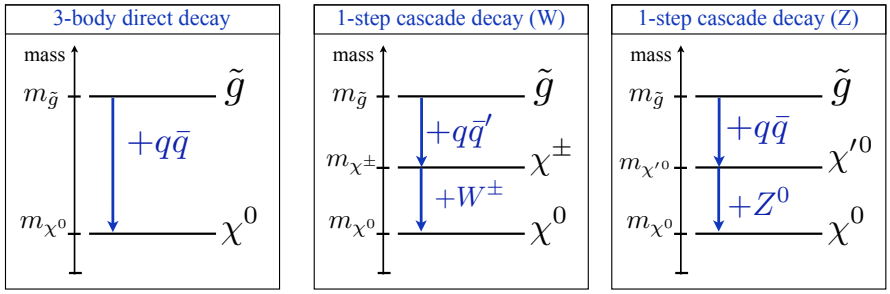

Figure 3.7.: Illustration of direct and cascade gluino decay modes within SUSY simplified models. [77]

Connection to Supersymmetry

Considering first the gluino pair-production models (Figure 3.7), we shall assume that the squarks are heavier and therefore kinematically inaccessible. If this were not the case, the phenomenology would be better described by the squark-type models.

In such supersymmetric models, the gluino may decay only via an off-shell squark [76]. This decay may be either directly to the LSP or indirectly via intermediate states. Direct decays correspond to SUSY scenarios where either [77]:

- $\widetilde{\chi}_1^0 \approx \widetilde{\mathrm{B}}$ and the $\widetilde{q}_R$ are lightest or the $\widetilde{\mathrm{W}}$ is kinematically inaccessible;
- $\widetilde{\chi}_1^0 \approx \widetilde{\mathrm{W}}$ and either $\widetilde{q}_L$ are lightest or there is no splitting between the left and right-handed squarks and
- $\widetilde{\chi}_1^0 \approx \widetilde{\mathrm{H}}$ and either heavy-flavour squarks are inaccessible or $\widetilde{\mathrm{B}}$ and $\widetilde{\mathrm{W}}$ are inaccessible.

This is not generally true in either mSUGRA or GMSB but does correspond to certain AMSB scenarios [77].

Alternatively, the gluino may undergo a cascade decay via an intermediate mass state, either a chargino or a heavy neutralino. This will subsequently decay to the LSP via either a W or Z boson.

The situation is similar in the case of squark pair-production, except that without the intermediate off-shell squark, the jet multiplicity is reduced [77].

Single Lepton Topologies

To provide a meaningful interpretation of the single lepton search detailed in Chapter 7, two simplified models have been chosen. The models, T3W and T2tt, have been chosen in particular since they offer topologies which are likely to enter the selection of a single lepton SUSY search.

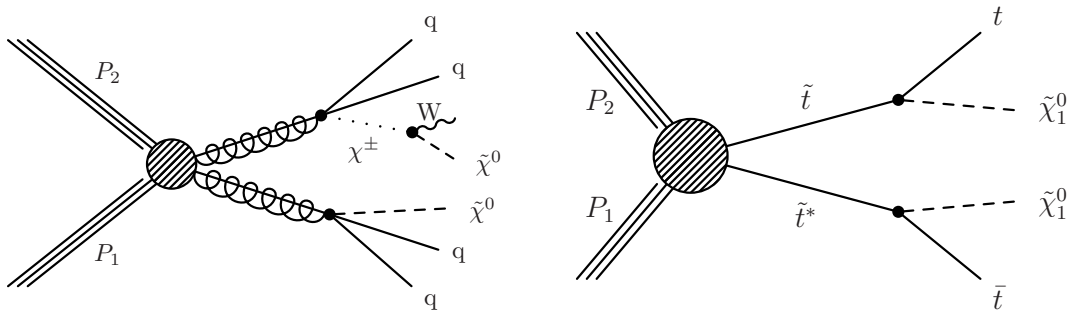

(a) T3W **(b)** T2tt

Figure 3.8.: Feynman diagrams illustrating two simplified model topologies suited to a single lepton SUSY search: (a) T3W and (b) T2tt [78]

The T3W model is a gluino pair-production model, in which one of the mother particles undergoes a cascade decay via an intermediate particle. The W in the model name indicates that this intermediate particle is then "forced" to decay to a W boson. This topology is illustrated in Figure 3.8a and is seen to be similar to the example SUSY decay illustrated in Figure 2.2. This model is parameterised by the mass of the mother particle, M_{gluino}, the mass of the daughter particle, M_{LSP} and the mass of the intermediate particle, M_{χ}.

The second model, T2tt, begins with squark pair production. Both mother particles decay directly to the LSP. Furthermore, both squarks are assumed to be stop particles

– the superpartner of the top quark – each decaying to a SM top quark. This decay topology is illustrated in Figure 3.8b. Such events with two top quarks in the final state, should give an experimental signature suitable for a single lepton search.

The T2tt model reflects scenarios in which the stop is the lightest of the squarks. These are theoretically attractive for a number of reasons (see [35, p. 202] and [79]). Since this does not contain an intermediate mass state, it has only two parameters: the mass of the mother, M_{stop} and the mass of the daughter, M_{LSP}.

3.3. Summary

A number of theoretical models have been reviewed, each of relevance to the analysis work presented in Chapters 6, 7 and 8. In the next chapter, aspects of the CMS experiment and the LHC will be discussed.

Chapter 4.

The Compact Muon Solenoid Experiment at the Large Hadron Collider

4.1. Introduction

The Large Hadron Collider (LHC) [80] is a proton-proton (pp) accelerator located at the CERN particle physics laboratory near Geneva, Switzerland. It has been designed to carry out a broad program of physics research using a number of specialised detectors. This chapter will give a very brief introduction to the LHC itself. The Compact Muon Solenoid (CMS) experiment, a large, general purpose detector at the LHC, will be discussed in detail.

4.2. The Large Hadron Collider

The LHC is a circular synchrotron, 27 km in circumference, sitting on the border between France and Switzerland. It has been built in a tunnel initially constructed to house the LEP accelerator, buried at a depth of between 50 and 175 m underground. Although primarily a pp accelerator, the LHC will also undertake a heavy-ion physics program. At full design specifications, 2808 bunches of protons will circulate around each direction of the ring, colliding at a centre-of-mass energy of 14 TeV. It is designed to eventually reach a proton bunch spacing of 25 ns and an instantaneous luminosity of 10^{34} cm^{-2} s^{-1}.

There are four primary experiments at the LHC: A Large Ion Collider Experiment (ALICE) [81], A Toroidal LHC Apparatus (ATLAS) [82], CMS [83, 84] and the Large Hadron Collider Beauty (LHCb) [85] experiment. Each one is constructed around one of the four interaction points and records the shower of particles produced from the colliding protons. ATLAS and CMS are large, general purpose detectors, designed to search for a variety of NP signatures as well as making higher precision measurements of many SM parameters. ALICE is optimised to examine the products of heavy-ion collisions (principally lead-lead – although a number of configurations are possible) in order to explore the quark-gluon plasma and related physics. Finally, the LHCb experiment is optimised for the study of B-meson decays. These are important for exploring CP violation within the SM but might also provide potential avenues for the discovery of NP.

In addition to the four larger detectors, two smaller experiments lie upstream of the ATLAS and CMS collision points in order to probe more specialised forward physics phenomena. These are the LHCf [86] and TOTEM [87] experiments.

4.2.1. Accelerator Complex

The LHC ring itself is the final stage in an injector chain which incorporates a series of accelerators built at CERN over the last 50 years. It is illustrated in Figure 4.1. Each stage supplies an incremental increase in the proton (or heavy ion) bunch energy. The first stage in this chain is a linear accelerator – either the Linac2 for proton injection or Linac3 during heavy-ion runs. The Linac2 injects protons into the Proton Synchrotron Booster (PSB) at an energy of 50 MeV. Similarly, the ions proceed first from the Linac3 to the Low Energy Ion Storage Ring (LEIR) before finally arriving at the Proton Synchrotron (PS). From here on, the paths of the protons and heavy-ions are the same. Proton bunches pass from the PSB to the PS at an energy of 1.4 GeV and then on to the Super Proton Synchrotron (SPS) at an energy of 26 GeV. Having arrived at the SPS, the protons circulate around a ring 2 km in diameter, where their energy is increased to 450 GeV. From here, kicker magnets inject the bunches into the LHC itself, where the proton energy can finally be increased to the design-specified 7 TeV per beam. The 2010 and 2011 data-taking periods were at 3.5 TeV, with an increase to 4 TeV planned for 2012.

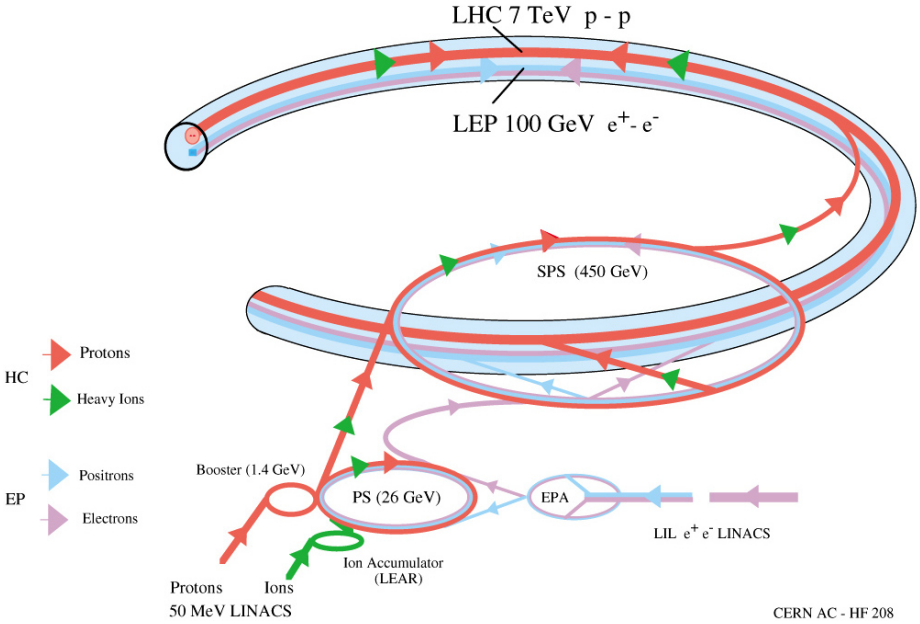

Figure 4.1.: Illustration of the LHC accelerator complex showing the path of protons and heavy-ions through a series of accelerators at CERN [88].

4.3. The Compact Muon Solenoid Experiment

CMS is a large, general purpose detector [84] at the LHC. It has been designed to search for the Higgs boson (see Section 1.4.3) as well as signatures of physics beyond the SM.

The design goals of CMS were as follows (paraphrasing the technical proposal document [83]):

1. a high quality, redundant muon system,
2. the best possible ECAL
3. high quality central tracking to complement these two systems and
4. an affordable detector.

CMS adopts a traditional cylindrical design (see Figure 4.2), 21.5 m in length and 15 m in diameter. A key feature of the detector is the superconducting solenoid, delivering a nominal 4 T magnetic field. The bending field supplied provides accurate muon momentum resolution up to energies of ≈ 1 TeV. The size of the solenoid placed stringent limitations on the volume of the inner detector subsystems (everything except for the muon chambers and return yoke).

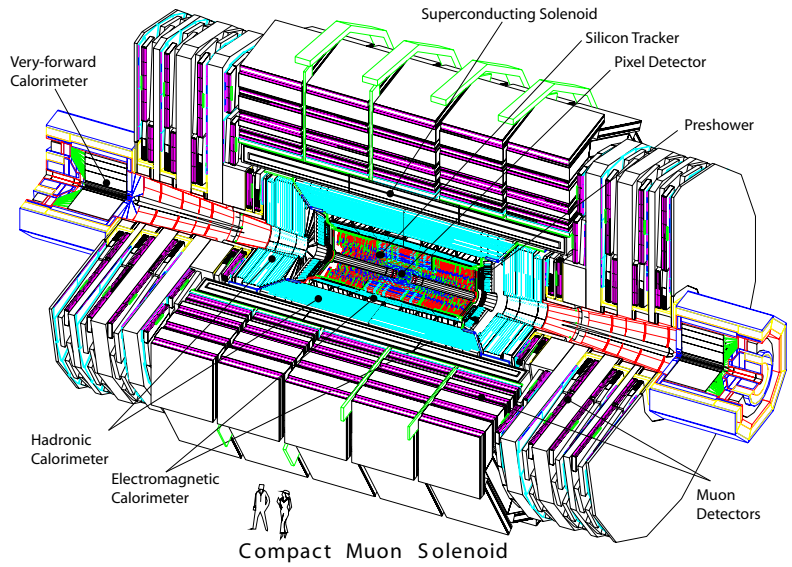

Figure 4.2.: Illustration of the CMS detector with subdetectors labelled [84].

4.3.1. Coordinate System

The coordinate system at CMS is right-handed, with its origin placed at the nominal beam collision point inside CMS. The x axis is then defined to point horizontally inwards towards the centre of the LHC ring and the y-axis, vertically upwards. The z-axis is aligned along the beam-line, pointing towards the nearby Jura mountains. Often a cylindrical coordinate system will be used where the azimuthal angle, ϕ, and radial coordinate, r, span the $x-y$ plane. The azimuthal angle is measured with respect to the x-axis. The pseudorapidity, $\eta = -\ln\tan\frac{\theta}{2}$ where θ is the polar angle measured with respect to the z-axis.

4.3.2. Silicon Tracker

The innermost subsystem of CMS is the silicon tracker [89], designed to provide highly precise measurements of particle trajectories close to the CMS interaction point. It is shown in cross section in Figure 4.3. The tracker extends to pseudorapidities of $|\eta| < 2.5$ and has an active silicon area of more than 200 m^2, making it the largest silicon tracker ever built.

The tracker design can be better understood by considering the expected particle flux at design luminosity as a function of radial distance, r, from the beam-line.

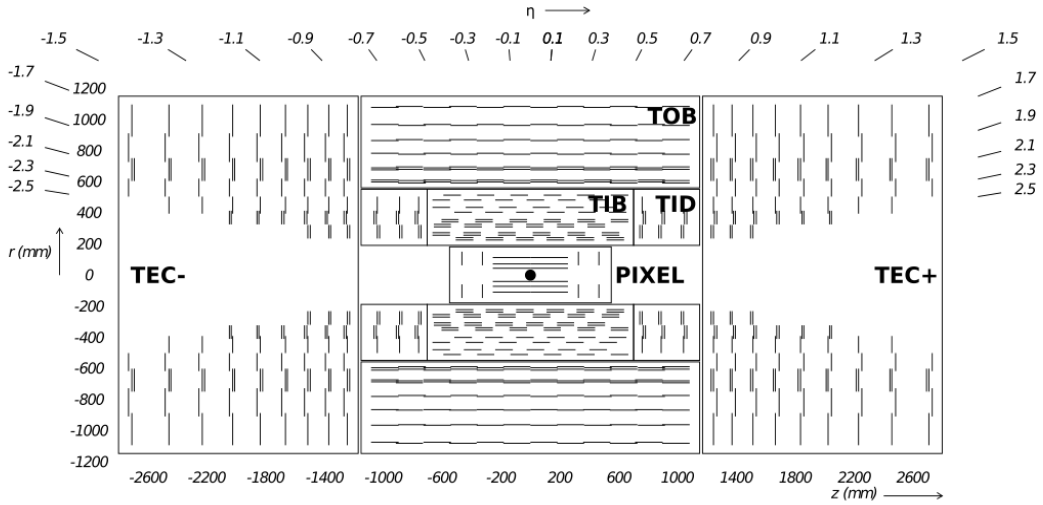

Figure 4.3.: Schematic cross section through the CMS tracker. Each line represents a detector module. Double lines indicate back-to-back modules which deliver stereo hits [84].

- At $r \approx 10$ cm the particle flux is highest. Accordingly, the innermost layer of the CMS tracker is comprised of hybrid pixels. With an area of 100×150 µm^2, particle densities are $O(10^{-4})$ per pixel per LHC bunch crossing.
- At a radius $20 < r < 55$ cm, reduced particle flux allows the use of silicon microstrip sensors. With a much larger area of 10 cm $\times$ 80 µm, average particle densities are $O(10^{-2})$ per strip per bunch crossing.
- At $r > 55$ cm, still larger silicon strips can be used, with sizes up to 25 cm $\times$ 180 µm. This gives a particle density of $O(10^{-2})$ per strip per bunch crossing.

Pixel Tracker

The hybrid pixels are placed closest to the interaction point. As well as maintaining an acceptable particle density per sensor, their close proximity to the interaction point allows the origin of collision products to be accurately determined. In the barrel region, 3 layers are placed at mean radii of 4.4, 7.3 and 10.2 cm. The detector has a length of 53 cm in the z direction. The end discs are instrumented with only two layers and are located at $|z| = 34.5, 46.5$ cm. The pixel modules in these layers are arranged in a "turbine-like" layout.

Strip Tracker

Further from the interaction point, the tracker is instrumented with silicon strip detectors. The barrel component can be further divided into the Tracker Inner Barrel (TIB) and the Tracker Outer Barrel (TOB). The TIB is composed of 4 layers and the TOB a further 6. The TOB extends to $z = \pm 118$ cm. Beyond this are the endcaps which can again be split into two components: the Tracker Endcap (TEC) made up of 9 disks and the Tracker Inner Disk (TID), 3. The silicon micro-strip sensors are 320 µm thick and oriented parallel to the z-axis in the barrel and radially in the disks.

Both the TIB and TID supply up to four measurements in $r - \phi$. The inner two layers of the TIB have a strip-pitch of 80 µm, and the outer two, 120 µm. These achieve single point resolutions of 23 and 35 µm respectively. In the TID, the strip pitch varies between 100 and 141 µm.

The TOB uses 500 µm thick sensors with a strip-pitch of 183 µm in the first four layers and 122 µm in the outer two. This gives a single point resolution of 53 µm and 35 µm respectively.

The first two layers of the TIB, TOB and TID and rings 1, 2 and 5 of the TEC are so-called "stereo modules". These are double-sided modules where the two layers of strips have a stereo angle of 100 mrad between them. This provides additional resolution in the z measurement in the barrel (or r in the endcaps). The resolution of this measurement is 230 µm and 530 µm in the TIB and TOB respectively.

4.3.3. Electromagnetic Calorimeter

The ECAL surrounds the silicon tracker and provides a high resolution measurement of electromagnetic showers within a homogeneous, hermetic calorimeter [90]. The barrel region alone comprises 61,200 lead tungstate ($PbWO_4$) crystals, with 7,324 in each of the two endcaps. This material was chosen for its high density, short radiation length and small Molière radius. Scintillation photons are then recorded by Avalanche Photodiodes (APDs) in the barrel and Vacuum Phototriodes (VPTs) in the endcap. The driving motivation for the ECAL design was the detection of the low-mass favoured Higgs decay channel $H \longrightarrow \gamma\gamma$.

ECAL Barrel

The ECAL Barrel (EB) extends in rapidity to $|\eta| < 1.479$ with a crystal segmentation of 360×85 in $\eta - \phi$ for each half-barrel. Each crystal is slightly tapered, with a cross-section of 0.0174×0.0174 in $\eta - \phi$. The crystals have a front cross section of 22×22 mm^2 and a length of 230 mm (corresponding to 25.8 radiation lengths).

ECAL Endcap

The ECAL Endcap (EE) occupies the rapidity range $1.479 < |\eta| < 3.0$. Crystals are grouped into 5×5 "supercrystals" within a carbon-fibre alveolar structure. The endcaps are split into two halves, known as "Dees", each holding 3,662 crystals.

The scintillation of the ECAL crystals as well as the amplification of the APDs varies as a function of temperature. This variation was found to be $\approx 4\%$ /°C. For this reason, the ECAL temperature is precisely regulated to within $\pm$ 0.05 °C.

ECAL Transparency and the CMS Laser Monitoring System

The $PbWO_4$ crystals that make up the ECAL are radiation resistant but quickly suffer a decrease in their optical transmission under irradiation [91]. This is a result of the formation of colour centres which absorb a fraction of the incident light. At a working temperature of 18 °C, the damage anneals, leading to an equilibrium in the optical transmission properties which are constant with dose rate. The consequence of this is a cyclic change in the optical transmittivity of the crystals as the LHC moves between colliding beams and machine refills. Since this depends on dose rate, the effect is a function of LHC luminosity and rapidity. It is expected to range from a shift of $\sim 2\%$ in the barrel at low luminosity to $> 10\%$ in the endcaps at high luminosity. The magnitude of this effect on energy and momentum measurements would be disastrous if not properly accounted for. Correction for this effect necessitates constant monitoring of the transparency – a task performed by the laser monitoring subsystem [92].

Three lasers are used for the transparency measurement: two blue ($\lambda \approx 440$ nm) and one near-infrared ($\lambda \approx 796$ nm). The blue laser (with a second fitted for redundancy purposes) is close to the scintillation emission peak and thus can be used to track the changes in the crystal transparency. The near-infrared laser is far from the emission peak and thus relatively stable to changes in the transparency. This can be used to

verify the stability of the system. The lasers are distributed to the crystals via optical fibres and a series of fan-outs. Approximately 1% of the LHC beam gap of 3.17 µs is used for transparency monitoring. A full scan of the entire ECAL can be achieved in approximately 30 minutes. The lasers can be pulsed at ≈ 80 MHz with a pulse timing jitter of 3 ns. This is adequate for synchronisation with the LHC bunch crossings.

The transparency of the crystals is derived from the response of the APD normalised to the height of the laser pulse, as measured using a silicon photodiode. Due to differences in path length and optical spectra between the laser and the scintillation light, the transparency of the crystals may be related to the measured transparency via a power law.

4.3.4. Hadronic Calorimeter

Accurate measurement of hadronic showers is crucial for analyses involving jets or missing energy signatures. The Hadronic Calorimeter (HCAL) [93] lies between the outer edge of the ECAL and the inner edge of the solenoid ($1.77\text{ m} < r < 2.95\text{ m}$). This constrains the size of the HCAL to a relatively compact design and necessitates the placement of a "tail catcher" outside of the solenoid.

HCAL Barrel

The HCAL Barrel (HB) comprises 36 azimuthal wedges, with 18 in each half barrel. Each wedge consists of alternating layers of brass absorber plates and plastic scintillators. The light from these plates is then carried via wavelength-shifting fibres to a Hybrid Photodiode (HPD) for readout. The number of interaction lengths increases with polar angle, from 5.82 at 90° to 10.6 at $|\eta| = 1.3$ [94].

HCAL Endcap

The HCAL Endcap (HE) covers the rapidity range $1.3 < |\eta| < 3$ and receives a larger radiation flux than the HB. Each endcap consists of 36 wedges, and wavelength shifting fibres are once again used to take light from plastic scintillators to HPDs. Including the ECAL, the HE depth is equivalent to ≈ 10 interaction lengths.

HCAL Outer

The HCAL Outer (HO) or "tail catcher" provides increased sampling depth in the rapidity region $|\eta| < 1.3$ where the HB and EB do not provide sufficient containment. Since the HO lies outside the solenoid, its design is constrained by that of the muon chambers – with 5 rings in η. The solenoid coil provides additional absorption, giving the calorimeter system a minimum depth of 11.6 interaction lengths.

HCAL Forward

The HCAL Forward (HF) is positioned in the rapidity range $|\eta| > 3$ and consequently must endure a much larger particle flux – approximately 760 GeV per proton-proton interaction (versus ≈ 100 GeV for the rest of the detector). Radiation hardness was thus a leading consideration in its design.

Quartz fibres are interleaved between steel absorbers. Shower particles above the Cherenkov threshold ($E \geq 190$ keV for electrons) produce Cherenkov light. This is routed to the rear of the calorimeter and read out by Photomultiplier Tubes (PMTs). The HF is most sensitive to the electromagnetic component of the shower.

4.3.5. Muon Chambers

Accurate measurement of muons is one of CMS' key design goals. The effect of radiative losses in the tracker is much less for muons than it is for electrons. Thus muons are able to provide a much finer mass resolution at low transverse momentum. This is an important advantage for a variety of physics searches and measurements at CMS. The muon system is responsible for muon identification, momentum measurement and triggering (for further detail see Section 4.3.6). Three types of detectors are used, chosen for different regions of the detector according to the magnetic field, muon rate and response time required for input to the trigger.

Drift Tubes

In the barrel region, the magnetic field is relatively uniform and the muon flux low enough to allow the use of the Drift Tube (DT) [95]. These identify muons in the region $|\eta| < 1.2$. The drift chamber was first developed as a refinement of earlier wire proportional chamber

designs in which the drift time of the electrons to the anode wire is used to provide additional spatial resolution. This allows the wire spacing to be increased, thus reducing the electronics requirements.

Each DT is composed of 2 (or 3) "super-layers", with each super-layer further divided into 4 layers of rectangular drift cells. Of the four concentric muon stations in the barrel, the inner three contain 60 drift chambers and the outermost, 70. The wires in the outer two layers of each drift cell are oriented parallel to the beam line, providing a measurement in the $r\phi$ direction (in the magnetic bending plane). The inner two layers are perpendicularly aligned, giving a measurement of the z coordinate.

Cathode Strip Chambers

In the endcap region, the large muon and background rate coupled with the strong, non-uniform magnetic field, prevent the use of DTs. Instead, an alternative instrument is used – the Cathode Strip Chamber (CSC) [96]. The CMS muon system endcap consists of 468 CSCs, each a trapezoidal multiwire proportional chamber arranged radially covering an azimuthal angle $\Delta\phi$ of either 10 or 20 degrees. Each CSC has 6 anode wire planes interleaved with 7 cathode strip planes. The wire readout provides a measurement of the r coordinate whilst a measurement of ϕ is obtained by interpolating charges on the cathode strips.

Resistive Plate Chambers

The trigger (see Section 4.3.6) requires a muon detector capable of providing a fast signal with adequate spatial resolution. This is the Resistive Plate Chamber (RPC) [97], a gaseous, parallel-plate detector with spatial resolution suitable for both barrel and endcap regions and a response time much less than the 25 ns between consecutive LHC bunch-crossings. This allows the RPC to unambiguously identify the bunch-crossing assignment for a muon track, even in the presence of the large backgrounds and high rates of the LHC environment.

4.3.6. Data Acquisition and Trigger System

The high luminosity of the LHC beam leads to a high particle flux in the detector. The separation of particles in the detector becomes increasingly difficult. In addition, many analyses benefit from precise position and momentum measurements. Consequently, the CMS subdetectors are constructed with an extremely fine granularity. Unavoidably, this requires an extremely large number of read-out channels - approximately 55 million across the whole detector. To make matters worse, the LHC is planned to achieve a bunch-spacing of only 25 ns. For these reasons, the Data Acquisition (DAQ) system at CMS faces the simultaneous challenges of large bandwidth and low-latency.

Tightly coupled to the DAQ is the trigger system [98]. The huge number of readout channels in CMS is not only a challenge in terms of the bandwidth of the DAQ but also poses serious difficulties relating to long-term storage requirements. A digitised, zero-suppressed event dump from CMS is approximately 2 MB in size. With an event rate of up to 40 MHz, this would require a storage rate of 80 TB/s. Despite the rapid improvement in disk storage technology over the last few decades, such storage capacities are clearly infeasible both in terms of capacity and Input/Output (IO) requirements. For these reasons, a system capable of quickly rejecting a very large fraction of collisions is required. This is known as the trigger.

Triggering at CMS

The trigger at CMS is split into two stages. The first stage, the Level 1 Trigger (L1T), must operate at the full LHC bunch-crossing frequency. To achieve adequate latency, it is implemented almost entirely within electronic logic – either Field Programmable Gate Arrays (FPGAs) or custom designed integrated circuits. The L1T must reduce the rate to 100 kHz.

In the second stage of the trigger, the High Level Trigger (HLT), the rate is further reduced to $O(100\,\text{Hz})$. Due to the reduced rate, the HLT is implemented in software running in a computing farm. Since the HLT has access to a full read-out of the detector, and more time to issue a trigger decision, more sophisticated trigger algorithms are used. Often these are similar to those used by the off-line reconstruction.

The Level 1 Trigger

The L1T must produce a trigger decision with minimal latency. This latency is chiefly limited by the size of the pipeline on the Analogue Pipeline Voltage 25 (APV25) chip used to readout from the silicon strip tracker. The APV25 samples the voltage from the silicon strips at 25 ns intervals. These are stored in a pipeline, 192 samples deep. This constrains the L1T to provide a decision within ≈ 3.2 µs.

The L1T has limited access to detector subsystems and only a limited time in which to issue a trigger decision. In particular, since tracker measurements are not available, distinction between electrons and photons is not possible. The challenge for the L1T is therefore not only to make a fast decision using limited information from the detector, but also to ensure that potentially interesting events are retained and passed onto the HLT for more thorough analysis.

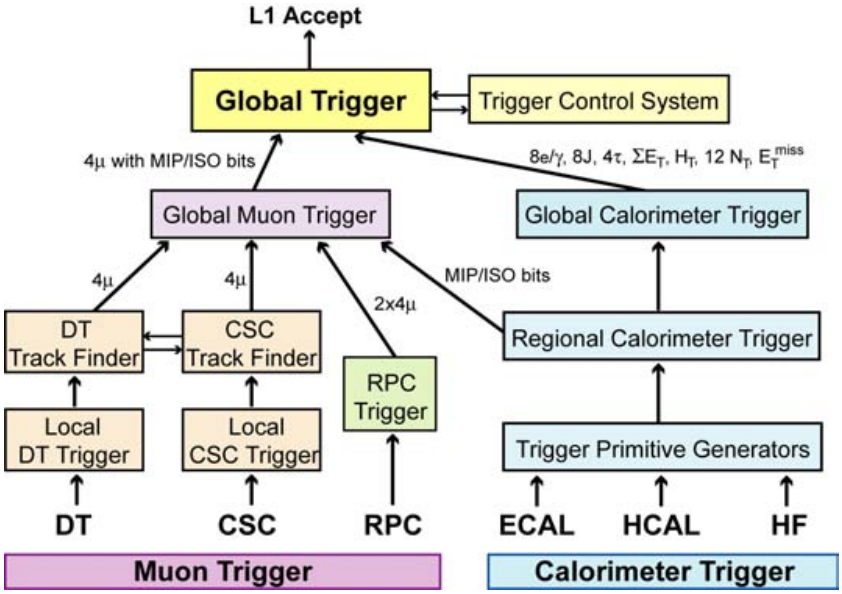

Figure 4.4.: Diagram showing the organisation of subsystems within the CMS L1T [84].

The structure of the L1T is shown in Figure 4.4. The Global Trigger (GT) is the final stage in the trigger chain. It receives "trigger objects" from two subsystems: the Global Calorimeter Trigger (GCT) and Global Muon Trigger (GMT). Objects, ranked according to their energy and quality, are received along with their coordinates in η and ϕ. These objects are processed by 128 algorithms, each of which produces a trigger decision. The final output of the GT is then determined by a configurable mask, which may be altered to meet different data-taking objectives. The final trigger decision is then sent to the Timing, Trigger and Control subsystem in order to initiate a read-out of the detector.

The calorimeter trigger subsystem begins with the Trigger Primitive Generator (TPG). This sums energy deposits from the ECAL and HCAL into "trigger towers". These are received by the Regional Calorimeter Trigger (RCT), where electron/photon candidates are found and the trigger tower energies summed into larger "RCT regions". These consist of 4×4 trigger towers (except in the HF where only a single trigger tower is included). The RCT also records a "tau-veto" bit, used to distinguish jets from hadronic tau decays.

The output of the RCT is then processed by the GCT [99]. The GCT logic is implemented primarily in FPGAs. The GCT performs a number of tasks in parallel. It sorts the list of electron/photon candidates and passes the four highest ranked objects to the GT. It also performs a simple jet-finding algorithm on the RCT regions, classifying them as *forward*, *central* and *tau* jets. The last category includes jets for which none of the constituent RCT regions has its tau-veto bit set. The four highest ranked of each category are then forwarded to the GT.

The final task of the GCT is to form global energy sums. These are the total transverse energy, missing transverse energy, jet counts and H_{T} (the scalar sum of the jet energies). These too are forwarded to the GT.

The muon trigger receives input from all three muon subdetectors: RPCs, CSCs and DTs. These are integrated in the GMT. The muons received from each subdetector are matched and sorted by transverse momentum and quality. The four highest rank candidates are forwarded to the GT.

4.3.7. Computing at CMS

To meet the extremely large computation and storage requirements of data analysis at the LHC, analysis tasks are performed using a dedicated computing grid [100]. Events are first sent to the "tier-0" storage site at CERN with additional copies forwarded to a number of "tier-1" sites around the world. Data is made available for analysis use, in various re-processed forms, at "tier-2" and "tier-3" grid sites. User analysis jobs are submitted to the grid, and routed automatically to a suitable site.

Events recorded by the CMS detector pass through a chain of reconstruction stages. At each stage, higher-level physics objects are built out of simpler ones, with a consequent reduction in the data size. Monte Carlo (MC) events are processed using either a detailed GEANT4 simulation [101], or a faster, parameterised model of the response known as

FastSim. This simulates the response of the CMS subdetectors to the generated particles. After the detector response has been simulated, MC is processed in exactly the same manner as data.

Chapter 5.

Physics Objects

5.1. Introduction

In the previous chapter details of the CMS detector were presented. We shall now begin to discuss the algorithms used to reconstruct analysis level objects and quantities which will be of fundamental importance in later chapters. The objects of primary interest for these purposes are leptons, jets and missing energy. The offline reconstruction algorithms used to reconstruct each object will be presented, along with issues and properties related to data analysis. Some details of the reconstruction performance at CMS will also be shown. Finally, the Particle Flow (PF) algorithm, which provides a global reconstruction of the event, will be explained in some detail. As will be seen, PF combines tracking and calorimeter measurements to provide excellent reconstruction of jets and missing energy.

5.2. Leptons

The reconstruction of electrons and muons at CMS will now be described. Since tau leptons are not used by either of the analyses presented in this work, their reconstruction will not be described here. The interested reader is directed to relevant literature [102,103].

5.2.1. Muons

The full details of muon reconstruction at CMS are presented in [104–106]. A brief overview will be presented here, focusing on the aspects pertinent to the following analysis

chapters. Muons are reconstructed in both the muon chambers and the silicon tracker. To exploit this redundancy in the measurement, several reconstruction algorithms have been developed.

Tracker Muons

Tracker muons begin as tracks in the silicon tracker. All tracks with a $p_{\mathrm{T}} > 0.5$ GeV and $p > 2.5$ GeV are considered as muon candidates and extrapolated to the muon stations, accounting for expected energy loss and multiple scattering effects. If at least one muon track segment matches the extrapolated tracker track, a tracker muon is reconstructed. This algorithm is more efficient at low momentum ($p < 5$ GeV) since it requires only a single segment in the muon chambers.

Standalone Muons

Standalone muons are based solely on measurements in the muon chambers. The hits in each chamber are fit individually to obtain seeds – a position and direction vector along with an estimate of the transverse momentum. These form the basis of a track fit in the muon chambers based on the Kalman-filter technique [107]. The fit is constrained to the vertex in order to reject cosmic ray muons. Since much of the calibration and validation work for the muon system was performed using cosmic rays, a separate algorithm was developed for this purpose [108].

Global Muons

Global muons are an extension of standalone muons to include measurements in the silicon tracker. For muons with a transverse momentum below ≈ 200 GeV, the tracker provides a better momentum resolution. For higher momentum muons, the tracks become straighter and the momentum measurement increasingly affected by uncertainty in the position measurement. In this regime, inclusion of hits in the muon chambers effectively benefits from the large lever arm and 3.8 T magnetic field in the region between the silicon tracker and the muon chambers.

For each standalone muon, the set of tracker tracks is searched and the best matching candidate selected. For each pairing found in this way, a Kalman-filter fit is again performed, this time using hits from both the silicon tracker and the muon chambers.

This fit accounts for average expected energy losses, magnetic field and multiple scattering effects. The tracks reconstructed by this procedure become global muons. Once again, certain modifications are required for reconstructing cosmic ray muons – for instance in the case that cosmic muons traverse the entire detector, leaving two standalone muons on either side of CMS.

Merging

Reconstructed muons from each of the algorithms detailed above are then merged into a single list of muon candidates. Candidates reconstructed as both global and tracker muons are merged. Standalone muon tracks are merged with tracker muons if they share a muon segment. The fit results from each algorithm are retained.

An analysis is then able to tune its identification cuts to meet certain efficiency or purity requirements for a particular kinematic range. A number of predefined selections are available.

- "Soft muons" are required to be reconstructed as tracker muons with a muon segment in the outermost station matching the position and direction expected from extrapolation of the track.
- "Global muons" are simply those muons reconstructed by the global muon algorithm described above.
- "Tight muons" must be reconstructed as both a global muon and a tracker muon with a series of additional requirements: a $p_{\mathrm{T}} > 3$ GeV, a global muon track fit with a normalised $\chi^2 < 10$, at least two muon stations with matching muon segments, at least 10 hits in the silicon tracker (with at least 1 pixel hit) and a transverse impact parameter $d_{xy} < 2$ mm. This selection significantly suppresses decays-in-flight at the cost of a small loss in efficiency for prompt muons.

Figure 5.1 shows the muon transverse momentum resolution as a function of muon p_{T}.

5.2.2. Electrons

Electron reconstruction at CMS makes use of measurements from both the silicon tracker and the ECAL. In the case of CMS, the large amount of material in the tracker causes electrons to radiate a large fraction of their energy before reaching the ECAL – 50%

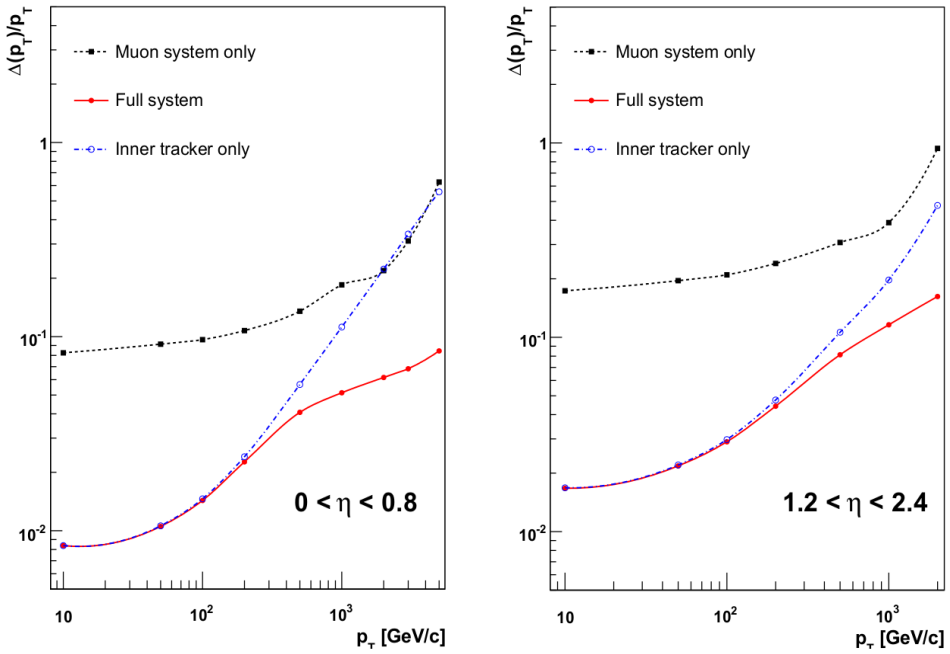

Figure 5.1.: Muon transverse momentum resolution as a function of transverse momentum shown for the muon system only, the inner tracking only and both. The left figure is for $|\eta| < 0.8$ and the right figure for $1.2 < |\eta| < 2.4$ [84].

of electrons radiate more than 50% of their energy in this way. To obtain an accurate measurement of the electron energy, this energy, radiated in the form of bremsstrahlung photons, must be reconstructed correctly.

Reconstruction

Electron seeds are derived using two separate algorithms: *tracker-driven* and *ECAL-driven* [109]. The tracker-driven algorithm was developed for the purposes of the PF algorithm. It is most suitable for low-p_{T} electrons and electrons produced inside jets. Seeds are found by extrapolating Gaussian Sum Filter (GSF) tracks in the tracker from their outermost measurement to the ECAL. If a matching cluster is found, a tracker-driven seed is created [110].

ECAL-driven seeds begin with the reconstruction of ECAL "superclusters" with transverse energy, $E_{\mathrm{T}} > 4$ GeV. A supercluster is a group of one or more ECAL clusters. It is formed to account for the narrow η width and spread in ϕ caused by the bending effect of the CMS magnet on electrons radiating in the tracker [111]. These superclusters are then matched to track seeds having two or three hits in the inner layers of the tracker.

Electron tracks are built from these track seeds. Trajectories are calculated accounting for energy loss in the tracker. These are then fit with a GSF [112].

Candidates found only by the tracker-driven method must pass a pre-selection based on a multivariate analysis [110]. Candidates found by the ECAL-driven algorithm are pre-selected by imposing an angular matching requirement between the GSF track and the supercluster. ECAL-driven seeds failing this matching requirement, but selected by the track-driven multivariate pre-selection, are kept.

As described in Section 4.3.3, electron energies are corrected to account for changes in the transparency of the ECAL crystals. For the W polarisation measurement, a set of "ad-hoc" corrections were calculated from fits to the Z mass. For the SUSY search analysis, more sophisticated corrections were available [92].

Electron Identification

The large bremsstrahlung-induced energy loss, coupled with larger backgrounds from jets and photons, means that electrons at CMS are fundamentally less well-defined objects than muons. There is therefore a much larger space to trade-off between signal efficiency and purity. Whilst more complex selection procedures are available (e.g. a multivariate approach), a simple cut-based selection was chosen for the measurement of the W cross-section [113, 114] and has been used in this work. The variables have been chosen for their background rejection capabilities but also for robustness during the early data-taking period.

A number of "working points" have been defined, each offering a fixed signal efficiency, as measured in a simulated $\mathrm{W} \longrightarrow \mathrm{e}\nu$ sample. In each case, the cuts were chosen to optimise background rejection power. These cuts were optimised independently in the CMS barrel and endcaps.

The cut variables used are described below, with cut-values for each working point shown in Table 5.1.

- $\sigma_{i\eta,i\eta}$ is a measure of the Root Mean Squared (RMS) shower width of the electron in the η direction.
- $\Delta\phi_{\mathrm{in}}$ and $\Delta\eta_{\mathrm{in}}$ represent the angular separation between the trajectory of the GSF track and the ECAL supercluster.

- Tracker, ECAL and HCAL isolation quantities summed in a cone $\Delta R < 0.3$ [115]. The energy deposits and track associated with the lepton are removed. A threshold of 700 MeV is applied to the tracks contributing to the sum. Similarly, in the ECAL, a zero-suppression cut is applied (0.08 GeV in EB and 0.1 GeV in EE). The isolation cone is centred on the track direction at the vertex for the tracker isolation, and the supercluster for the calorimeter quantities. The combined isolation, I_{comb}, is then defined as

$$I_{\text{comb}} = \frac{\sum_{\text{tracks}} p_T^{\text{track}} + \sum_{\text{dep}} E_T^{\text{em}} + \sum_{\text{dep}} E_T^{\text{had}}}{P_{\text{T}}^{\text{e}}},$$

  where the sums run over the aforementioned tracks, ECAL energy deposits and HCAL energy deposits respectively.

- H/E is the ratio of the energy deposited in the HCAL behind the electron seed to that in the ECAL. This might also be called the "HCAL leakage".

The remaining variables are used to reject electrons arising from converted photons [116]. For conversions which occur after the first layer of the tracker, a pattern of *missing hits* may be observed. These are layers of the inner tracker without a hit, where one would be expected from extrapolation of the track. Conversions can be rejected by requiring either no such missing hits, or a single missing hit – depending on the desired efficiency.

Further rejection against photon conversions is provided by the variables Dist and $\Delta \cot \Theta$. These are calculated as follows (see Figure 5.2). Firstly, potential conversion partners are found by pre-selecting all Combinatorial Track Finder (CTF) tracks in a cone $\Delta R < 0.3$ of the GSF track and having opposite charge.

- $\Delta \cot \Theta$ is defined as

$$\Delta \cot \Theta = \cot\left(\Theta_{\text{CTF track}}\right) - \cot\left(\Theta_{\text{GSF track}}\right),$$

  where the Θ represent the polar angles of the respective tracks and

- Dist is defined as the two-dimensional distance in the $x - y$ plane between the two tracks, at the point at which they would be parallel when extrapolated.

The choice of CTF tracks is restricted to avoid picking the track associated with the electron. Conversion electrons will tend to have smaller values of $|\Delta \cot \Theta|$ and |Dist|. If a suitable partner track is found, the electron is rejected if both |Dist| and $|\Delta \cot \Theta|$ are below given thresholds.

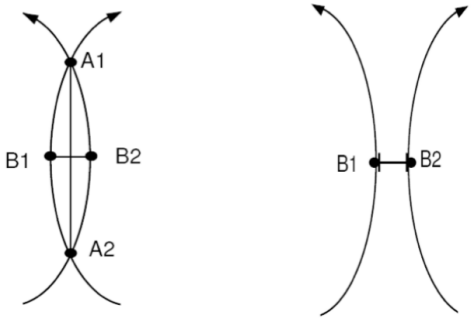

Figure 5.2.: Diagram illustrating the electron conversion rejection variables, Dist and $\Delta \cot \Theta$. Dist is the distance between points B1 and B2 in the $x-y$-plane. Here, the two tracks from the photon conversion are parallel. Dist is negative when the two tracks overlap and positive otherwise [116].

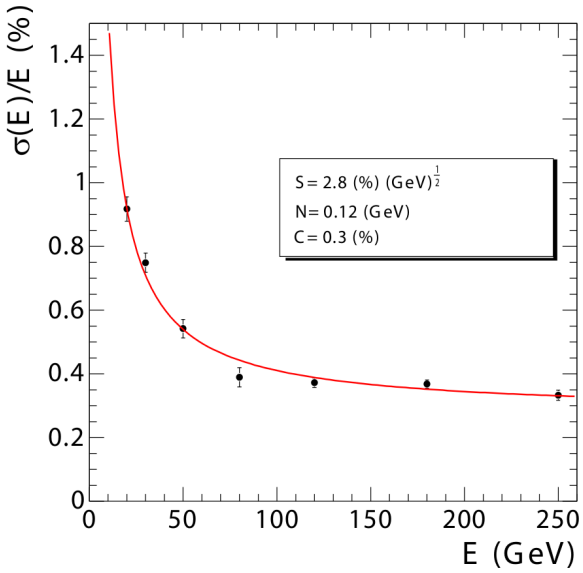

Figure 5.3.: ECAL energy resolution as a function of electron energy from the results of a test beam measurement. The energy has been measured in an array of 3×3 crystals with an electron impacting the central crystal. The values of the stochastic (S), noise (N) and constant (C) terms are also shown [84].

The pseudorapidity acceptance for electrons is $|\eta| < 2.5$. However, the barrel-endcap transition region, $1.4442 < |\eta| < 1.566$ is explicitly excluded.

Figure 5.3 shows the ECAL energy resolution as a function of electron energy from the results of a beam test. The electron fake rate is shown as a function of E_{T} and η for the 95% and 80% efficiency working points in Figure 5.4.

Table 5.1.: Cut values for the simple cut-based electron indentification working points [114].

Efficiency	0.95	0.9	0.85	0.8	0.7	0.6
Conversion Rejection						
Missing Hits $\leq$	1	1	1	0	0	0
|Dist|	-	0.02	0.02	0.02	0.02	0.02
$\lvert\Delta \cot \Theta\rvert$	-	0.02	0.02	0.02	0.02	0.02
Barrel						
$I_{\text{comb}} <$	0.15	0.1	0.09	0.07	0.04	0.03
$\sigma_{i\eta,i\eta} <$	0.01	0.01	0.01	0.01	0.01	0.01
$\Delta\phi_{\text{in}} <$	0.8	0.8	0.06	0.06	0.03	0.025
$\Delta\eta_{\text{in}} <$	0.007	0.007	0.006	0.004	0.004	0.004
$H/E <$	0.15	0.12	0.04	0.04	0.025	0.025
Endcaps						
$I_{\text{comb}} <$	0.1	0.07	0.06	0.06	0.03	0.02
$\sigma_{i\eta,i\eta} <$	0.03	0.03	0.03	0.03	0.03	0.03
$\Delta\phi_{\text{in}} <$	0.7	0.7	0.04	0.03	0.02	0.02
$\Delta\eta_{\text{in}} <$	0.01	0.009	0.007	0.007	0.005	0.005
$H/E <$	0.07	0.05	0.025	0.025	0.025	0.025

5.3. Jets

Four types of jets are reconstructed at CMS: Calorimeter (Calo) jets, PF jets, Jet Plus Tracks (JPT) jets and track jets [117]. Calo jets are reconstructed from energy deposits in the ECAL and HCAL, combined into *calorimeter towers*. Calorimeter towers consist of one or more HCAL cells with geometrically matched ECAL crystals. Electronics noise is suppressed by applying a threshold to the calorimeter cells, with pile-up effects reduced by a requirement placed on the tower energy.

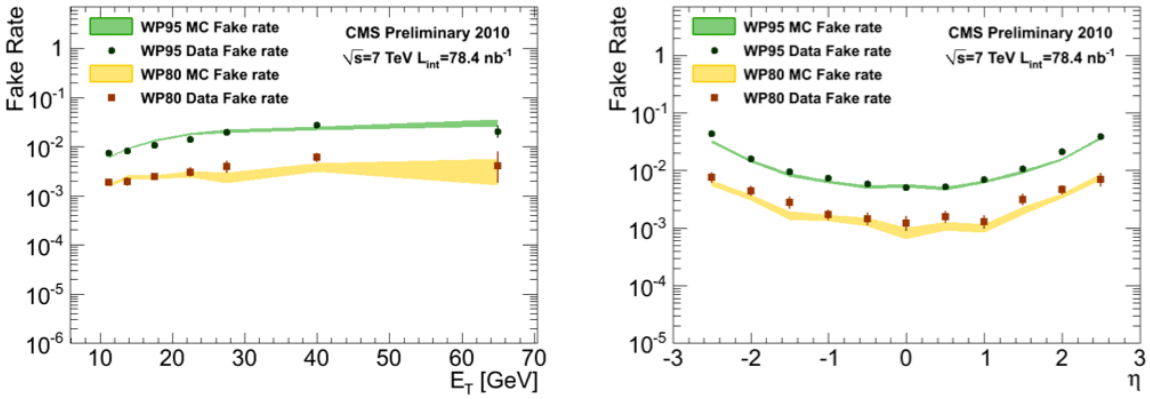

(a) (b)

Figure 5.4.: Electron fake rate per reconstructed electron as a function of (a) E_{T} and (b) η for the 95% and 80% efficiency working points. Results are shown for data and MC [111].

JPT jets associate tracks with Calo jets – using the tracker to give enhanced p_{T} resolution and response. PF jets are products of the Particle Flow algorithm described in Section 5.5. Finally, track jets are reconstructed from well measured tracks in the central tracker. Jets are clustered using the anti-k_t algorithm [118] with a size parameter, $R = 0.5$.

A useful jet-derived quantity is the "transverse hadronic energy" or H_{T}. This is simply defined as the scalar sum of the transverse momentum of jets in the event. The jets considered will be selected according to some quality and acceptance criteria.

5.3.1. Jet Energy Corrections and Jet Energy Scale

In general, the jet energy – as measured in the calorimeters – will be different from the corresponding particle jet energy. In order to correct for this difference, jet energy corrections are applied [119, 120]. The calibration of the jet energy will be referred to as the Jet Energy Scale (JES).

At CMS, jet energy corrections have been been factorised into three parts:

- *offset corrections* remove excess energy due to electronics noise and pile-up;
- *relative corrections* attempt to remove variations in jet response with respect to pseudorapidity and
- *absolute corrections* attempt to remove variations in jet response with respect to p_{T}.

These are measured using a variety of techniques, including the balancing of dijets, γ + jets and Z + jets events. Figure 5.5 shows the total correction factor as a function of η, for two values of the jet p_{T}. With these corrections applied, the residual uncertainty on the JES has been evaluated as a function of jet η and p_{T}. This will turn out to be a significant source of systematic uncertainty for the analyses presented in Chapters 6 and 7.

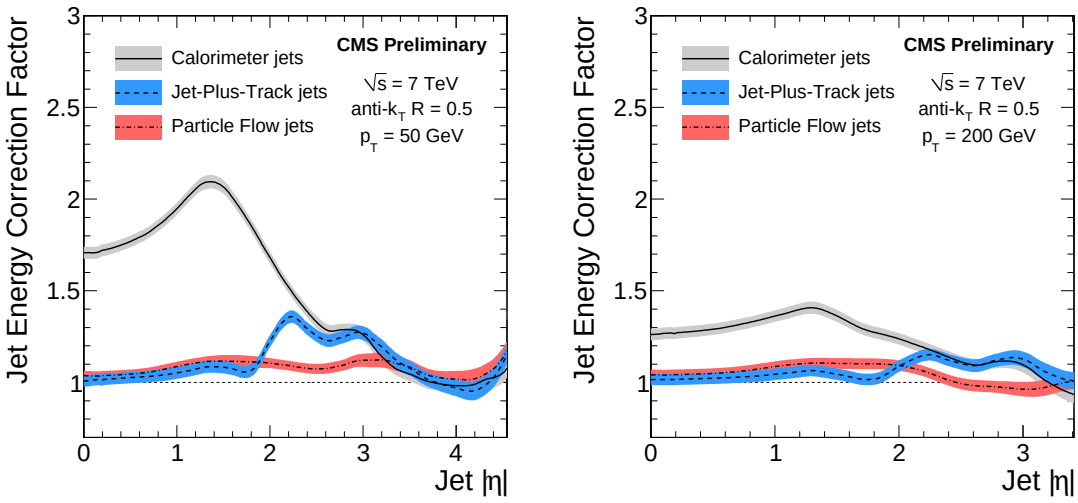

(a) 50 GeV **(b)** 200 GeV

Figure 5.5.: Total jet energy correction factor as a function of η for jets with transverse momenta of (a) 50 GeV and (b) 200 GeV. Corrections are shown for Calo, JPT and PF jets separately. The bands indicate the corresponding uncertainties [120].

5.4. Missing Energy

Certain particles, such as neutrinos, are not reconstructed by the CMS detector. However, their presence may be inferred by considering the total momentum of particles reconstructed by the detector and comparing this with the momentum of the initial state. Any imbalance in these quantities can be attributed to the presence of some "invisible" particles – a *missing energy* signature.

At a hadron collider, the situation is complicated by the fact that the boost of the initial partons parallel to the beam-line is not known. Hence missing energy measurement along this axis is not possible. For this reason, transverse quantities are used instead – most

commonly the *missing transverse energy*, $\vec{E}_T^{\text{miss}}$. This can be defined generically as

$$\vec{E}_T^{\text{miss}} = -\sum_{o \in \text{objects}} \vec{p}_T^{\,o},$$

where p_T^o represents the transverse momentum of object, o. The choice of a suitable set of objects then leads to a number of alternative definitions of $\vec{E}_T^{\text{miss}}$. The magnitude of this quantity, often used in event selection, will be denoted E_T^{miss}. Similar notation will be used for other transverse vector quantities.

At CMS, the simplest measurement of $\vec{E}_T^{\text{miss}}$ is *Calo* $\vec{E}_T^{miss}$ which sums over the calorimeter tower energies (ECAL and HCAL). An energy threshold is applied to the towers in order to reject electronics noise. Alternatively, *PF* $\vec{E}_T^{miss}$ sums over the candidate particles output by the PF algorithm. This will be discussed further in Section 5.5. As will be seen, this provides the most sensitive $\vec{E}_T^{\text{miss}}$ measurement at CMS and thus is used throughout the following analysis work. It should be assumed, unless otherwise noted, that references to $\vec{E}_T^{\text{miss}}$ or derived quantities make use of the PF measurement.

Alternative missing energy quantities can be defined for other purposes. The *missing transverse hadronic energy*, H_T^{miss}, is formed by taking the vector sum,

$$\vec{H}_T^{\text{miss}} = -\sum_{j \in \text{jets}} \vec{E}_T^{\,j}.$$

This is used to measure the transverse energy of particles recoiling against the jets in an event. For example, in W + jets events, the recoiling system is the W boson. $\vec{H}_T^{\text{miss}}$ is therefore one possible measurement of the W boson transverse momentum, $\vec{P}_{\text{T}}^{\text{W}}$.

5.5. Particle Flow at CMS

The PF algorithm [121, 122] attempts to provide a global reconstruction of the event – accurate determination of the type, energy and direction of all stable particles – by combining measurements from all subdetectors in CMS. This strategy is well suited for use with the CMS detector. The silicon tracker is able to reconstruct charged particle tracks with high efficiency and purity, down to transverse momenta as low as 150 MeV. Additionally, the granularity of the ECAL is sufficient for the separation of photons and charged particle energy deposits in jets with p_{T} of a few hundred GeV [121]. In contrast, the HCAL is much coarser. However, the combined energy resolution of both calorimeters

is $\sim 10\%$ at 100 GeV. This allows identification of the energy deposits associated with neutral hadrons as an excess on top of that accounted for by matching the deposits with charged tracks. The PF algorithm is able to reconstruct the components of jets and hadronic tau decays – primarily charged hadrons, neutral hadrons and photons. This provides an improved measurement of the jet energy and thus also of $\vec{E}_T^{\text{miss}}$.

The particle flow algorithm proceeds by linking tracks and energy clusters to form "blocks". An event display which illustrates this process is shown in Figure 5.6. A single block may contain a combination of a charged particle track, one or more energy clusters and a muon. The fine granularity of the CMS detector ensures that blocks typically contain 1, 2 or 3 elements. The links between each block are parameterised by a "distance" which encodes the quality of the link. Advanced tracking and calorimeter clustering algorithms have been developed to meet the needs of PF reconstruction. These will be discussed in the following sections.

5.5.1. Iterative Tracking

The tracker provides far superior measurements of the momentum and direction of charged hadrons than is possible with the calorimeters. It is important therefore that the tracks, which form the input to the PF procedure, be reconstructed with near 100% efficiency. The fake rate must also be low to avoid excess energy counting.

To meet these requirements, tracks are reconstructed using an iterative algorithm. This begins by reconstructing tracks with very tight selection requirements. Hits which can be unambiguously assigned in this step are then removed from consideration. The algorithm is iterated, and reconstruction of tracks from the remaining hits is attempted, this time with loosened selection criteria. This procedure is repeated with progressively looser selection criteria. This ensures high efficiency, whilst the removal of hits at each stage reduces the fake rate induced by combinatorics. After three iterations, tracks originating close to the beam line are reconstructed with an efficiency of 99.5% for muons and $> 90\%$ for charged hadrons. The fourth and fifth iterations relax constraints on the vertex, allowing the reconstruction of secondary charged particles.

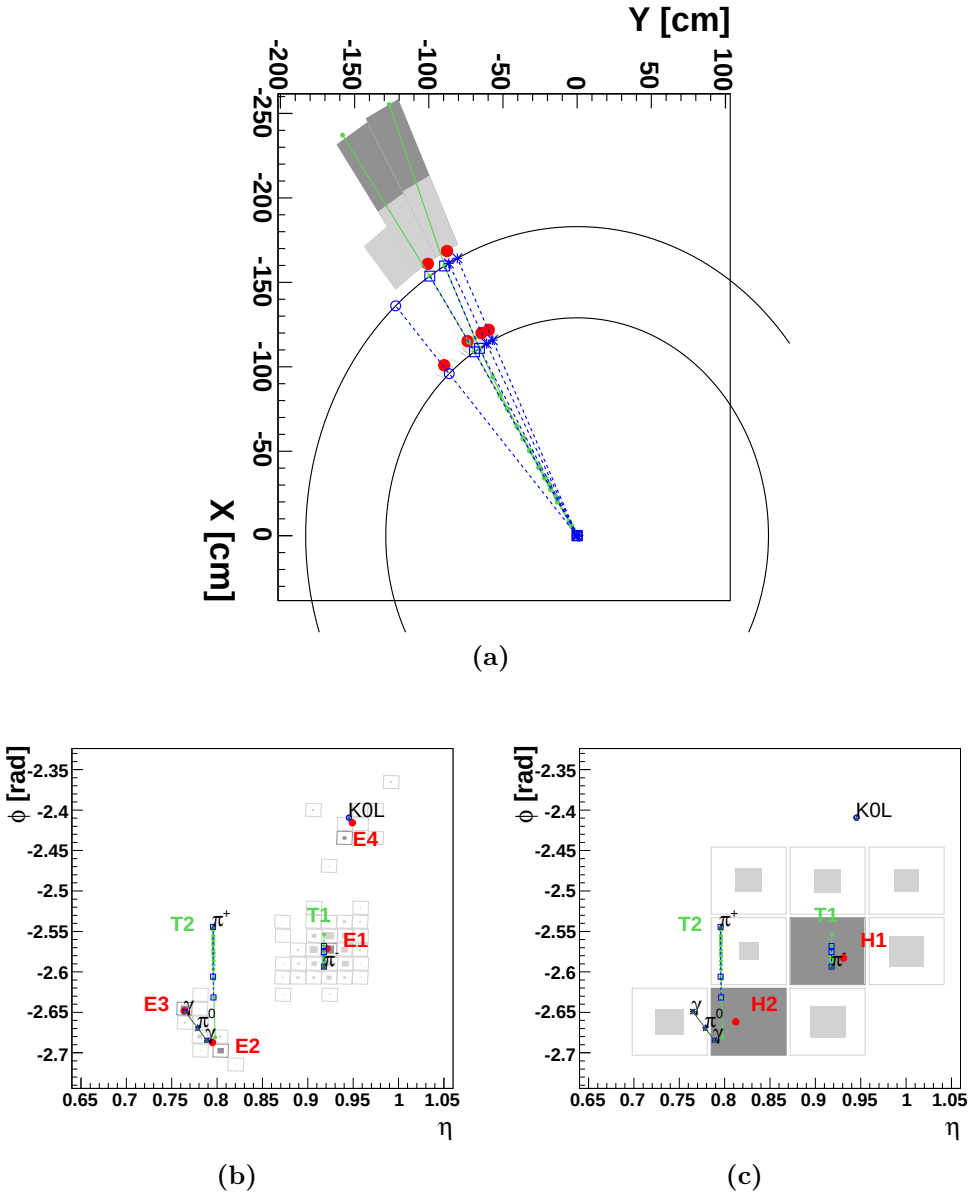

Figure 5.6.: An event display showing a hadronic jet in (a) the (x, y)-plane, (b) an (η, ϕ) view at the surface of the ECAL and (c) the same orientation at the surface of the HCAL. These two surfaces appear as circular arcs in (a). The K^0_L, π^-, π^+, π^0 and the two photons from its decay are shown. The K^0_L, π^- and two photons result in clear, well-separated ECAL clusters – round points labelled E1 to E4 (b). The π^+ and π^- are reconstructed as charged tracks – green lines labelled T1 and T2 – which point to the two HCAL clusters – round points labelled H1 and H2 [121].

5.5.2. Calorimeter Clustering

The success of the PF reconstruction also depends on certain aspects of the energy-clustering algorithm. In particular, as for the tracks, the clustering must be highly efficient and able to distinguish closely-spaced energy deposits. To this end, a specialised clustering algorithm was developed. This algorithm is used in the ECAL, HCAL and PS but not in the HF, where each cell is treated as a single cluster.

The first step of the algorithm produces *seed clusters*. These are local maxima in the calorimeter cell energies which have passed a minimum threshold requirement. These seed clusters are then extended to include cells sharing at least one side in common with a cell already in the cluster and an energy exceeding a threshold chosen according to the standard deviation of electronics noise in the calorimeter. These *topological clusters* are then transformed into *particle flow clusters*, with a separate particle flow cluster for each seed within the topological cluster. The energy and position of each particle flow cluster is determined iteratively, with the energy of each cell shared among the particle flow clusters.

5.5.3. Building Links

Each track is extrapolated from the position of its last measured hit to: the PS, the ECAL at a depth corresponding to the expected maximum for an electron shower and the HCAL at a depth of 1 interaction length. In each case, if the extrapolated track position lies within the envelope of a cluster, a link is created. The link distance is the (η, ϕ) distance between the extrapolated track and the cluster. The envelope may be enlarged with respect to the cluster by the extent of a single cell.

Energy contributions from bremsstrahlung photons are included by extrapolating the track-tangent at each tracker layer to the ECAL. If the extrapolated track lies within the envelope of the cluster, a link is created. Links are also created between calorimeter clusters in different subdetectors if the cluster position in the finer-grained calorimeter lies within the envelope of the more coarsely grained calorimeter. The link distance is taken to be the (η, ϕ) separation of the two clusters.

Muons are included when a global fit between a track in the tracker and a muon track in the muon chambers yields an acceptable χ^2. If several global muons are found for

a single muon track, only that possessing the smallest χ^2 is retained – with the link distance determined by the χ^2.

5.5.4. Particle Reconstruction

In the first stage, muons are reconstructed. Each global muon gives rise to a particle flow muon, providing that its momentum, as determined from the global fit, is compatible with the track momentum to within 3 standard deviations. The corresponding track is then removed from the block.

The next step is electron reconstruction. Electron tracks in the block are first selected by a pre-identification step. This exploits the fact that electrons often leave short tracks and lose energy via bremsstrahlung. Pre-identified electrons are then refit with a GSF (see Section 5.2.2) and projected into the ECAL. Candidates passing tracking and calorimetric criteria are reconstructed as particle flow electrons. The track and associated ECAL clusters are then removed from the block.

Tracks remaining are then subjected to a tighter set of quality requirements, in particular that the track p_{T} uncertainty be smaller than the relative calorimeter energy resolution for a charged hadron. Whilst some real hadrons are lost by this requirement, the energy will be retained in the more accurate measurement from the calorimeter.

Reconstruction of photons and neutral hadrons involves comparison of the track momentum to the calorimetric energy. The cluster energies in the ECAL are calibrated for photons and in the HCAL, for 50 GeV pions. For the comparison to be valid, these must be re-calibrated to account for non-linearities in the HCAL, as well as the differing response of the ECAL to hadrons.

In the case that several tracks are linked to a single HCAL cluster, the total momentum of the tracks is compared to the calibrated calorimetric energy. Tracks linked to multiple clusters are resolved by preserving the closest link or in certain cases, links. The track momentum is then compared to the total calibrated calorimetric energy.

In the rare case that the energy is smaller than the track momentum by more than three standard deviations, a relaxed search for fake tracks and global muons is initiated. Global muons are identified as PF muons if their momentum is measured with an uncertainty below 25%. Tracks are then progressively removed from the block, those with largest momentum uncertainty first, until either all tracks with an uncertainty > 1 GeV have

been considered or the total track momentum has decreased below the calorimetric energy. The remaining tracks are interpreted as charged hadrons with momentum and energy measurements taken from the track momentum, assuming the charged pion mass hypothesis. If the calorimeter energy and track momentum are compatible within their uncertainties, the momentum is redefined by a fit of the measurements in the tracker and the calorimeters. This is helpful at very high energies, where the track parameters may be less well measured.

In the case that the calibrated energy is greater than the total track momentum by more than the calorimetric energy resolution, the excess is interpreted as a photon and possibly a neutral hadron. If the excess is greater than the ECAL energy, a photon is created with this energy and the rest of the excess interpreted as a neutral hadron. Otherwise, only a photon is reconstructed from the uncalibrated ECAL energy. This stems from the observation that photons carry 25% of the energy of a jet, and neutral hadrons leave only 3% of the jet energy in the ECAL.

Remaining ECAL and HCAL clusters not linked to a track (or for which the associated track was disabled in the previous steps) are reconstructed as photons and neutral hadrons respectively.

PF jets are then reconstructed by applying the anti-k_T algorithm to the full set of PF objects.

5.5.5. Physics Performance

Two aspects of the performance of the PF reconstruction are of relevance to the analysis description that will follow: measurement of $\vec{E}_T^{\text{miss}}$ and jet reconstruction. Figure 5.7 shows a comparison of the jet energy resolution of PF and Calo jets as a function of jet p_{T}. The angular resolution is compared in Figure 5.8. The improvement given by the PF algorithm can be clearly seen, particularly at low jet momentum. A similar comparison of the E_T^{miss} resolution can be seen in Figure 5.9. Again, the PF algorithm is seen to offer significantly improved resolution.

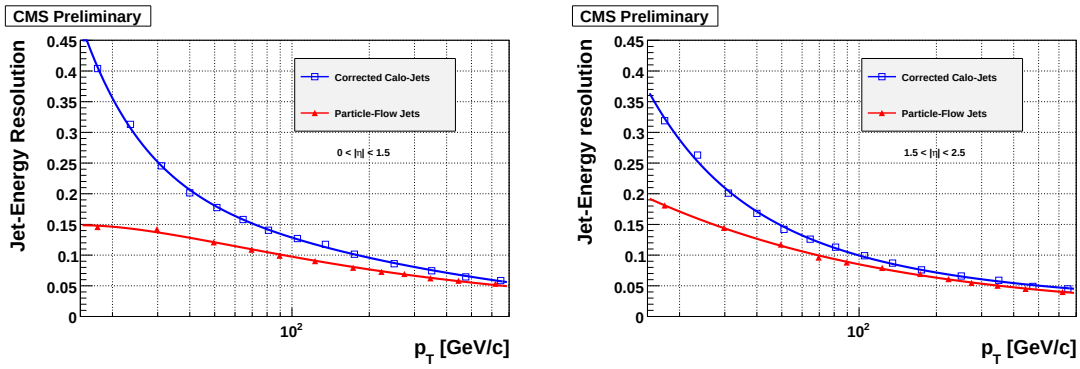

(a) Barrel **(b)** Endcap

Figure 5.7.: Jet energy resolution as a function of p_{T} for the (a) barrel and (b) endcap. Calo-jet values are displayed as open squares and PF jet as upwards triangles. The curves are fit to the sum of a constant term, a stochastic term and a noise term [121].

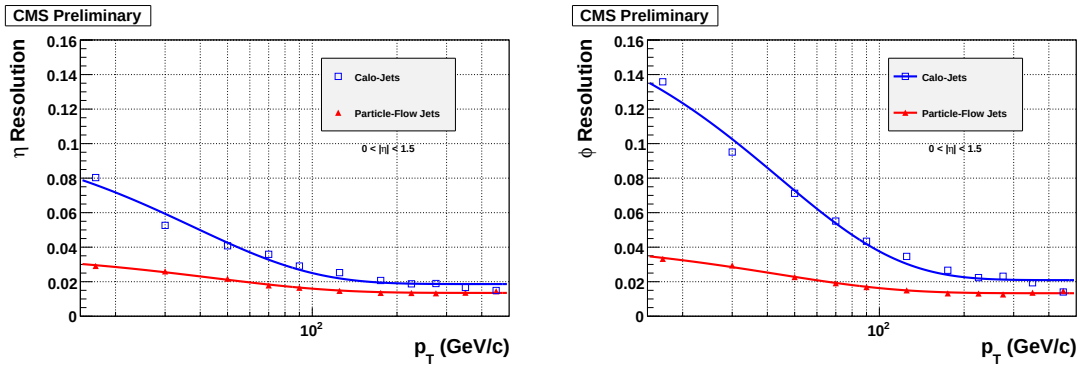

(a) η **(b)** ϕ

Figure 5.8.: Jet angular resolution (RMS) as a function of p_{T} for (a) η and (b) ϕ. Calo-jets are shown as open squares and PF jets as upward triangles. The curves are fit with an exponential function of p_{T} [121].

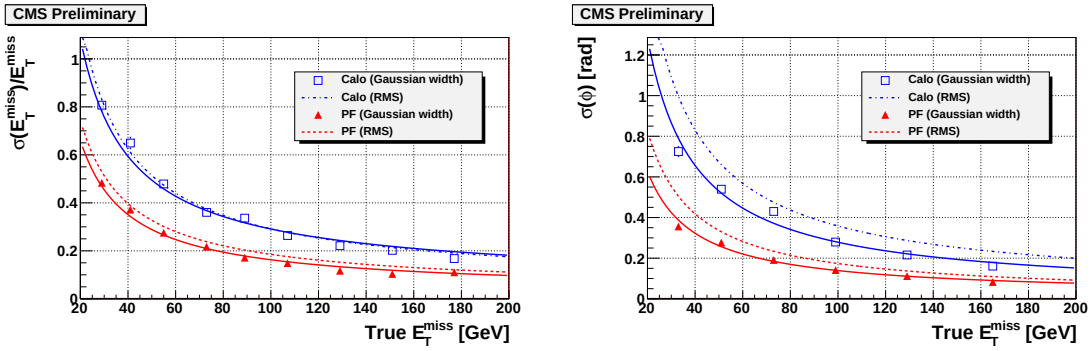

(a) $\sigma(E_T^{\text{miss}})/E_T^{\text{miss}^{\text{true}}}$ **(b)** $\sigma(\phi)$

Figure 5.9.: (a) $\sigma(E_T^{\text{miss}})/E_T^{\text{miss}^{\text{true}}}$ and (b) $\sigma(\phi)$ as a function of true E_T^{miss} in $\mathrm{t\bar{t}}$ events as determined by a Gaussian fit to each $E_T^{\text{miss}^{\text{true}}}$ bin. Squares represent Calo-E_T^{miss}, and upwards triangles PF E_T^{miss}. The solid curves ares fits through these points. The dashed lines indicate the RMS width of each bin [121].

Chapter 6.

Measurement of the Polarisation of the W Boson

6.1. Introduction

The study of W + jets production at a hadron collider is an important avenue for the further understanding of the underlying electroweak and QCD processes. In particular, since it is one of a relatively small number of processes for which highly precise NLO calculations have been performed (see Section 3.1.2), experimental measurements can provide constraints on the PDFs. W + jets production is also of considerable interest in the context of NP searches where these events are often a significant background. Finally, in the leptonic decay mode, the neutrino provides a source of "real" missing energy. This is useful in the understanding of detector effects relevant to searches for WIMP particles present in a number of NP theories - including SUSY.

6.2. Measuring the Helicity Fractions of the W Boson

6.2.1. Generator and Simulation Level Expectations

As will become clear, any measurement of the helicity fractions will depend to some extent on MC input. Therefore, it is important to study the effect, both at the generator-level, and at the level of reconstructed simulated events. This firstly ensures that the expected

effects are adequately modelled by the chosen MC generator. Secondly it allows the testing of the theoretical expectations in the context of "real" detector-level quantities. This is vital to ensure that the measurement of the helicity fractions is actually feasible and not washed out by some experimental effect.

Unless otherwise noted, the W + jets samples used are produced using the MADGRAPH [123] generator interfaced to PYTHIA version 6 [124]. The generated sample comprises approximately 15 million events with the PDFs taken from the CTEQ6L1 set within the LHAPDF software package [125, 126].

The $\cos\theta^*$ distributions (see Section 3.1.5), in bins of P_T^{W}, are shown in Figure 6.1 for W^+ bosons at generator level. Also shown is a fit to Eqn. 3.6. The dominance of left-handed W bosons is manifest in the peak at $\cos\theta^* = -1$. This corresponds to the dominant $(1 - \cos\theta^*)^2$ term. This reflects the fact that the left-handed particle (the neutrino in this case) is taking most of the energy. Similarly for W^-, the peak is at $\cos\theta^* = 1$, where this time the charged lepton is more energetic.

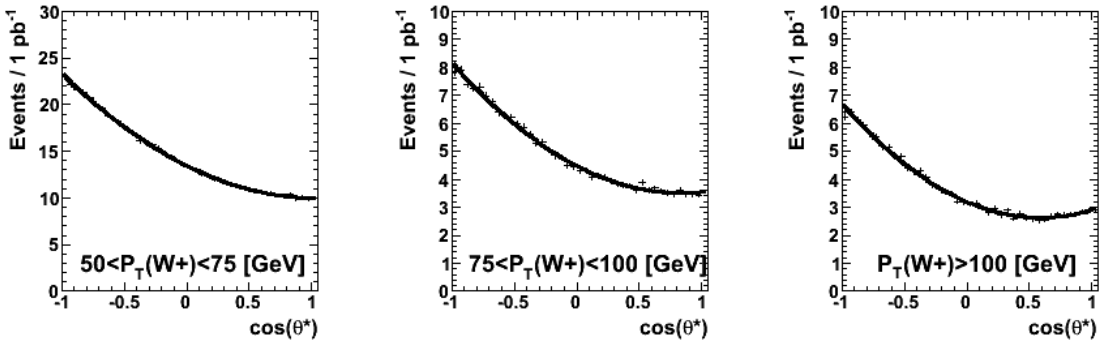

Figure 6.1.: Distribution of $\cos\theta^*$ for W^+ bosons in three bins of P_T^{W}. The black lines show the results of an analytical fit [67].

6.2.2. The Lepton Projection Variable

In order to calculate the value of $\cos\theta^*$, the W boson rest frame must be reconstructed. This requires knowledge of both the charged and neutral lepton momenta. At a hadron collider, the neutrino escapes undetected and is reconstructed as a missing energy signal. As described in Section 5.4, at a hadron collider, the boost of the colliding partons is not known and thus the component of the neutrino momentum parallel to the beam-line cannot be inferred from the missing momentum. This prevents unique determination of the W boson momentum, introducing a two-fold ambiguity on the measurement of

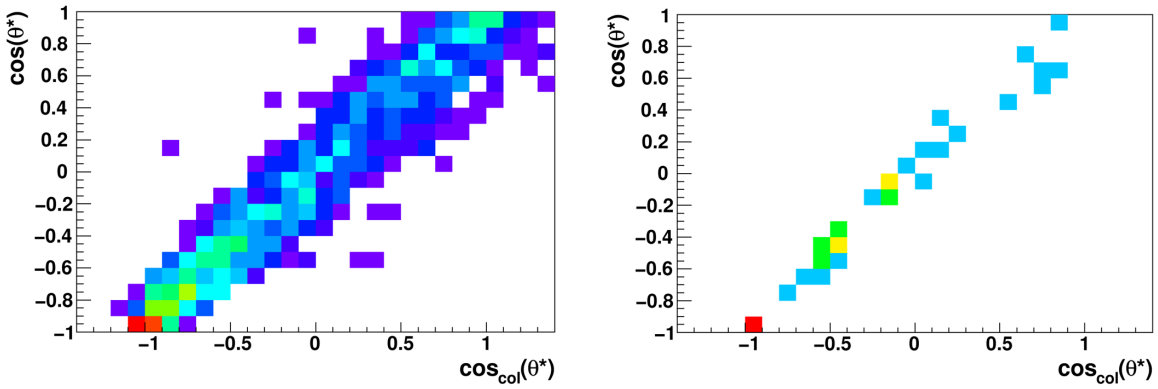

(a) $P_T^{\mathrm{W}} > 200$ GeV **(b)** $[P_T^{\mathrm{W}} > 400$ GeV

Figure 6.2.: Correlation of $\cos\theta^*$ and $cos_{\mathrm{col}}(\theta^*) \equiv 2L_{\mathrm{P}} - 1$ for W bosons in MC. The correlation is shown for two different cuts on the transverse momentum, P_T^{W} [67].

P_z^{W} and thus making it impossible to fully reconstruct the helicity frame. One solution would be to simply choose one solution and then apply correction factors to compensate for this effect in the results. Alternatively, both solutions could be taken and weighted using MC.

For the sake of simplicity, a variable is chosen which is known to be highly correlated with $\cos\theta^*$ at suitably high P_T^{W}, and yet also directly calculable from transverse detector-level quantities. This variable is the *Lepton Projection* variable or L_{P} and is defined as follows [67, 127],

$$L_{\mathrm{P}} = \frac{\vec{P}_{\mathrm{T}}^{\ell}.\vec{P}_{\mathrm{T}}^{\mathrm{W}}}{\left|\vec{P}_{\mathrm{T}}^{\mathrm{W}}\right|^2}, \tag{6.1}$$

where $\vec{P}_{\mathrm{T}}^{\ell}$ and $\vec{P}_{\mathrm{T}}^{\mathrm{W}}$ are the transverse momenta of the charged lepton and W boson respectively. Generically, the P_T^{W} is measured from the recoil of the jets in the event. This can be measured in several ways at CMS leading to alternative definitions of P_T^{W}. This will be discussed further in Section 6.3.5.

Correlation with $\cos\theta^*$

To motivate the use of the L_{P} variable in measuring $\cos\theta^*$ at high P_T^{W}, the correlation can be demonstrated analytically. Consider the decay lepton momentum in the helicity

frame,

$$|\vec{P}^{\ell}_{\mathrm{H}}|^2 = |\vec{P}^{\ell}_{\mathrm{H},\parallel}|^2 + |\vec{P}^{\ell}_{\mathrm{H},\perp}|^2$$

where $\vec{P}^{\ell}_{\mathrm{H},\parallel}$ and $\vec{P}^{\ell}_{\mathrm{H},\perp}$ are, respectively, the components of the lepton momentum parallel and perpendicular to the z-axis of the helicity frame. Neglecting the mass of the lepton, $|\vec{P}^{\ell}_{\mathrm{H}}| = M_{\mathrm{W}}/2$, where M_{W} is the mass of the W boson. Therefore

$$|\vec{P}^{\ell}_{\mathrm{H},\parallel}| = \frac{M_{\mathrm{W}}}{2}\cos\theta^* \qquad |\vec{P}^{\ell}_{\mathrm{H},\perp}| = \frac{M_{\mathrm{W}}}{2}\sin\theta^*.$$

Boosting into the lab frame (i.e. along the $-z$ axis of the helicity frame), one obtains

$$|\vec{P}^{\ell}_{\mathrm{L},\parallel}| = \gamma\frac{M_{\mathrm{W}}}{2}\left(\cos\theta^* + \beta\right) \qquad |\vec{P}^{\ell}_{\mathrm{L},\perp}| = |\vec{P}^{\ell}_{\mathrm{H},\perp}|,$$

where γ and β have their usual definitions (see Appendix A).

To see the correlation, we first consider the quantity ${L_{\mathrm{P}}}^{3D}$ [127], defined as follows,

$${L_{\mathrm{P}}}^{3D} = \frac{|\vec{P}^{\ell}|}{|\vec{P}^{\mathrm{W}}|}.$$

This can be rewritten as follows,

$$\begin{aligned}
{L_{\mathrm{P}}}^{3D} &= \frac{|\vec{P}^{\ell}_{\mathrm{L}}|}{|\vec{P}^{\mathrm{W}}|} = \frac{1}{|\vec{P}^{\mathrm{W}}|}\sqrt{|\vec{P}^{\ell}_{\mathrm{L},\parallel}|^2 + |\vec{P}^{\ell}_{\mathrm{L},\perp}|^2} \\
&= \frac{M_{\mathrm{W}}}{2|\vec{P}^{\mathrm{W}}|}\sqrt{\gamma^2(\cos\theta^* + \beta)^2 + \sin^2\theta^*} \\
&= \frac{M_{\mathrm{W}}}{2|\vec{P}^{\mathrm{W}}|}\sqrt{\gamma^2\cos^2\theta^* + 2\gamma^2\cos\theta^*\beta + \gamma^2\beta^2 + \sin^2\theta^*} \\
&= \frac{M_{\mathrm{W}}}{2|\vec{P}^{\mathrm{W}}|}\sqrt{\left(\frac{|\vec{P}^{\mathrm{W}}|}{M_{\mathrm{W}}}\right)^2\cos^2\theta^* + 2\gamma^2\cos\theta^*\beta + \gamma^2\beta^2 + 1} \\
&= \frac{M_{\mathrm{W}}}{2|\vec{P}^{\mathrm{W}}|}\sqrt{\left(\frac{|\vec{P}^{\mathrm{W}}|}{M_{\mathrm{W}}}\right)^2\cos\theta^{*2} + 2\frac{|\vec{P}^{\mathrm{W}}|E^{\mathrm{W}}}{{M_{\mathrm{W}}}^2}\cos\theta^* + \left(\frac{|\vec{P}^{\mathrm{W}}|}{M_{\mathrm{W}}}\right)^2 + 1} \\
&= \frac{1}{2|\vec{P}^{\mathrm{W}}|}\sqrt{{|\vec{P}^{\mathrm{W}}|}^2\cos^2\theta^* + 2|\vec{P}^{\mathrm{W}}|E^{\mathrm{W}}\cos\theta^* + {|\vec{P}^{\mathrm{W}}|}^2 + {M_{\mathrm{W}}}^2} \\
&= \frac{1}{2|\vec{P}^{\mathrm{W}}|}\left(|\vec{P}^{\mathrm{W}}|\cos\theta^* + E^{\mathrm{W}}\right),
\end{aligned}$$

where E^{W} is the W-boson energy. Rearranging, it is seen that

$$\cos\theta^* = 2{L_{\mathrm{P}}}^{3D} - \frac{E^{\mathrm{W}}}{|\vec{P}^{\mathrm{W}}|}.$$

In the high P_T^{W} limit, the z component of the W can be neglected and thus ${L_{\mathrm{P}}}^{3D} \longrightarrow L_{\mathrm{P}}$ and $|\vec{P}^{\mathrm{W}}| \longrightarrow E^{\mathrm{W}}$. Therefore

$$\cos\theta^* \longrightarrow 2L_{\mathrm{P}} - 1.$$

The correlation between $\cos\theta^*$ and $2L_{\mathrm{P}} - 1$ is shown in Figure 6.2 for W bosons with $P_T^{\mathrm{W}} > 200$ GeV and $P_T^{\mathrm{W}} > 400$ GeV.

Correlation with ϕ^*

For large P_T^{W}, L_{P} is mostly uncorrelated with ϕ^* since even for values $\phi^* > \frac{\pi}{2}$, the lepton will still be collinear with the W in the lab frame. In contrast, for low values of P_T^{W}, the lepton may have a large angular separation from the W in the lab frame. In extreme cases, the lepton and the W may even be anti-parallel in the lab frame. This leads to a widening of the L_{P} distribution and a much larger correlation with ϕ^*.

6.2.3. Template Re-weighting Method

As has been seen, the $\cos\theta^*$ distribution is of central importance to the study of the W polarisation. The L_{P} variable can be used to probe this distribution and may be calculated in a straightforward manner from detector-level quantities. However, it has already been seen that the $\cos\theta^*$ distribution cannot be inferred directly from the L_{P} distribution, thus preventing a direct measurement of the helicity fractions. In addition, the L_{P} distribution will be subject to a number of detector and acceptance related effects, changing its shape.

Re-weighting $\cos\theta^*$

To account for the aforementioned experimental issues, a template "re-weighting" method is employed [67]. Effectively, MC simulation is used to derive three re-weighting factors, each a function of $\cos\theta^*$ and binned according to W boson charge, transverse momentum,

P_T^{W}, and rapidity, $\left|Y^{\mathrm{W}}\right|$. These can be written as

$$Q_i^{\pm}\left(\cos\theta^*, P_T^{\mathrm{W}}, \left|Y^{\mathrm{W}}\right|\right) = \frac{\sigma_i^{\pm}\left(\cos\theta^*\right)}{\sum_{j=-1}^{j=+1} f_j{}^{\pm}\left(P_T^{\mathrm{W}}, \left|Y^{\mathrm{W}}\right|\right)\sigma_j^{\pm}\left(\cos\theta^*\right)}, \tag{6.2}$$

where the index, i is one of the three helicity states of the W boson. The $f_j{}^{\pm}$ are constants derived from an analytical fit to the $\cos\theta^*$ distribution in bins of P_T^{W}, $\left|Y^{\mathrm{W}}\right|$ and charge. These are effectively the helicity fractions "baked in" to the MC. The factor, $Q_i^{\pm}$, will then re-weight the $\cos\theta^*$ distribution in MC such that it corresponds to the pure helicity state, i. The functional forms of the $\sigma_i^{\pm}$ are taken from Eqn. 3.6 as follows,

$$\begin{aligned}
\sigma_{-1}^{\pm} &= \frac{1}{4}\left(1 \mp \cos\theta^*\right)^2, \\
\sigma_{0}^{\pm} &= \frac{1}{2}\left(1 - \cos^2\theta^*\right) \quad \text{and} \\
\sigma_{+1}^{\pm} &= \frac{1}{4}\left(1 \pm \cos\theta^*\right)^2.
\end{aligned}$$

For each simulated event, the value of $\cos\theta^*$ is calculated. A re-weighting factor is then derived from Eqn. 6.2, accounting for the P_T^{W}, Y^{W} and charge of the W boson. The binning is important, as the helicity fractions are expected to vary significantly with these parameters.

This re-weighting procedure avoids the need to generate separate MC event samples for each polarisation state. Using the re-weighted sample, any distribution may be produced corresponding to a pure sample of polarised W bosons. In particular, this allows the derivation of L_{P} shape templates, which may then be fit to the corresponding data distribution in order to extract the helicity fractions. This ensures that all experimental and acceptance effects are accounted for – providing of course that they are adequately modelled by the detector simulation.

In reality, a small modification to Eqn. 6.2 is required to account for the finite statistical precision of the generated sample. The functions $\sigma_i^{\pm}$ are replaced by integrals over a

small slice ($\Delta\cos\theta^* = 0.01$) of a binned $\cos\theta^*$ distribution:

$$Q_i^{\pm}\left(\cos\theta^*, P_T^{\mathrm{W}}, \left|Y^{\mathrm{W}}\right|\right) = \frac{\int_b^{b+0.01} \sigma_i^{\pm}\left(\cos\theta^*\right)}{\int_{-1}^{1} \sigma_i^{\pm}\left(\cos\theta^*\right)} \div \frac{\int_b^{b+0.01} \sum_{j=-1}^{j=+1} f_j{}^{\pm}\left(P_T^{\mathrm{W}}, \left|Y^{\mathrm{W}}\right|\right) \sigma_j^{\pm}\left(\cos\theta^*\right)}{\int_{-1}^{1} \sum_{j=-1}^{j=+1} f_j{}^{\pm}\left(P_T^{\mathrm{W}}, \left|Y^{\mathrm{W}}\right|\right) \sigma_j^{\pm}\left(\cos\theta^*\right)}$$

where b is a bin within the $\cos\theta^*$ distribution and the integration elements, $d(\cos\theta^*)$, have been suppressed.

P_T^{W} and Y^{W} Dependence

Although the $\cos\theta^*$ templates for each helicity state are independent of P_T^{W} and Y^{W}, the L_{P} templates are seen to vary. Additionally, the f_i parameters are also known to vary across the phase space of the W boson. The intent of this analysis is to measure the *average values* of these parameters across a region of the W phase space. Consequently, the L_{P} helicity templates must be corrected to account for these variations. Put another way, the left-handed template, for example, should embody the L_{P} shape in regions of the phase space known to contain more left-handed W bosons. This step is not necessary for the $\cos\theta^*$ templates, since by definition, they are invariant across the W phase space.

An extra re-weighting factor is defined which effectively gives preference to regions containing more W bosons of the desired helicity,

$$R_i^{\pm}\left(P_T^{\mathrm{W}}, \left|Y^{\mathrm{W}}\right|\right) = \frac{f'_i{}^{\pm}\left(P_T^{\mathrm{W}}, \left|Y^{\mathrm{W}}\right|\right)}{f'_i{}^{\pm,\,\mathrm{all}}},$$

where $f'_i{}^{\pm}\left(P_T^{\mathrm{W}}, \left|Y^{\mathrm{W}}\right|\right)$ is the fraction of $\mathrm{W}^{\pm}$ bosons in the appropriate P_T^{W} and $\left|Y^{\mathrm{W}}\right|$ bin with helicity i. $f'_i{}^{\pm,\,\mathrm{all}}$ is the same fraction integrated over all of the phase space bins. The prime added to the fraction is significant. It indicates that the phase space of the helicity fractions is that obtained after a reconstruction-level cut on P_T^{W}. This must be the same cut value as used in the analysis itself and is, due to experimental and resolution effects, significantly different from a generator-level cut on the same quantity. The W phase space is shown in Figure 6.3 after a reconstruction-level cut, $P_T^{\mathrm{W}} > 50$ GeV.

To summarise, the re-weighting procedure depends on two factors: $Q_i^{\pm}$ and $R_i^{\pm}$. The first "alters" the shape of the $\cos\theta^*$ distribution to represent a certain polarisation state, i. The second accounts for the variation in the helicity fractions across the phase space of the W boson. Both factors are used to re-weight W + jets events in MC in order to model each helicity state. The next section will describe closure tests performed to validate this procedure.

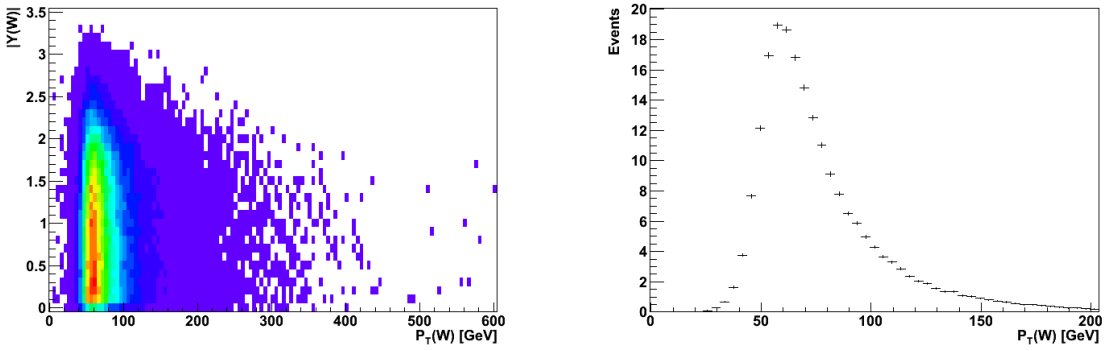

(a) $|Y^{\mathrm{W}}|$ vs P_T^{W} **(b)** P_T^{W}

Figure 6.3.: Generator level W phase space distributions after a reconstruction-level cut, $P_T^{\mathrm{W}} > 50$ GeV [67].

Closure Tests

To ensure that the method is working correctly, several closure tests are performed. Firstly, the generator-level helicity fractions, within the phase-space of the reconstruction-level W acceptance cuts, are extracted. The $\cos\theta^*$ distribution is taken from simulated events which have passed the reconstruction-level P_T^{W} cut. The distribution is fit, once again using Eqn. 3.6, and values of f_0, f_{L} and f_{R} are extracted for both boson charges. This defines the baseline expectation for the helicity fractions and is shown in Table 6.1.

As a first closure test, the generator level L_{P} templates for each helicity state are generated using the re-weighting method as described in Section 6.2.3. The phase-space again corresponds to the reconstruction-level cut on P_T^{W}. The binned maximum-likelihood fit is then performed (see Section 6.5) and the parameters thus obtained are shown in Table 6.1. The agreement with the aforementioned generator-level values is seen to be within the statistical uncertainty of the simulated sample. This test is performed only in the muon channel, since the electron channel is not expected to be significantly different at the generator level.

Finally, a full reconstruction-level closure test is performed in both electron and muon channels and applying all of the analysis cuts listed in Section 6.3.6. The results are also shown in Table 6.1. The muon channel is seen to recover the "true" helicity fractions to within the uncertainty of the analytical fit. The electron channel, further complicated by QCD contributions, is seen to close within the statistical uncertainty of the reconstruction-level fit. This corresponds to 100 pb^{-1} of simulated data.

Table 6.1.: Fit results for the helicity fractions, $f_L^{\pm}$ and $f_R^{\pm}$, for several closure tests of the re-weighting method described in Section 6.2.3. The results of an analytical fit to the $\cos\theta^*$ distribution, having applied reconstruction-level cuts on the W boson, are shown in the first column. The second column shows results from fits to the L_{P} distribution at generator level in the muon channel. The final two columns show the results of a full, reconstruction-level closure test in both lepton channels. The uncertainties have not been included for the reconstruction-level muon fit since it is seen to close within the uncertanties of the analytical fit.

	Analytical Fit	Template Fit: Generator-Level	μ Reconstruction-Level	e Reconstruction-Level
f_L^-	0.5138 ± 0.0032	0.5149	0.5169	0.519 ± 0.038
f_R^-	0.2714 ± 0.0027	0.2708	0.2690	0.263 ± 0.040
f_L^+	0.5485 ± 0.0026	0.5506	0.5507	0.549 ± 0.048
f_R^+	0.2270 ± 0.0021	0.2286	0.2291	0.235 ± 0.019

6.3. Analysis Method

6.3.1. Introduction

To summarise what has already been said, the goal of this analysis is to extract the helicity fractions (f_{L}, f_{R} and f_0) of the W boson and thus establish the dominant left-handed polarisation effect present in theoretical predictions at high P_T^{W}. The f_i coefficients determine the polar angle distribution via Eqn. 3.6. This distribution cannot be recovered directly, due to an ambiguity in the reconstruction of the W boson rest frame. Instead the L_{P} variable, which is found to be highly correlated with $\cos\theta^*$ in the limit of large P_T^{W}, is used. Via a re-weighting method, L_{P} distributions are constructed from MC events. These correspond to 100% left-handed, right-handed and longitudinally polarised W bosons. These shapes may then be fit to data in order to extract the helicity fractions themselves.

It should be noted that the f_i coefficients are expected to differ between W^+ and W^-. However, they are not expected to depend on the flavour of the decay lepton. This is relevant to two aspects of this analysis. Firstly, as shall be seen, the $W \longrightarrow \tau\nu$ decays, where the τ decays to either an electron or a muon, are included throughout. Secondly, measurements in both electron and muon channels may be combined in order to further constrain the helicity fractions.

For the purposes of this analysis, a highly pure sample of events containing W bosons is required. Additional background contamination must be accounted for in the fitting procedure, either by subtraction or by incorporating an appropriate shape template. However this is handled, it will inevitably introduce additional uncertainty into the fit. In the case of subtraction, uncertainty on the shape and normalisation must be accounted for and propagated into the uncertainties on the helicity fractions. Introducing an appropriate template into the fit adds an additional parameter to account for the relative normalisation as well as uncertainties stemming from the template shape. This is particularly problematic in the case of QCD events where the underlying processes are known to be poorly understood (see Section 1.5). This necessitates the use of a data-driven template which, as will be seen, brings an additional set of complications.

6.3.2. Backgrounds

It will be helpful to begin with a discussion of the backgrounds relevant to this analysis. However, in order to understand the composition of the backgrounds, the fundamental selection requirements should first be discussed. The topologies of interest are leptonic W decays, $W \longrightarrow \ell\nu$. In addition, the polarisation effect described in Section 3.1.4 is associated with W bosons produced with a large transverse momentum. As was previously described, this serves to enhance the quark-gluon interactions which lead to a strong left-handed polarisation. Therefore, we find that the two most essential selection requirements are as follows.

- A single isolated lepton typical of a W decay.
- An event topology consistent with a large transverse momentum W. As will be seen in Section 6.3.5, there is some freedom in the exact variables used to achieve this selection.

Taking only these two requirements, significant background contamination will remain. As will be shown, this can be largely eliminated via additional selection criteria. The principal background sources may be categorised as follows [65].

- Drell-Yan production leading to a dilepton final state in which one of the leptons is missed due to limited acceptance, poor reconstruction or other detector effects such as electronics noise.
- $t\bar{t}$ production where $t \longrightarrow bW$. The W then decays leptonically.
- QCD multi-jet events. In the muon channel, this can result from jet punch-through overlapping with a charged hadron or heavy-flavour decays. Electrons face a much higher background, due primarily to photon conversions and overlap between charged hadrons and π^0. The charged hadron leaves a track, whilst the π^0 decay leads to a shower of photons in the ECAL.
- For the electron channel only, there is an additional background from the conversion of promptly produced photons in $\gamma + \text{jets}$ events.

The Drell-Yan and $t\bar{t}$ processes will be referred to collectively as Electroweak (EWK) backgrounds.

6.3.3. Leptons

The first selection requirement is to choose events with a charged lepton consistent with that of a W decay. Such events should, at a minimum, contain at least one reconstructed electron or muon. Wherever possible, the lepton selection criteria adopted are those used for the W cross-section analysis [65]. These requirements are chosen to be as robust as possible during the period of early data-taking at CMS.

Muons

The requirements placed on the muon are as follows [65, 105, 113].

- The muon is required to be reconstructed as both a global muon and a tracker muon. This is to guard against either global muons mismatched with the tracker or noisy muon chambers in the case of tracker muons. For further information on muon identification, see Section 5.2.1.

- More than 10 hits in the tracker.
- Bad muon fits are rejected by requiring $\chi^2 < 10$ on the global muon fit (tracker and muon chambers)
- The transverse impact parameter of the muon with respect to the beam-spot is required to be < 2 mm. This is a fairly loose requirement but still rejects the majority of cosmic muons.
- At least 1 hit is required in the pixels of the tracker in order to remove in-flight decays.
- The tracker muon reconstruction must involve at least 2 muon stations. This suppresses punch-through and accidental matchings and ensures compatibility with the trigger.
- The global muon reconstruction must involve at least 1 valid hit in the muon chambers; again to guard against decays in flight and punch-through.
- A cut on the muon pseudorapidity $|\eta| < 2.1$ in order to ensure compatibility with the trigger requirements.
- A cut on the *combined isolation*,

$$I_{\text{comb}} = \frac{\sum_{\text{tracks}} p_T^{\text{track}} + \sum_{\text{dep}} E_T^{\text{em}} + \sum_{\text{dep}} E_T^{\text{had}}}{P_{\text{T}}^{\mu}} < 0.1, \tag{6.3}$$

  where the sums run over the tracks in the tracker or the energy deposits in the ECAL and HCAL within a cone of size, $\Delta R = \sqrt{(\Delta\eta)^2 + (\Delta\phi)^2} < 0.3$. A threshold of 0.7 GeV is placed on the tracks contributing to the isolation sum.

Muons passing this set of selection criteria will be referred to as **Tight**. Global muons failing one or more of these criteria will be referred to as **Loose**.

Electrons

The electron identification variables used are as described in Section 5.2.2 [65, 111, 128]. In order to achieve a strong suppression of the QCD background, the decision was made to choose a tighter working point than other CMS analyses – the 70% efficiency working point (see Section 6.6.3). Electrons passing these criteria will be referred to as **Tight**.

For the purposes of vetoing dilepton events, the 95% efficiency cuts are used. These will be referred to as **Loose** electrons.

In addition to the requirements of Section 5.2.2, three independent measurements of the charge are required to agree. These are measured as follows [129]:

- from the direction of curvature of the GSF track;
- from the track trajectory reconstructed using a Kalman filter and
- from the azimuthal angle between the vector from the nominal interaction point to the ECAL cluster and the vector joining the interaction point to the innermost hit of the GSF track.

This requirement ensures that the charge misidentification rate is suitably low so that any resulting systematic uncertainty may be neglected (see Section 6.7.1).

6.3.4. Jets

In order to reject events coming from $t\bar{t}$ decays, which tend to have a large jet multiplicity, an upper limit is placed on the number of jets in the event. This analysis makes use of PF jets, described in Section 5.5.

Additionally, cleaning is applied to events in which a jet overlaps with the leading lepton. These cases are assumed to result from some poor reconstruction and thus should be excluded from the analysis. In the case of the electron, the nature of the reconstruction algorithms introduces many such overlaps. Consequently, jets found to lie within a cone $\Delta R < 0.3$ of the highest p_{T} lepton in the event are simply removed from consideration. In contrast, for the muon channel, a much tighter cut can be afforded. Events are completely vetoed from the selection if a single jet is found to lie within a cone $\Delta R < 0.5$ of the muon.

6.3.5. Kinematic Cuts

Transverse Momentum of the W Boson

The most vital kinematic cut to the analysis is the cut on the transverse momentum of the W, P_T^{W}. As has been discussed, requiring W bosons with a large P_T^{W} serves to

enhance the polarisation effect described in Section 3.1.4. It also ensures the correlation of L_{P} with $\cos\theta^*$ and thus improves the measurement of the helicity fractions.

There are several means of reconstructing the $\vec{P}_{\mathrm{T}}^{\,\mathrm{W}}$ at CMS. The first, which was initially used for this analysis, is the missing transverse hadronic energy or $\vec{H}_T^{\,\mathrm{miss}}$. This is defined in Section 5.4. The W must balance with the jet system in the lab frame. Hence this provides a measurement of $\vec{P}_{\mathrm{T}}^{\,\mathrm{W}}$, referred to as $\vec{P}_{\mathrm{T}}^{\,\mathrm{W,\,had}}$. However, a higher resolution measurement can be achieved by instead using the $\vec{E}_T^{\,\mathrm{miss}}$, which is effectively the neutrino momentum, and the charged lepton in the event. This leads to the definition,

$$\vec{P}_{\mathrm{T}}^{\,\mathrm{W,\,lep}} = \vec{P}_{\mathrm{T}}^{\,\ell} + \vec{E}_T^{\,\mathrm{miss}}.$$

This provides a higher resolution measurement of P_T^{W}, as can be seen in Figure 6.4. It is thus the variable adopted in this analysis.

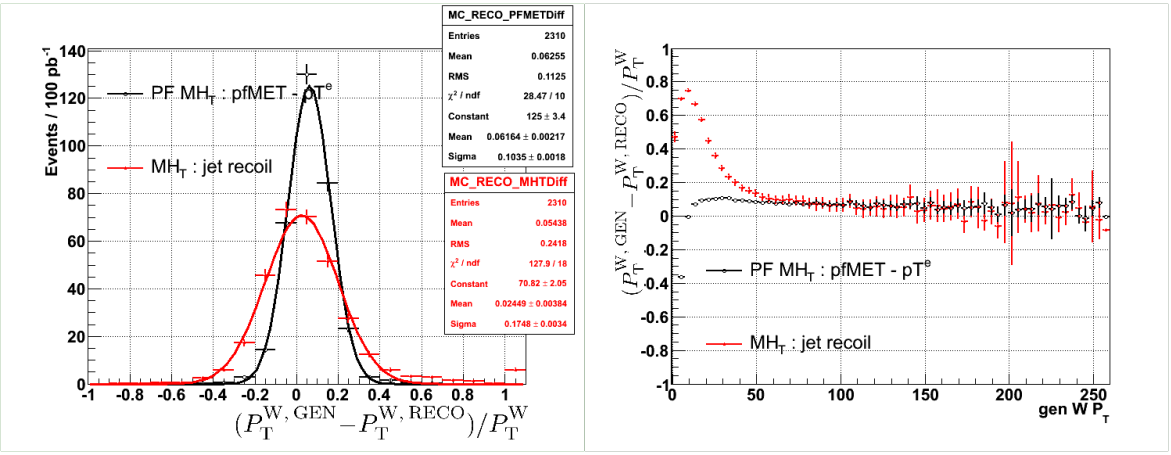

(a) **(b)**

Figure 6.4.: P_T^{W} resolution at reconstruction-level. (a) shows $(P_{\mathrm{T}}^{\mathrm{W,\,GEN}} - P_{\mathrm{T}}^{\mathrm{W,\,RECO}})/P_{\mathrm{T}}^{\mathrm{W,\,GEN}}$. This is shown as a function of $P_{\mathrm{T}}^{\mathrm{W,\,GEN}}$ in (b). Two measurements of P_T^{W} are shown: $P_{\mathrm{T}}^{\mathrm{W,\,lep}}$ (black) and $P_{\mathrm{T}}^{\mathrm{W,\,had}}$ (red).

A second question is then the choice of the minimum cut value to place on P_T^{W}. A tight cut on this quantity will reduce the efficiency of the analysis selection, increasing the statistical uncertainty on the measurement. In addition, the simulated $\mathrm{W} \longrightarrow \ell\nu$ sample contains relatively few events at high P_T^{W}. With too tight a cut on P_T^{W}, the statistical uncertainty on the helicity templates will become significant. On the other hand, by placing a tighter cut on P_T^{W}, the dominance of the left-handed polarisation will be enhanced. The correlation of L_{P} and $\cos\theta^*$ will also increase.

The possibility of performing separate fits in bins of P_T^{W} was also considered. In the end the limitations mentioned above made this infeasible. For a larger integrated luminosity, and given an adequate sample of simulated events, such a measurement would be interesting. For this analysis, a moderate cut, $P_T^{\mathrm{W}} > 50$ GeV, is adopted.

Missing Energy

As already stated, the QCD background is problematic due to the fact that it is relatively poorly modelled by MC event generators. The simplest way to reject such events is via a missing energy type cut. QCD events do not typically contain a source of genuine missing energy. Significant E_T^{miss} from these events is typically due to jet mismeasurements, detector noise or other problems in the event reconstruction. In addition, for the high P_T^{W} events of interest to this analysis, the missing energy component (i.e. the neutrino) is often quite large. A relatively moderate cut on the E_T^{miss} is therefore able to reject the majority of such QCD events.

However, a cut applied directly on the E_T^{miss} introduces an additional problem. Specifically, in the case of events containing a W boson, the E_T^{miss} cut is effectively a selection on the momentum of the neutrino. This removes events where, for instance, the charged lepton has taken the majority of the momentum from the W and so the neutrino has a small momentum. This alters the shape of the L_{P} distribution. This will be accounted for in the template shapes – to be specific the left-handed and right-handed templates will become more similar in shape. This increases their correlation in the fit and is thus undesirable. More will be said of this in relation to the electron measurement in Section 6.6.3.

It is desirable to cut on a variable that is not intrinsically correlated with either the charged or neutral lepton momentum. The transverse mass, M_{T}, is one such variable. Transverse mass is a variable chosen to approximate the invariant mass of a particle by using only transverse quantities. It is defined as follows:

$$M_{\mathrm{T}} = \sqrt{2P_{\mathrm{T}}^{\ell} E_T^{\mathrm{miss}} \left(1 - \cos\Delta\phi\left(\vec{P}_{\mathrm{T}}^{\ell}, \vec{E}_T^{\mathrm{miss}}\right)\right)}.$$

The angular dependence (i.e. the $\cos\Delta\phi$ term) will effectively compensate W decays in which either the charged or neutral lepton is soft – since these topologies will in general have a larger angular separation. Since a momentum imbalance is exactly what

is expected from the dominant left-handed polarisation, the M_{T} cut avoids directly suppressing this effect.

Now consider the effect of the M_{T} cut on the background processes. It is not expected to strongly suppress either the $\mathrm{Z}+\mathrm{jets}$ or $\mathrm{t\bar{t}}$ backgrounds since these both contain actual decays of a heavy particle. For the majority of QCD events passing the analysis selection, a balanced jet system has been badly reconstructed such that one of the jets has been misidentified as a lepton. In general, the E_T^{miss} in these events will be small and thus rejected by the M_{T} cut. In the rare case that the E_T^{miss} component is large due to significant jet mismeasurement, there are two possibilities.

- The fake E_T^{miss} is collinear with the jet that has been misidentified as a lepton. Since $\Delta\phi \sim 0$, the M_{T} cut should strongly suppress these events.
- The angle between the fake E_T^{miss} and lepton is large, leading to significant M_{T}. Note however, that these events will in general be suppressed by the cut on P_T^{W}.

QCD events surviving the combined P_T^{W} and M_{T} cuts tend towards larger values of P_{T}^{ℓ}.

For the muon channel, it is found that a moderate cut, $M_{\mathrm{T}} > 30$ GeV, is able to reduce the QCD background to negligible levels. This is demonstrated first in simulation and then cross-checked by comparison with genuine data. In the case of the electrons, the background proved far more problematic. In the end, an $M_{\mathrm{T}} > 50$ GeV cut is chosen for the sake of simplicity. For more detail on the optimisation study in the electron channel, see Section 6.6.3.

6.3.6. Selection Requirements

Having discussed the selection requirements to be used in this analysis, the actual cuts and cut values are shown in Table 6.2.

6.3.7. Triggers

During the 2010 data taking period, the LHC instantaneous luminosity continued to evolve rapidly. The increased luminosity necessitated tightening of the various object trigger requirements in order to maintain a suitable rate for offline storage. This required

Table 6.2.: Selection requirements for the muon and electron channels in the W polarisation analysis.

Selection	Electron Channel	Muon Channel
1 tight lepton	$P_T^{\mathrm{e}} > 25$ GeV, $\lvert\eta^{\mathrm{e}}\rvert < 2.4$	$P_T^{\mu} > 15$ GeV, $\lvert\eta^{\mu}\rvert < 2.1$
Veto 2nd loose electron or muon	$P_T^{\mathrm{e}} > 15$ GeV, $\lvert\eta^{\mathrm{e}}\rvert < 2.4$ $P_T^{\mu} > 15$ GeV , $\lvert\eta^{\mu}\rvert < 2.1$	$P_T^{\mu} > 10$ GeV, $\lvert\eta^{\mu}\rvert < 2.1$ $P_T^{\mathrm{e}} > 15$ GeV, $\lvert\eta^{\mathrm{e}}\rvert < 2.1$
< 4 PF jets	$p_{\mathrm{T}} > 30$ GeV, $\lvert\eta\rvert < 5.0$	$p_{\mathrm{T}} > 20$ GeV, $\lvert\eta\rvert < 5.0$
Jet overlap veto	-	$\Delta R_{\mathrm{min}}(\mu, \mathrm{jet}) > 0.5$
W Boson p_{T}	$P_T^{\mathrm{W}} > 50$ GeV	
M_{T}	$M_{\mathrm{T}} > 50$ GeV	$M_{\mathrm{T}} > 30$ GeV

careful selection of triggers for the analysis to ensure efficiency with respect to the offline cuts.

For the muon channel, the triggers evolved less rapidly. In general, the cleaner muon signature makes the triggers less susceptible to pile-up effects. The triggers used are as follows:

$$\begin{cases} \texttt{HLT\_Mu9} & \text{run} < 147146 \\ \texttt{HLT\_Mu15\_v1} & \text{run} \geq 147146. \end{cases}$$

Run numbers are assigned by the CMS DAQ, and are incremented during the data-taking period. The naming scheme is that used by the HLT at CMS. The number in the trigger name indicates the p_{T} threshold applied to the lepton. The string `vX` differentiates different versions of the trigger key.

In contrast, the electron trigger thresholds evolved more rapidly,

$$\begin{cases} \texttt{HLT\_Ele10\_LW\_L1R} & \text{run} < 140041 \\ \texttt{HLT\_Ele15\_SW\_L1R} & 140041 \leq \text{run} < 143963 \\ \texttt{HLT\_Ele15\_SW\_CaloEleId\_L1R} & 143963 \leq \text{run} < 146428 \\ \texttt{HLT\_Ele17\_SW\_CaloEleId\_L1R} & 146428 \leq \text{run} < 147117 \\ \texttt{HLT\_Ele17\_SW\_TightEleId\_L1R} & 147117 \leq \text{run} < 148819 \\ \texttt{HLT\_Ele22\_SW\_TightEleId\_L1R\_v2} & \text{run}148819 \leq \text{run} < 149181 \\ \texttt{HLT\_Ele22\_SW\_TightEleId\_L1R\_v3} & \text{run} \geq 149181, \end{cases}$$

where `EleX` indicates an electron with $p_T >$ X GeV. The `LW` and `SW` stand for *large window* and *small window* respectively [130]. Here, window refers to the electron pixel-matching window and thus the large window cut is looser and intended to be used during start-up conditions. All triggers include an H/E cut, $H/E < 0.15$. In addition, those with `CaloEleId` or `TightEleId` impose additional electron identification requirements. The former applies an additional $\sigma_{i\eta,i\eta}$ cut (0.014 in the barrel and 0.032 in the endcaps). The latter applies constraints on the angular matching variables between the track and the supercluster ($\Delta\eta_{\text{in}} < 0.01$, $\Delta\phi_{\text{in}} < 0.08$) in addition to the $\sigma_{i\eta,i\eta}$ requirement. These should be compared with the values given in Table 5.1.

6.4. Validation in Simulation

Simulated Samples

For each background component listed in Section 6.3.2, an appropriate simulated sample is used. In the case of the Z + jets, $t\bar{t}$ and γ + jets processes, the generator setup is as for the W + jets sample – the MADGRAPH matrix element generator interfaced to PYTHIA. In the case of the QCD background, a number of samples are used. For the Muon channel, this is a sample generated using PYTHIA and binned in terms of the transverse momentum of the hard interaction, $\hat{p}_{\text{T}}$. This ensures adequate statistical precision, even in the regions of high $\hat{p}_{\text{T}}$ that will tend to pass the analysis selection.

For the electrons, larger MC samples are required in order to study the QCD background properties. QCD samples are enriched towards the analysis level selection by selecting generator-level electrons, photons, charged pions and charged kaons passing a set of loose generator-level identification cuts (these approximate the isolation quantities and H/E). This will be referred to as the EMENRICHED sample. An additional sample, BCTOE, is enriched with decays from b and s hadrons. Both samples are again binned in $\hat{p}_{\text{T}}$. This generator level enrichment is intended to reduce the costs, in terms of time and disk space, in processing a much larger number of events – the majority of which will be rejected by basic analysis cuts. An unfortunate side effect of this enrichment is that the variables used in the filtering procedure may no longer be studied in their full range. This can be a problem for some background estimation methods which might wish to invert these cuts.

Both data and MC samples have been processed using CMSSW version 3.8. Details of the MC samples used for this analysis can be found in Table D.1.

6.4.1. Signal and Background Expectations in Simulation

The expected event yields for the relevant simulated samples are shown in Tables 6.3 and 6.4 for electrons and muons respectively. The component marked QCD denotes the unenriched sample in the case of the muons and the sum of the EMEnriched and BCtoE in the case of the electrons.

Table 6.3.: MC event yields in the electron channel after each of the selection requirements listed in Table 6.2. The yields shown correspond to 1 pb^{-1} of integrated luminosity. Two measures of the signal significance, S/B and $S/\sqrt{B}$, are also given.

Cut	W+Jets	QCD	Z+Jets	γ+jets	$t\bar{t}$	S/B	$S/\sqrt{B}$
Trigger	6887.0	621013	804.4	1664.1	85.7	0.0	8.7
$N_e = 1, N_\mu = 0$	2819.6	214.5	169.9	64.4	12.1	6.1	131.3
< 4 jets	2816.2	213.5	169.2	64.4	6.7	6.2	132.2
$P_T^{\text{W}} > 50$ GeV	182.2	17.2	28.4	15.9	5.0	2.7	22.3
$M_{\text{T}} > 50$ GeV	122.8	2.7	3.7	3.1	3.3	9.6	34.3

6.5. Fitting Procedure

In order to extract the helicity fractions in Eqn. 3.6, a binned maximum likelihood fit is performed. The L_{P} shape templates from the three W helicity states are taken, along with templates for the QCD and EWK backgrounds. These are then fit to the L_{P} distribution in data and the helicity fractions extracted. In order to test the procedure, this method is also applied to MC "pseudodata" to ensure that the fitted helicity fractions match those derived from the analytical fit to within their quoted uncertainties – see Section 6.2.3. The fit itself is implemented in the RooFit software framework [131, 132],

Table 6.4.: Simulated event yields in the muon channel after each of the selection requirements listed in Table 6.2. The yields shown correspond to 1 pb^{-1} of integrated luminosity. Two measures of the signal significance, S/B and $S/\sqrt{B}$, are also given.

Cut	W+Jets	QCD	Z+Jets	$t\bar{t}$	S/B	$S/\sqrt{B}$
Trigger	7033	493887	909	28.1	0.01	1.00
$N_\mu = 1$, $N_e = 0$	5086	27792	376	11.4	0.18	30.3
< 4 jets	5067	27740	368	5.5	0.18	30.2
$\Delta R_{\text{min}}(\mu, \text{jet}) < 0.5$	4979	26762	358	5.3	0.18	30.2
Second Muon Veto	4973	26762	232	4.3	0.19	30.3
$P_T^{\text{W}} > 50$ GeV	264	21.3	14.6	3.1	6.8	42.3
$M_{\text{T}} > 30$ GeV	218	0.0	5.4	2.0	26.0	80.1

which assists in constructing an appropriate likelihood function and performing the necessary minimisation using the MINUIT numerical optimisation code [133].

The number of signal events in a given histogram bin, j, can be written in terms of the helicity fractions as

$$S^j = f_{\text{L}} h^j_{\text{L}} + f_{\text{R}} h^j_{\text{R}} + (1 - f_{\text{L}} - f_{\text{R}}) h^j_0, \tag{6.4}$$

where h^j_i are each binned helicity templates derived from the re-weighting method described in Section 6.2.3. The f_0 coefficient has been rewritten using the relation $f_{\text{L}} + f_{\text{R}} + f_0 = 1$ and thus it is seen to be a two parameter fit.

6.5.1. Electroweak Backgrounds

As shown in Section 6.4.1, a non-negligible background component is present in both channels arising from EWK backgrounds: Drell-Yan and $\text{t}\bar{\text{t}}$ production.

For these processes, the MC is known to be accurate enough to use L_{P} shape templates taken from simulation. These are included as a single shape in the fit. Its normalisation is fixed with respect to the W + jets template assuming NLO cross-section calculations [59,

62, 134–136]. It is incorporated into the fit as follows:

$$E^j = f_{\text{sig}} S^j + (1 - f_{\text{sig}}) B^j,$$

where f_{sig} is the ratio of the simulated $\text{W} + \text{jets}$ yield to the total simulated yield and B^j is the combined L_{P} template for the $\text{Z} + \text{jets}$ and $\text{t}\bar{\text{t}}$ backgrounds. It should be emphasised that the variable f_{sig} is not free in the fit and thus does not introduce an additional degree of freedom.

6.5.2. QCD and $\gamma +$ jets Backgrounds

The previous formula is adequate for modelling the muon channel. For the electron channel, it has already been shown (see Table 6.3) that QCD multi-jet and $\gamma + \text{jets}$ events give a non-negligible additional background contribution. To deal with this, the formula is extended as follows,

$$N^j = (1 - f_{\text{QCD}}) E^j + f_{\text{QCD}} Q^j,$$

where f_{QCD} is the ratio of the QCD multi-jet/$\gamma + \text{jets}$ background to the total event yield and Q^j is a shape template derived via the procedure described in Section 6.6.4. From the perspective of the fitting procedure, an important issue is that the fraction, f_{QCD}, cannot be predicted from simulation. It is therefore allowed to float freely in the fit. This procedure could be improved by the inclusion of an independent measurement of the QCD contamination, for instance from a fit to the E_T^{miss} shape. This would likely achieve better separation of the QCD component from the other backgrounds and thus a tighter constraint on f_{QCD}.

6.5.3. Fitting $(f_{\text{L}} - f_{\text{R}})$ and f_0

For the final result, Equation 6.4 is modified to fit instead in terms of the parameters $(f_{\text{L}} - f_{\text{R}})$ and f_0,

$$S^j = (f_{\text{L}} - f_{\text{R}}) \left(h^j_{\text{L}} - h^j_{\text{R}}\right) + (1 - f_0) \left(h^j_{\text{L}} + h^j_{\text{R}}\right) + f_0 h^j_0.$$

This is appropriate given that f_0 and $(f_{\text{L}} - f_{\text{R}})$ are related to the underlying parameters A_0 and A_4. It is also allows a more intuitive interpretation in the context of the expected

transverse polarisation effect. It should be noted that since all helicity fractions must be non-negative, $(f_{\mathrm{L}} - f_{\mathrm{R}}) \leq (f_{\mathrm{L}} + f_{\mathrm{R}})$. Since $f_{\mathrm{L}} + f_{\mathrm{R}} + f_0 = 1$, it can be seen that $(f_{\mathrm{L}} - f_{\mathrm{R}}) + f_0 \leq 1$. This inequality defines the physical region of the parameter space.

6.5.4. Combined Fit

It has been noted that the helicity fractions are charge *dependent* but lepton flavour *independent*. This suggests that the measurement may be refined by simultaneously fitting both muon and electron channels. Due to the lower efficiencies in the electron channel, this is not quite a doubling of the sample size but should still significantly reduce the statistical uncertainty.

6.6. Electron Channel

6.6.1. QCD and $\gamma +$ jets Backgrounds

The principal difficulty faced by the electron channel over-and-above the muon channel arises from the QCD and $\gamma +$ jets backgrounds. As has been seen, these remain even after tight kinematic and lepton identification cuts. Since these backgrounds share similar characteristics, they will often be discussed together.

QCD and $\gamma +$ jets events enter the selection due to some mismeasurement leading to a significant "fake" P_T^{W} in association with a lepton – which may be either real or fake. They are highly problematic since their kinematics may depend strongly on poorly understood QCD processes – namely the production, hadronisation and measurement of hadronic jets. Because of this, currently available simulation codes cannot be fully relied upon to correctly model the kinematics of these events. This is particularly true in the case of the L_{P} variable, which is sensitive to both the leptonic and missing energy components in the event.

To address this problem, two approaches have been taken. The first, described in Section 6.6.3, sought to suppress the background as much as possible. This has resulted in the tightened kinematic and identification cuts which have already been detailed. The second focused on accurately modelling the remaining background component using a data-driven procedure. This will be described in Section 6.6.4. It should be noted that

these two strategies do not always complement each other. It is possible to achieve larger background suppression whilst worsening the fit result. This occurs because the data-driven template becomes "flatter" and the fit is less able to distinguish it from the helicity templates.

6.6.2. Kinematics

Before continuing, it is useful to discuss the form of the QCD and $\gamma + \text{jets}$ backgrounds in terms of the L_{P} variable. Consider the measurement of $\vec{P}_{\mathrm{T}}^{\,\mathrm{W}}$ via the hadronic recoil, $\vec{P}_{\mathrm{T}}^{\,\mathrm{W,\,had}}$, in a balanced QCD multi-jet event where a single jet has been misreconstructed as an electron. In this case, the hadronic recoil will tend to point along the axis of the fake electron. If $\vec{P}_{\mathrm{T}}^{\,\mathrm{W,\,had}}$ is used as a measurement of $\vec{P}_{\mathrm{T}}^{\,\mathrm{W}}$, it will be approximately collinear with the $\vec{P}_{\mathrm{T}}^{\,\ell}$ of the fake electron and thus will yield a value of $L_{\mathrm{P}} \sim 1$.

This can also be seen when the P_T^{W} measurement is taken from $\vec{P}_{\mathrm{T}}^{\,\mathrm{W,\,lep}}$. In general, QCD and $\gamma + \text{jets}$ events passing the selection tend to have a large fake lepton p_{T} and a relatively small E_T^{miss}. This again leads to values of $L_{\mathrm{P}} \sim 1$.

6.6.3. Optimisation of Selection Requirements

The QCD and $\gamma + \text{jets}$ backgrounds may be suppressed by the choice of tightened selection requirements. Figure 6.5 shows the effect of two possible kinematic cuts on the L_{P} shape in MC. Background processes are shown along with the fitted helicity templates. Figure 6.5a shows the effect of a cut $E_T^{\mathrm{miss}} > 30\,\mathrm{GeV}$ and Figure 6.5b, a cut $M_{\mathrm{T}} > 30\,\mathrm{GeV}$. The E_T^{miss} cut is clearly more effective in suppressing the QCD background. However, the E_T^{miss} cut also tends to remove events with a soft neutrino, or alternatively, a large $P_{\mathrm{T}}^{\mathrm{e}}$. This is apparent in the shape of the right-handed helicity template which has been "cut away" at $L_{\mathrm{P}} \sim 1$. This increases the correlation of the left-handed and right-handed templates. This will lead to an increase in the statistical uncertainty of the fit.

An optimisation study was undertaken to determine the optimal kinematic and lepton identification cuts, as determined by the uncertainties from the template fit. Some indication of the effect of the kinematic cuts is given in Figure 6.6. This shows the signal and background yields in simulation as a function of varying E_T^{miss} and M_{T} cuts, and including all preceding cuts listed in Table 6.2. The background yield in this case is the

sum of all of the processes listed in Section 6.3.2. Also shown are two possible measures of the signal significance, again with varying E_T^{miss} and M_{T} cuts. As can be seen, the E_T^{miss} cut is significantly more effective at suppressing the background. However, this comes at the cost of considerably reduced signal efficiency.

This point is further informed by Figure 6.7. Here the x and y-axes give a range of cut values on E_T^{miss} and M_{T}. For each point on the plot, the fraction of the total event yield due to QCD/γ + jets production is plotted for those events surviving a combined cut on the M_{T} and E_T^{miss}. It is clear that an M_{T} cut can only achieve limited rejection of these backgrounds. A combined cut on E_T^{miss} and M_{T} was considered but ultimately rejected due to the difficulty of fitting the resulting "flattened" shape. Instead, a simpler $M_{\text{T}} > 50$ GeV cut is chosen.

In Figure 6.8 the L_{P} shape in signal and background events is compared for two different electron selections: the 70% and 80% efficiency working points of Table 5.1. It is clear that the 70% efficiency cuts achieve significantly better rejection of the QCD multi-jet background. This motivated its use in this analysis.

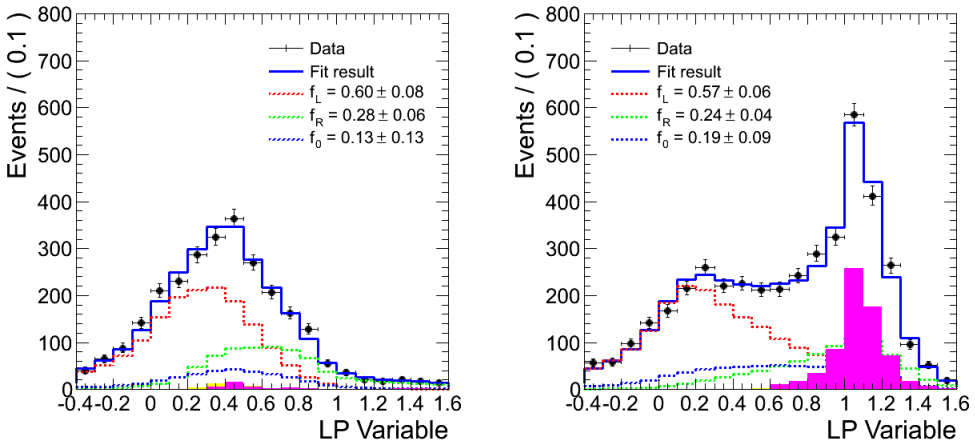

Figure 6.5.: Comparison of fits to the e^+ L_{P} distribution in MC with two alternative cuts applied: (a) $E_T^{\text{miss}} > 30$ GeV and (b) $M_T > 30$ GeV. The W helicity templates, EWK (yellow) and QCD/γ + jets (purple) backgrounds are also shown.

6.6.4. Data-Driven Background Estimation

To obtain a reliable shape template for QCD and γ + jets events, a data-driven procedure is used. For this purpose, a control sample is needed, enriched with QCD and γ + jets

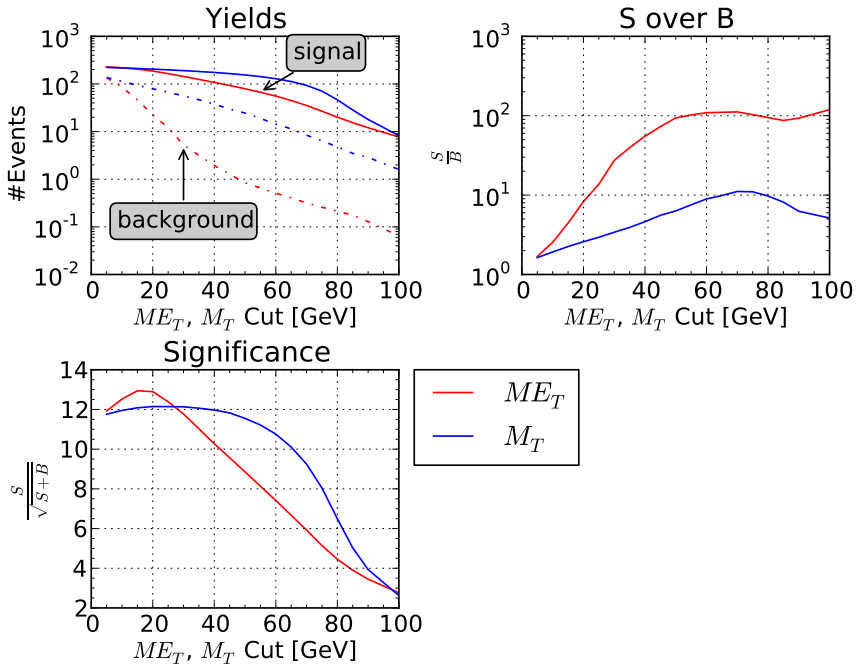

Figure 6.6.: Plots illustrating the signal significance in the electron channel with respect to varying cuts on E_T^{miss} and M_{T}. Results are derived from simulation with all other selection requirements applied. Top-left shows the dependence of the signal (solid lines) and background yields (dotted lines) for varying E_T^{miss} (red) and M_{T} (blue) cuts. Similarly top-right shows the signal significance using the metric S/B and bottom-left using the metric $S/\sqrt{S+B}$.

events which are known to resemble those entering the analysis selection. Such a control sample is often constructed by "anti-selection". Consider the variables used for the analysis selection as a multi-dimensional space, in which the cut values enclose some region containing the selected sample – the "selected" region. The "anti-selected" sample is then constructed by inverting the cuts on a subset of these variables. The region in this space selected by the inverted cuts is then referred to as the anti-selected region. Since the majority of the cuts are common to both selected and anti-selected samples, it can be expected that they will share similar kinematic properties.

A suitable variable must satisfy two criteria. Firstly, it must provide separation power between the QCD/γ + jets backgrounds and the other EWK signal and background processes. Secondly, the L_{P} shape must be similar between the selected and anti-selected regions. Put another way, the inverted variable must be uncorrelated with L_{P}. An additional requirement is that the anti-selected region (which may be obtained by

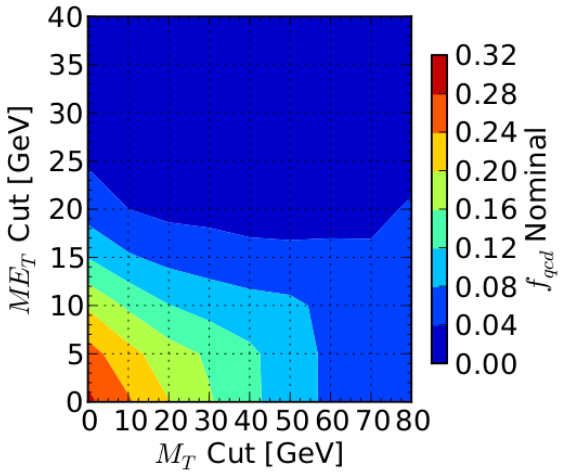

Figure 6.7.: Two dimensional plot showing the dependence of f_{QCD} on a combined E_T^{miss} and M_{T} cut in the electron channel as observed in simulation. f_{QCD} represents the fraction of the total event yield originating from QCD multi-jet events. All other selection requirements have been applied.

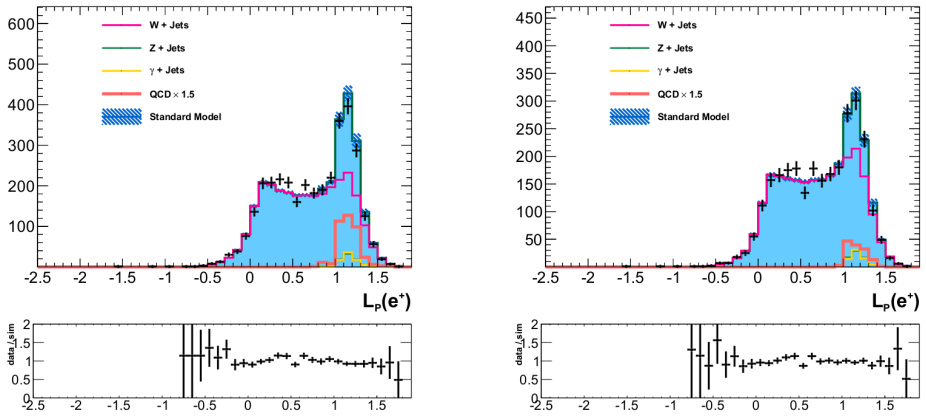

(a) 80% efficiency selection **(b)** 70% efficiency selection

Figure 6.8.: The e^+ L_P distribution in data and MC for two sets of electron identification cuts: (a) the 80% efficiency selection and (b) the 70% efficiency selection. The QCD component has been scaled by a factor of 1.5 to fit the data.

inverting several variables) contain an adequate number of data events for construction of a shape template.

As the analysis developed, a variety of anti-selection strategies were tested in simulation. The enriched QCD samples are used to ensure adequate statistical precision. Since these samples have an implicit cut on the electron isolation, it is not possible to study the

inversion of this variable. Many combinations of the electron identification variables were tried. Many proved to be correlated with L_{P} via either the leptonic or missing energy component.

In the end, a compromise is achieved by inverting the track-supercluster matching parameters, $\Delta\eta_{\mathrm{in}}$ and $\Delta\phi_{\mathrm{in}}$, on the leading electron. A comparison of the selected and anti-selected shapes derived from this procedure is shown in Figure 6.9, before and after the $M_{\mathrm{T}} > 50$ GeV cut. The L_{P} shape for these backgrounds is known to be charge independent. This allows the shapes for positive and negative charge to be combined in order to mimimise the statistical uncertainty of the template.

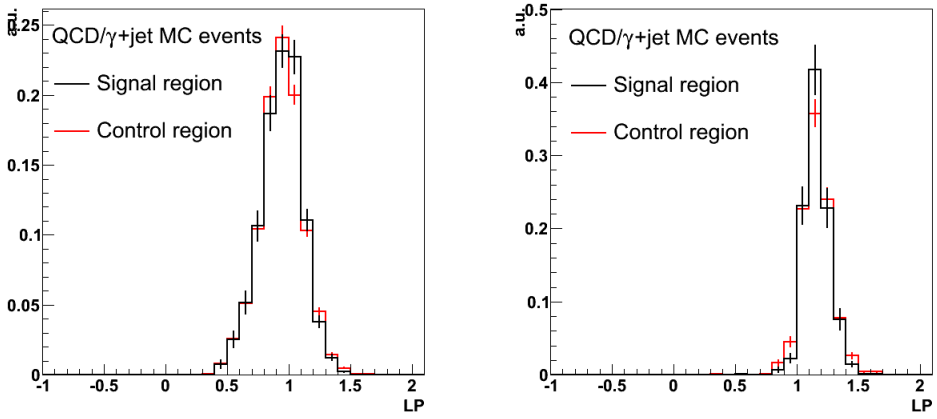

(a) $P_T^{\mathrm{W}} > 50$ GeV **(b)** $M_{\mathrm{T}} > 50$ GeV

Figure 6.9.: The L_{P} variable shown for selected (black) and anti-selected (red) simulated QCD/γ + jets events after (a) $P_T^{\mathrm{W}} > 50$ GeV and (b) $M_{\mathrm{T}} > 50$ GeV

6.7. Systematic Uncertainties

The template re-weighting method used to extract the helicity fractions introduces an inescapable dependence on MC. One of the challenges for this analysis is to ensure that any potential mismodelling within the simulation, which might affect the construction of the L_{P} templates, is properly accounted for and included in the systematic uncertainty on the final result. Two kinds of uncertainty will be considered: those stemming from experimental effects, and those due to uncertainties in the theoretical inputs to the measurement.

6.7.1. Experimental Uncertainties

In considering the potential sources of systematic uncertainty, it is helpful to think first in terms of the construction of the L_{P} variable. It involves two detector level quantities: the missing transverse energy, $\vec{E}_T^{\mathrm{miss}}$, and the transverse momentum of the charged lepton, $\vec{P}_{\mathrm{T}}^{\ell}$. The first quantity is derived from the particle flow algorithm, as discussed in Section 5.5.

Jet Energy Scale

The JES is discussed in Section 5.3. The uncertainty on its calibration has been thoroughly studied and is parameterised as a function of jet p_{T} and η. In the case of a global miscalibration, jet energy measurements in data would be pushed "upwards" or "downwards" with respect to the values predicted by simulation. If one imagines a perfectly balanced di-jet system in the centre of the detector, the resulting effect on the $\vec{E}_T^{\mathrm{miss}}$ will of course be cancelled. However, this will rarely be the case. In particular, in the case of $\mathrm{W}+\mathrm{jets}$ production, the hadronic system will be recoiling against the W boson. In this case, a shift in the JES is likely to have a significant effect on the L_{P} variable as well as P_T^{W} and M_{T}. The resulting systematic uncertainty has been fully evaluated in simulation.

Figure 6.10 shows the fractional change of the muon L_{P} distribution for upward and downward shifts in the JES. Clearly, the effect is quite large and most severe towards the edges of the L_{P} distribution (i.e. $L_{\mathrm{P}} < 0$ and $L_{\mathrm{P}} > 1$). There are two reasons for this. Firstly, that in these regions the L_{P} distribution is rising or falling rapidly. Bin-to-bin migration will thus yield larger changes. Secondly, the change in the value of L_{P}, for a single event, in response to a change in the JES is expected to be linear in L_{P} to first order [137].

The JES is the dominant source of systematic uncertainty in the muon channel and very significant in the electron channel. The effect can be mitigated somewhat however by the observation that a restricted fit range will "insulate" the measurement from the most severe changes to the L_{P} shape. Whilst the edges of the L_{P} distribution are the source of the largest JES uncertainty, they are significant to the fit. Reducing the range too drastically may remove too much information from the fit, increasing the statistical uncertainty and negating any benefits from the reduced systematic uncertainty. The optimal range was determined by considering the quadratic sum of the statistical and

systematic uncertainties for a selection of fit-ranges. It was determined that a range of $[0, 1.3]$ was an appropriate choice for both channels and both charges.

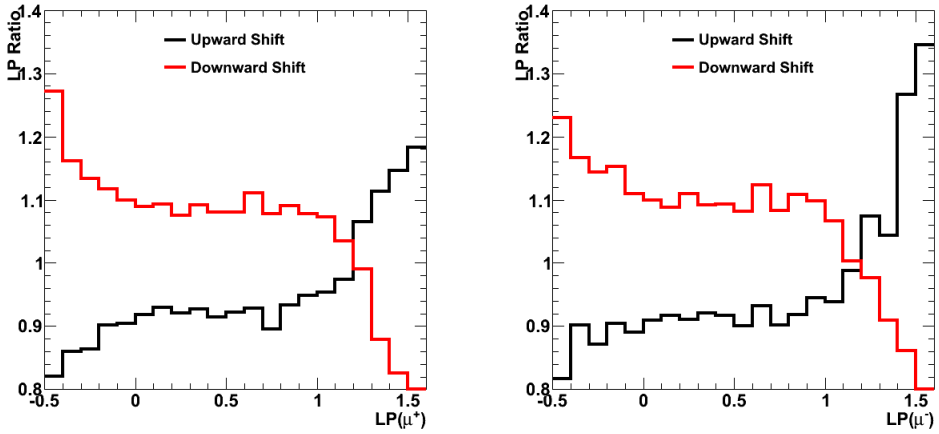

(a) $L_{\mathrm{P}}(\mu^+)$ **(b)** $L_{\mathrm{P}}(\mu^-)$

Figure 6.10.: Relative change of the muon L_{P} distribution due to a change in the JES. The black line corresponds to an upward shift with respect to the original distribution, and the red line a downward shift.

The JES uncertainty follows the standard prescription for CMS analyses. Firstly, the unclustered component of the missing energy is calculated as,

$$\vec{E}_T^{\text{unclustered}} = \vec{E}_T^{\text{miss}} + \vec{P}_{\mathrm{T}}^{\ell} + \sum_i \vec{p}_T^{\text{jet},i},$$

where the index, i, runs over all jets with $p_{\mathrm{T}} > 10$ GeV in the event as reconstructed by the particle flow algorithm. The unclustered energy is then scaled either up or down within its uncertainty – taken to be 5% [120]. $\vec{E}_T^{\text{miss}}$ is then recalculated from this shifted unclustered energy,

$$\vec{E}_T^{\text{miss}} \longrightarrow \vec{E}_T^{\text{unclustered}} - \vec{P}_{\mathrm{T}}^{\ell} - \sum_i (1 \pm u(p_T, \eta)) \times \vec{p}_T^{\text{jet},i},$$

where $u(p_T, \eta)$ is a map specifying the relative uncertainty on the JES as a function of jet transverse momentum and pseudorapidity. The scale applied to the jet momenta will be in the same sense as that on the unclustered energy. When calculating the effect on the results, this displaced value is then used in place of the $\vec{E}_T^{\text{miss}}$ and all $\vec{E}_T^{\text{miss}}$ derived quantities. The results of this procedure are two modified L_{P} shapes. These correspond to upward and downward fluctuations in the JES. Since the shifted $\vec{E}_T^{\text{miss}}$ has been

applied consistently throughout the analysis, the smaller effects on P_T^{W} and M_{T} are also included.

Finally, the value of the JES uncertainty is determined in simulation by fitting the unaltered template, with no JES adjustment, to pseudodata resulting from the upward and downward shifts. Taking the difference of the upward and downward scaled cases with respect to the unaltered values, yields asymmetric uncertainties on $(f_{\mathrm{L}} - f_{\mathrm{R}})$ and f_0. The final systematic uncertainty is then taken to be largest of the two.

$\boldsymbol{E_T^{\mathrm{miss}}}$ Resolution

In addition to the modelling of the JES, another possible source of mismeasurement stems from resolution effects included in the detector simulation. The resolution predicted by the MC is known to considerably underestimate that observed in the data [138, 139]. To account for this, additional "smearing" is applied to the E_T^{miss} in simulation. The difference between this "increased resolution" case and the nominal conditions in simulation is then taken as an additional source of systematic uncertainty.

As the first step of the procedure, the resolution on P_T^{W} is extracted from the simulation in bins of P_T^{W} at generator-level, $P_{\mathrm{T}}^{\mathrm{W,\,GEN}}$. For simulated $\mathrm{W}+\mathrm{jets}$ events with a reconstructed electron or muon and a matching generator-level particle or a generator level τ, the following quantity is calculated,

$$\Delta P_T^{\mathrm{W}} = \frac{P_{\mathrm{T}}^{\mathrm{W,\,GEN}} - P_{\mathrm{T}}^{\mathrm{W,\,RECO}}}{P_{\mathrm{T}}^{\mathrm{W,\,GEN}}},$$

where $P_{\mathrm{T}}^{\mathrm{W,\,RECO}}$ is the P_T^{W} as measured at reconstruction-level. Each $P_{\mathrm{T}}^{\mathrm{W,\,GEN}}$ bin is fit with a Gaussian distribution in order to extract the resolution, σ_{W} as a function of P_T^{W}. This is the P_T^{W} resolution as modelled by the detector simulation.

The simulated sample is then used again. $P_{\mathrm{T}}^{\mathrm{W,\,RECO}}$ is "smeared" such that the resolution is increased by 10%. This is the value measured in [138]. This shape is then fit using the "unsmeared" templates and the difference with respect to the nominal is assigned as a systematic uncertainty. A less conservative estimate could be obtained by correcting the resolution in simulation to match the data and then assigning the uncertainty of the correction as the systematic uncertainty. However, since this uncertainty has not been precisely estimated, the simpler, more conservative estimate is used.

Lepton Momentum Scale

The second contribution to the L_{P} shape uncertainty comes from the measurement of P_{T}^{ℓ}. The source and magnitude of this uncertainty is quite different between the electron and muon channels.

The uncertainty on the muon momentum scale, due to material and B-field uncertainties, is known to be small [106]. However, a charge asymmetric p_{T} bias might appear via "χ^2 invariant modes" [140, section 2.4]. The difference in the Z mass between events with a positively and negatively charged leading muon is calculated in terms of P_{T}^{ℓ}. This allows the size of this effect to be judged. No significant effect is observed in data. The uncertainties on this measurement are used to place an upper bound on the size of this effect. It is found to be less than 1% at a P_{T}^{μ} of 100 GeV. This is assigned as a systematic uncertainty. It is propagated into the helicity fractions by adjusting the P_{T}^{μ} in simulation by $\pm 1\%$ and taking the difference with respect to the unaltered case.

Uncertainty on the electron momentum scale is dominated by the effect of the ECAL transparency changes described in Section 4.3.3. Corrections to account for this effect were derived for the W charge asymmetry measurement [64]. The detector is divided into 6 bins in η. The $\mathrm{Z} \longrightarrow \mathrm{ee}$ mass distribution in data is then divided into $6 + \binom{6}{2}$ categories corresponding to cases where a Z is reconstructed from electrons in η bins i and j. For each category a mass template is derived from simulation. A simultaneous fit is then performed over the 21 categories, where each template is scaled by the factor $1/\sqrt{s_i s_j}$ and smeared by a resolution term $\sqrt{\sigma_i^2 + \sigma_j^2}$. This results in a set of 6 scale terms, s_i and 6 resolution terms, σ_i. These are shown in Figure 6.11. The scale terms should be applied to data and the resolution terms to simulation.

The scale corrections have been applied in data. A conservative 50% uncertainty is taken on the value of the correction factors. The lepton momentum in simulation is then adjusted by $\pm 50\%$ of the correction factor. The resulting change in the fit results with respect to the unaltered case is taken as a systematic uncertainty. This is equivalent to correcting the data by either 50% or 150% of the scale factor.

The effect of the resolution corrections on the fit results is also judged by applying them in MC. The resulting change is found to be negligible, and thus these factors are not applied.

The method described above effectively corrects the mean of the lepton p_{T} distribution. However, the width of this distribution will also be increased. By making use of

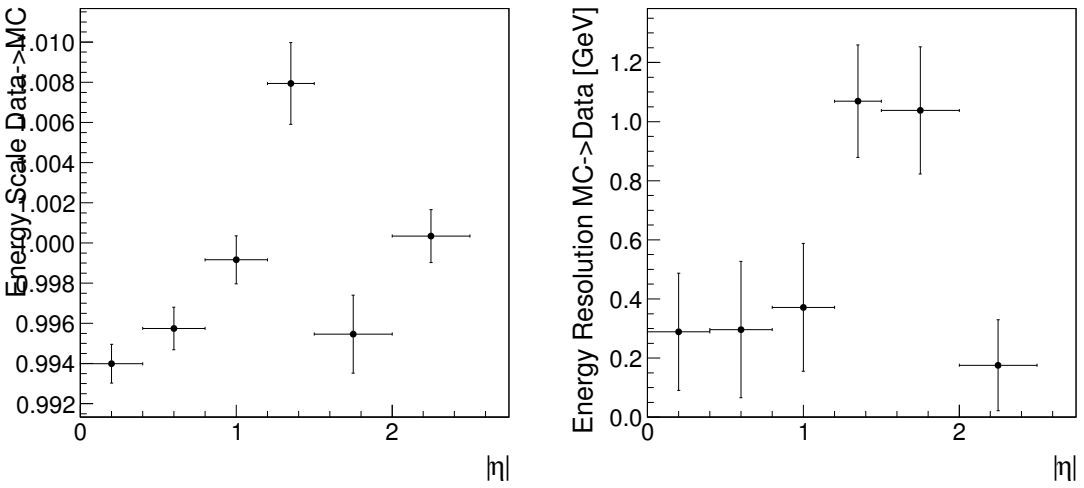

(a) Scale corrections, s_i **(b)** Resolution corrections, σ_i

Figure 6.11.: ECAL transparency correction factors as a function of pseudorapidity, η. These are determined from a fit to the Z mass distribution as described in the text [141].

the continuous measurements provided by the laser monitoring system, this could be significantly improved. These corrections were not fully validated on the timescale of the analysis. As a cross-check, the analysis was also performed using a preliminary version of the continuous corrections. The results were found to be fully consistent with those obtained using the global corrections.

Electron QCD/γ + jets Background Estimation

As discussed in Section 6.6.4, the template used to fit the QCD and γ + jets backgrounds in the electron channel has been derived using a data-driven method. As was seen, the simulation shows a very similar L_{P} shape between the selected and anti-selected samples. However, the small differences that can be seen, coupled with the limited statistical precision of the template, necessitate the inclusion of additional systematic uncertainties. These are evaluated using the QCD and γ + jets MC samples.

The first uncertainty represents the degree, as far as can be judged from the enriched QCD and γ + jets samples, that the anti-selected template mis-models the L_{P} shape in the selected region. In other words, this is the bias introduced by any correlation between L_{P} and the track-supercluster matching variables, which are used to define the anti-selected region. To evaluate this uncertainty, 500 toy MC experiments are performed. In each experiment, a "re-diced" L_{P} distribution is generated from MC pseudodata (in

the selected sample). This involves randomly fluctuating, or "re-dicing" the bins of the L_{P} shape according to their statistical uncertainties.

The L_{P} distribution from each toy experiment is then fit using both the actual QCD/γ + jets shape as well as the anti-selected template (with contamination from other processes included). The ensemble distributions of the fit parameters are then compared between the "true" case, using the actual MC background shapes, and the "data-driven" case, using the anti-selected template. The difference in the means of the ensemble distributions of the parameters f_0 and $(f_{\mathrm{L}} - f_{\mathrm{R}})$ is then taken as a systematic uncertainty.

A further uncertainty is included to account for the limited statistical precision of the anti-selected template. Again, 500 toy MC experiments are performed. In each case, the anti-selected template, derived from MC, is re-diced. The template uncertainties correspond to the integrated luminosity of the measurement. Each re-diced template is fit, along with the standard signal and EWK background templates, to MC pseudodata. The ensemble distributions of f_0 and $(f_{\mathrm{L}} - f_{\mathrm{R}})$ are then constructed. The RMS widths of these distributions are assigned as systematic uncertainties.

Vertex Multiplicity

The vertex multiplicity changed rapidly during data taking. Due to the long lead-time in the production of simulated samples, it was not feasible to produce samples with vertex multiplicity distributions exactly matching those present in data. In order to correct the simulation to match the data, the simulated and observed vertex distributions are compared. The simulated samples are then reweighted to account for this difference. A systematic uncertainty is assigned by allowing the re-weighting factors to vary within their statistical uncertainties. The uncertainty is tested in the muon channel and found to be negligible.

Charge Misidentification

Misidentification of the reconstructed lepton charge causes events to migrate between the W^+ and W^- samples. Since the templates are different for each charge, this could bias the results of the fit. Any possible effect in the muons is found to be negligible. For the electrons, the three charge requirement brings the charge misidentification rate below 1%. At this level, this uncertainty is negligible in comparison to other effects.

6.7.2. Theoretical Uncertainties

In addition to the experimental uncertainties, the method relies upon theoretical assumptions. These will also have an effect on the measurement of $(f_L - f_R)$ and f_0.

A_i Dependence

Measurement of f_0 and $(f_L - f_R)$ will depend on the values of the other A_i coefficients (besides A_0 and A_4). This is tested in simulation by varying each parameter A_i by 10% of its value – an uncertainty derived from comparison of LO and NLO calculations by the Blackhat collaboration [61]. The value of $(f_L - f_R)$ is found to have a very small dependence on the values of the other A_i.

Parton Distribution Functions

This analysis uses a W + jets MC sample generated using the CTEQ6L1 PDF set [142]. This is a set of 41 PDF distributions. All results in this analysis are calculated using the best fit value of this set. To determine the uncertainty associated with this assumption, each alternative PDF from the set is selected and applied to the MC via a re-weighting procedure. From this, 40 separate L_P distributions are derived, each representing pseudodata corresponding to the choice of an alternative PDF. Each distribution is then fit using the standard set of templates. The effect on the fit results is seen to be negligible across the set of alternate PDFs. The average fluctuation from the nominal fit value is found to be $< 0.01\%$ across all polarisation parameters.

Z + jets and $t\bar{t}$ Backgrounds

For the purposes of the fit, the cross-sections of the EWK backgrounds are fixed both relative to each other and also to the W + jets sample. To account for uncertainties on their cross-sections and efficiencies, the Z + jets and $t\bar{t}$ contributions are varied by $\pm 25\%$ and $\pm 50\%$ respectively. These values are chosen conservatively according to the uncertainties on the corresponding cross-section measurements at CMS [113, 143]. The uncertainty on $(f_L - f_R)$ and f_0 is then taken to be the largest resulting fluctuation from the nominal fit value. This has been calculated for both lepton channels.

Table 6.5.: The relative effects on the values of f_0 and $(f_L - f_R)$ in the muon channel for the uncertainties described. The absolute values are shown in brackets.

Uncertainty	$(f_L - f_R)^-$	${f_0}^-$	$(f_L - f_R)^+$	${f_0}^+$
JES	±11% (0.029)	±56% (0.123)	±3% (0.011)	±42% (0.092)
E_T^{miss} Resolution	±4% (0.012)	±3% (0.006)	±4% (0.012)	±2% (0.004)
Muon Scale ±1%/100 GeV	∓0.8% (0.002)	∓ 11% (0.004)	±1.2% (0.004)	∓16.0% (0.036)
Quadratic sum	±12% (0.031)	±56% (0.123)	±5% (0.017)	±45% (0.099)

Summary

The experimental uncertainties on $(f_L - f_R)$ and f_0 are shown in Tables 6.5 and 6.6 for muons and electrons respectively. In the muon channel, the largest systematic uncertainty on $(f_L - f_R)$ is due to the JES. In the electron channel the E_T^{miss} resolution uncertainty is dominant. For the measurement of f_0, the JES uncertainty dominates in both channels. For electrons, the QCD background estimation uncertainty is generally larger in the W^- channel. As will be seen in Table 6.10, this is due to an increase in the correlation of $(f_L - f_R)$ and f_{QCD}.

The effect of the leading uncertainties on the combined fit is shown in Table 6.7. The introduction of the electron channel is seen to increase the overall systematic uncertainty. Theoretical uncertainties are shown in Table 6.8. The uncertainties from the other A_i parameters are seen to be small. The dependence on the $Z + \text{jets}$ and $t\bar{t}$ cross-sections is also seen to be small, mostly $< 1\%$. The total theoretical uncertainty is seen to be similar in both lepton channels.

Table 6.6.: The relative effects on the values of f_0 and $(f_L - f_R)$ in the electron channel for the uncertainties described. The absolute values are shown in brackets.

	$(f_L - f_R)^-$	${f_0}^-$	$(f_L - f_R)^+$	${f_0}^+$
JES	±16% (0.042)	±68% (0.150)	±9% (0.027)	±37% (0.078)
E_T^{miss} Resolution	±18% (0.046)	±21% (0.047)	±12% (0.037)	±18% (0.039)
Electron Scale Corrections ±50%	±6.7% (0.017)	±6.4% (0.014)	±6.1% (0.019)	±7.6% (0.016)
BG Estimation	±5.5% (0.014)	±31.3% (0.066)	±0.6% (0.002)	±1.4% (0.003)
BG Estimation (Stat.)	±2.8% (0.007)	±17.1% (0.036)	±0.6% (0.002)	±6.4% (0.014)
Quadratic Sum	±26% (0.066)	±79% (0.174)	±16% (0.050)	±43% (0.090)

Table 6.7.: The relative effects on the values of f_0 and $(f_L - f_R)$ in the combined fit for the uncertainties described. The absolute values are shown in brackets.

	$(f_L - f_R)^-$	${f_0}^-$	$(f_L - f_R)^+$	${f_0}^+$
JES	±13% (0.033)	±60% (0.133)	±5% (0.016)	±40% (0.087)
E_T^{miss} Resolution	±14% (0.035)	±10% (0.023)	±8% (0.027)	±7% (0.015)
Electron Scale ±50%	±5% (0.013)	∓5% (0.011)	∓4% (0.012)	±4% (0.008)
Muon Scale ±1%/100GeV	∓ < 1% (0.002)	∓3% (0.007)	± < 1% (0.003)	∓4% (0.008)
Quadratic Sum	±20% (0.050)	±62% (0.136)	±11% (0.034)	±40% (0.089)

Table 6.8.: The relative effects on the values of f_0 and $(f_L - f_R)$ from theoretical uncertainties. The absolute values are shown in brackets.

	$(f_L - f_R)^-$	${f_0}^-$	$(f_L - f_R)^+$	${f_0}^+$
$A_1 \pm (A_1 \times 10\%)$	±0.2% (0.0005)	∓4.4% (0.0094)	±0.2% (0.0006)	∓4.9% (0.0105)
$A_2 \pm (A_2 \times 10\%)$	±1.3% (0.0033)	∓3.8% (0.0081)	∓0.5% (0.0016)	∓3.9% (0.0084)
$A_3 \pm (A_3 \times 10\%)$	∓0.4% (0.0010)	± <0.1% (0.0002)	± <0.1% (0.0003)	± <0.1% (0.0002)
$A_0 + (A_0 \times 10\%)$	<0.1%	+10.6%	<0.1%	+10.5%
$A_4 + (A_4 \times 10\%)$	+9.7%	<0.1%	+10.2%	<0.1%
Z changed by 25% (muon)	<0.5% (0.0013)	<0.5% (0.0011)	<0.5% (0.0016)	<0.5% (0.0011)
$t\bar{t}$ changed by 50% (muon)	<0.1% (0.0003)	<0.1% (0.0002)	<0.1% (0.0003)	<0.1% (0.0002)
Quadratic sum (muon)	±1.47% (0.0037)	±5.84% (0.0125)	±0.75% (0.0024)	±6.28% (0.0135)
Z changed by 25% (electron)	<1% (0.0022)	<1% (0.0020)	<0.2% (0.0006)	<0.5% (0.0010)
$t\bar{t}$ changed by 50% (electron)	1.6% (0.0041)	2.1% (0.0045)	<0.2% (0.0005)	0.9% (0.0019)
Quadratic sum (electron)	±2.3% (0.0058)	±6.1% (0.013)	±0.61% (0.0019)	±6.2% (0.0136)

6.8. Results

For this analysis, the full CMS 2010 dataset is used with an estimated integrated luminosity of 36 pb^{-1} at a centre-of-mass energy, $\sqrt{s} = 7$ TeV.

A number of kinematic distributions are compared between data and simulation in Figures 6.12 and 6.13. For both channels, the EWK backgrounds are taken from the corresponding MC samples. The QCD component is negligible in the muon channel. For the electron channel, it is taken from the anti-selected data sample (see Section 6.6.4). The agreement in both channels is seen to be reasonable. Moreover, the data-driven

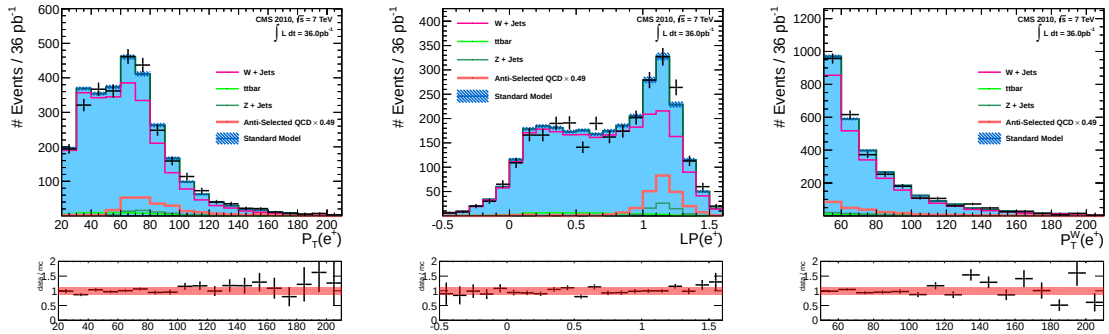

(a) $P_{\mathrm{T}}^{\ell}\,(\mathrm{e}^{+})$ **(b)** $L_{\mathrm{P}}\,(\mathrm{e}^{+})$ **(c)** $P_{T}^{\mathrm{W}}\,(\mathrm{e}^{+})$

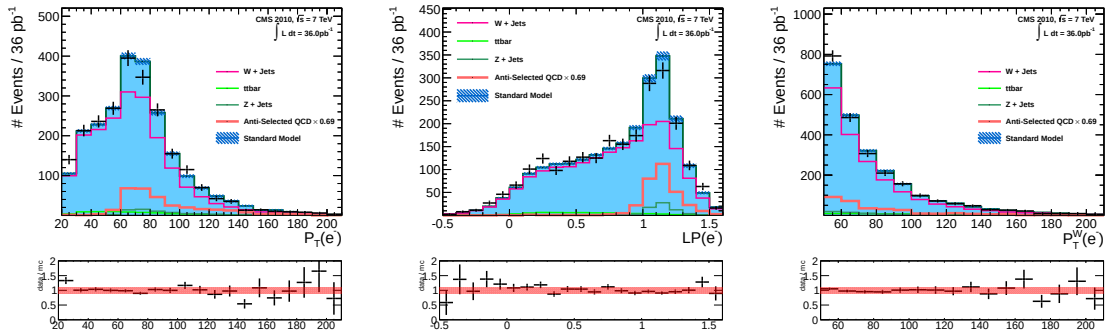

(d) $P_{\mathrm{T}}^{\ell}\,(\mathrm{e}^{-})$ **(e)** $L_{\mathrm{P}}\,(\mathrm{e}^{-})$ **(f)** $P_{T}^{\mathrm{W}}\,(\mathrm{e}^{-})$

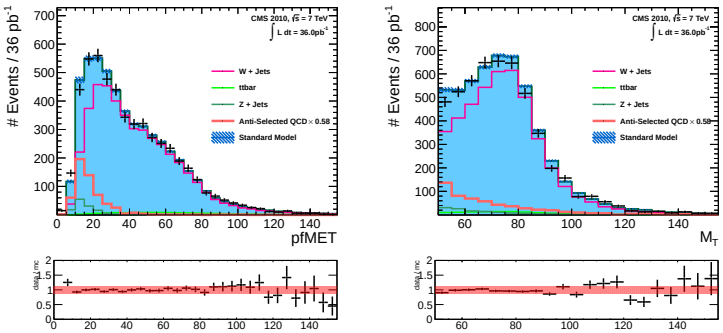

(g) $E_{T}^{\mathrm{miss}}\,(\mathrm{e})$ **(h)** $M_{\mathrm{T}}\,(\mathrm{e})$

Figure 6.12.: Comparison of kinematic distributions in data and MC for the electron channel. All selection requirements have been applied. The lower panel in each plot shows the ratio of the data to simulation. EWK processes are taken from the appropriate simulated sample. The QCD shape in each case is taken from the anti-selected data sample. Its normalisation has been chosen by subtracting the total EWK background yield from that observed in data and scaling the anti-selected sample to fit the remainder. The data are shown as black points, with the sum of the EWK subprocesses in blue. The hatching indicates the statistical uncertainty.

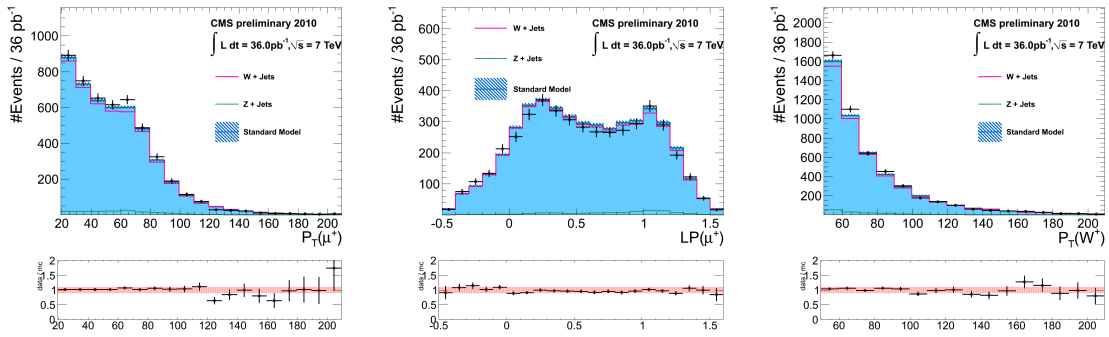

(a) $P_{\mathrm{T}}^{\ell}\,(\mu^{+})$ **(b)** $L_{\mathrm{P}}\,(\mu^{+})$ **(c)** $P_{T}^{\mathrm{W}}\,(\mu^{+})$

(d) $P_{\mathrm{T}}^{\ell}\,(\mu^{-})$ **(e)** $L_{\mathrm{P}}\,(\mu^{-})$ **(f)** $P_{T}^{\mathrm{W}}\,(\mu^{-})$

Figure 6.13.: Comparison of kinematic distributions in data and MC for the muon channel. All selection requirements have been applied. The lower panel in each plot shows the ratio of the data to simulation. EWK processes are taken from the appropriate simulated sample. The QCD contribution is negligible and thus not included. The data are shown as black points, with the sum of the EWK subprocesses in blue. The hatching indicates the statistical uncertainty.

template appears to model the QCD/γ + jets background well – and significantly better than the simulated samples.

6.8.1. Fit Results

The individual fits of the e^+, e^-, μ^+ and μ^- channels to the 2010 dataset are shown in Figures 6.14 and 6.15. The signal and background templates are shown individually, along with the fitted values of $(f_L - f_R)$ and f_0. The 68% error contours in the $((f_L - f_R), f_0)$ plane are shown in Figures 6.16 and 6.17 for electrons and muons respectively. The shading indicates the unphysical region of the parameter space as described in Section 6.5.3. The left-handed polarisation is seen to dominate in both case. The effect predicted in Section 3.1.4 is observed with a large significance.

The error contours for the two combined fits – one per lepton charge – are shown in Figure 6.18. The results of each fit are presented in Table 6.9 along with statistical and systematic uncertainties. In each case, the correlation between the polarisation parameters is shown along with the χ^2/ndof measure of the goodness-of-fit. Table 6.10 shows the results for the parameter f_{QCD} in the electron-only and combined fits.

It is seen that the most precise measurement is provided by the muon channel alone. All three measurements are found to be consistent within their quoted uncertainties. The statistical uncertainty in the electron channel is approximately two times larger than for the muon channel, due to the significantly tighter selection requirements. Whilst the combined fit offers a small improvement in statistical precision over the muon channel alone, this is more than offset by the larger systematic uncertainties in the electron channel. The χ^2/ndof values indicate that a reasonable minimum has been found in each case. The e^+ channel appears to be slightly worse – possibly due to the dip at $L_P \approx 0.5$ in the data distribution (see Figure 6.14a).

Table 6.10 suggests that the parameter f_{QCD} has been fit consistently throughout. No significant charge asymmetry is expected and none is observed. The larger correlation of $(f_L - f_R)$ in the W^- channels appears to be consistent with Figure 6.14b, where the left-handed and QCD templates show considerable similarity in shape. In the combined fits, the correlation between the helicity parameters and f_{QCD} is reduced by the addition of the muon channel.

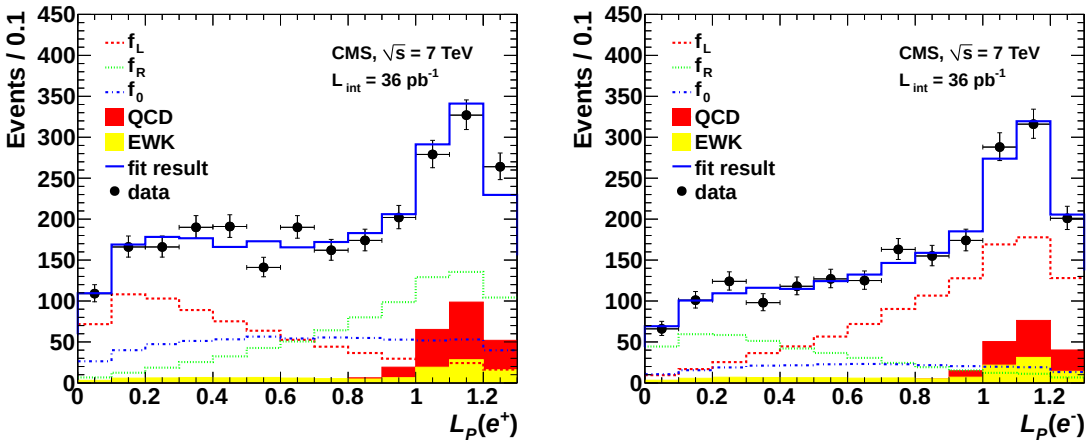

(a) e^+ (b) e^-

Figure 6.14.: Results of the binned maximum likelihood fit in the electron channel. The left-handed helicity template is shown in red, the right-handed in green and the longitudinal in blue, with normalisations as found by the fit. The yellow and red shaded regions are the EWK and QCD background shapes respectively, where the latter is obtained from data.

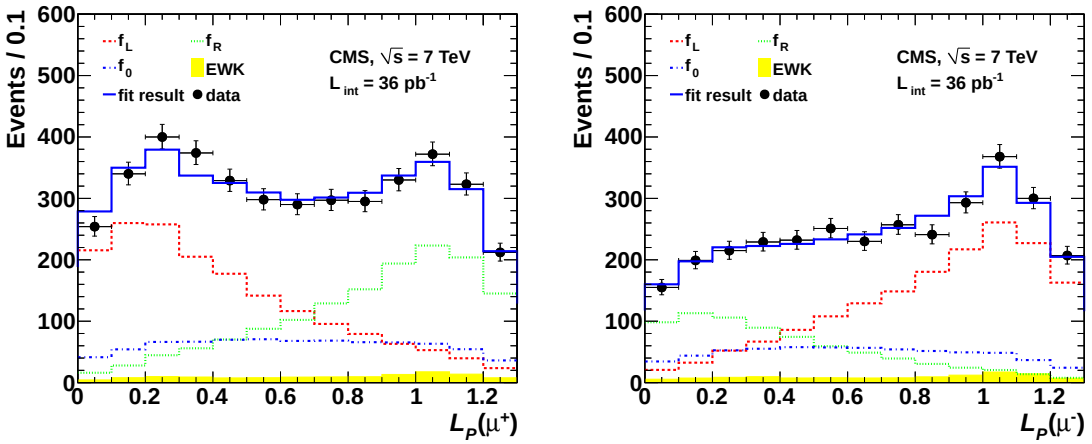

(a) μ^+ (b) μ^-

Figure 6.15.: Results of the binned maximum likelihood fit in the muon channel. The left-handed helicity template is shown in red, the right-handed in green and the longitudinal in blue, with normalisations as found by the fit. The yellow shaded region is the EWK background shape.

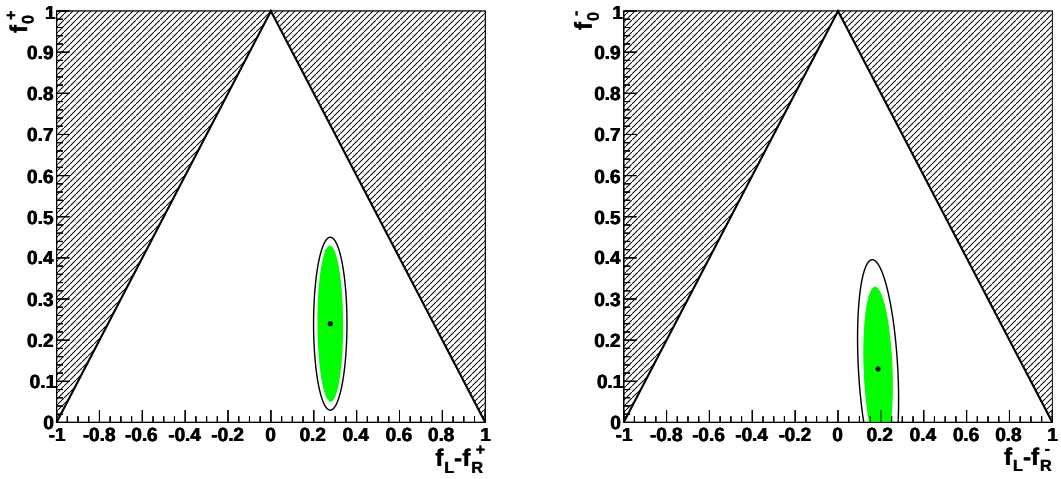

(a) e^+ (b) e^-

Figure 6.16.: Error ellipses in the $((f_L - f_R), f_0)$ plane for 36 pb^{-1} of data in the electron channel. The black point indicates the best fit value. The 68% confidence level contour is shown as a green shaded ellipse for the statistical uncertainty and as a black outline for the total uncertainty. The shaded area represents the unphysical region of the parameter space.

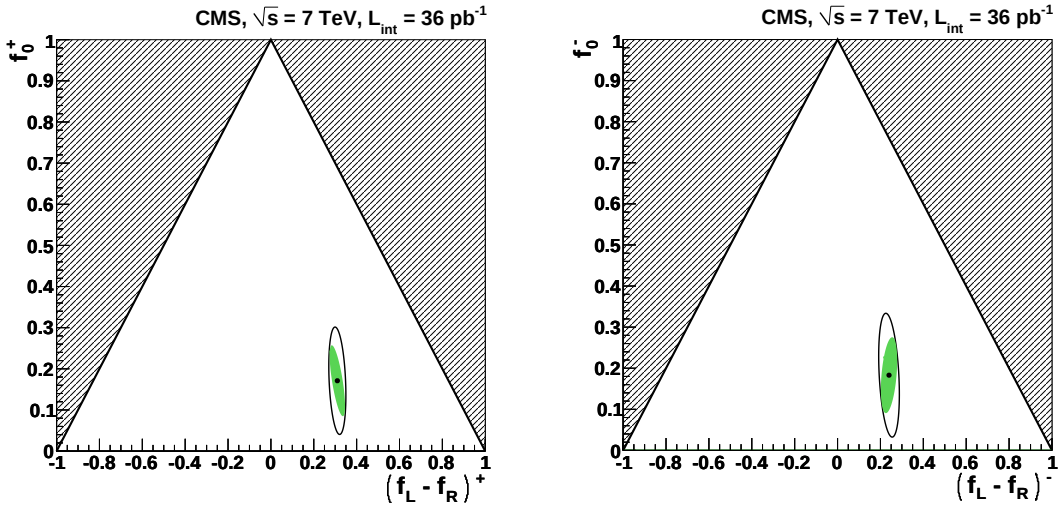

(a) μ^+ (b) μ^-

Figure 6.17.: Error ellipses in the $((f_L - f_R), f_0)$ plane for 36 pb^{-1} of data in the muon channel. The black point indicates the best fit value. The 68% confidence level contour is shown as a green shaded ellipse for the statistical uncertainty and as a black outline for the total uncertainty. The shaded area represents the unphysical region of the parameter space.

Table 6.9.: A summary of the fit results for $(f_L - f_R)$ and f_0 in the muon, electron and combined channels. The statistical and systematic uncertainties are given for each measurement. The correlation between the two parameters is also shown for each case as well as the χ^2/ndof measure of the goodness-of-fit.

	Data Fit Result
$\mu : (f_L - f_R)^-$	0.240 ± 0.036 (stat.) ± 0.031 (syst.)
$\mu : {f_0}^-$	$0.183 \pm 0.087 \pm 0.123$
Correlation	0.395 (stat.)
χ^2/ndof	0.767 (stat.)
$\mu : (f_L - f_R)^+$	$0.310 \pm 0.036 \pm 0.017$
$\mu : {f_0}^+$	$0.171 \pm 0.085 \pm 0.099$
Correlation	-0.721
χ^2/ndof	0.967
$e : (f_L - f_R)^-$	0.187 ± 0.069 (stat.) ± 0.066 (syst.)
$e : {f_0}^-$	$0.130 \pm 0.200 \pm 0.174$
Correlation	-0.204 (stat.)
χ^2/ndof	0.872 (stat.)
$e : (f_L - f_R)^+$	$0.277 \pm 0.060 \pm 0.050$
$e : {f_0}^+$	$0.24 \pm 0.190 \pm 0.090$
Correlation	-0.295
χ^2/ndof	2.239
comb: $(f_L - f_R)^-$	0.226 ± 0.031 (stat.) ± 0.050 (syst.)
comb: ${f_0}^-$	$0.162 \pm 0.078 \pm 0.136$
Correlation	0.304 (stat.)
comb: $(f_L - f_R)^+$	$0.300 \pm 0.031 \pm 0.034$
comb: ${f_0}^+$	$0.192 \pm 0.075 \pm 0.089$
Correlation	-0.660

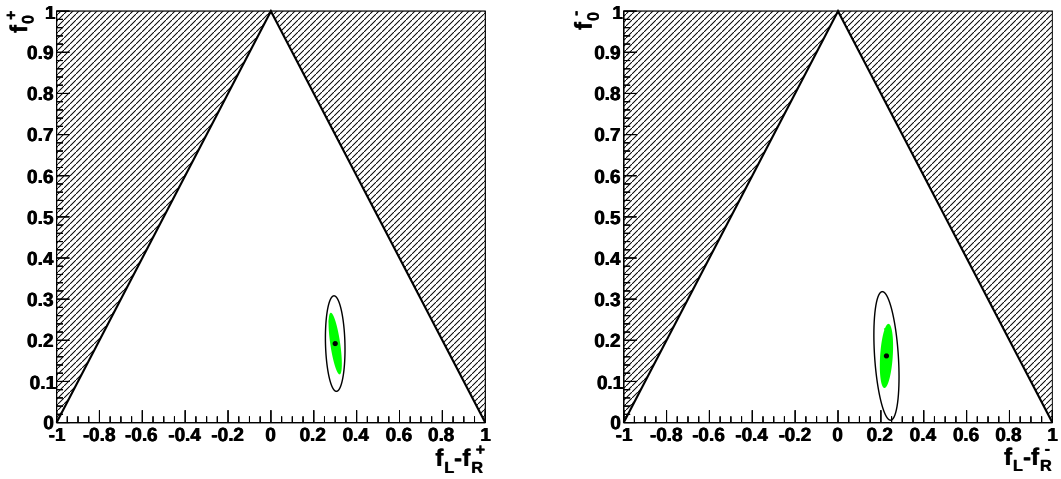

(a) e^+/μ^+ **(b)** e^-/μ^-

Figure 6.18.: Error ellipses in the $((f_{\mathrm{L}} - f_{\mathrm{R}}), f_0)$ plane for 36 pb^{-1} of data combined across electron and muon channels. The black point indicates the best fit value. The 68% confidence level contour is shown as a green shaded ellipse for the statistical uncertainty and as a black outline for the total uncertainty. The shaded area represents the unphysical region of the parameter space.

Table 6.10.: A summary of the fit results for the QCD background component in the electron-only and combined fits. f_{QCD} is the fraction of QCD events determined from the fit. N_{QCD} is the estimated number of QCD events. The correlation with the polarisation fit parameters is also given. The uncertainties quoted are purely statistical.

	f_{QCD}	N_{QCD}	correlation $((f_L - f_R),f_{QCD})$	correlation (f_0,f_{QCD})
e^-	0.094 ± 0.056	221.3 ± 131.8	-0.540	0.840
e^+	0.098 ± 0.042	284.5 ± 121.9	0.198	0.808
$(e+\mu)^-$	0.089 ± 0.025	209.5 ± 58.9	-0.172	0.493
$(e+\mu)^+$	0.094 ± 0.020	272.9 ± 58.1	0.018	0.476

Table 6.11.: Comparison of the CMS combined W polarisation measurement with theoretical results from [60]. The theoretical predictions are at NLO ME+PS and LO. The difference between the NLO and ME+PS may be taken as an approximate theoretical uncertainty.

	$(f_L - f_R)^-$	f_0^-	$(f_L - f_R)^+$	f_0^+
CMS	$0.226 \pm 0.031 \pm 0.050$	$0.162 \pm 0.078 \pm 0.136$	$0.300 \pm 0.031 \pm 0.034$	$0.192 \pm 0.075 \pm 0.089$
NLO	0.248	0.193	0.308	0.200
ME+PS	0.222	0.179	0.283	0.187
LO	0.235	0.190	0.309	0.198

6.9. Summary

As has been seen, the polarisation of the W bosons with large transverse momentum has been measured at CMS using 36 pb^{-1} of data from the 2010 run of the LHC. The parameters, $(f_\text{L} - f_\text{R}) \sim A_4$ and $f_0 \sim A_0$, have been measured independently for muons and electrons of identical charge and for W bosons with transverse momentum greater than 50 GeV. In addition, a combined measurement has been obtained via a simultaneous fit to both channels, again separated by lepton charge.

The most precise measurement of $(f_\text{L} - f_\text{R})$ is provided by the muon channel alone. The dominant left-handed polarisation effect described in Section 3.1.4 is established with a significance of 7.8 and 5.1 σ, for W^+ and W^- respectively. The same effect is observed in the electron channel, with 3.5 and 2.0 σ respectively. Finally, a simultaneous fit yields significances of 6.5 and 3.8 σ.

After publication of this result [144], a set of theoretical predictions at NLO were published [60]. The Blackhat MC generator was used to compare like-for-like with the results of this analysis. The comparison is shown in Table 6.11. The theoretical predictions are seen to be in good agreement with the experimental results.

Chapter 7.

Searching for Supersymmetry in the Single Lepton Final State

7.1. Introduction

The W polarisation measurement, as well as being an interesting analysis in its own right, also finds application in searches for New Physics (NP). First of all, it provides a more complete understanding of the E_T^{miss} distribution in W + jets events – an important background to many SUSY searches. Secondly, the W polarisation can be used, along with the methods described in the previous chapter, to discriminate SUSY events from SM backgrounds. In the following sections, a SUSY search applying these ideas will be described [137].

7.2. Distinguishing SUSY from SM Backgrounds

Assuming that R-parity is conserved, a typical SUSY event, with a charged lepton in the final state, is expected to contain 3 invisible particles: two LSPs and a neutrino. As a result, the total E_T^{miss} in an event will often be larger than the transverse momentum of the charged lepton and relatively uncorrelated with it in terms of direction. In contrast, the large boost and polarisation of a typical W decay lead to a more even balance between $\vec{E}_T^{\text{miss}}$ and $\vec{P}_{\text{T}}^{\ell}$, as well as greater correlation of their directions. These two consideration can be applied to both W + jets and $\text{t}\bar{\text{t}}$ events – the two dominant backgrounds to a single lepton SUSY search.

In order to make use of the W polarisation effects, this analysis employs the $L_{\rm P}$ variable, as described in Section 6.2.2. For events containing a charged lepton in association with $E_T^{\rm miss}$ from the decay of a W with large transverse momentum, the alignment of the charged lepton and neutrino gives an $L_{\rm P}$ distribution confined to the range $[0, 1]$. In contrast, for SUSY events, the $E_T^{\rm miss}$ component is often larger than the lepton momentum and thus $\vec{P}_{\rm T}^{\rm W}$ is likely to point in the direction of $\vec{E}_T^{\rm miss}$. Since the direction of the charged lepton momentum and $\vec{E}_T^{\rm miss}$ will be mostly uncorrelated, $L_{\rm P}$ will tend to small values. Rewriting Eqn. 6.1,

$$L_{\rm P} = \frac{P_{\rm T}^{\ell}}{P_T^{\rm W}} \cos\Delta\phi \left(\vec{P}_{\rm T}^{\rm W}, \vec{P}_{\rm T}^{\ell}\right),$$

it can be seen that in cases where the angle between the $\vec{E}_T^{\rm miss}$ and $\vec{P}_{\rm T}^{\ell}$ is more than 90°, $L_{\rm P}$ will become negative.

A second important difference between SUSY and SM events is related to the overall energy scale. As discussed in Chapter 2, SUSY decays are expected to begin with initial states much heavier than in SM events. To provide some measure of this energy scale without biasing the polarisation, the variable $S_T^{\rm lep}$ is constructed as follows,

$$S_T^{\rm lep} = P_{\rm T}^{\ell} + E_T^{\rm miss},$$

where it should be noted that $S_T^{\rm lep}$ is a scalar quantity. For decays of a W boson with large $P_T^{\rm W}$, $S_T^{\rm lep} \approx P_T^{\rm W}$. Since the energy scale of SUSY is unknown, $S_T^{\rm lep}$ is used to define search regions. This allows the search to be optimised without introducing a strong dependence on the energy scale. For the purposes of this analysis, 4 $S_T^{\rm lep}$ bins are employed. These are: $150 < S_T^{\rm lep} < 250$, $250 < S_T^{\rm lep} < 350$, $350 < S_T^{\rm lep} < 450$ and $S_T^{\rm lep} > 450$ GeV. The lowest of these is taken to be at too low an energy scale to contain SUSY processes not excluded by previous searches. It is thus used as a control region to validate the analysis method.

SUSY cascade decays often give rise to a large number of jets. Consequently, searches often apply a cut on the jet multiplicity as well as a cut on the hadronic energy, $H_{\rm T}$.

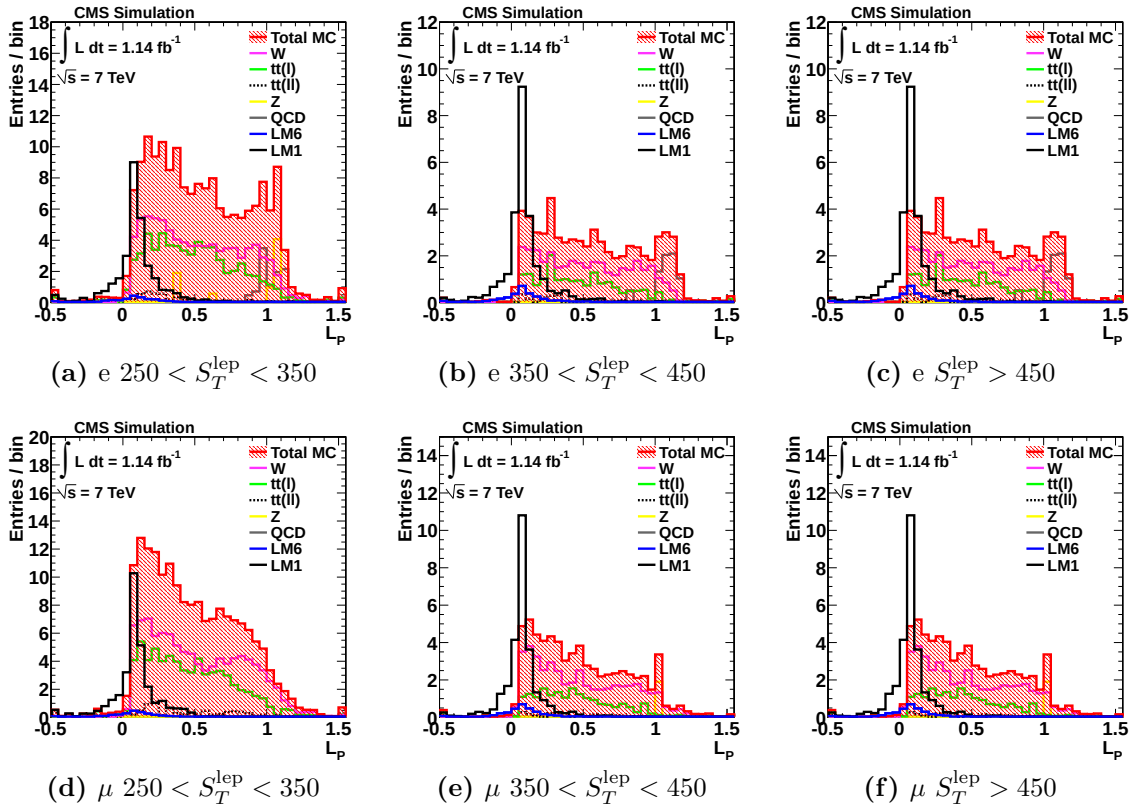

(a) e $250 < S_T^{\text{lep}} < 350$ **(b)** e $350 < S_T^{\text{lep}} < 450$ **(c)** e $S_T^{\text{lep}} > 450$

(d) μ $250 < S_T^{\text{lep}} < 350$ **(e)** μ $350 < S_T^{\text{lep}} < 450$ **(f)** μ $S_T^{\text{lep}} > 450$

Figure 7.1.: Distributions showing the L_{P} variable in the three highest S_T^{lep} bins, as measured in MC. SM background processes are shown along with two benchmark SUSY models: LM6 and LM1.

7.3. Analysis Method

The L_{P} distributions for SM backgrounds and two benchmark SUSY models are shown in Figure 7.1. The benchmark points LM1 and LM6 correspond to the CMSSM points $(m_0, m_{\frac{1}{2}}) = (60, 250)$ and $(85, 400)$ respectively, with $\tan\beta = 10$ and $A_0 = 0$. Firstly it can be seen that the heuristic discussion of the L_{P} shape given in Section 7.2 is confirmed by the simulation – with SM events at $L_{\text{P}} > 0$ and SUSY events clustering around $L_{\text{P}} \sim 0$.

In order to make use of the discrimination power afforded by the L_{P} shape, signal and control regions are defined. The signal region is defined such that an enriched sample of SUSY events is obtained, without being highly model-dependent. It should be stressed that the intent is not to eliminate the background altogether in this region. The control region, likewise, must select a sample of SM background events with sufficient efficiency, whilst guarding against excessive signal contamination from SUSY. By studying the L_{P}

distribution across the CMSSM parameter space, $L_{\mathrm{P}} < 0.15$ for the signal region and $L_{\mathrm{P}} > 0.3$ for the control region are found to be suitable choices.

To predict the SM background contamination in the $L_{\mathrm{P}} < 0.15$ region, a translation factor, R^{CS} is calculated in simulation. This is defined as

$$R^{\mathrm{CS}} = \frac{N^{\mathrm{MC}}(L_{\mathrm{P}} < 0.15)}{N^{\mathrm{MC}}(L_{\mathrm{P}} > 0.3)}, \tag{7.1}$$

where $N^{\mathrm{MC}}(L_{\mathrm{P}} < 0.15)$ and $N^{\mathrm{MC}}(L_{\mathrm{P}} > 0.3)$ represent the population, as calculated in simulation, of SM events in the signal and control regions respectively. Once calculated, R^{CS} may be used, along with a measurement from the control region in data, to predict the SM background contribution present in the signal region,

$$N^{\mathrm{data}}(L_{\mathrm{P}} < 0.15) = R^{\mathrm{CS}} N^{\mathrm{data}}(L_{\mathrm{P}} > 0.3).$$

One benefit of using the translation factor, R^{CS}, is that many systematic uncertainties should cancel, to some extent, in the ratio. This includes, in particular, the JES uncertainty that proved to be significant for the W polarisation analysis (see Section 6.7.1). Since these uncertainties do not cancel completely, they will be fully evaluated in Section 7.9 and are included in the statistical treatment described in Chapter 8.

One last point concerning R^{CS} is that values of $R^{\mathrm{CS}} < 1$ are preferable. This ensures that the prediction is not dominated by uncertainties stemming from the limited statistical precision of the control region. As we will see, relatively small values of R^{CS} are obtained using the definitions given above.

7.4. Object Definitions

The basic object selection requirements are defined to be consistent between several complementary leptonic SUSY searches at CMS. They are described and motivated further in [145].

7.4.1. Jets and Missing Energy

Jets and missing energy quantities are taken from the PF algorithm, as described in Section 5.5. In addition, jets are required to pass the "LOOSE" selection criteria, namely:

- at least two particles – at least one of them charged – in the jet;
- the fraction of jet energy carried by neutral hadrons less than 99% and
- charged and neutral electromagnetic fractions both less than 99%.

All jets are required to have a transverse momentum, $p_{\mathrm{T}} > 40$ GeV and must lie within the fiducial region of the tracker, $|\eta| < 2.4$. The total hadronic transverse energy, H_{T} is calculated from jets passing this selection.

7.4.2. Muons

Muon reconstruction is described in Section 5.2.1. Global muons are selected with a number of additional quality requirements. These are similar to those used in the W polarisation analysis (see Section 6.3.3), with certain adjustments made to ensure consistency with other SUSY analyses:

- a normalised $\chi^2 < 10$ on the global muon fit;
- more than 10 hits in the tracker (including at least 1 pixel hit) and ≥ 2 matching segments in the muon chambers;
- a transverse distance to the nominal interaction point, $d_0 < 200$ µm, and longitudinal distance to the primary vertex, $d_z < 1$ cm;
- the uncertainty on the muon transverse momentum, $\sigma(p_{\mathrm{T}})/{p_{\mathrm{T}}}^2 < 0.001$ GeV^{-1};
- each global muon must also qualify as a tracker muon and
- a combined relative isolation (see Eqn. 6.3) $I_{\mathrm{comb}} < 0.1$.

Tight muons are defined by the requirements given above. **Loose** muons use an identical selection but with the I_{comb} cut loosened to 0.15 and the d_0 cut to 0.1 cm.

7.4.3. Electrons

Tight electrons are reconstructed as described in Section 5.2.2 using the 80% efficiency working point, but with impact parameter requirements identical to those used for the muons. **Loose** electrons use the 95% efficiency working point, with the impact parameter criteria loosened as for the muon case.

7.4.4. Resolving Ambiguities

Since the leptons in this analysis use the traditional reconstruction methods at CMS, while jets and $\vec{E}_T^{\text{miss}}$ are taken from the PF algorithm, ambiguities can exist. In order to avoid double counting, these ambiguities are resolved by several cleaning steps.

To remove jets dominated by a lepton, any jet found within a cone of 0.1 (0.3) of a selected muon (electron) is removed from consideration. In addition, muons within a cone of 0.3 of any jet are rejected.

A second step corrects the $\vec{E}_T^{\text{miss}}$ for differences between PF and global muon reconstruction. Each global muon is matched to a corresponding PF muon within a cone of $\Delta R < 0.1$. The absolute relative difference between the transverse momenta is then calculated. For cases where no match is found or this difference is $> 20\%$, the event is rejected. For cases where the difference is smaller than 20%, the $\vec{E}_T^{\text{miss}}$ receives a vectorial correction.

7.5. Analysis Selection

Selection begins with a set of event cleaning cuts common to many analyses at CMS. These address known detector and reconstruction problems as well as suppressing machine backgrounds. They are fully detailed in [145].

Lepton selection requires exactly one **Tight** electron or muon. To remove dilepton events and minimise overlap with searches in multilepton final states, events containing a second **Loose** lepton are vetoed.

After the initial lepton selection cuts, events can enter two independent samples. The first is a control sample obtained by inverting the jet multiplicity cut. This selects a sample known to be overwhelmingly dominated by SM backgrounds. To compensate for

the inverted jet multiplicity cut, this sample is selected with a slightly relaxed H_{T} cut. The second sample is then used for the actual search. A jet multiplicity cut, $N^{\mathrm{jets}} \geq 3$ is applied, as well as an $H_{\mathrm{T}} > 500$ GeV cut.

The data-driven control sample is used to test the analysis techniques before applying them to the search dataset. During this time, the search dataset was not studied (or "blinded") to avoid changes in the analysis procedure that might bias the result. Once the analysis method was fully refined, the search sample was "unblinded" and major changes to the analysis were no longer allowed.

Due to the unavailability of suitable efficient and unbiased triggers, the control sample is considered only for the muon channel. For the electron channel, validation work is performed instead in the $150 < S_T^{\mathrm{lep}} < 250$ GeV bin. Trigger thresholds in the control sample necessitated an increase in the transverse momentum cut applied on the muon to 35 GeV.

The full sequence of selection requirements is shown in Table 7.1. The corresponding event yields, as measured in simulation are shown in Tables 7.2 and 7.3 for the signal and control regions respectively.

7.6. Triggers and Datasets

Due to the construction of S_T^{lep}, events may be selected with moderate E_T^{miss} (and a large lepton p_{T}) or large E_T^{miss} (and a moderate lepton p_{T}). This necessitates a different trigger strategy to that used in other leptonic SUSY searches at CMS, which typically only select high E_T^{miss} events.

For the search sample, a set of single-lepton "cross-triggers" are used, selecting events with a single lepton in association with a large amount of hadronic activity, H_{T}. As the luminosity increased during the 2011 run, it was necessary to introduce a third requirement: a moderate cut on the E_T^{miss}.

The full list of triggers used for both lepton search channels and the muon control sample is shown in Table 7.4. The naming scheme is similar to that used in Section 6.3.7. `HTX` and `PFMHTX` refer to cuts $H_{\mathrm{T}} >$ X GeV and particle-flow $H_T^{\mathrm{miss}} >$ X GeV respectively. The string `CaloId` indicates cuts applied on H/E and $\sigma_{i\eta,i\eta}$. `TrkId` uses the angular

Table 7.1.: Selection requirements for the SUSY search in both the search samples and the muon control sample. The lepton selection and veto requirements are common to both samples.

Lepton Selection	Exactly one **Tight** electron or muon
	$\lvert\eta^{\mu}\rvert < 2.1$, $\lvert\eta^{\mathrm{e}}\rvert < 2.5$
Lepton Veto	Zero additional leptons passing **Loose** criteria
	$P_T^{\mu} > 15$ GeV, $P_T^{\mathrm{e}} > 20$ GeV
	$\lvert\eta^{\mu}\rvert < 2.5$, $\lvert\eta^{\mathrm{e}}\rvert < 2.5$
Control Sample (μ only)	< 3 jets
	$P_T^{\mu} > 35$ GeV
	$H_{\mathrm{T}} > 200$ GeV
Analysis Sample	≥ 3 jets
	$P_T^{\ell} > 20$ GeV
	$H_{\mathrm{T}} > 500$ GeV

matching variables: $\Delta\eta_{\mathrm{in}}$ and $\Delta\phi_{\mathrm{in}}$. Similarly, `CaloIso` and `TrkIso` select using the corresponding isolation variables. The suffixes `VL`, `L` and `T` stand for "very-loose", "loose" and "tight" respectively - referring to the "tightness" of the cut applied to the concerned quantity. The `VL` selection requirements are broadly comparable to the `CaloEleId` and `TightEleId` triggers used for the W polarisation analysis. The `T` requirements are looser than the 80% efficiency working point. All trigger requirements are chosen to be looser than the offline selection.

All signal and background MC samples are from the Summer11 CMS 7 TeV production using CMSSW version 4.2. All processes are simulated using the MADGRAPH matrix element generator, with the exception of the QCD and SUSY signal samples which use PYTHIA version 6. All datasets, with the exception of the SUSY signal scan used to derive the limit, make use of the full detector simulation. The SUSY signal scan uses the FASTSIM simplified simulation package to reduce processing time. All samples contain data-like pile-up conditions, with a re-weighting procedure used throughout to reflect the vertex multiplicity distribution in data.

Table 7.2.: MC event yields in the signal region, $L_{\mathrm{P}} < 0.15$, normalised to 1.14 fb^{-1}. Both muon and electron channels are shown. The contribution from QCD multi-jet events is expected to be negligible and thus is not shown.

$L_{\mathrm{P}} < 0.15$	Muons: S_T^{lep} range (GeV)			Electrons: S_T^{lep} range (GeV)		
Sample	[250-350]	[350-450]	[450-inf]	[250-350]	[350-450]	[450-inf]
$\mathrm{t\bar{t}}$ (ℓ)	11.4 ± 0.9	2.91 ± 0.4	0.8 ± 0.2	7.8 ± 0.7	3.0 ± 0.4	1.0 ± 0.3
$\mathrm{t\bar{t}}$ $(\ell\ell)$	2.2 ± 0.4	0.6 ± 0.2	0.1 ± 0.1	2.4 ± 0.4	0.7 ± 0.2	0.4 ± 0.2
W	14.5 ± 0.6	8.0 ± 0.5	5.6 ± 0.4	10.5 ± 0.5	5.2 ± 0.4	4.7 ± 0.3
Z	0 ± 1.5	0 ± 1.5	0 ± 1.5	0 ± 1.5	0 ± 1.5	0 ± 1.5
Total MC	28.1 ± 1.1	11.5 ± 0.7	6.5 ± 0.4	20.8 ± 1.0	8.8 ± 0.6	6.1 ± 0.5
LM1	24.2 ± 0.9	23.1 ± 0.9	16.2 ± 0.7	22.9 ± 0.9	20.8 ± 0.8	14.7 ± 0.7
LM3	24.8 ± 0.8	16.7 ± 0.6	9.7 ± 0.5	22.8 ± 0.7	14.8 ± 0.6	9.7 ± 0.5
LM6	1.9 ± 0.0	2.5 ± 0.1	5.9 ± 0.1	1.7 ± 0.0	2.3 ± 0.1	5.3 ± 0.1

Table 7.3.: MC event yields in the control region, $L_{\mathrm{P}} > 0.3$, normalised to 1.14 fb^{-1}. Both muon and electron channels are shown.

$L_{\mathrm{P}} > 0.30$	Muons: S_T^{lep} range (GeV)			Electrons: S_T^{lep} range (GeV)		
Sample	[250-350]	[350-450]	[450-inf]	[250-350]	[350-450]	[450-inf]
$\mathrm{t\bar{t}}$ (ℓ)	43.4 ± 1.7	12.3 ± 0.9	2.7 ± 0.4	42.2 ± 1.7	11.4 ± 0.8	2.9 ± 0.4
$\mathrm{t\bar{t}}$ $(\ell\ell)$	5.2 ± 0.6	1.6 ± 0.3	0.4 ± 0.2	2.5 ± 0.4	1.4 ± 0.3	0.3 ± 0.1
W	67.1 ± 1.3	27.5 ± 0.8	15.3 ± 0.6	57.5 ± 1.2	24.3 ± 0.8	14.7 ± 0.6
Z	0 ± 1.5	1.7 ± 1.5	0 ± 1.5	7.5 ± 3.6	0 ± 0	0 ± 0
QCD	0 ± 1.5	0 ± 1.5	0 ± 1.5	10.4 ± 3.0	7.2 ± 1.7	3.8 ± 0.7
Total MC	116 ± 2	43.4 ± 2.3	18.4 ± 0.8	120 ± 5	44.3 ± 2.1	21.7 ± 1.1
LM1	2.8 ± 0.3	1.4 ± 0.2	0.8 ± 0.2	2.9 ± 0.3	2.0 ± 0.3	1.3 ± 0.2
LM3	9.7 ± 0.5	4.2 ± 0.3	2.3 ± 0.2	9.1 ± 0.5	4.2 ± 0.3	2.5 ± 0.2
LM6	0.5 ± 0.0	0.4 ± 0.0	0.9 ± 0.0	0.5 ± 0.0	0.4 ± 0.0	0.9 ± 0.0

Table 7.4.: Triggers used in the SUSY search analysis for muon and electron search samples and the muon control sample

	Search Sample
μ	HLT_Mu8_HT200_v*
	HLT_Mu15_HT200_v*
	HLT_Mu15_HT250_PFMHT20_v*
e	HLT_Ele10_CaloIdL_CaloIsoVL_TrkIdVL_TrkIsoVL_HT200_v*
	HLT_Ele15_CaloIdT_CaloIsoVL_TrkIdT_TrkIsoVL_HT250_v*
	HLT_HT250_Ele5_CaloIdVL_TrkIdVL_CaloIsoVL_TrkIsoVL_PFMHT35_v*
	HLT_HT300_Ele5_CaloIdVL_TrkIdVL_CaloIsoVL_TrkIsoVL_PFMHT40_v*
	Control sample
μ	HLT_Mu20_v*, HLT_IsoMu17_v*
	HLT_Mu30_v*, HLT_IsoMu24_v*

In addition to the standard W + jets sample, an enriched sample with a generator-level $H_{\mathrm{T}} > 300$ GeV cut is used. The larger event sample reduces the statistical error on R^{CS}. The MC samples used for this analysis are shown in Table D.2.

7.7. Control Sample

In order to test that the simulation of EWK background processes can be relied upon for the calculation of the translation factor R^{CS}, the procedure is first performed in the control sample. With the jet multiplicity cut inverted, any SUSY signal should be highly diluted in this sample. It is expected therefore that the background prediction in the signal region should agree well with the observed signal yield. Furthermore, the level of agreement between data and simulation is also important in establishing the method.

A summary of the yields in the $L_{\mathrm{P}} > 0.3$ and $L_{\mathrm{P}} < 0.15$ regions in the < 3 jet control sample is given in Table 7.5. The yields for each SM subprocess are shown, used to calculate the factor R^{CS}, as well as the yields in data and the resulting background prediction. The background prediction is seen to agree, within errors, with the observed number of events in the signal region. The uncertainties stem from the limited population of the control region and the limited MC sample used in the calculation of R^{CS}.

Table 7.5.: Event yields in the $L_{\mathrm{P}} < 0.15$ and $L_{\mathrm{P}} > 0.3$ regions for the < 3 jet control sample in the muon channel. Expected MC yields are shown for each SM background and as a total. The "SM Estimate" row gives the SM background as predicted from the control region using the MC translation factor R^{CS}. The first uncertainty is from the statistical uncertainty on the yield in the control region. The second is from the statistical uncertainty on R^{CS} due to the limited MC sample. The expected yield for a benchmark SUSY point, LM6, is also shown.

	Control Region: $L_{\mathrm{P}} > 0.3$			Signal Region: $L_{\mathrm{P}} < 0.15$		
Sample	[250-350]	[350-450]	[450-inf]	[250-350]	[350-450]	[450-inf]
$t\bar{t}$	50.1 ± 1.8	7.8 ± 0.7	2.8 ± 0.4	10.5 ± 0.8	2.8 ± 0.4	0.7 ± 0.2
W	959 ± 24	162 ± 9.7	46.2 ± 5.2	83.7 ± 7.0	22.8 ± 3.7	12.3 ± 2.8
Z	45.3 ± 9.2	4.7 ± 2.9	3.9 ± 2.8	1.8 ± 1.8	0 ± 1.8	0 ± 1.8
QCD	2.7 ± 1.7	0.8 ± 0.8	0 ± 0.8	0 ± 1.4	0 ± 1.3	0 ± 1.3
Total MC	1054 ± 26	174 ± 10.2	52.9 ± 5.9	96 ± 7.3	25.6 ± 3.7	13 ± 2.8
Data	1051	179	52	92	24	11
SM Estimate				$95.8 \pm 10.2 \pm 7.6$	$26.3 \pm 5.5 \pm 4.1$	$12.8 \pm 4.0 \pm 3.0$
LM6	0.3 ± 0.0	0.2 ± 0.0	0.4 ± 0.0	1.0 ± 0.0	1.0 ± 0.0	2.4 ± 0.1

Comparisons of the variables S_T^{lep}, M_{T} and P_{T}^{μ} between data and simulation are shown in Figure 7.2. A similar comparison is shown for the L_{P} variable, in bins of S_T^{lep}, in Figure 7.3. These distributions are those used to derive the numbers shown in Table 7.5. The data are seen to be adequately described by the simulation. There are some discrepancies apparent in the L_{P} distributions of Figures 7.3b and 7.3c, perhaps due to inefficiency in the triggers used. However, as has been noted, Table 7.5 shows that the background predictions close within the quoted uncertainties.

7.8. Background Prediction

As for the W polarisation analysis, the background from QCD multi-jet events again presents a difficulty. In the muon channel, the QCD contribution is once again small-to-negligible as evidenced by Table 7.3. Therefore, it is sufficient to calculate only an upper bound. For the electron channel, as before, the contribution is much larger. Fortunately, the methods outlined in Section 6.6.4 prove to be effective again, with some modification.

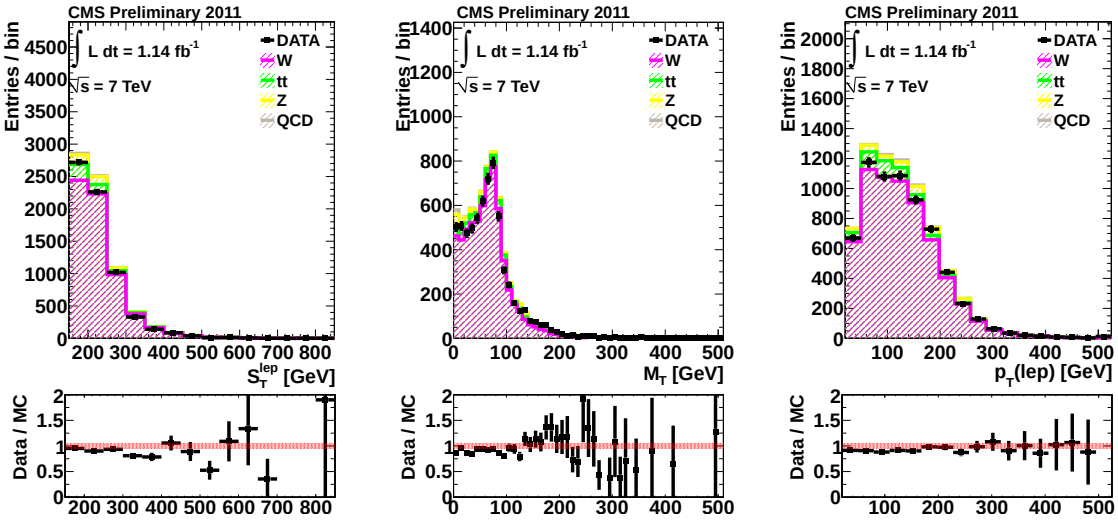

(a) S_T^{lep} (b) M_{T} (c) P_{T}^{μ}

Figure 7.2.: Distributions of kinematic variables as measured in the muon control sample. These are (a) S_T^{lep}, (b) M_{T} and (c) P_{T}^{μ}. MC distributions for SM background processes are shown for comparison.

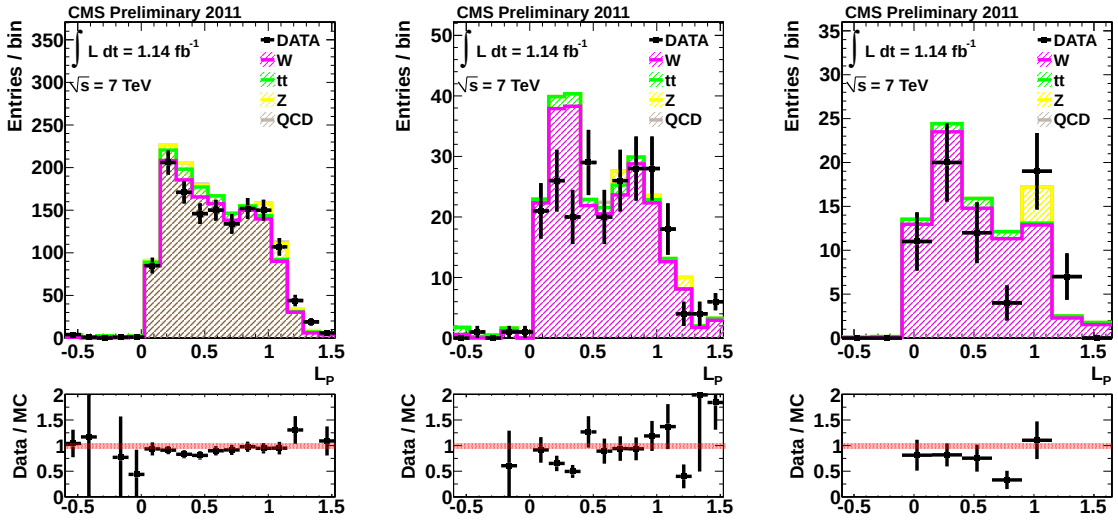

(a) $250 < S_T^{\mathrm{lep}} < 350$ (b) $250 < S_T^{\mathrm{lep}} < 450$ (c) $S_T^{\mathrm{lep}} > 450$

Figure 7.3.: Distribution of the L_{P} variable as measured in the muon control sample. The distributions shown are for the three highest S_T^{lep} bins. MC distributions for SM background processes are shown for comparison.

7.8.1. Muons

A conservative upper limit on the QCD background in the muon channel is obtained from a data-driven control sample defined by an isolation requirement, $0.2 < I_{\text{comb}} < 0.5$. In order to further enrich QCD events, whilst suppressing EWK backgrounds in this sample, a cut, $E_T^{\text{miss}} < 20$ GeV, is also applied. Even with these cuts, significant EWK contamination remains. The significance of the vertex impact parameter is used as an additional handle, by requiring $\sigma(D_0) > 3$. By selecting muons displaced from the primary vertex, backgrounds from hadron decays are enhanced [146]. The ratio $N(I_{\text{comb}} < 0.1)/N(0.2 < I_{\text{comb}} < 0.5)$ in this sample is then used to derive an upper limit on the QCD contribution. This limit is conservative given that EWK backgrounds are present in the ratio. The QCD background is found to be negligible in all S_T^{lep} bins and is ignored in the subsequent analysis.

7.8.2. Electrons

In the case of the electrons, a strategy similar to that used in the W polarisation analysis is employed. As before, the electron identification variables $\Delta\eta_{\text{in}}$ and $\Delta\phi_{\text{in}}$ are inverted. In addition, to ensure adequate statistical precision, the D_0 and D_z cuts are removed and the isolation cut is relaxed. The D_0 and D_z cuts were not present in the W polarisation selection. Although the present analysis benefits from a dataset ~ 30 times larger than that used for the previous measurement, this increase is partly offset by generally tighter kinematic cuts.

In addition, it was observed during measurement of the W polarisation that the shape of the QCD template is affected by a cut on P_T^{W}. Thus it should be assumed to depend too on S_T^{lep}, necessitating the use of independent templates for each S_T^{lep} bin. A comparison of the selected and anti-selected shapes in simulated QCD events is shown in Figure 7.4. This may be compared with those derived in the W polarisation analysis (see Figure 6.9). Differences may be accounted for by the modified electron selection and kinematic cuts.

As in the W polarisation analysis, a binned maximum likelihood fit is performed, using templates for the EWK backgrounds derived from simulation. To avoid the potential effects of SUSY signal contamination, the fit region is restricted to $L_{\text{P}} > 0.3$ and the fit-result is extrapolated into $L_{\text{P}} < 0.15$. The results of these fits are shown in Figure 7.5. The predictions of the QCD and EWK background contamination can be seen in Table 7.9. The QCD contamination in the signal region is found to be negligible.

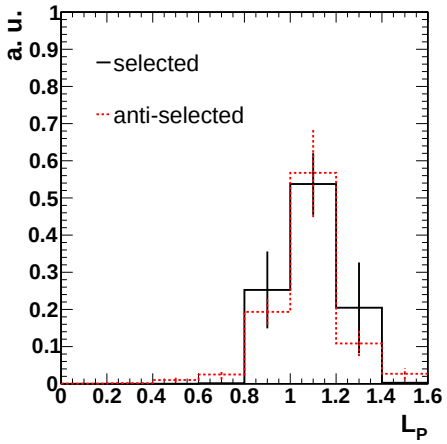

Figure 7.4.: A comparison of the L_P shape between simulated QCD events in the selected and anti-selected electron samples [147].

The results of the fit can be used to directly predict the background contamination in the signal region. However, in order to compare systematic uncertainties with the muon channel, R^{CS} values are calculated from the results of the fit. The systematic uncertainties are then evaluated in terms of their effect on R^{CS}. For the limit procedure described in Chapter 8, it is technically simpler to use the fit results to correct the control region yield in order to subtract the QCD contribution. Since the QCD contamination in the signal region is negligible, this does not make a significant difference to the limit.

In summary, the QCD contamination in the electron channel is accounted for by taking the background prediction in the signal region from the fitted number of EWK and QCD events. The additional uncertainties introduced by this procedure will be covered in Section 7.9.

7.9. Systematic Uncertainties

For this analysis, as with the W polarisation measurement, unavoidable dependence on simulation requires careful evaluation of associated systematic uncertainties. It has already been said that the construction of R^{CS} is intended to minimise some of these uncertainties by ensuring some degree of cancellation. Experience from the W polarisation measurement showed that the L_P variable is highly sensitive to certain uncertainties – in particular the JES. The size of these uncertainties was thus evaluated early-on in the development of the analysis and continued throughout. Several of the procedures for

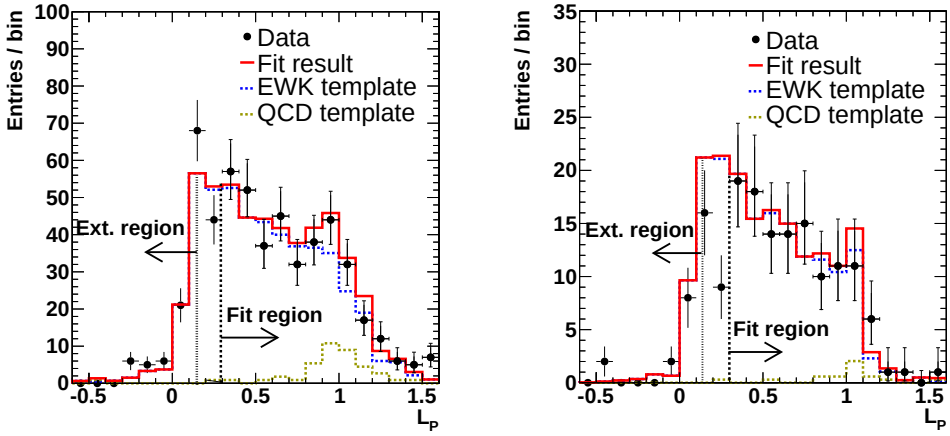

(a) Fit results $150 < S_T^{\text{lep}} < 250$ **(b)** Fit results $250 < S_T^{\text{lep}} < 350$

Figure 7.5.: Results of fits to the QCD background shape in the electron channel shown for two S_T^{lep} bins [137]

evaluating systematic uncertainties were adopted or adapted from those used for the previous measurement (see Section 6.7).

The background prediction may be written as follows,

$$N_i^{\text{bkg}} = R_i^{\text{CS}} \times N_i^{\text{control}},$$

where N_i^{bkg} is the predicted background for $L_{\text{P}} < 0.15$ in S_T^{lep} bin i, R_i^{CS} the corresponding translation factor and N_i^{control} the EWK yield in the region $L_{\text{P}} > 0.3$.

The uncertainty assigned to the background prediction, N^{bkg}, comes from two sources: uncertainty on the translation factor, R^{CS}, and uncertainty on the EWK yield in the control region, N^{control}. For the electron channel, each of the sources of uncertainty affecting R^{CS} include an additional contribution to account for the uncertainty associated with the fitting procedure. The evaluation of each systematic uncertainty will now be described.

7.9.1. Control Region $L_{\text{P}} > 0.3$

A statistical uncertainty must be included to account for the finite event yield in the control region. The effect is naturally more pronounced in the higher S_T^{lep} bins. For the muon channel, this is simply calculated as the Poisson uncertainty on the number

of events in the control region. For electrons, this is taken as the uncertainty on the background estimate as determined from the fit (see Section 7.8.2).

7.9.2. Monte Carlo Statistical Uncertainty

The limited number of simulated events results in a systematic uncertainty on the calculation of R^{CS} for both lepton channels. This is calculated by simple propagation of errors.

For the electron channel, the QCD fitting procedure introduces additional complications. The EWK templates used in the fit are taken from finite MC samples. This results in an additional source of uncertainty on the background prediction. This is accounted for in a similar manner to the statistical uncertainty of the QCD template in the W polarisation analysis (see Section 6.7.1). The templates are randomly fluctuated 200 times according to the statistical uncertainty per bin. Each re-diced template is then used to repeat the fit procedure. The variance of this ensemble of fits is then taken to be the statistical uncertainty. For the systematic uncertainty quoted in Table 7.7, this is propagated into R^{CS}. For the limit, as will be seen, it is taken as an uncertainty on N^{control}.

7.9.3. Jet Energy Scale

This procedure was changed with respect to the W polarisation measurement in order to harmonise with other analyses. Each jet in the event, as well as the remaining hadronic recoil are scaled upwards or downwards by 5%. The larger of the two shifts on R^{CS} is then taken as the uncertainty. If the uncertainty is found to be smaller than the MC statistical uncertainty (Section 7.9.2), the larger of the two is assigned.

7.9.4. $\boldsymbol{E_T^{\mathrm{miss}}}$ Resolution

As for the W polarisation measurement, the E_T^{miss} resolution measured in data is seen to be 10% larger than predicted by simulation [138, 139]. To account for this, the recoil is smeared by an additional 10% perpendicular and parallel to its direction. The resulting shift in R^{CS} is taken as the uncertainty. As for the W polarisation case, this is a conservative estimate.

7.9.5. W + jets and $t\bar{t}$ Backgrounds

The use of R^{CS} avoids any dependence on the absolute values of theoretical cross-sections. However, since the W + jets and $t\bar{t}$ backgrounds have different shapes in L_{P}, changes to their relative normalisations will result in changes to R^{CS}. To account for this, the $t\bar{t}$ and W + jets contributions are each scaled up and down by 30% and 50% respectively. The former is again taken from a cross-section measurement at CMS [148] (improved with respect to that cited in the W polarisation measurement). The latter is evaluated by studying the agreement between data and MC in Z + jets events with ≥ 4 jets. The difference is found to be at most 50%.

The shift in R^{CS} with respect to the unscaled case is then calculated. The shifts are performed simultaneously to give the most extreme change in R^{CS}, i.e. one background is shifted up, the other down. The largest such shift is taken as the uncertainty. As for the jet energy scale, a shift smaller than the statistical uncertainty of the simulated sample is taken to be the statistical uncertainty. Additionally, the uncertainty is calculated simultaneously for both lepton channels, in order to maximise the statistical precision.

7.9.6. Muon Momentum Scale

Studies of the Z mass indicate a bias of 1% [105]. To estimate this effect, the muon momentum is varied as follows [137]:

$$P_{\mathrm{T}}^{\mu\prime} = P_{\mathrm{T}}^{\mu} + \mathrm{sign}(\mu) \times 0.01 P_{\mathrm{T}}^{\mu\,2}/100\ \mathrm{GeV} \times (1 + \sin(\phi)).$$

7.9.7. W and $t\bar{t}$ Polarisation

The polarisation in $t\bar{t}$ events is 5%. Since the effect on R^{CS} is less than 5%, this is assigned as a conservative uncertainty.

For the W polarisation, the uncertainties from the previous measurement are taken and used to assign a 15% uncertainty on the difference of the left-handed and right-handed fractions, $(f_{\mathrm{L}} - f_{\mathrm{R}})$ (see Section 6.8). To account for this, the simulation is re-weighted to reflect an upward and downard shift of 15% on $(f_{\mathrm{L}} - f_{\mathrm{R}})$ with respect to the nominal values. This is done in a manner similar to that used for the actual measurement (see Section 6.2.3), but using 5 bins in P_T^{W} instead of 3. The effect is shown for the lowest and

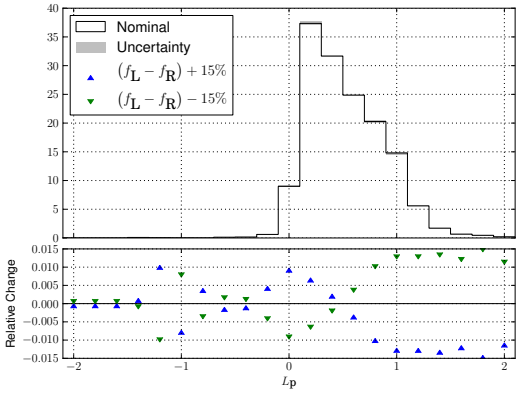

(a) e^+, $150 < S_T^{lep} < 250$

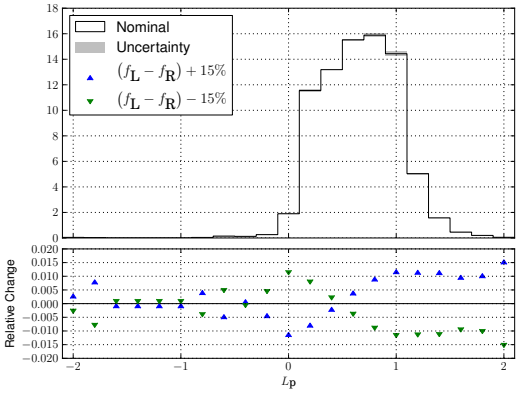

(b) e^-, $150 < S_T^{lep} < 250$

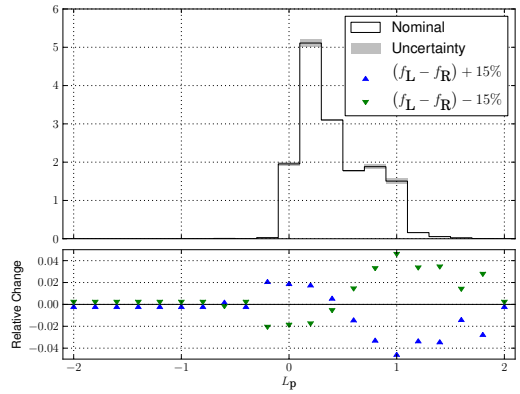

(c) e^+, $S_T^{lep} > 450$

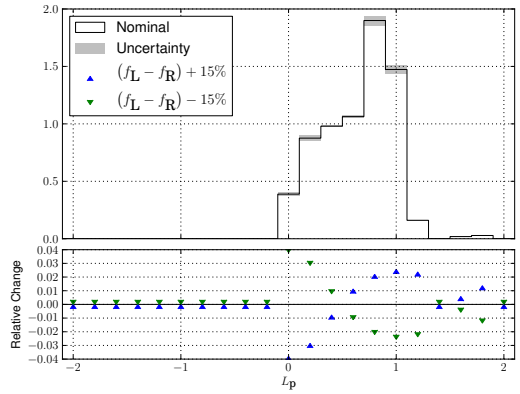

(d) e^-, $S_T^{lep} > 450$

Figure 7.6.: The effect of a 15% shift in $(f_L - f_R)$ on the reconstruction-level L_P distribution in simulated $W \longrightarrow e\nu$ events. Figures 7.6a and 7.6b show the effect for e^+ and e^- in the $150 < S_T^{lep} < 250$ bin. Figures 7.6c and 7.6d show the same distributions in the $S_T^{lep} > 450$ bin. The upper panels show the nominal L_P distribution in black. The uncertainty due to upward and downward shifts in $(f_L - f_R)$ is shaded grey. The lower panels show the relative change in the distribution for an upward shift (blue, upward-pointing arrows) and a downward shift (green, downward-pointing arrows).

highest S_T^{lep} bins in Figure 7.6. The largest of the two shifts is taken to be the systematic uncertainty.

7.9.8. Fully Leptonic $t\bar{t}$

The fraction of events passing the selection in which a second lepton is not identified, either due to reconstruction or acceptance effects, is estimated in simulation. Since this is a relatively small fraction of the background, a conservative 50% uncertainty is assumed. The resulting change in the L_{P} shape is then propagated into R^{CS}.

7.9.9. Parton Distribution Functions

The systematic uncertainty due to the choice of PDF was previously evaluated for the W polarisation analysis (see Section 6.7.2). It was found to be negligible. For this analysis, an alternative test was performed.

The MC is reweighted to the central value of both CTEQ66 and MSTW2008NLO68CL PDF sets [149–152]. The resulting change in R^{CS} is found to be 1% for $S_T^{\mathrm{lep}} < 450$ GeV and 5% for $S_T^{\mathrm{lep}} > 450$ GeV.

7.9.10. Trigger Efficiency

The exact selection of triggers listed in Table 7.4 was unavailable in the MC samples. Small differences in the efficiency in the plateau of the trigger turn-on curve are observed in both channels as well as a dependence on the pseudorapidity of the lepton. The effect of these differences is evaluated by applying the `HLT_Mu15` trigger in simulation. The effect on R^{CS} is found to be $< 1\%$ across all η bins.

7.9.11. Summary

The relative uncertainties on R^{CS} for each significant systematic effect listed above are shown in Table 7.6 for the muon channel and Table 7.7 for the electron channel. In the highest S_T^{lep} bins, the limited statistical precision of the control region is seen to be the dominant source of systematic uncertainty for both lepton channels. The second largest source of uncertainty (and the largest in some bins), is due to the JES. This was also a significant source of uncertainty in the W polarisation analysis, and therefore is expected.

An additional systematic effect which could affect this analysis is the uncertainty in the prediction of the jet multiplicity given by the MC generator. The W polarisation is

Table 7.6.: Sources of systematic uncertainty and their effect on the translation factor, R^{CS}, in the muon channel. The relative uncertainty on the estimated number of events in the signal region, stemming from the limited yield in the control region, is also listed.

	S_T^{lep} Range (GeV)			
	[150-250]	[250-350]	[350-450]	> 450
R^{CS}	0.19	0.24	0.26	0.35
Systematic Uncertainty (%)	15	17	21	34
Control Region Stat. (%)	5	10	15	24
MC Stat. (%)	4	4	8	8
JES (Flat 5%) (%)	10	9	8	19
E_T^{miss} Resolution (10%) (%)	1	3	2	3
Lepton p_{T} Scale (%)	2	2	1	3
W/$\mathrm{t\bar{t}}$ Ratio (%)	5	5	6	10
$\mathrm{t\bar{t}}$ ($\ell\ell$) (%)	5	4	2	1
W Polarization (%)	1	1	2	2
$\mathrm{t\bar{t}}$ Polarization (%)	5	5	5	5

known to depend only weakly on the jet multiplicity [60] and hence this uncertainty can be neglected.

7.10. Results

Once the analysis procedure had been finalised, the search region was "unblinded". The L_{P} distributions in data, along with the expected shapes in MC, are shown in Figure 7.7 for the three S_T^{lep} bins considered for the search. The predicted and observed background yields are then shown in Table 7.8 for muons and 7.9 for electrons. Comparison of the predicted and observed numbers are shown graphically in Figure 7.8. It is clear, that no significant excess is seen. In the next chapter, the results are used to set limits on allowed parameter space for the CMSSM and more general simplified models.

Table 7.7.: Sources of systematic uncertainty and their effect on the translation factor, R^{CS}, in the electron channel. The relative uncertainty on the estimated number of events in the signal region, stemming from the limited yield in the control region, is also listed.

	S_T^{lep} Range (GeV)			
	[150-250]	[250-350]	[350-450]	> 450
R^{CS}	0.16	0.18	0.19	0.23
Systematic Uncertainty (%)	14	20	24	34
Control Region Stat. (%)	5	9	17	24
MC Stat. (%)	1	10	7	8
JES (Flat 5%) (%)	9	10	10	19
E_T^{miss} Resolution (10%) (%)	2	2	5	7
W/$\mathrm{t\bar{t}}$ Ratio (%)	6	7	6	10
$\mathrm{t\bar{t}}$ ($\ell\ell$) (%)	6	7	6	2
W Polarization (%)	1	1	2	3
$\mathrm{t\bar{t}}$ Polarization (%)	5	5	5	5

Table 7.8.: Event yields in data and MC for the muon search sample. The column "Total MC" shows the expected yield from MC. The column "SM Estimate" gives the result of the background prediction procedure described in the text.

	Control Region ($L_{\mathrm{P}} > 0.3$)		Signal Region ($L_{\mathrm{P}} < 0.15$)		
S_T^{lep} Range (GeV)	Total MC	DATA	Total MC	SM Estimate	DATA
$[150 - 250]$	385 ± 7	368	73.9 ± 3.0	70.6 ± 11	84
$[250 - 350]$	116 ± 2	112	28.1 ± 1.1	27.2 ± 4.6	29
$[350 - 450]$	43.4 ± 2	41	11.5 ± 0.7	10.9 ± 2.3	9
> 450	18.4 ± 0.8	15	6.5 ± 0.4	5.3 ± 1.8	6

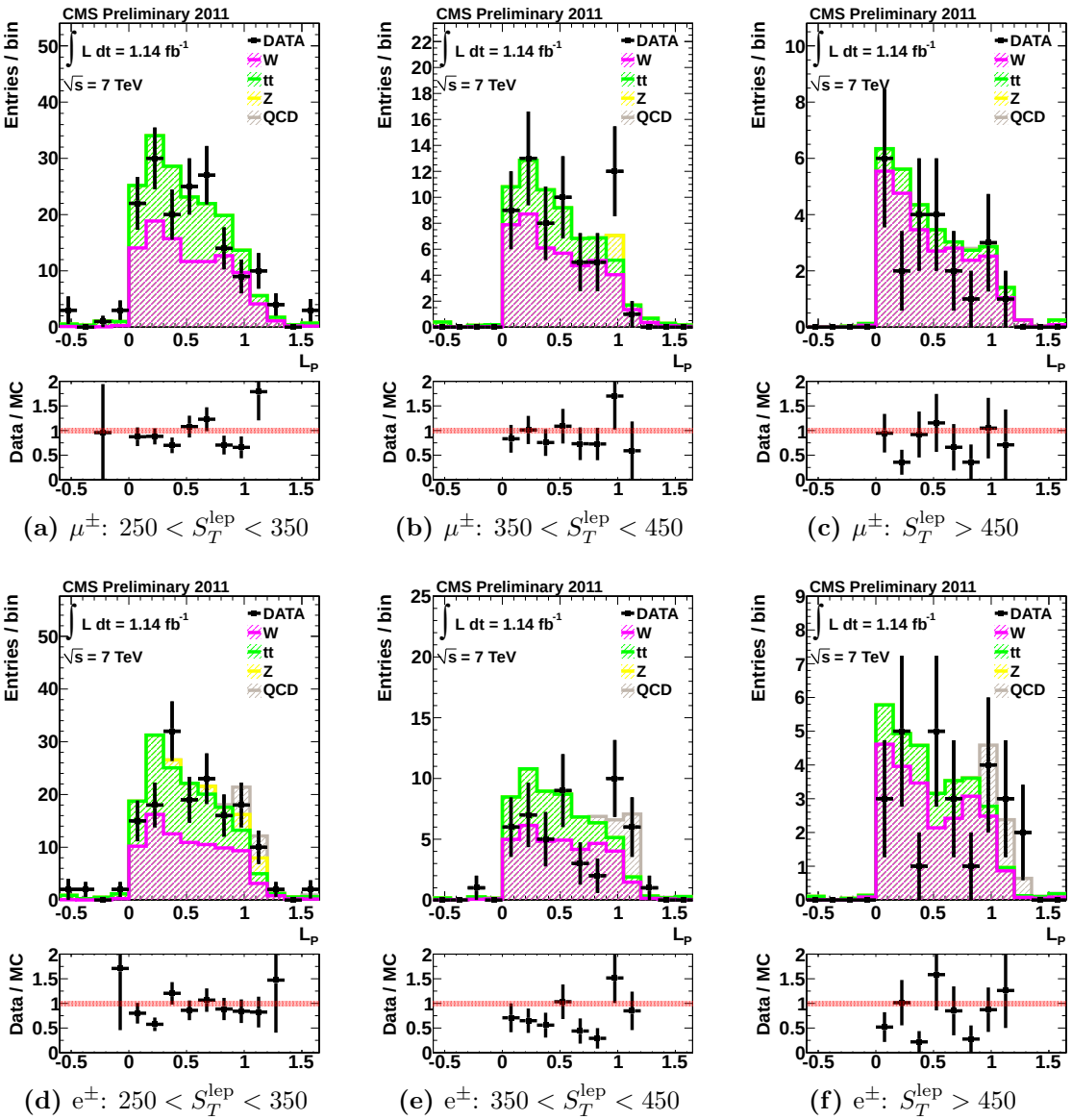

(a) $\mu^{\pm}$: $250 < S_T^{\text{lep}} < 350$ (b) $\mu^{\pm}$: $350 < S_T^{\text{lep}} < 450$ (c) $\mu^{\pm}$: $S_T^{\text{lep}} > 450$

(d) $e^{\pm}$: $250 < S_T^{\text{lep}} < 350$ (e) $e^{\pm}$: $350 < S_T^{\text{lep}} < 450$ (f) $e^{\pm}$: $S_T^{\text{lep}} > 450$

Figure 7.7.: Comparison of L_{P} distributions between data and MC for the muon and electron channels. Distributions are shown for the three highest S_T^{lep} bins used for the search.

Table 7.9.: Event yields in data and predictions for the numbers of EWK and QCD events in the electron search sample. The sum of the EWK and QCD predictions is constrained to be equal to the number of events in data. The column "SM Estimate" gives the result of the background prediction procedure described in the text. The uncertainties on these values include the full systematic uncertainties. The uncertainties in the EWK and QCD columns are only statistical.

	Control Region ($L_{\mathrm{P}} > 0.3$)			Signal Region ($L_{\mathrm{P}} < 0.15$)			
S_T^{lep} Range (GeV)	QCD	EWK	DATA	QCD	EWK	SM Estimate	DATA
$[150 - 250]$	39.5 ± 15.5	350 ± 24	390	1.0 ± 0.3	60.8 ± 4.1	61.8 ± 8.7	69
$[250 - 350]$	5.0 ± 5.2	117 ± 12	122	0	22.2 ± 2.2	22.2 ± 4.4	21
$[350 - 450]$	7.1 ± 3.9	28.9 ± 6.2	36	0	6.9 ± 1.5	6.9 ± 1.7	7
> 450	6.5 ± 5.7	12.5 ± 3.8	19	0	4.3 ± 1.3	4.3 ± 1.5	3

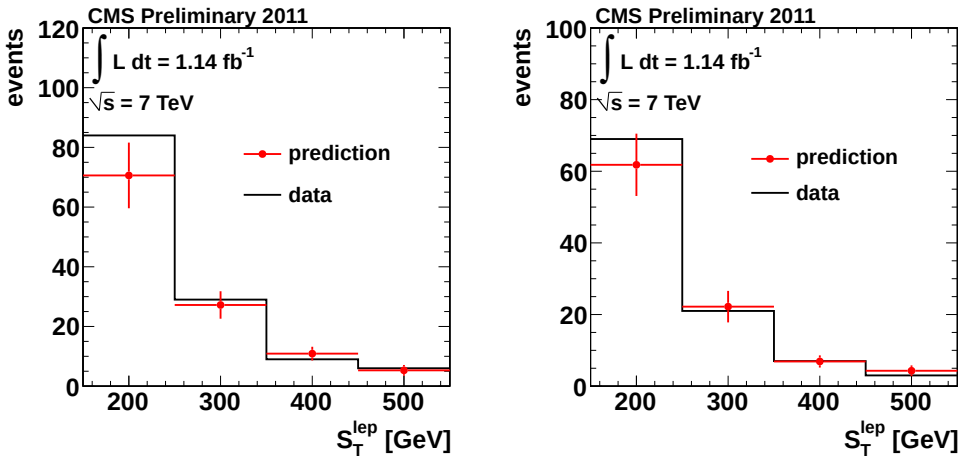

(a) (b)

Figure 7.8.: Comparison of the number of events observed in data and the background prediction in bins of S_T^{lep}. Results are shown for (a) the muon channel and (b) the electron channel. The red error-bars indicate the statistical uncertainty of the data.

Chapter 8.

Interpretation of Search Results

8.1. Introduction

It is very often the case that a search for NP will yield results consistent with the currently accepted theory (which in most particle physics contexts would be the SM). In the absence of a discovery, it is often desirable to provide additional information in the form of a statistical interpretation of the results. Such an interpretation typically serves the following goals.

- To indicate the sensitivity of the analysis to the proposed model or set of models. This can then be used as an objective measure by which to compare different analyses or to benchmark the progress of a single analysis as data is collected.
- To falsify, to some confidence level, a particular theory or some region of parameter space within that theory.
- To guide the choice of analysis cuts and object selection requirements.

Providing an interpretation invariably necessitates some choice of theory or phenomenological model against which to test the results. The range of theories will of course depend strongly on the inclusiveness of the experiment. Indeed, in many cases a single theory will have motivated the analysis in the first place and the choice of model will be clear. In other cases, the analysis has been designed to be as inclusive as possible and therefore sensitive to an array of theories. Typically this is achieved by focusing on a particular detector signature (for instance missing transverse energy), where a deviation from the SM is a common feature of many NP scenarios.

As was seen in Chapter 3, LHC searches have typically interpreted the results of SUSY searches in the context of the CMSSM. This provides a convenient benchmark space for the comparison of different searches. However, it restricts the range of physics signatures rather more than is desirable. It was seen that by selecting models from a spectrum of simplified models, searches can provide more generic and useful interpretations of their results.

This chapter will describe the statistical methods used to interpret the results of the single lepton search. These will then be applied to the CMSSM and to the two simplified models described in Chapter 3: T3W and T2tt.

8.2. Statistical Methods

8.2.1. The Likelihood Function

Consider some statistical model, believed to describe a set of experimental data and depending on a set of parameters, θ. The *likelihood* of given values of θ in light of experimental observations, X, is the probability of observing X given θ [153, 154]. Considered as a function of the parameter θ, given experimental measurements, X, the likelihood may be written

$$\mathcal{L}(\theta|X) = P(X|\theta), \tag{8.1}$$

where $P(X|\theta)$ should be read as "the probability of X given θ".

Likelihood functions are an important tool in comparing theoretical expectations to experiment. Often, two proposed values for the parameter θ will be compared using the *likelihood ratio*,

$$\ell = \frac{\mathcal{L}(\theta_1|X)}{\mathcal{L}(\theta_2|X)} = \frac{\alpha P(X|\theta_1)}{\alpha P(X|\theta_2)}. \tag{8.2}$$

Here, the numerator and denominator are related to Eqn. 8.1 by a constant α. Here, as in many uses of the likelihood function, such constant factors can be safely ignored. This is known as a *likelihood ratio test* and may be used to compare two hypotheses.

An important use of the likelihood function is in estimation of θ given some set of observations. The value of θ which maximises $\mathcal{L}$ is known as the Maximum Likelihood

Estimator (MLE) of θ, denoted $\hat{\theta}$. Often it will be convenient to work with the logarithm of the likelihood function, $\ln \mathcal{L}$. Since the logarithm is a monotonically increasing function, its maxima coincide with those of $\mathcal{L}$.

8.2.2. Profile Likelihood and Wilks' Theorem

The likelihood function for a complex experiment may depend on a large number of free parameters. A number of these may be introduced to describe experimental effects such as backgrounds or uncertainties which are not directly relevant to the underlying measurement. These are known as *nuisance parameters*. In contrast, the parameters to be measured by the experiment are known as *parameters of interest*.

The full likelihood function may be reduced to a *profile likelihood*, by rewriting the nuisance parameters in terms of the parameters of interest. The profile likelihood ratio is defined as

$$\lambda = \frac{\mathcal{L}\left(\mu, \hat{\hat{\nu}}\left(\mu\right)\right)}{\mathcal{L}\left(\hat{\mu}, \hat{\nu}\right)},$$

where μ are the parameters of interest and ν the nuisance parameters. $\hat{\mu}$ and $\hat{\nu}$ are the MLEs of μ and ν respectively. $\hat{\hat{\nu}}$ is the *conditional* MLE of ν - the MLE of ν for a given value of μ.

It is frequently the case that, in addition to calculating a maximum-likelihood estimate for a given parameter, it is also desirable to estimate a range in which the "true" value of the parameter can be said to lie with a given degree of certainty. This procedure is known as *interval estimation*, and the resulting interval, a *confidence interval*.

Wilks' theorem states that, under certain assumptions, $-2\ln\ell$ is distributed as a χ^2 distribution [153, 155, 156]. The number of degrees of freedom of this distribution is determined by the difference in the number of free parameters in the numerator and denominator of the likelihood ratio (θ_1 and θ_2 in Eqn. 8.2). In the case of the profile likelihood ratio, this is equal to the number of parameters of interest, μ. Wilks' theorem can therefore be used to provide an interval estimate for μ. This will be referred to as the Profile Likelihood (PL) method.

8.2.3. Hypothesis Testing

It has been seen that the likelihood ratio may be used to compare two hypotheses H_0 and H_1. Typically H_0 will be referred to as the "null hypothesis" and H_1, the "alternate hypothesis". For a given hypothesis H and observation, X, the *p-value* gives the probability of making a measurement as consistent or less with the hypothesis H, than X [153].

There are a variety of techniques for choosing between competing hypotheses. Typically, a certain *test statistic* is used – for instance the number of signal events observed or the likelihood ratio. For a given hypothesis, a critical region W, can be defined where the probability of making such an observation, assuming the hypothesis, is below some threshold, α,

$$P\left(x \in W|H\right) \leq \alpha,$$

where x is the test statistic. α is often chosen as 0.05. Then, if the measured value of x is found to be in the critical region, the hypothesis H can be said to be rejected with 95% confidence.

One way to define such an interval is to run toy MC experiments to generate the distributions of the test statistic corresponding to the null and alternate hypotheses. It is then straightforward to define the critical region as that point at which the p-value reaches a suitably low threshold, say 0.05. This is illustrated in Figure 8.1a.

8.2.4. The CL_{s} Method

One deficiency of the above method is that often the two hypotheses will not be so well separated. This situation is shown in Figure 8.1b. In this case, the p-value for the alternate hypothesis is small and so would result in an exclusion. This is undesirable since the test statistic is clearly not sensitive enough to distinguish between the two hypotheses.

To address this problem, the CL_{s} hypothesis test may be used instead [157, 158],

$$CL_{\mathrm{s}} = \frac{CL_{\mathrm{s+b}}}{CL_{\mathrm{b}}},$$

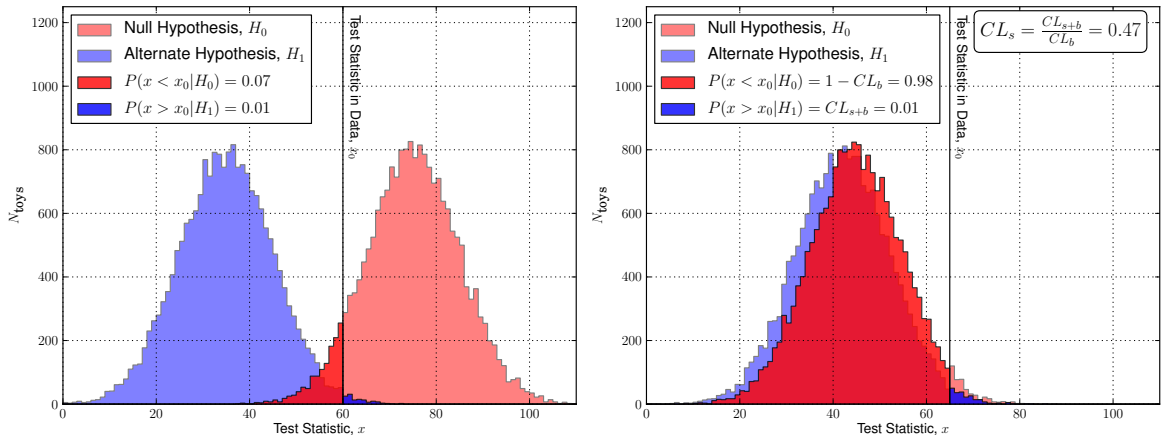

(a) **(b)**

Figure 8.1.: Illustration showing the use of the CL_s method. (a) shows the evaluation of a p-value in the presence of two hypotheses, well-separated in the test statistic. (b) shows an example where the null and alternate hypothesis are not well separated. In this case, the calculation of CL_s is shown.

where, for the example shown in Figure 8.1b,

$$CL_{s+b} = P\left(x > x_0|H_1\right)$$
$$CL_b = 1 - P\left(x < x_0|H_0\right),$$

and the null hypothesis now represents a background-only scenario, b, and the alternate, signal-plus-background, s+b. Using CL_s to test the alternate hypothesis, instead of a p-value, penalises cases where the test statistic provides little sensitivity – since CL_b will be large. For a 95% exclusion, $CL_s < 0.05$ is required as before. The CL_s method may also be used to derive an upper limit on some parameter by scanning through a range of values of the parameter of interest. This is known as "hypothesis test inversion".

Several additional details are relevant to the discussion here. For the toy experiments used to generate the test statistic distributions, the nuisance parameters are each sampled randomly according to their expected distributions. This ensures that the full range of their uncertainties is covered. The test statistic that has been used is the one-sided profile likelihood ratio, $q_\mu = -2 \ln \lambda$ [159–162].

8.3. The Single Lepton Supersymmetry Search

The full development of the likelihood function used to model the single lepton SUSY search is covered in Appendix B.1. In this section, only a few pertinent points will be discussed. Firstly, the evaluation of model-dependent systematic effects associated with the signal yield. And secondly, details of validation work performed to demonstrate that the statistical procedure and software infrastructure are functioning as expected. The statistical procedure has been implemented using the RooStats software framework [163, 164].

8.3.1. Systematic Uncertainties on Signal Efficiency

As can be seen in Table B.1, a number of nuisance parameters are assigned for systematic uncertainties affecting the expected signal yield.

Both the luminosity estimate and the trigger efficiency are subject to uncertainties which would affect the expected signal yield. Uncertainties of 4% and 1% are assigned respectively.

The signal efficiency will also be affected by the choice of PDFs in the simulated samples and the calculation of the NLO cross-sections. Whilst in principal, these would be expected to vary across the parameter space of a given theoretical model, a conservative 10% uncertainty is assigned instead.

For the JES and E_T^{miss} resolution uncertainties, these are calculated as for the background case (see Sections 7.9.3 and 7.9.4). They are calculated individually for different signal hypotheses. A summary of all uncertainties assigned for the signal efficiencies, along with their exact or approximate size, is shown in Table 8.1.

8.3.2. Validation

To validate the model, a number of cross-checks are performed. Firstly, the PL and CL_{s} methods are compared and found to agree. In general, the CL_{s} method is expected to be more conservative by covering the full range of the nuisance parameters in the model.

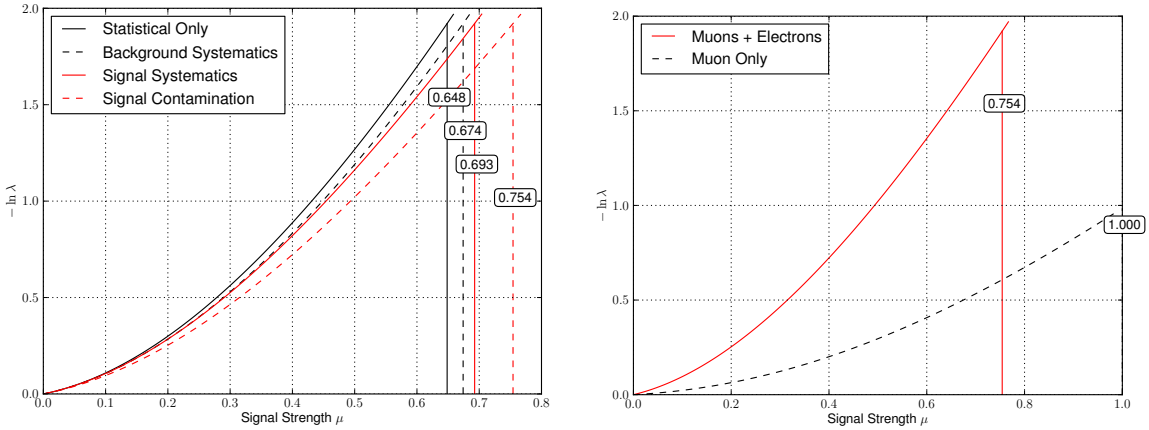

(a) Systematic effects **(b)** Muon channel only

Figure 8.2.: The negative log PL ratio as a function of μ (a) with different systematic effects included in the likelihood and (b) with the electron channel removed. The vertical lines and numbers represent the 95% confidence level upper limits on μ. The results are shown for the CMSSM point $(m_0, m_{\frac{1}{2}}) = (80, 400)$.

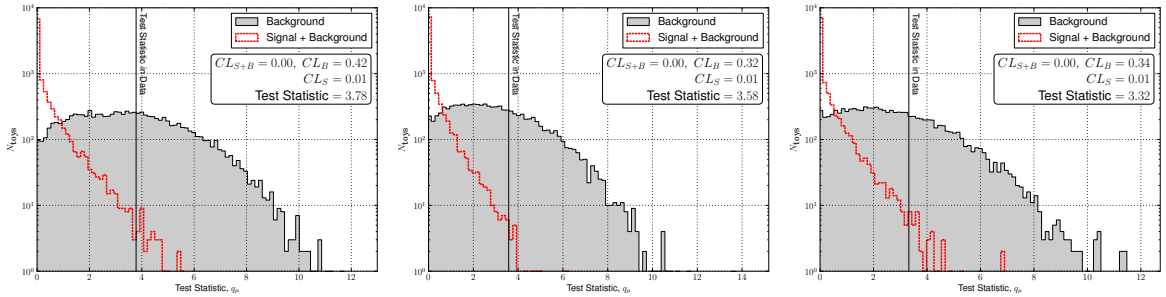

(a) Statistical Unc. **(b)** Background Unc. **(c)** Signal Unc.

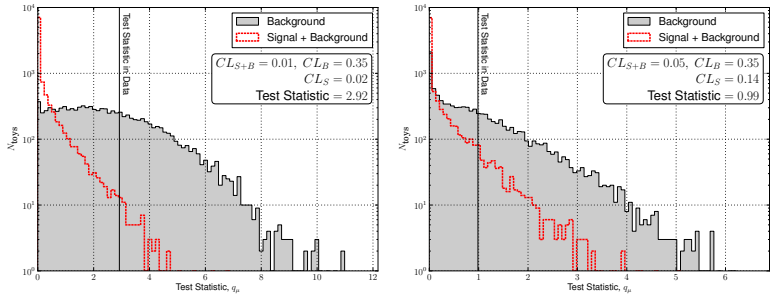

(d) Signal Contamination **(e)** Muon Channel Only

Figure 8.3.: Distribution of the test statistic, q_μ, for null and alternate hypotheses with different systematic effects included and with the electron channel removed. These distributions have been made for the CMSSM point $(m_0, m_{\frac{1}{2}}) = (80, 400)$. The values of CL_{b}, $CL_{\mathrm{s+b}}$ and CL_{s} are also shown.

Table 8.1.: Summary table of systematic uncertainties related to the signal efficiency.

Uncertainty	Value
$\mathcal{L}$	4.5%
trigger efficiency	1%
JES 5%	Model dependent (10-15% for CMSSM)
PFMET resolution 10%	Model dependent (0.5-15% for CMSSM)
PDF and NLO	10%

To see how the PL and CL_s results change with modifications to the likelihood function, a representative point in the CMSSM plane ($\tan\beta = 10$, $A_0 = 0$, $\mu > 0$) has been chosen. This is $(m_0, m_{\frac{1}{2}}) = (80, 400)$ - close to the edge of the region excluded by the data (additional detail can be found in Appendix B.2).

Figure 8.2 shows the negative log PL ratio, $-\ln\lambda$, as a function of the signal strength parameter, μ. The signal strength is defined as the ratio of the considered cross-section to that predicted by the CMSSM. As expected, the inclusion of systematic effects pushes the exclusion to larger values of μ. A similar, but more pronounced, effect can be seen when removing the electron channel. This shows, qualitatively at least, that the model is behaving as expected. For this particular model point, the signal contamination appears to have the largest effect, followed by the background uncertainties and then the signal uncertainties. Note that certain uncertainties are included in all cases: the effect of the statistical uncertainty in the control region, and the luminosity uncertainty. The former is actually the dominant uncertainty on the background prediction. This perhaps explains why the addition of the other systematic uncertainties appears to have relatively little effect.

The distributions of the test statistic used to calculate CL_s are shown in Figure 8.3. The results are seen to be qualitatively similar to the PL case. This particular point goes from being strongly excluded at $> 95\%$ confidence level with both lepton channels, to not being excluded when the electron channel is removed.

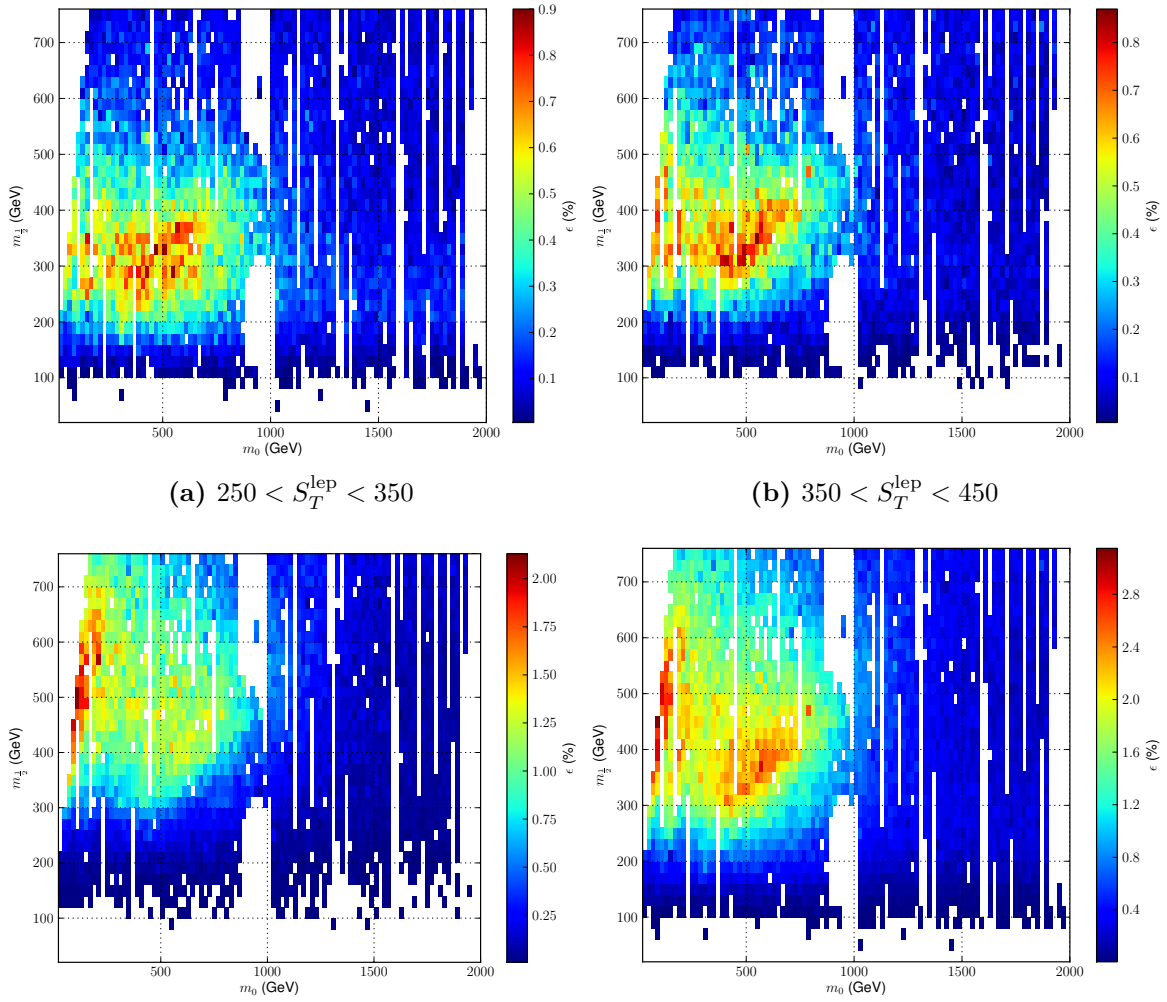

(a) $250 < S_T^{\text{lep}} < 350$ **(b)** $350 < S_T^{\text{lep}} < 450$

(c) $S_T^{\text{lep}} > 450$ **(d)** Total

Figure 8.4.: Signal efficiency for the muon channel in the CMSSM. The efficiency is shown separately for each S_T^{lep} bin and as a total. The efficiency is shown in the $(m_0, m_{\frac{1}{2}})$ plane with $\tan\beta = 10$, $A_0 = 0$ and $\mu > 0$.

8.4. Results

The statistical machinery described so far has been used to give interpretations in the context of several NP models. First of all, the CMSSM, and subsequently two simplified models: T2tt and T3W. These are fully described in Section 3.2.

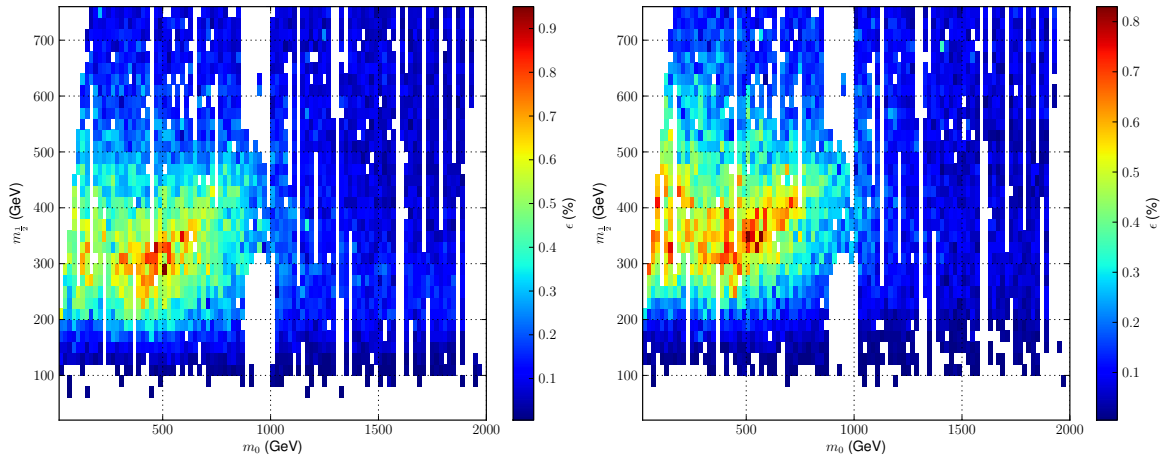

(a) $250 < S_T^{\text{lep}} < 350$

(b) $350 < S_T^{\text{lep}} < 450$

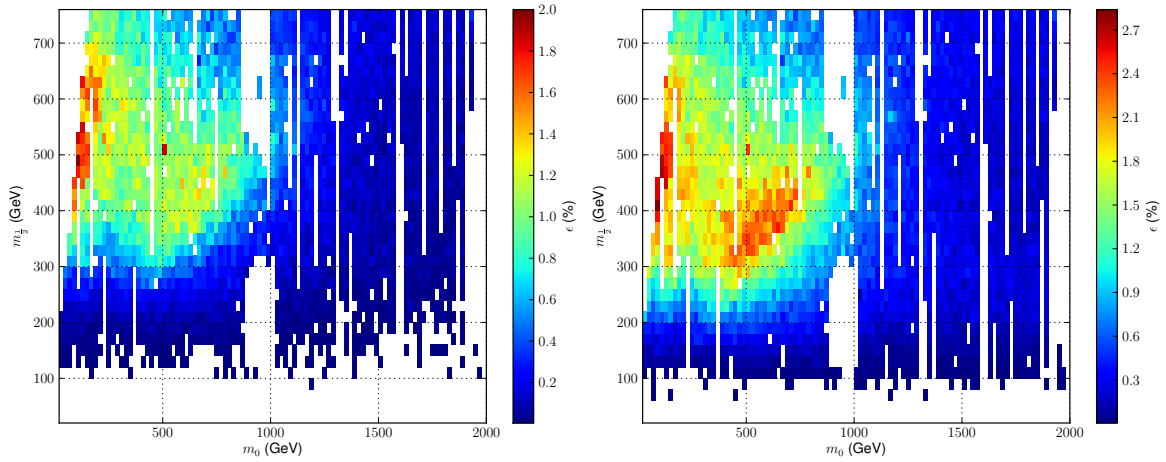

(c) $S_T^{\text{lep}} > 450$

(d) Total

Figure 8.5.: Signal efficiency for the electron channel in the CMSSM. The efficiency is shown separately for each S_T^{lep} bin and as a total. The efficiency is shown in the $(m_0, m_{\frac{1}{2}})$ plane with $\tan\beta = 10$, $A_0 = 0$ and $\mu > 0$.

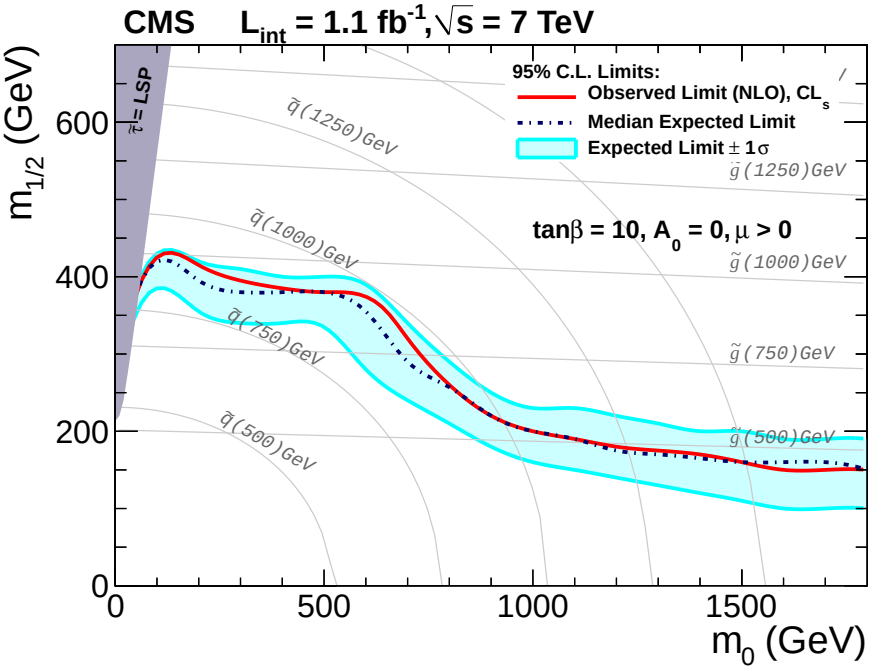

Figure 8.6.: 95% confidence level exclusion plot for the CMSSM. The observed (red), expected (blue dotted) and $\pm 1\sigma$ exclusion bands (light blue shaded) are shown. These are calculated using the CL_s method. Lines of constant squark and gluino mass are also shown.

8.4.1. The CMSSM

The CMSSM was previously described in Section 3.2.1. As explained, the CMSSM makes a number of somewhat arbitrary choices which restrict the SUSY topologies it is able to encompass. Whilst these make it relatively undesirable as a framework for theoretical interpretation, it is nonetheless useful as a common yardstick by which to compare experiments and searches.

The CMSSM results are presented as a 95% exclusion in a two-dimensional plane of the parameter space where the two mass parameters, m_0 and $m_{\frac{1}{2}}$, are allowed to vary. Other parameters are fixed as follows: $A_0 = 0$, $\tan\beta = 10$ and $\mu > 0$.

Technical Details

The likelihood function detailed in Section B.1 takes as input the signal efficiencies for each bin of S_T^{lep}. In the case of the CMSSM, these must be evaluated for each point in the $(m_0, m_{\frac{1}{2}})$-plane. These are evaluated using the same analysis procedure as used for

the data and SM MC samples. The CMSSM sample is produced using the PYTHIA event generator, with the two mass parameters varied independently in steps of 20 GeV to produce a grid. For each grid point, 10000 events are generated. Due to the large number of events, the detector response is simulated using the FASTSIM simulation package (see Section 4.3.7). This has been extensively validated and tuned against the full detector simulation and shown to give adequate results for many analyses.

Having evaluated the efficiencies per S_T^{lep} bin for each CMSSM grid point, the NLO cross-sections are calculated using the PROSPINO package [165] and SOFTSUSY is used to solve the renormalisation group equations [166]. The cross-sections are calculated individually for each SUSY subprocess and then combined according to the composition of the analysis selection. These are then input to the limit code, along with the required uncertainties and model-independent parameters.

Efficiencies

The efficiency per S_T^{lep} bin of the analysis selection as a function of the CMSSM parameter space is shown in Figures 8.4 and 8.5 for muons and electrons respectively. The "holes" in the CMSSM sample are due to incomplete data samples at the time of publication.

The efficiencies give a good indication of the sensitivity of the analysis to different regions of the parameter space. Firstly, it can be seen that regardless of the S_T^{lep} bin, significant efficiency is achieved only for values of $m_0 < 1000$ GeV. The correlation of S_T^{lep} and $m_{\frac{1}{2}}$ should also be noted - with the higher bins generally sensitive to larger values of $m_{\frac{1}{2}}$.

It should be noted that the areas of greatest signal efficiency appear to form two distinct regions, one at $m_0 \approx 100$ GeV, close to the stau LSP region, and the other at $m_0 \approx 500$ GeV. A possible explanation is that these correspond to scenarios in which either left or right-handed sleptons are dominantly produced.

Exclusion

For consistency with other SUSY searches at the LHC, a limit has been set using the CL_{s} method described in Section 8.2.3. Whilst it is possible to set an upper limit on the signal strength parameter, μ, this becomes highly computationally intensive. Instead, a simple exclusion is produced assuming NLO cross-sections. This is shown in Figure 8.6. All terms discussed in Appendix B.1 have been included. The expected limit and $\pm 1\sigma$

bands are evaluated by setting the observations for each bin to be exactly that predicted from data.

The exclusion seems to be well predicted by the efficiency maps, with significant exclusion on the $m_{\frac{1}{2}}$ axis only at low m_0. As can be seen, squark masses below ≈ 900 GeV and gluino masses below ≈ 500 GeV are excluded at 95% confidence.

8.4.2. Simplified Models

Technical Details

The simplified models described in Section 3.2.2 are simulated using the PYTHIA generator by reusing SUSY subprocesses. The mass parameters in each model are varied in steps. By varying the masses of the squark or gluino, LSP and other intermediate particles, a grid of simplified model points is created. These are then processed further as for the CMSSM.

For the simplified models shown here, the mother and daughter particle's masses (M_{gluino} or M_{stop} and M_{LSP}) are varied in steps of 25 GeV. Since the mother particle must be at least as massive as the daughter, half of the parameter space is unphysical and hence excluded.

To provide the most detailed interpretation of the simplified models, it is desirable to calculate an upper limit on the cross-section for each grid point. This can be contrasted to the case of the CMSSM, where the cross-section at each point is known and a simple exclusion contour is sufficient. Due to the computational difficulty of calculating a confidence interval using the CL_{s} method, the PL method has been used instead. In addition, further simplification of the likelihood is achieved by including a single nuisance parameter for the signal efficiency uncertainty. This is then assigned a conservative 25% uncertainty, constant across the model parameter space. This value is chosen by taking representative values of the E_T^{miss} scale and resolution uncertainties given in Table 8.1, for the CMSSM, and adding in quadrature with the 10% PDF uncertainty:

$$\sqrt{\underbrace{(10\%)^2}_{\text{PDF}} + \underbrace{(15\%)^2}_{\text{JES}} + \underbrace{(10\%)^2}_{E_T^{\text{miss}}\ \text{resolution}}} \approx 20\%.$$

For the following limit plots, holes in the sample have been filled by taking the average observed limit of surrounding points. A similar procedure has also been used to produce smooth exclusion contours.

T3W

For the T3W model, the intermediate mass state in the cascade decay introduces an additional mass parameter, $m_{\widetilde{\chi}^{\pm}}$. Of course, this parameter should lie somewhere between the mother and daughter particles' masses. To study a range of scenarios without having to consider the full three-dimensional volume of the parameter space, three scenarios are considered. Choosing values of the intermediate particle mass according to

$$M_{\chi} = xM_{\text{gluino}} + (1-x)M_{\text{LSP}}, \tag{8.3}$$

limits have been set for 3 values of the parameter x – 0.25, 0.5 and 0.75. Intuitively, these represent cases where the intermediate particle mass is closer to the daughter, intermediate between daughter and mother and closer to the mother respectively.

Figure 8.7 shows total efficiency as a function of $(M_{\text{gluino}}, M_{\text{LSP}})$ for each plane in x, separated by lepton channel. The efficiency is seen to decrease as the mother and daughter move closer in mass. When the mass splitting is small, less energy is available for hadronic and leptonic activity in the event, and thus the efficiency of the analysis cuts is reduced.

The observed limits for each value of x (0.25, 0.5 and 0.75) are shown in Figures 8.8, 8.9 and 8.10 respectively. The exclusion contours are compared to a reference cross-section for squark production calculated using Prospino assuming QCD-strength couplings. For $x = 0.25$ and an LSP mass of 200 GeV, gluino masses below 600 GeV are excluded. For $x = 0.5$, the same LSP mass yields an exclusion $M_{\text{gluino}} < 500$ GeV. For $x = 0.75$, the excluded region is $M_{\text{gluino}} < 450$ GeV.

For points where $M_{\text{gluino}} \approx M_{\text{LSP}}$, there is relatively little energy available in the cascade. This generally reduces the H_{T} present in the event, and consequently the efficiency. Events entering the sample in this region tend to be dominated by Initial State Radiation (ISR). The modelling of ISR in simulation has a significant associated uncertainty. For this reason, the region immediately below the diagonal has been excluded from the limit. This excluded range is chosen to remove regions where the upper limit appears to fluctuate at random. For $x = 0.50$ and $x = 0.75$, the region $M_{\text{gluino}} - M_{\text{LSP}} < 100$ GeV is excluded.

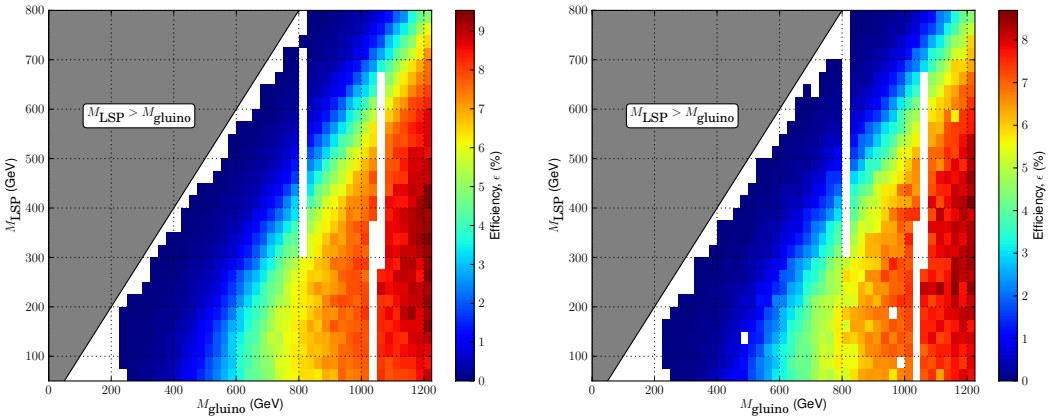

(a) μ, $x = 0.25$ **(b)** e, $x = 0.25$

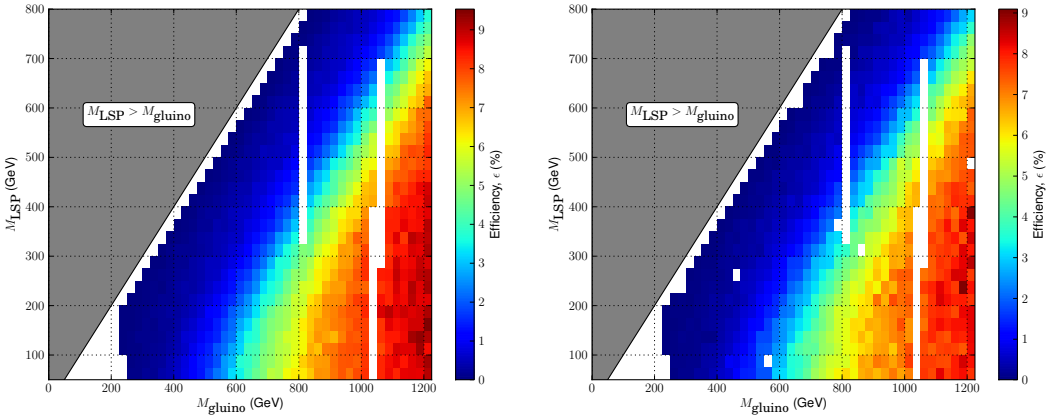

(c) μ, $x = 0.5$ **(d)** e, $x = 0.5$

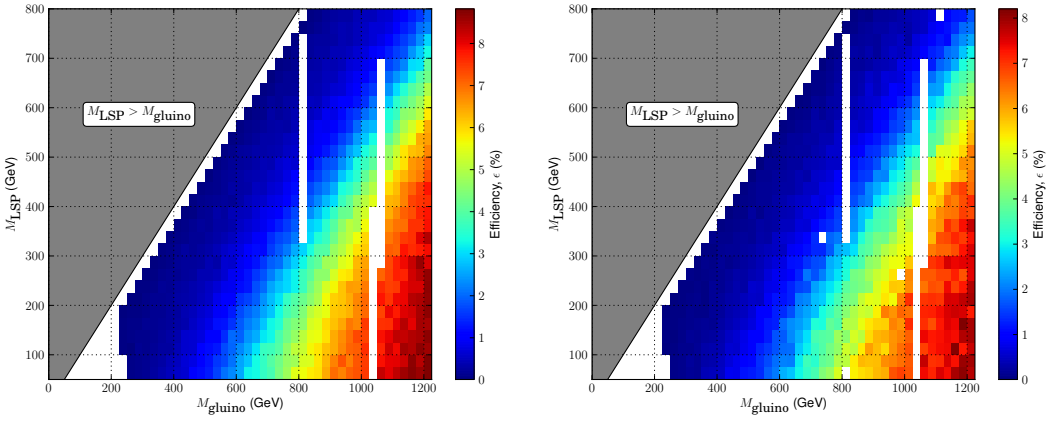

(e) μ, $x = 0.75$ **(f)** e, $x = 0.75$

Figure 8.7.: Plots of total signal efficiency for muon and electron channels in the T3W simplified model. Each plot shows efficiency as a function of $(M_{\text{gluino}}, M_{\text{LSP}})$ for a given value of M_{χ}.

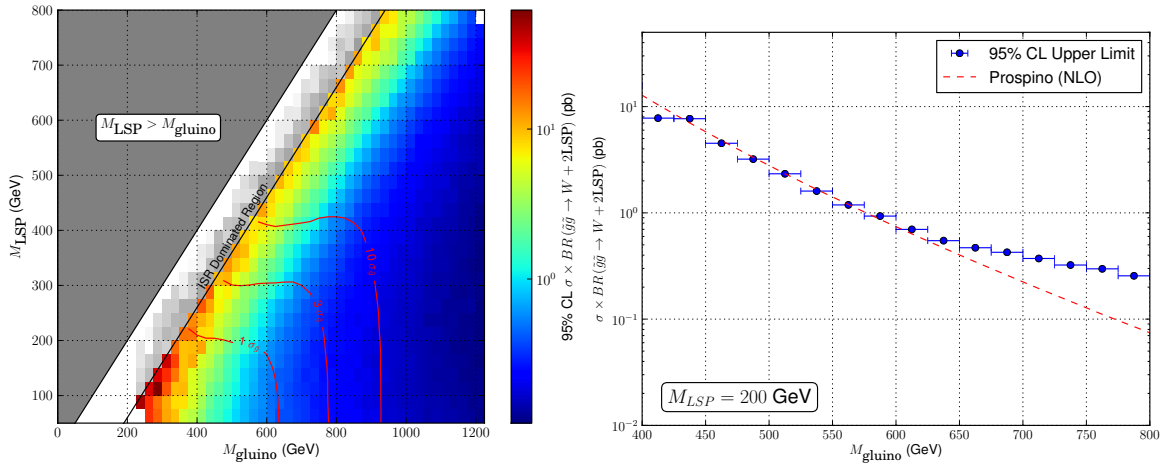

(a) **(b)**

Figure 8.8.: Limit in the T3W simplified model with M_χ set assuming $x = 0.25$. The 95% confidence level upper limit on the cross-section as a function of $(M_{\mathrm{gluino}}, M_{\mathrm{LSP}})$ is shown in (a). Overlayed are contours showing this exclusion in terms 1, 3 and 10 times the gluino cross-section predicted by QCD. Figure (b) shows the same upper limit as a function of M_{gluino} with $M_{\mathrm{LSP}} = 200$ GeV. Overlayed is the QCD cross-section for gluino production as a function of M_{gluino}.

For $x = 0.25$, M_χ is close to M_{LSP} and presumably the efficiency is more sensitive to the modelling of ISR. In this case, the region $M_{\mathrm{gluino}} - M_{\mathrm{LSP}} < 140$ GeV is ignored.

Comparing the exclusion contours, there does not appear to be a strong dependence on M_χ. But the reach of the search can be seen to improve slightly for lower values of x, when the mass splitting between the mother and the LSP is reasonably large. From Eqn. 8.3, these models have an intermediate particle with a mass closer to the LSP than to the mother. In such events, the W would be expected to be relatively soft and the jets from the cascade hard. With respect to the analysis selection, the efficiency of the H_{T} cut would be expected to increase. On the other hand, for a softer W, the S_T^{lep} efficiency may decrease due to the lower charged lepton momentum. Overall, the second effect is likely to be small since S_T^{lep} is likely to be dominated by the missing energy from the LSPs.

In the cases where the mass splitting between mother and LSP is smaller, models with M_χ close to M_{gluino} appear to give better exclusion. In these cases, one might guess that the harder W has a greater effect on the efficiency since there is less hadronic energy available from the cascade.

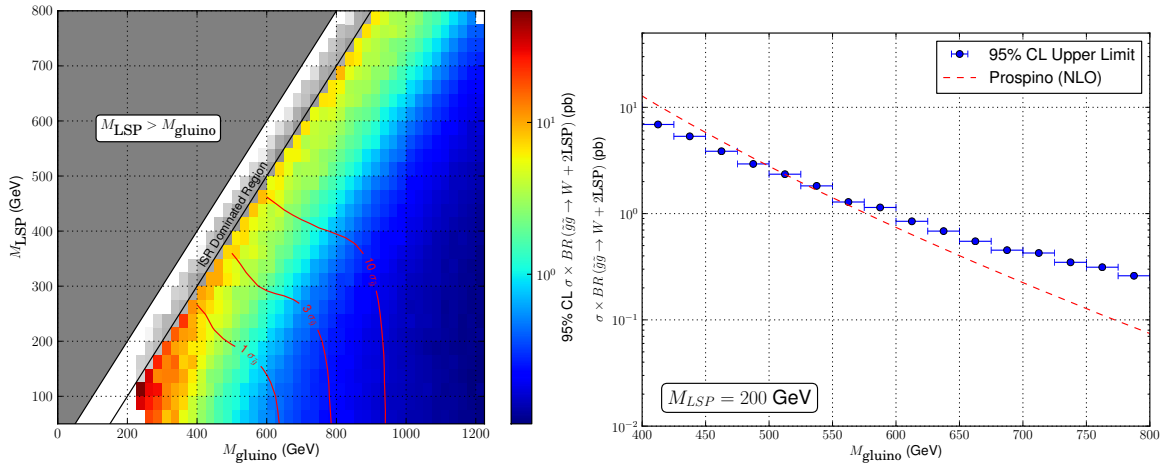

(a) **(b)**

Figure 8.9.: Limit in the T3W simplified model with M_χ set assuming $x = 0.5$. The 95% confidence level upper limit on the cross-section as a function of $(M_{\mathrm{gluino}}, M_{\mathrm{LSP}})$ is shown in (a). Overlayed are contours showing this exclusion in terms 1, 3 and 10 times the gluino cross-section predicted by QCD. Figure (b) shows the same upper limit as a function of M_{gluino} with $M_{\mathrm{LSP}} = 200$ GeV. Overlayed is the QCD cross-section for gluino production as a function of M_{gluino}.

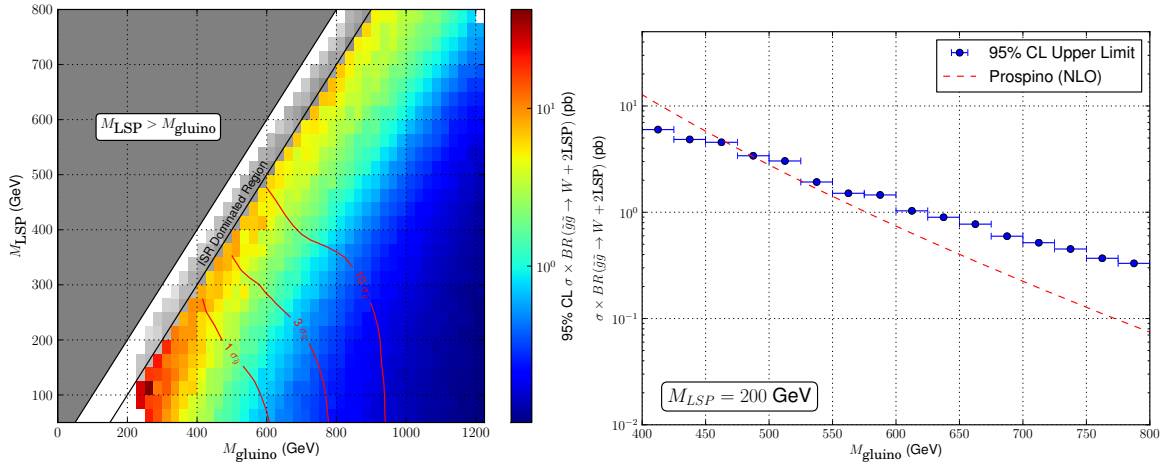

(a) **(b)**

Figure 8.10.: Limit in the T3W simplified model with M_χ set assuming $x = 0.75$. The 95% confidence level upper limit on the cross-section as a function of $(M_{\mathrm{gluino}}, M_{\mathrm{LSP}})$ is shown in (a). Overlayed are contours showing this exclusion in terms 1, 3 and 10 times the gluino cross-section predicted by QCD. Figure (b) shows the same upper limit as a function of M_{gluino} with $M_{\mathrm{LSP}} = 200$ GeV. Overlayed is the QCD cross-section for gluino production as a function of M_{gluino}.

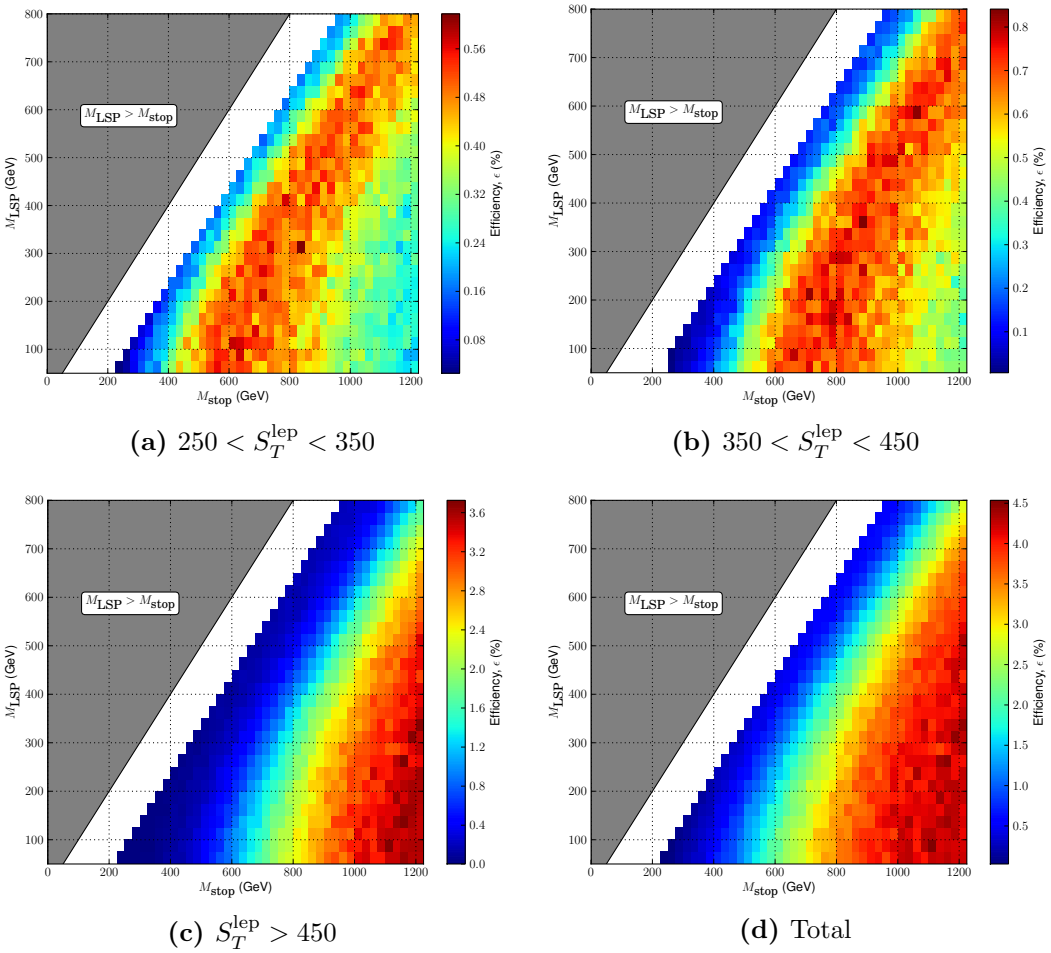

(a) $250 < S_T^{\text{lep}} < 350$ **(b)** $350 < S_T^{\text{lep}} < 450$

(c) $S_T^{\text{lep}} > 450$ **(d)** Total

Figure 8.11.: Signal efficiency maps for the muon channel in the T2tt simplified model. Efficiency is shown as a function of $(M_{\text{stop}}, M_{\text{LSP}})$ for each S_T^{lep} bin and for the total across all three bins.

T2tt

The T2tt model, as previously discussed, is of theoretical interest for describing SUSY theories with light stop squarks.

Efficiencies for each point in the $(M_{\text{stop}}, M_{\text{LSP}})$ plane are shown in Figures 8.11 and 8.12 for muons and electrons respectively. Efficiencies are shown per S_T^{lep} bin in order to gauge the effect of this cut on the efficiency.

The observed limit is shown in a similar fashion to the T3W case in Figure 8.13. It can be seen that no exclusion is possible with respect to the stop cross-section predicted by QCD. It is possible that a dedicated search using B-tagged jets would provide significantly improved sensitivity.

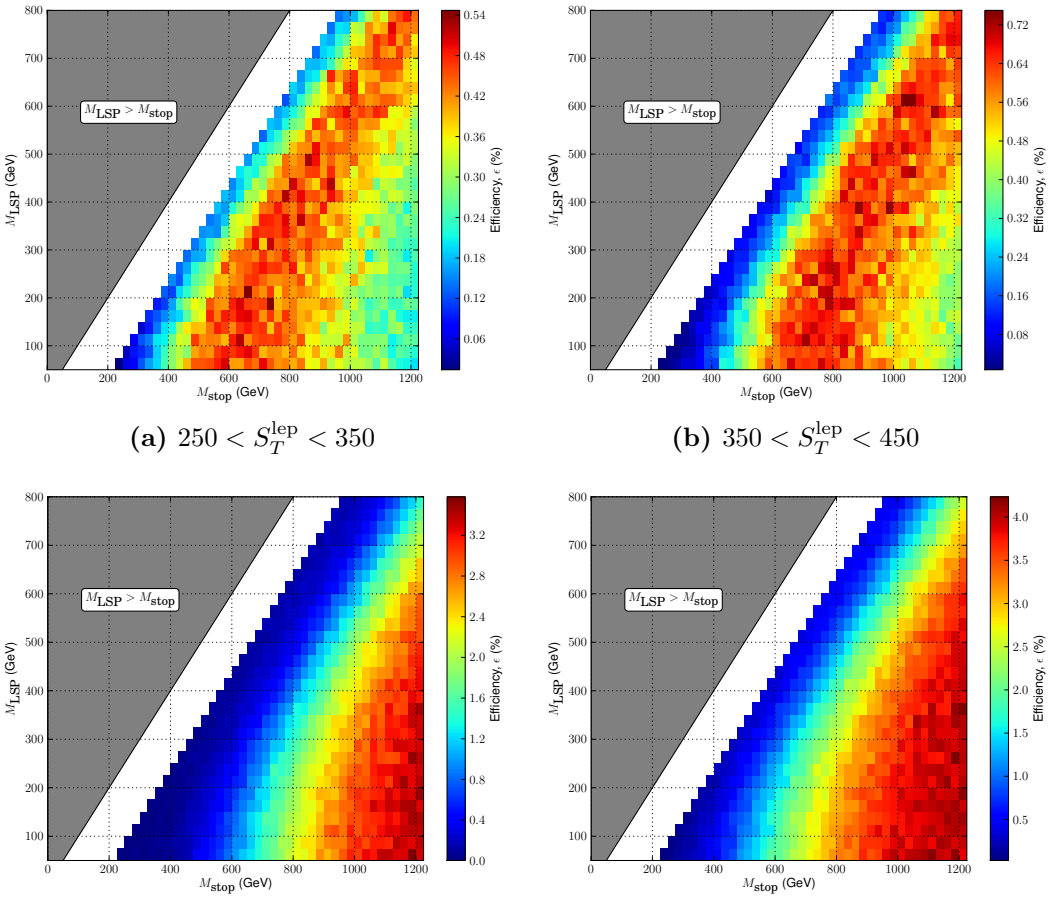

(a) $250 < S_T^{\text{lep}} < 350$ **(b)** $350 < S_T^{\text{lep}} < 450$

(c) $S_T^{\text{lep}} > 450$ **(d)** Total

Figure 8.12.: Signal efficiency maps for the electron channel in the T2tt simplified model. Efficiency is shown as a function of $(M_{\text{stop}}, M_{\text{LSP}})$ for each S_T^{lep} bin and for the total across all three bins.

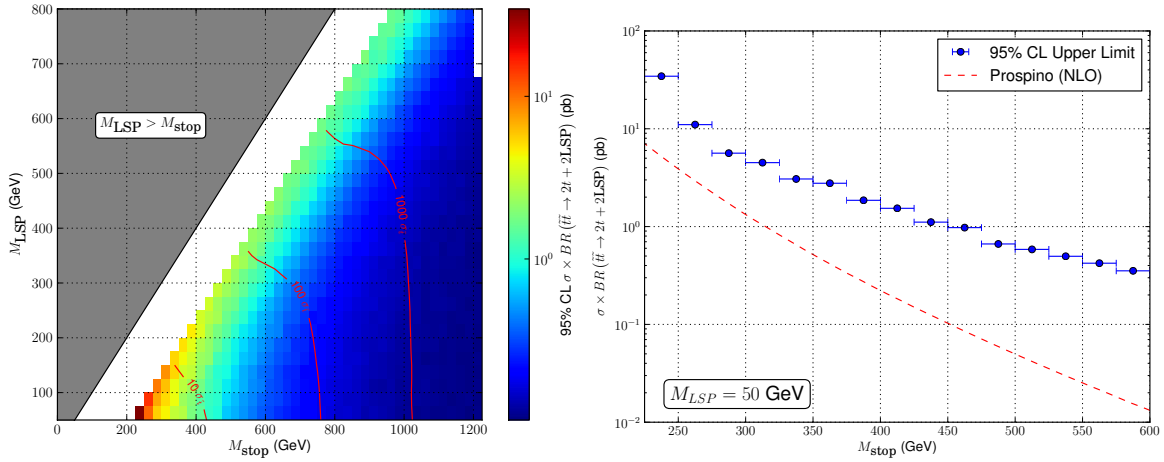

(a) **(b)**

Figure 8.13.: Limit in the T2tt simplified model. The 95% confidence level upper limit on the cross-section as a function of $(M_{\text{stop}}, M_{\text{LSP}})$ is shown in (a). The overlayed contours show this exclusion in terms of 1, 10 and 1000 times the stop production cross-section predicted by QCD. The upper limit is shown as a function of M_{stop} in (b) for $M_{\text{LSP}} = 50$ GeV. Overlayed is the QCD cross-section for stop production as a function of M_{stop}.

8.5. Summary

The single lepton SUSY search detailed in Chapter 7 has been interpreted within the context of several models. A likelihood function has been developed which embodies all significant statistical and systematic uncertainties. The CL_{s} procedure has been used to calculate an excluded region in the CMSSM. The single lepton SUSY search is seen to exclude a significant portion of the parameter space.

Additionally, two simplified models have been investigated: T3W and T2tt. The PL method has been used to set an upper limit as a function of the model parameter space in each case. This has also been compared to a cross-section calculation assuming QCD-strength coupling. In the T3W case, significant regions of the parameter space have been excluded. The T2tt model is of theoretical interest from the perspective of SUSY models containing a light stop squark. In this case, the sensitivity of this particular analysis is seen to be limited. Sensitivity could be enhanced with the addition of b-tagged jets to the analysis. This could be an interesting avenue for future study.

Conclusion

As described in the introduction, the overall theme of this work has been the search for some sign of physics beyond the SM. More specifically, a search for SUSY or SUSY-like theories which predict the existence of a heavy, stable WIMP. As was seen, these theories are attractive for a number of reasons, not least that they provide an answer to the dark matter problem described in Chapter 2.

The search for new physics was inspired by a previous measurement undertaken using data taken at CMS during 2010. This sought to measure the polarisation of W bosons with large transverse momentum at the LHC. An enriched sample of $\mathrm{W} \longrightarrow \ell\nu$ events with large transverse momentum was selected from 36 pb^{-1} of data.

The L_{P} variable was devised to probe the $\cos\theta^*$ distribution of the W boson. Shape templates in this variable were constructed from simulated $\mathrm{W} \longrightarrow \ell\nu$ events. Each gives the shape of L_{P} for left-handed, right-handed and longitudinally polarised W bosons. With the inclusion of appropriate templates for the remaining background processes, the helicity fractions have been extracted via a binned maximum likelihood fit. The results are expressed as the difference between the left-handed and right-handed helicity fractions, $(f_{\mathrm{L}} - f_{\mathrm{R}})$, and the longitudinal polarisation, f_0.

Independent measurements were performed for each lepton charge and flavour. A combined measurement has also been performed using both lepton channels. These confirm the existence of a novel effect at the LHC - namely that the left-handed polarisation states come to dominate over the right-handed at large P_T^{W}. Furthermore the values of $(f_{\mathrm{L}} - f_{\mathrm{R}})$ and f_0 appear to agree, within uncertainties, with theoretical predictions [60].

In addition to being a useful and novel confirmation of the SM, the W polarisation measurement provides a powerful set of techniques for undertaking a SUSY search in events containing a missing transverse energy, jets and a single lepton.

The L_{P} variable from the W polarisation analysis is used to discriminate SUSY events from SM backgrounds. An additional variable, S_T^{lep} is used to parameterise the scale of

the interaction. A search has been performed with 1.1 fb^{-1} of data at CMS. No excess over expected SM backgrounds has been observed.

Finally, this null observation has been used to set limits in a number of NP models. For this, considerable effort was invested in constructing a suitable likelihood model capturing all statistical and systematic effects. Within the context of the CMSSM – a standard benchmark for SUSY searches – squark masses below ≈ 900 GeV and gluino masses below ≈ 500 GeV have been excluded at 95% confidence.

In addition to the CMSSM exclusion, two simplified models were selected - T3W and T2tt. The T3W model considers events arising from pair-production of a gluino type particle which then decay to the LSP via an intermediate particle. Limits in the T3W model exclude the parameter space $M_{\text{gluino}} < 600$ GeV, $M_{\text{LSP}} < 200$ GeV when the mass of the intermediate particle is close to that of the LSP. This assumes a gluino production cross-section with QCD strength couplings. These limits are seen to vary only slightly with the mass of the intermediate particle.

The T2tt model considers events initiated by pair production of stop squarks (or similar), both decaying directly to the LSP. This is inspired by theoretically appealing SUSY models in which the stop is light. Whilst an upper limit on the cross-section is set, no exclusion is possible with respect to that predicted by QCD.

In summary, a precision measurement of the SM has been performed in addition to a search for new physics. Whilst new light has been shed on well-known physics, no statistically significant deviation or excess has been observed.

Appendix A.

Kinematics

A Lorentz transformation can be written as

$$\begin{pmatrix} E' \\ p'_{\parallel} \end{pmatrix} = \begin{pmatrix} \gamma & -\gamma\beta \\ -\gamma\beta & \gamma \end{pmatrix} \begin{pmatrix} E \\ p_{\parallel} \end{pmatrix}, \tag{A.1}$$

and

$$p'_{\perp} = p_{\perp}, \tag{A.2}$$

where γ is the Lorentz factor and $\beta = v/c$ [29].

Boosting from a particle's rest frame into the lab frame,

$$\begin{pmatrix} E \\ P \end{pmatrix} = \begin{pmatrix} \gamma & -\gamma\beta \\ -\gamma\beta & \gamma \end{pmatrix} \begin{pmatrix} M \\ 0 \end{pmatrix}, \tag{A.3}$$

and so

$$\begin{aligned} E &= \gamma M \Longrightarrow \gamma = \frac{E}{M} \\ |P| &= \gamma\beta M \Longrightarrow \beta = \frac{|P|}{\gamma M} = \frac{|P|}{E}. \end{aligned}$$

Also,

$$\begin{aligned}\gamma &= \frac{\sqrt{|P|^2 + M^2}}{M} \\ &= \sqrt{1 + \left(\frac{|P|}{M}\right)^2}.\end{aligned}$$

Appendix B.

Statistics

B.1. Modelling the Single Lepton Analysis

As suggested in Chapter 8, the core component of many statistical interpretations is the construction of an appropriate likelihood function. The likelihood must model all statistical and systematic effects and is thus highly dependent on the experiment. The situation is considerably complicated when shape information is included, for which relevant bin-to-bin correlations must be evaluated.

B.1.1. Notation

It will be helpful to define some notation. In the following, a subscript index is assumed to run over the binned variable in the analysis (i.e. S_T^{lep} bins). The notation $\nu^{(\alpha)}$ denotes one or more nuisance parameters, where the superscript is taken to represent either a set of uncertainties or a single (unspecified) uncertainty. When referring to a particular uncertainty, for instance the JES uncertainty, the associated nuisance parameter will be written simply ν^{jes}. Certain variables x are known to have a functional dependence on a given nuisance parameter and are written $x(\nu)$. The nominal value of this variable, being that which is measured in MC or in real data is denoted $\bar{x}$.

B.1.2. The Likelihood Function

In constructing the likelihood, we start by writing down the number of events expected for each bin:

$$N_i^{\text{exp}} = N_i^{\text{sig}}(\mu, \nu^{(\text{sig})}) + N_i^{\text{bkg}}(\nu^{(\text{bkg})}),$$

where N_i^{sig} is the expected signal yield for a chosen signal model and N_i^{bkg} is the data-driven background prediction. As can be seen, the signal yield is a function of the parameter of interest (poi), μ and a number of nuisance parameters, $\nu^{(\text{sig})}$. These represent the set of systematic uncertainties relevant to the signal yield. Ignoring signal contamination effects (which will be discussed later), the background yield depends only on the nuisance parameters, $\nu^{(\text{bkg})}$. These represent uncertainties affecting the background yield. Certain uncertainties will affect both signal and background yields and thus will be present in both sets.

Without giving an explicit functional form for the signal yield and background prediction, the form of the likelihood function may be constructed. The likelihood must include the following terms.

1. Statistical terms representing the likelihood of observing some number of events given a certain expectation for the signal and background yields.
2. Terms providing prior constraints on the various nuisance parameters. Certain uncertainties are statistical in nature and thus, independent nuisance parameters are assigned per bin along with a corresponding prior probability distribution function (pdf). In other cases, the underlying systematic variation is considered to have a 100% correlated effect across the bins. In these cases, a single nuisance parameter and prior pdf is assigned.

The form of the likelihood is as follows,

$$\mathcal{L} = \prod_i \mathcal{P}(N_i^{\text{exp}}; N_i^{\text{obs}}) \prod_\theta X_\theta(\nu^{(\theta)}),$$

where:

- $\mathcal{P}(\mu; x)$ denotes a Poisson distribution with mean μ and value x and
- $X_\theta(\nu^{(\theta)})$ represents some prior pdf associated with each systematic uncertainty θ.

B.1.3. The Signal Yield

The signal yield per bin is constructed as follows:

$$N_i^{\text{sig}} = \mu \times \epsilon_i(\nu^{(\text{sig})}) \times \sigma \times L \times \nu^{\text{lumi}},$$

where:

- $\epsilon_i(\nu^{(\text{sig})})$ is the efficiency of the ith bin, assumed to be dependent on a set of nuisance parameters $\nu^{(\text{sig})}$;
- σ is the cross-section of the signal model being considered;
- L is the integrated luminosity and
- ν^{lumi} is a nuisance parameter associated with uncertainty in the estimate of the integrated luminosity.

The poi, μ then represents the ratio of the cross-section being considered to the cross-section of the chosen model, σ. Note that for the simplified model limits, the parameter σ was set to 1 and therefore the poi itself represents a cross-section.

B.1.4. Background Prediction

The background prediction per bin is then written as

$$N_i^{\text{bkg}} = R_i^{\text{CS}}(\nu_i^{(\alpha)}, \nu^{(\beta)}) \times N_i^{\text{control}}(\nu_i^{(\gamma)}),$$

where:

- R_i^{CS} is the translation factor as defined in Eqn. 7.1 (excluding contributions from QCD processes);
- the nuisance parameters $\nu_i^{(\alpha)}$ and $\nu_i^{(\gamma)}$ represent statistical uncertainties uncorrelated between the bins;
- the nuisance parameters $\nu^{(\beta)}$ represent systematic uncertainties assumed to be 100% correlated across the bins and
- N_i^{control} the number of EWK events observed in the control region ($L_{\text{P}} > 0.3$)

B.1.5. Parameterising Systematic Uncertainties

In reality, it is almost always impossible to obtain a full functional form for a variable x (e.g. R_i^{CS}, N_i^{control}) in terms of a set of nuisance parameters $\nu^{(\alpha)}$. Writing the Taylor expansion of $x(\nu^{(\alpha)})$ for two terms to second order, one obtains:

$$x(\nu^{(A)},\nu^{(B)})\Big|_{\substack{\nu^{(A)}=a\\ \nu^{(B)}=b}} \approx x(a,b) + (\nu^{(A)}-a)\left.\frac{\partial x}{\partial \nu^{(A)}}\right|_{\nu^{(A)}=a} + (\nu^{(B)}-b)\left.\frac{\partial x}{\partial \nu^{(B)}}\right|_{\nu^{(B)}=b} +$$
$$\frac{1}{2!}\left[(\nu^{(A)}-a)^2\frac{\partial^2 x}{\partial\left(\nu^{(A)}\right)^2} + (\nu^{(B)}-b)^2\frac{\partial^2 x}{\partial\left(\nu^{(B)}\right)^2} + 2(\nu^{(A)}-a)(\nu^{(B)}-b)\frac{\partial^2 x}{\partial\nu^{(A)}\partial\nu^{(B)}}\right].$$

Assuming the expansion is performed with respect to the mean of x, $\bar{x}$, the values of a and b are seen to be the mean values of the corresponding nuisance parameters. For small deviations from the mean,

$$(\nu^{(A)}-a) \sim (\nu^{(B)}-b) \sim \epsilon \longrightarrow 0,$$

and ignoring terms $O(\epsilon^2)$,

$$x(\nu^{(A)},\nu^{(B)}) \approx \bar{x} + (\nu^{(A)}-a)\left.\frac{\partial x}{\partial \nu^{(A)}}\right|_{\nu^{(A)}=a} + (\nu^{(B)}-b)\left.\frac{\partial x}{\partial \nu^{(B)}}\right|_{\nu^{(B)}=b}. \tag{B.1}$$

Since the derivatives in Eqn. B.1 will in practice be derived from some finite variation of the underlying quantity associated with each nuisance parameter, the infinitesimal derivatives must be replaced by finite changes. It is also sensible to set $a = b = 0$,

$$x(\nu^{(A)},\nu^{(B)}) \approx \bar{x} + \nu^{(A)}\frac{\Delta x}{\Delta\nu^{(A)}} + \nu^{(B)}\frac{\Delta x}{\Delta\nu^{(B)}}. \tag{B.2}$$

Since the value of x is often associated with a physical quantity, such as an efficiency or an event yield, it is desirable to constrain it to take on only positive values. This can be achieved providing the range of each nuisance parameter is set such that,

$$\nu^{(\alpha)} \times \frac{\Delta x}{\Delta\nu^{(\alpha)}} < \bar{x}.$$

The previous derivation can be simply extended to $N > 2$ nuisance parameters. Generalising and rewriting Eqn. B.2,

$$\begin{aligned} x(\nu^{(A)}, \nu^{(B)}, \ldots) &\approx \bar{x} + \nu^{(A)} \frac{\Delta x}{\Delta \nu^{(A)}} + \nu^{(B)} \frac{\Delta x}{\Delta \nu^{(B)}} + \ldots \\ &\approx \frac{1}{\bar{x}^{N-1}} \left\{ \bar{x}^N + \bar{x}^{N-1} \nu^{(A)} \frac{\Delta x}{\Delta \nu^{(A)}} + \bar{x}^{N-1} \nu^{(B)} \frac{\Delta x}{\Delta \nu^{(B)}} + \ldots \right\}. \end{aligned}$$

If we attempt to rewrite as a product,

$$\begin{aligned} \prod_{\theta=A,B,\ldots} \left(\bar{x} + \frac{\Delta x}{\Delta \nu^{(\theta)}} \right) &= \bar{x}^N + \bar{x}^{N-1} \sum_{\alpha=A,B,\ldots} \nu^{(\alpha)} \frac{\Delta x}{\Delta \nu^{(\alpha)}} \\ &\quad + \bar{x}^{N-2} \sum_{\alpha=A,B,\ldots} \sum_{\beta=A,B,\ldots} \nu^{(\alpha)} \nu^{(\beta)} \frac{\Delta x}{\Delta \nu^{(\alpha)}} \frac{\Delta x}{\Delta \nu^{(\beta)}} \\ &\quad + \ldots + O(\nu^N). \end{aligned}$$

Ignoring terms greater than $O(\nu^2)$,

$$\begin{aligned} \prod_{\theta=A,B,\ldots} \left(\bar{x} + \frac{\Delta x}{\Delta \nu^{(\theta)}} \right) &\approx \bar{x}^N + \bar{x}^{N-1} \sum_{\alpha=A,B,\ldots} \nu^{(\alpha)} \frac{\Delta x}{\Delta \nu^{(\alpha)}} \\ &\approx \bar{x}^{N-1} x(\nu^{(A)}, \nu^{(B)}, \ldots), \end{aligned}$$

and therefore we find

$$x(\nu^{(A)}, \nu^{(B)}, \ldots) \approx \frac{1}{\bar{x}^{N-1}} \prod_{\alpha=A,B,\ldots} \left(\bar{x} + \frac{\Delta x}{\Delta \nu^{(\alpha)}} \right) \approx \bar{x} \prod_{\alpha=A,B,\ldots} \frac{1}{\bar{x}} \left(\bar{x} + \frac{\Delta x}{\Delta \nu^{(\alpha)}} \right). \quad \text{(B.3)}$$

Using Eqn. B.3, the signal yield can be rewritten as follows:

$$N_i^{\text{sig}} = \mu \times \bar{\epsilon}_i \times \prod_{\alpha} \left(\frac{\bar{\epsilon}_i + \nu^{(\alpha)} \frac{\Delta \epsilon_i}{\Delta \nu^{(\alpha)}}}{\bar{\epsilon}_i} \right) \sigma \times L \times \nu^{\text{lumi}},$$

and the background prediction,

$$N_i^{\text{bkg}} = \bar{R}_i^{\text{CS}} \times \prod_{\alpha} \left(\frac{\bar{R}_i^{\text{CS}} + \nu^{(\alpha)} \frac{\Delta R_i^{\text{CS}}}{\Delta \nu^{(\alpha)}}}{\bar{R}_i^{\text{CS}}} \right) \times \bar{N}_i^{\text{control}} \times \prod_{\beta} \left(\frac{\bar{N}_i^{\text{control}} + \nu^{(\beta)} \frac{\Delta N_i^{\text{control}}}{\Delta \nu^{(\beta)}}}{\bar{N}_i^{\text{control}}} \right).$$

B.1.6. Nuisance Parameters

The nuisance parameters incorporated in the model described thus far are of two types.

1. Statistical uncertainties assumed to be uncorrelated across analysis bins. This includes uncertainties arising from the limited statistical precision of the MC sample and limited data in the control region.

2. Systematic uncertainties arising from detector artefacts or theoretical uncertainties such as the JES, standard model cross-section calculations and the luminosity measurement [167].

For uncertainties of the first kind, independent nuisance parameters must be included for each analysis bin. For uncertainties of the second kind, a single nuisance parameter will be included for all bins – giving the desired correlation. A full list of the nuisance parameters used is shown in Table B.1. For the work presented here, Gaussian prior distributions have been assigned for all nuisance parameters.

Table B.1.: Summary of nuisance parameters included in the single lepton likelihood function.

Uncertainty	Correlated	N_i^{sig}	R_i^{CS}	N_i^{control}	Nuisance Parameters
Luminosity	✓	✓			ν^{lumi}
Jet Energy Scale (JES)	✓	✓	✓	[c]	ν^{jes}
E_T^{miss} Resolution	✓	✓	✓	[c]	ν^{metres}
W/t $\bar{\text{t}}$ Ratio	✓		✓		$\nu^{W\text{t}\bar{\text{t}}}$
W Polarisation	✓		✓		$\nu^{\text{W pol}}$
Muon Momentum Scale[a]	✓		✓		ν^{lep}
Limited MC Statistics			✓		ν_i^{MC}
Limited Data Statistics				✓	ν_i^{data}
Signal Contamination	[d]			✓	$\nu_i^{\text{sig cont}}$
PDF Uncertainties	✓	✓			ν_i^{pdf}
QCD Background Prediction[b]				✓	ν_i^{qcd}

[a] Muon channel only

[b] Electron channel only

[c] In the electron channel, the use of MC templates in the QCD background estimate introduces a dependence on the JES. Whilst the ability to include these correlations was added to the statistics package, it was not used in the results shown.

[d] The signal contamination nuisance parameters are correlated in the sense that they are related to the signal strength. For further details, see Section B.1.7.

An additional nuisance parameter reflecting signal contamination in the control region requires a more careful choice of likelihood terms. This is described in the next section.

B.1.7. Signal Contamination

It can be seen in Figure 7.1 that the region $L_{\rm P} > 0.3$ may have a substantial component of SUSY events. This depends on the particular model under consideration. Signal contamination increases $N^{\rm control}$ leading to an over-prediction of $N^{\rm bkg}$. To account for this, the $N_i^{\rm bkg}$ term is modified to reflect the assumption that some fraction of the yield, $N_i^{\rm control}$, will be due to SUSY contamination. Rewriting,

$$N_i^{\rm bkg}(\mu,\nu^{(\alpha)}) = \bar{R}_i^{\rm CS} \times \prod_{\alpha}\left(\frac{\bar{R}_i^{\rm CS} + \nu^{(\alpha)}\frac{\Delta R_i^{\rm CS}}{\Delta\nu^{(\alpha)}}}{\bar{R}_i^{\rm CS}}\right) \times \bar{N}_i^{\rm control} \times f_i^{\rm SM}(\mu) \times \prod_{\beta}\left(\frac{\bar{N}_i^{\rm control} + \nu^{(\beta)}\frac{\Delta N_i^{\rm control}}{\Delta\nu^{(\beta)}}}{\bar{N}_i^{\rm control}}\right), \tag{B.4}$$

where $f_i^{\rm SM}$ represents the fraction of $N_i^{\rm control}$ expected due to SM processes given the current signal hypothesis i.e.

$$f_i^{\rm SM}(\mu) = \frac{N_i^{\rm SM}}{N_i^{\rm SM} + N_i^{\rm SUSY}(\mu)}.$$

The expected number of SUSY events $N_i^{\rm SUSY} = \mu \times \epsilon_i^{\rm control} \times \sigma \times L$ where $\epsilon_i^{\rm control}$ is the efficiency calculated for SUSY events entering the $L_{\rm P} > 0.3$ control region. To reflect these constraints, we set up an appropriate prior distribution,

$$X(\nu^{\rm SM}) = \mathcal{G}\left(\frac{N_i^{\rm SM}}{N_i^{\rm SM} + \mu \times \epsilon_i^{\rm control} \times \sigma \times L}; \nu^{\rm SM}\right),$$

and $f_i^{\rm SM} \equiv \nu_i^{\rm SM}$. Calculating the expected value of the nuisance parameter,

$$\begin{aligned} < f_i^{\rm SM} > &= \frac{N_i^{\rm SM}}{N_i^{\rm SM} + \mu N_i^{\rm SUSY}} \\ &= \frac{1}{1 + \mu\frac{N_i^{\rm SUSY}}{N_i^{\rm SM}}}. \end{aligned} \tag{B.5}$$

Technical problems associated with adding a functional dependence on the poi, μ, to the mean of the prior distribution necessitate a slightly altered formulation. As will be shown, this formulation is approximately equivalent given certain assumptions about the range of μ and the degree of signal contamination. The prior distribution included in $\mathcal{L}$ is rewritten as

$$X(\nu_i^{\mathrm{SM}}) = \mathcal{G}\left(\frac{N_i^{\mathrm{SM}}}{N_i^{\mathrm{SM}} + \epsilon_i^{\mathrm{control}} \times \sigma \times L}; \nu_i^{\mathrm{SM}}\right).$$

The term included in the background prediction (Eqn. B.4) is modified to

$$f_i^{\mathrm{SM}} = 1 - \mu \times \left(1 - \nu_i^{\mathrm{SM}}\right).$$

It can be seen that for $\mu = 0$, $f_i^{\mathrm{SM}} = 1$ and for $\mu = 1$, $f_i^{\mathrm{SM}} = \nu_i^{\mathrm{SM}}$ as required. It will now be shown that for a suitable range of μ and for small values of $N_i^{\mathrm{SUSY}}/N_i^{\mathrm{control}}$, the expectation value of f_i^{SM} will be equivalent to Eqn. B.5:

$$\begin{aligned}
< f_i^{\mathrm{SM}} > &= 1 - \mu \times \left(1 - < \nu^{\mathrm{SM}} >\right) \\
&= 1 - \mu + \mu \frac{N_i^{\mathrm{SM}}}{N_i^{\mathrm{SM}} + N_i^{\mathrm{SUSY}}} \\
&= \frac{(1-\mu)\left(N_i^{\mathrm{SM}} + N_i^{\mathrm{SUSY}}\right) + \mu N_i^{\mathrm{SM}}}{N_i^{\mathrm{SM}} + N_i^{\mathrm{SUSY}}} \\
&= \frac{N_i^{\mathrm{SM}} + (1-\mu) N_i^{\mathrm{SUSY}}}{N_i^{\mathrm{SM}} + N_i^{\mathrm{SUSY}}} \\
&= \frac{N_i^{\mathrm{SM}}\left(1 + (1-\mu)\frac{N_i^{\mathrm{SUSY}}}{N_i^{\mathrm{SM}}}\right)}{N_i^{\mathrm{SM}} + N_i^{\mathrm{SUSY}}} \\
&= \frac{N_i^{\mathrm{SM}}}{(N_i^{\mathrm{SM}} + N_i^{\mathrm{SUSY}})\left(1 + (1-\mu)\frac{N_i^{\mathrm{SUSY}}}{N_i^{\mathrm{SM}}}\right)^{-1}} \\
&\approx \frac{N_i^{\mathrm{SM}}}{(N_i^{\mathrm{SM}} + N_i^{\mathrm{SUSY}})\left(1 - (1-\mu)\frac{N_i^{\mathrm{SUSY}}}{N_i^{\mathrm{SM}}}\right)} \\
&= \frac{N_i^{\mathrm{SM}}}{N_i^{\mathrm{SM}} + \mu N_i^{\mathrm{SUSY}} - (1-\mu)\frac{N_i^{\mathrm{SUSY}^2}}{N_i^{\mathrm{SM}}}} \\
&= \frac{1}{1 + \mu\frac{N_i^{\mathrm{SUSY}}}{N_i^{\mathrm{SM}}} - (1-\mu)\left(\frac{N_i^{\mathrm{SUSY}}}{N_i^{\mathrm{SM}}}\right)^2} \\
&\approx \frac{1}{1 + \mu\frac{N_i^{\mathrm{SUSY}}}{N_i^{\mathrm{SM}}}}
\end{aligned}$$

as required.

B.1.8. Uncertainties on N_i^{control}

The dominant systematic uncertainty relating to the $L_{\text{P}} > 0.3$ region yield arises from the limited number of events in the sample. This is especially true at high S_T^{lep}. Accordingly, a nuisance parameter is added to the likelihood and assigned a Gaussian prior with a width derived assuming a Poisson uncertainty on the N_i^{control} yield.

An additional complication arises in the case of the electron channel, where the $L_{\text{P}} > 0.3$ region has a non-negligible component of QCD events. These are unreliably modelled by event generators and thus not included in the calculation of R_i^{CS}. This additional contribution to N_i^{control} would again lead to an over-prediction of the background. To correct this, an additional factor is included in Equation B.4, f_i^{ewk}, derived from the results of the QCD fit detailed in Section 7.8.2. The uncertainty derived from the fit procedure is modelled as a Gaussian prior on an additional nuisance parameter, ν_i^{QCD}. It has been assumed, and confirmed by the results of the fit in data, that the region $L_{\text{P}} < 0.15$ is "QCD free".

The uncertainty included via the prior distribution of ν^{QCD} is the quadrature sum of the statistical uncertainty from the fitting procedure and an uncertainty accounting for the finite number of MC events used to construct the fit templates. Additional errors coming from the JES uncertainty and missing energy resolution are found to be small. Proper inclusion of these into the likelihood would need to ensure correlation with the nuisance parameters representing these uncertainties. The relevant terms were set up but not included in the final calculations.

B.2. Validation Plots

Additional validation plots for the CMSSM point $(m_0, m_{\frac{1}{2}}) = (80, 240)$ are shown in Figures B.1 and B.2. This is a point far below the edge of the excluded region. They are otherwise identical to the plots shown in Section 8.3.2.

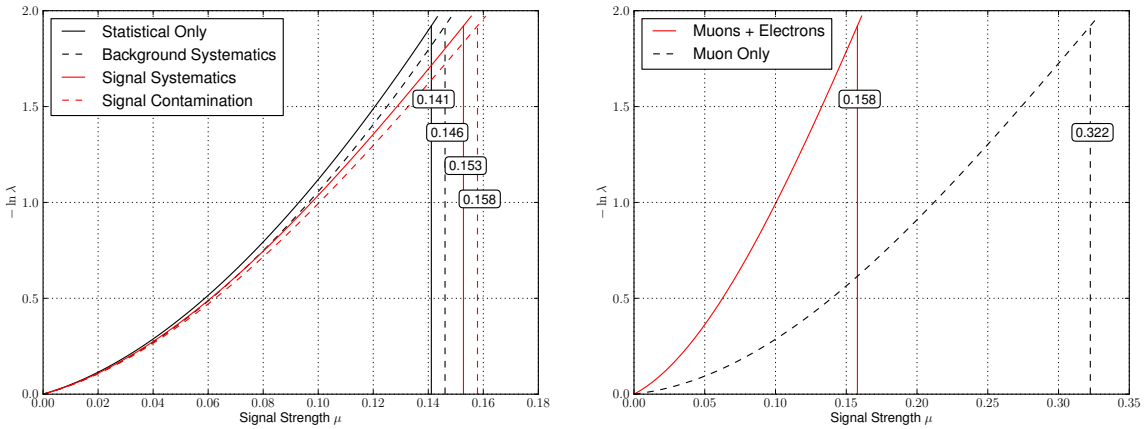

(a) **(b)**

Figure B.1.: The negative log PL ratio as a function of μ (a) with different systematic effects included in the likelihood and (b) with the electron channel removed. The vertical lines and numbers represent the 95% confidence level upper limits on μ. The results are shown for the CMSSM point $(m_0, m_{\frac{1}{2}}) = (80, 240)$

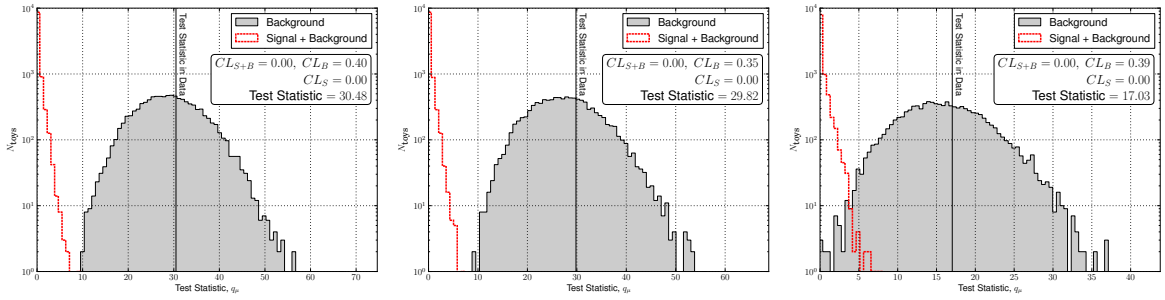

(a) Statistical Unc. **(b)** Background Unc. **(c)** Signal Unc.

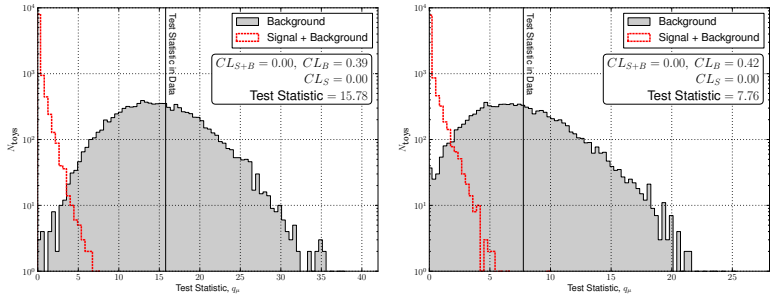

(d) Signal Contamination **(e)** Muon Channel Only

Figure B.2.: Distribution of the test statistic, q_μ, for null and alternate hypotheses with different systematic effects included and with the electron channel removed. These distributions have been made for the CMSSM point $(m_0, m_{\frac{1}{2}}) = (80, 240)$. The values of CL_{b}, $CL_{\mathrm{s+b}}$ and CL_{s} are also shown.

Appendix C.

Service Work

C.1. SusyV2 Analysis Framework

SusyV2 is a standalone, ROOT-based analysis framework. Analysis scripts are written in the Python programming language. These make use of low-level, high-performance classes written in C++. This provides a good compromise between speed and flexibility.

The SusyV2 package has been used for a number of analyses at CMS. These have primarily been SUSY-based analyses. It has also been used for the W polarisation measurement as well as several other projects. The vast majority of the initial code was written by Dr. John Jones with subsequent contributions from a number of others.

The SusyV2 code aims to minimise the number of reads performed on a ROOT tree by reading branches on demand and performing lazy calculations as required to satisfy analysis code requests for higher-level observables. The dependency chain between calculated quantities may be viewed as a tree. The leaves of this tree correspond to quantities stored directly in the ROOT file (or an alternative serialisation format). To minimise computation, each node in this tree performs its calculation (or IO in the case of the leaf nodes) only once per event. The results are then cached. Subsequent use of this quantity then returns the cached result directly. Furthermore, access to quantities dependent on others which have already been calculated will require the minimum necessary calculation, reutilising cached values and minimising further IO or CPU usage.

As well as the performance advantages of this approach, it has the benefit of enforcing a kind of "referential transparency" – repeated access to a given quantity must always yield the same result (at the single-event level). Whilst this makes certain tasks more

involved – e.g. iterative cleaning of events – it ensures that analysis selections must "commute" - since they are unable to mutate any of the quantities on which they select. This emulates some of the benefits available in purely functional programming languages such as Haskell [168].

My contributions were in the maintenance and development of this code-base, the addition of a flexible Python-based configuration system, support for the ROOT TChain class, infrastructure for managing and monitoring batch submissions, and the implementation of a fast "cross-cleaner". The cross-cleaner must resolve ambiguities between physics objects. The detected ambiguities may form cyclic graphs, which require careful resolution.

C.2. The Global Calorimeter Trigger

The Global Calorimeter Trigger (GCT), previously described in Section 4.3.6, formed the focus of my service work during the PhD. This followed on from previous work on the "jet-finder" component which formed the basis of my MSci project.

As well as undertaking shift-work and on-call duties, I was responsible for debugging problems experienced before the start of data-taking with the *source card* components. These boards receive data from the RCT and then transmit it, via optical fibres, to the *leaf cards* of the GCT. The data is organised in a manner suited to the processing performed by the GCT. The data is received from the RCT on 6×68 pin differential Emitter-Coupled Logic (ECL) Small Computer System Interface (SCSI) cables running at 80 MHz. Errors were occurring intermittently in pattern tests run at the experimental service cavern. These problems could not be reproduced in the test setup. It was eventually discovered that the errors were caused by deficiencies in the SCSI cables linking the source cards to the RCT. The problematic cables were replaced, eliminating the errors.

I was also responsible for testing a hardware implementation of an improved L1T tau algorithm. This is illustrated in Figure C.1. In addition to, or instead of the use of the tau veto bit (see Section 4.3.6), an isolation requirement is placed on the tau-jet. To be classified as a tau, seven of the eight surrounding regions must be below a programmable threshold. This is found to reduce the rate by a factor of two, whilst maintaining efficiency. The algorithm was added to the firmware present on the FPGAs in the GCT's leaf cards. I was responsible for testing the algorithm in hardware. Firstly, a test suite written in

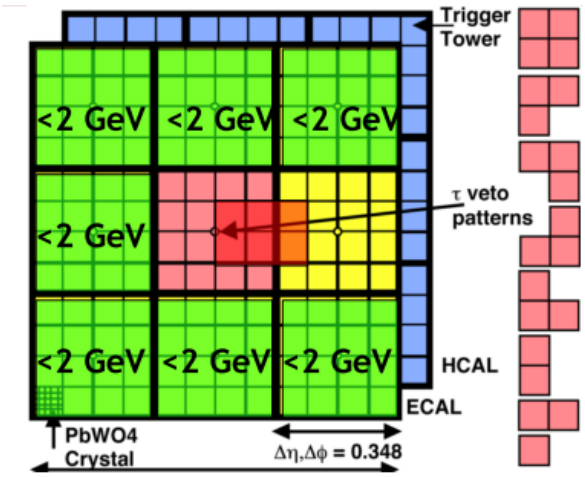

Figure C.1.: Illustration of the improved tau algorithm at the L1T. A 3×3 region sliding window algorithm is used to find jets. Tau-jets are identified as those for which none of the nine tau-veto bits are set. The improved algorithm augments or replaces this requirement with an isolation cut. Seven of the eight regions surrounding the central location must be below a programmable threshold – here set to 2 GeV.

the Python programming language was used to generate many combinations of energy patterns. These were then run through the hardware in order to verify that the basic implementation was correct. It was then subsequently tested with a number of random patterns. A software emulation of the hardware was used to verify the results. A number of problems were found both in the hardware implementation and in the consistency of the emulator and hardware. These problems were subsequently fixed.

Appendix D.

Monte Carlo Samples

Table D.1.: MC samples used in the W polarisation analysis. The MC generator used, number of simulated events, cross-section times branching ratio and equivalent integrated luminosity are also shown.

Sample	Process	Generator	N_{events}	$\sigma \times \text{BR}$	$\mathcal{L}$
W + jets	$W \to \ell\nu$ + jets	MADGRAPH	15168266	31314	484 pb^{-1}
Z + jets	$Z \to \ell^+\ell^-$ + jets	MADGRAPH	1084921	3048	356 pb^{-1}
$t\bar{t}$	$t\bar{t}$ + jets	MADGRAPH	1164640	157	7.42 fb^{-1}
QCD EMENRICHED	$20 < \hat{p}_T < 30$	PYTHIA	30898517	1719150	18.0 pb^{-1}
	$30 < \hat{p}_T < 80$	PYTHIA	62707742	3498700	17.9 pb^{-1}
	$80 < \hat{p}_T < 170$	PYTHIA	5494911	134088	41.0 pb^{-1}
QCD BCTOE	$20 < \hat{p}_T < 30$	PYTHIA	2461023	108330	22.7 pb^{-1}
	$30 < \hat{p}_T < 80$	PYTHIA	2075597	138762	15.0 pb^{-1}
	$80 < \hat{p}_T < 170$	PYTHIA	1208674	9422	128 pb^{-1}
γ + jets [a]	$\hat{p}_T > 15$	PYTHIA	1223390	192200	6.37 pb^{-1}
	$\hat{p}_T > 30$	PYTHIA	1026794	20070	51.2 pb^{-1}
	$\hat{p}_T > 80$	PYTHIA	1187711	556.5	2.13 fb^{-1}
	$\hat{p}_T > 170$	PYTHIA	939400	24.37	38.5 fb^{-1}
	$\hat{p}_T > 300$	PYTHIA	1024266	1.636	626 fb^{-1}
	$\hat{p}_T > 470$	PYTHIA	1091179	0.136	8.02 ab^{-1}
	$\hat{p}_T > 800$	PYTHIA	1065640	0.003477	306 ab^{-1}
	$\hat{p}_T > 1400$	PYTHIA	1291025	1.286×10^{-5}	100 zb^{-1}
QCD PYTHIA [a]	$\hat{p}_T > 15$	PYTHIA	6095857	8.762×10^{8}	6.96 nb^{-1}
	$\hat{p}_T > 30$	PYTHIA	5069664	6.041×10^{7}	83.9 nb^{-1}
	$\hat{p}_T > 80$	PYTHIA	2065792	9.238×10^{5}	2.24 pb^{-1}
	$\hat{p}_T > 170$	PYTHIA	3171950	2.547×10^{4}	125 pb^{-1}
	$\hat{p}_T > 300$	PYTHIA	2976108	1.256×10^{3}	2.37 fb^{-1}
	$\hat{p}_T > 470$	PYTHIA	2159497	87.98	24.5 fb^{-1}
	$\hat{p}_T > 800$	PYTHIA	2181700	2.186	998 fb^{-1}
	$\hat{p}_T > 1400$	PYTHIA	1185024	0.01122	105 ab^{-1}

[a] These samples are binned in overlapping ranges of $\hat{p}_T$. A reweighting procedure is used to account for the overlaps in the samples.

Table D.2.: MC samples used in the SUSY analysis. The MC generator used, number of simulated events, cross-section times branching ratio and equivalent integrated luminosity are also shown.

Sample	Process	Generator	N_{events}	$\sigma \times \text{BR}$	$\mathcal{L}$
$\text{W} + \text{jets}$	$\text{W} \to \ell\nu + \text{jets}$	MADGRAPH	76968640	31314	2.46 fb^{-1}
	$H_T > 300$ GeV	MADGRAPH	3314904	54.678	60.6 fb^{-1}
$\text{Z} + \text{jets}$	$\text{Z} \to \ell^+\ell^- + \text{jets}$	MADGRAPH	2329439	3048	764 pb^{-1}
$\text{t}\bar{\text{t}}$	$\text{t}\bar{\text{t}} + \text{jets}$	MADGRAPH	3701947	157.5	23.5 fb^{-1}
QCD	$50 < \hat{p}_{\text{T}} < 80$	PYTHIA	5605000	6.359×10^6	881 nb^{-1}
	$80 < \hat{p}_{\text{T}} < 120$	PYTHIA	6589956	7.843×10^5	8.40 pb^{-1}
	$120 < \hat{p}_{\text{T}} < 170$	PYTHIA	5073528	1.151×10^5	44.1 pb^{-1}
	$170 < \hat{p}_{\text{T}} < 300$	PYTHIA	5473920	2.426×10^4	226 pb^{-1}
	$300 < \hat{p}_{\text{T}} < 470$	PYTHIA	4452669	1.168×10^3	3.81 fb^{-1}
	$470 < \hat{p}_{\text{T}} < 600$	PYTHIA	3210085	70.22	45.7 fb^{-1}
	$600 < \hat{p}_{\text{T}} < 800$	PYTHIA	4105695	15.55	264 fb^{-1}
	$800 < \hat{p}_{\text{T}} < 1000$	PYTHIA	3833888	1.844	2.08 ab^{-1}
	$1000 < \hat{p}_{\text{T}} < 1400$	PYTHIA	2053222	0.3321	6.18 ab^{-1}
	$1400 < \hat{p}_{\text{T}} < 1800$	PYTHIA	2156200	0.01087	198 ab^{-1}
	$1800 < \hat{p}_{\text{T}} < \infty$	PYTHIA	273139	3.575×10^{-4}	764 ab^{-1}

Appendix E.

List of Acronymns

ADC Analogue-Digital Converter

ALICE A Large Ion Collider Experiment

AMSB Anomaly-Mediated Supersymmetry Breaking

APD Avalanche Photodiode

APV25 Analogue Pipeline Voltage 25

ASIC Application-Specific Integrated Circuit

ATLAS A Toroidal LHC Apparatus

CERN Conseil Europen pour la Recherche Nuclaire

CKM Cabibbo Kobayashi Maskawa

CMSSM Constrained Minimal Supersymmetric Standard Model

CMS Compact Muon Solenoid

CSC Cathode Strip Chamber

CTEQL1 CTEQ L1

CTF Combinatorial Track Finder

Calo Calorimeter

DAQ Data Acquisition

DT Drift Tube

EB ECAL Barrel

ECAL Electromagnetic Calorimeter

ECL Emitter-Coupled Logic

EE ECAL Endcap

EWK Electroweak

EWSB Electroweak Symmetry Breaking

FPGA Field Programmable Gate Array

GCT Global Calorimeter Trigger

GMSB Gauge-Mediated Supersymmetry Breaking

GMT Global Muon Trigger

GSF Gaussian Sum Filter

GT Global Trigger

GUT Grand Unified Theory

HB HCAL Barrel

HCAL Hadronic Calorimeter

HE HCAL Endcap

HF HCAL Forward

HLT High Level Trigger

HO HCAL Outer

HPD Hybrid Photodiode

IO Input/Output

ISR Initial State Radiation

JES Jet Energy Scale

JPT Jet Plus Tracks

L1T Level 1 Trigger

LEIR Low Energy Ion Storage Ring

LEP Large Electron-Positron

LHCb Large Hadron Collider Beauty

LHCf Large Hadron Collider Forward

LHC Large Hadron Collider

LO Leading Order

LSP Lightest Supersymmetric Particle

mSUGRA Minimal Supergravity

MC Monte Carlo

ME+PS Matrix Element Plus Truncated Shower

MLE Maximum Likelihood Estimator

MSSM Minimal Supersymmetric Standard Model

NLO Next-To-Leading Order

NP New Physics

pdf probability distribution function

poi parameter of interest

PDF Parton Distribution Function

PF Particle Flow

PL Profile Likelihood

PMT Photomultiplier Tube

PSB Proton Synchrotron Booster

PS Proton Synchrotron

QCD Quantum Chromodynamics

RCT Regional Calorimeter Trigger

RMS Root Mean Squared

RPC Resistive Plate Chamber

SCSI Small Computer System Interface

SMS Simplified Model Spectrum

SM Standard Model

SPS Super Proton Synchrotron

SQED Scalar Quantum Electrodynamics

SUSY Supersymmetry

TEC Tracker Endcap

TIB Tracker Inner Barrel

TID Tracker Inner Disk

TOB Tracker Outer Barrel

TOTEM Total Elastic and Diffractive Cross Section Measurement

TPG Trigger Primitive Generator

VPT Vacuum Phototriode

WIMP Weakly Interacting Massive Particle

Bibliography

[1] A. A. Michelson and E. W. Morley, "On the Relative Motion of the Earth and the Luminiferous Ether", *Am. J. Sci.* **34** (1887), no. 203, 333–345.

[2] I. Aitchison and A. Hey, "Gauge Theories in Particle Physics. Volume I: From Relativistic Quantum Mechanics to QED". Institute of Physics Publishing, 2003.

[3] D. Griffiths, "Introduction to Elementary Particles". John Wiley & Sons, New York, USA, 1987.

[4] M. E. Peskin and D. V. Schroeder, "An Introduction to Quantum Field Theory (Frontiers in Physics)". Perseus Books, 2008.

[5] S. Novaes, "Standard model: An Introduction", arXiv:hep-ph/0001283.

[6] S. L. Glashow, "Partial-symmetries of weak interactions", *Nucl. Phys.* **22** (1961), no. 4, 579 – 588. doi:10.1016/0029-5582(61)90469-2.

[7] S. Weinberg, "A Model of Leptons", *Phys. Rev. Lett.* **19** (Nov, 1967) 1264–1266. doi:10.1103/PhysRevLett.19.1264.

[8] A. Salam, "Renormalizability of Gauge Theories", *Phys. Rev.* **127** (Jul, 1962) 331–334. doi:10.1103/PhysRev.127.331.

[9] F. Englert and R. Brout, "Broken Symmetry and the Mass of Gauge Vector Mesons", *Phys. Rev. Lett.* **13** (Aug, 1964) 321–323. doi:10.1103/PhysRevLett.13.321.

[10] P. Higgs, "Broken symmetries, massless particles and gauge fields", *Phys. Lett.* **12** (1964), no. 2, 132 – 133. doi:10.1016/0031-9163(64)91136-9.

[11] UA1 Collaboration, "Experimental observation of isolated large transverse energy electrons with associated missing energy at $\sqrt{s} = 540$ GeV", *Phys. Lett. B* **122** (1983), no. 1, 103 – 116. doi:10.1016/0370-2693(83)91177-2.

[12] UA1 Collaboration, "Experimental observation of lepton pairs of invariant mass around 95 GeV/c^2 at the CERN SPS collider", *Phys. Lett. B* **126** (1983), no. 5, 398 – 410. doi:10.1016/0370-2693(83)90188-0.

[13] E. Majorana, "Teoria simmetrica dell'elettrone e del positrone", *Nuovo Cimento* **14** (1937) 171–184.

[14] F. T. Avignone, S. R. Elliott, and J. Engel, "Double beta decay, Majorana neutrinos, and neutrino mass", *Rev. Mod. Phys.* **80** (Apr, 2008) 481–516. doi:10.1103/RevModPhys.80.481.

[15] A. Zee, "Quantum Field Theory in a Nutshell". Princeton Univ. Press, Princeton, NJ, 2003.

[16] C. N. Yang and R. L. Mills, "Conservation of Isotopic Spin and Isotopic Gauge Invariance", *Phys. Rev.* **96** (Oct, 1954) 191–195. doi:10.1103/PhysRev.96.191.

[17] C. S. Wu, E. Ambler, R. W. Hayward et al., "Experimental Test of Parity Conservation in Beta Decay", *Phys. Rev.* **105** (Feb, 1957) 1413–1415. doi:10.1103/PhysRev.105.1413.

[18] S. Dawson, "Introduction to Electroweak Symmetry Breaking", in *High Energy Physics and Cosmology, 1998 Summer School*, A. Masiero, G. Senjanovic, & A. Smirnov, ed., p. 1. 1999. arXiv:arXiv:hep-ph/9901280.

[19] Y. Nambu, "Quasi-Particles and Gauge Invariance in the Theory of Superconductivity", *Phys. Rev.* **117** (Feb, 1960) 648–663. doi:10.1103/PhysRev.117.648.

[20] J. Goldstone, "Field theories with "Superconductor" solutions", *Il Nuovo Cimento (1955-1965)* **19** (1961) 154–164. 10.1007/BF02812722.

[21] G. S. Guralnik, C. R. Hagen, and T. W. B. Kibble, "Global Conservation Laws and Massless Particles", *Phys. Rev. Lett.* **13** (Nov, 1964) 585–587. doi:10.1103/PhysRevLett.13.585.

[22] R. K. Ellis, W. J. Stirling, and B. R. Webber, "QCD and Collider Physics", volume 8. Cambridge University Press, 1996.

[23] N. Cabibbo, "Unitary Symmetry and Leptonic Decays", *Phys. Rev. Lett.* **10** (Jun, 1963) 531–533. doi:10.1103/PhysRevLett.10.531.

[24] M. Kobayashi and T. Maskawa, "CP-Violation in the Renormalizable Theory of Weak Interaction", *Prog. Theor. Phys.* **49** (February, 1973) 652–657. doi:10.1143/PTP.49.652.

[25] R. Gupta, "Introduction to Lattice QCD: Course", arXiv:hep-lat/9807028.

[26] D. J. Gross and F. Wilczek, "Ultraviolet Behavior of Non-Abelian Gauge Theories", *Phys. Rev. Lett.* **30** (Jun, 1973) 1343–1346. doi:10.1103/PhysRevLett.30.1343.

[27] Hadron Spectrum Collaboration, J. Bulava, S. Cohen et al., "Exploring the spectrum of QCD using the lattice", *J. Phys. Conf. Ser.* **180** (July, 2009) 012067, arXiv:0907.4516. doi:10.1088/1742-6596/180/1/012067.

[28] G. Sterman, J. Smith, J. C. Collins et al., "Handbook of perturbative QCD", *Rev. Mod. Phys.* **67** (Jan, 1995) 157–248. doi:10.1103/RevModPhys.67.157.

[29] K. Nakamura and Particle Data Group, "Review of Particle Physics", *J. Phys. G Nucl. Partic.* **37** (2010), no. 7A, 075021. doi:10.1088/0954-3899/37/7A/075021.

[30] M. Green, J. Schwarz, and E. Witten, "Superstring Theory. Volume 1: Introduction". Cambridge University Press, 1988.

[31] A. Corichi, "Loop quantum geometry: A Primer", *J. Phys. Conf. Ser.* **24** (2005) 1–22, arXiv:gr-qc/0507038. doi:10.1088/1742-6596/24/1/001.

[32] Super-Kamiokande Collaboration Collaboration, "Evidence for oscillation of atmospheric neutrinos", *Phys. Rev. Lett.* **81** (1998) 1562–1567, arXiv:hep-ex/9807003.

[33] T. Kajita, "Discovery of neutrino oscillations", *Rep. Prog. Phys.* **69** (2006), no. 6, 1607.

[34] S. P. Martin, "A Supersymmetry primer", *pre-print* (1997) arXiv:hep-ph/9709356.

[35] M. Drees, R. Godbole, and P. Roy, "Theory and Phenomenology of Sparticles: An Account of Four-dimensional N=1 Supersymmetry in High Energy Physics". World Scientific, Singapore, 2004.

[36] G. Bertone, D. Hooper, and J. Silk, "Particle dark matter: Evidence, candidates

and constraints", *Phys. Rep.* **405** (2005) 279–390, arXiv:hep-ph/0404175. doi:10.1016/j.physrep.2004.08.031.

[37] D. Clowe, M. Bradac, A. H. Gonzalez et al., "A direct empirical proof of the existence of dark matter", *Astrophys. J.* **648** (2006) L109–L113, arXiv:astro-ph/0608407. doi:10.1086/508162.

[38] N. Jarosik, C. Bennett, J. Dunkley et al., "Seven-Year Wilkinson Microwave Anisotropy Probe (WMAP) Observations: Sky Maps, Systematic Errors, and Basic Results", *Astrophys. J. Suppl. S.* **192** (2011) 14, arXiv:1001.4744. doi:10.1088/0067-0049/192/2/14.

[39] DAMA Collaboration, "First results from DAMA/LIBRA and the combined results with DAMA/NaI", *Eur. Phys. J. C* **56** (2008) 333–355, arXiv:0804.2741. doi:10.1140/epjc/s10052-008-0662-y.

[40] H. Georgi and S. L. Glashow, "Unity of All Elementary-Particle Forces", *Phys. Rev. Lett.* **32** (Feb, 1974) 438–441. doi:10.1103/PhysRevLett.32.438.

[41] S. Coleman and J. Mandula, "All Possible Symmetries of the S Matrix", *Phys. Rev.* **159** (Jul, 1967) 1251–1256. doi:10.1103/PhysRev.159.1251.

[42] R. Haag, J. T. opuszaski, and M. Sohnius, "All possible generators of supersymmetries of the S-matrix", *Nucl. Phys. B* **88** (1975), no. 2, 257 – 274. doi:10.1016/0550-3213(75)90279-5.

[43] A. H. Chamseddine, R. Arnowitt, and P. Nath, "Locally Supersymmetric Grand Unification", *Phys. Rev. Lett.* **49** (Oct, 1982) 970–974. doi:10.1103/PhysRevLett.49.970.

[44] G. Giudice and R. Rattazzi, "Theories with gauge mediated supersymmetry breaking", *Phys. Rep.* **322** (1999) 419–499, arXiv:hep-ph/9801271. doi:10.1016/S0370-1573(99)00042-3.

[45] L. Randall and R. Sundrum, "Out of this world supersymmetry breaking", *Nucl. Phys. B* **557** (1999) 79–118, arXiv:hep-th/9810155. doi:10.1016/S0550-3213(99)00359-4.

[46] S. Dimopoulos and H. Georgi, "Softly broken supersymmetry and SU(5)", *Nucl. Phys. B* **193** (1981), no. 1, 150 – 162. doi:10.1016/0550-3213(81)90522-8.

[47] C. Albajar, M. Albrow, O. Allkofer et al., "Events with large missing transverse

energy at the CERN collider: III. Mass limits on supersymmetric particles", *Phys. Lett. B* **198** (1987), no. 2, 261 – 270. doi:10.1016/0370-2693(87)91509-7.

[48] D. Buskulic, I. De Bonis, D. Dcamp et al., "Search for supersymmetric particles in e^+ e^- collisions at centre-of-mass energies of 130 and 136 GeV", *Phys. Lett. B* **373** (Feb, 1996) 246–260. 21 p. doi:10.1140/epjc/s2003-01355-5.

[49] D0 Collaboration, "Search for Squarks and Gluinos in $p\overline{p}$ Collisions at $\sqrt{s} = 1.8$ TeV", *Phys. Rev. Lett.* **75** (Jul, 1995) 618–623. doi:10.1103/PhysRevLett.75.618.

[50] F. Aaron, C. Alexa, V. Andreev et al., "Search for Squarks in R-parity Violating Supersymmetry in ep Collisions at HERA", *Eur. Phys. J. C* **71** (2011) 1572, arXiv:1011.6359. doi:10.1140/epjc/s10052-011-1572-y.

[51] O. Buchmueller, R. Cavanaugh, A. De Roeck et al., "Supersymmetry in light of 1/fb of LHC data", *Eur. Phys. J. C* **72** (February, 2012) 1878, arXiv:1110.3568. doi:10.1140/epjc/s10052-012-1878-4.

[52] C. Aulakh and R. Mohapatra, "The neutrino as the supersymmetric partner of the majoron", *Phys. Lett. B* **119** (1982), no. 13, 136 – 140. doi:10.1016/0370-2693(82)90262-3.

[53] H. Baer, C.-h. Chen, F. Paige et al., "Signals for minimal supergravity at the CERN large hadron collider: Multi - jet plus missing energy channel", *Phys. Rev. D* **52** (1995) 2746–2759, arXiv:hep-ph/9503271. doi:10.1103/PhysRevD.52.2746.

[54] CMS Collaboration, "CMS Physics Technical Design Report Volume I: Detector Performance and Software". Technical Design Report CMS. CERN, Geneva, 2006.

[55] R. Field, "Min-Bias and the Underlying Event at the LHC", *Acta Phys. Pol. B* **42** (2011) 2631–2656, arXiv:1110.5530. doi:10.5506/APhysPolB.42.2631.

[56] CDF Collaboration Collaboration, "The Underlying event in hard scattering processes", *eConf* **C010630** (2001) P501, arXiv:hep-ph/0201192.

[57] P. M. Nadolsky, "Theory of W and Z boson production", *AIP Conf. Proc.* **753** (2005) 158–170, arXiv:hep-ph/0412146. doi:10.1063/1.1896698.

[58] J. M. Campbell, J. Huston, and W. Stirling, "Hard Interactions of Quarks and Gluons: A Primer for LHC Physics", *Rep. Prog. Phys.* **70** (2007) 89,

arXiv:hep-ph/0611148. doi:10.1088/0034-4885/70/1/R02.

[59] R. Ellis, K. Melnikov, and G. Zanderighi, "W+3 jet production at the Tevatron", *Phys. Rev. D* **80** (2009) 094002, arXiv:0906.1445. doi:10.1103/PhysRevD.80.094002.

[60] Z. Bern, G. Diana, L. J. Dixon et al., "Left-handed W bosons at the LHC", *Phys. Rev. D* **84** (Aug, 2011) 034008. doi:10.1103/PhysRevD.84.034008.

[61] C. F. Berger, Z. Bern, L. J. Dixon et al., "Next-to-leading order QCD predictions for W + 3-jet distributions at hadron colliders", *Phys. Rev. D* **80** (Oct, 2009) 074036. doi:10.1103/PhysRevD.80.074036.

[62] C. Berger, Z. Bern, L. J. Dixon et al., "Precise Predictions for W + 4 Jet Production at the Large Hadron Collider", *Phys. Rev. Lett.* **106** (2011) 092001, arXiv:1009.2338. doi:10.1103/PhysRevLett.106.092001.

[63] E. Mirkes and J. Ohnemus, "W and Z polarization effects in hadronic collisions", *Phys. Rev. D* **50** (November, 1994) 5692–5703. doi:10.1103/PhysRevD.50.5692.

[64] CMS Collaboration, "Measurement of the lepton charge asymmetry in inclusive W production in pp collisions at $\sqrt{s} = 7$ TeV", *J. High Energy Phys.* **2011** (2011) 1–31, arXiv:1010.5994. 10.1007/JHEP04(2011)050. doi:10.1007/JHEP04(2011)050.

[65] CMS Collaboration, "Measurement of the inclusive W and Z production cross sections in pp collisions at $\sqrt{s} = 7$ TeV with the CMS experiment", *J. High Energy Phys.* **2011** (2011) 1–76. 10.1007/JHEP10(2011)132.

[66] C.-H. Kom and W. J. Stirling, "Charge asymmetry in W + jets production at the LHC", *Eur. Phys. J. C* **C69** (2010) 67–73, arXiv:1004.3404. doi:10.1140/epjc/s10052-010-1353-z.

[67] O. Buchmueller, G. Karapostoli, J. Marrouche et al., "Measuring the polarization of W bosons in W + jets events at the LHC using the CMS experiment", Analysis Note AN-2010-309, CMS, 2010.

[68] E. Mirkes, "Angular decay distribution of leptons from W-bosons at NLO in hadronic collisions", *Nucl. Phys. B* **387** (1992), no. 1, 3 – 85. doi:10.1016/0550-3213(92)90046-E.

[69] J. Strologas, "Measurement of the differential angular distribution of the W boson produced in association with jets in proton-antiproton collisions at $\sqrt{s} = 1.8$ TeV". PhD thesis, University of Illinois at Urbana-Champaign, 2002.

[70] H. Veltman, "The equivalence theorem", *Phys. Rev. D* **41** (Apr, 1990) 2294–2311. doi:10.1103/PhysRevD.41.2294.

[71] M. S. Chanowitz and M. K. Gaillard, "The TeV physics of strongly interacting W's and Z's", *Nucl. Phys. B* **261** (1985), no. 0, 379 – 431. doi:10.1016/0550-3213(85)90580-2.

[72] G. J. Gounaris, R. Kögerler, and H. Neufeld, "Relationship between longitudinally polarized vector bosons and their unphysical scalar partners", *Phys. Rev. D* **34** (Nov, 1986) 3257–3259. doi:10.1103/PhysRevD.34.3257.

[73] J. M. Cornwall, D. N. Levin, and G. Tiktopoulos, "Derivation of gauge invariance from high-energy unitarity bounds on the S matrix", *Phys. Rev. D* **10** (Aug, 1974) 1145–1167. doi:10.1103/PhysRevD.10.1145.

[74] C. C. Tully, "Elementary particle physics in a nutshell". Princeton Univ. Press, Princeton, NJ, 2011.

[75] G. L. Kane, C. F. Kolda, L. Roszkowski et al., "Study of constrained minimal supersymmetry", *Phys. Rev. D* **49** (1994) 6173–6210, arXiv:hep-ph/9312272. doi:10.1103/PhysRevD.49.6173.

[76] J. Alwall, P. Schuster, and N. Toro, "Simplified Models for a First Characterization of New Physics at the LHC", *Phys. Rev. D* **79** (2009) 075020, arXiv:0810.3921. doi:10.1103/PhysRevD.79.075020.

[77] D. Alves, N. Arkani-Hamed, S. Arora et al., "Simplified Models for LHC New Physics Searches", *arXiv:1105.2838* (May, 2011) arXiv:1105.2838.

[78] CMS Collaboration, "Interpretation of Searches for Supersymmetry", Physics Analysis Summary SUS-11-016, CMS, 2012.

[79] M. Carena, A. Freitas, and C. Wagner, "Light stop searches at the LHC in events with one hard photon or jet and missing energy", *J. High Energy Phys.* **2008** (2008), no. 10, 109. doi:10.1088/1126-6708/2008/10/109.

[80] O. S. Bruning, P. Collier, P. Lebrun et al., "LHC Design Report". CERN, Geneva, 2004.

[81] ALICE Collaboration, "ALICE: Technical proposal for a Large Ion collider Experiment at the CERN LHC". LHC Tech. Proposal. CERN, Geneva, 1995.

[82] ATLAS Collaboration, "ATLAS: technical proposal for a general-purpose pp experiment at the Large Hadron Collider at CERN". LHC Tech. Proposal. CERN, Geneva, 1994.

[83] CMS Collaboration, "Technical proposal". LHC Tech. Proposal. CERN, Geneva, 1994. Cover title : CMS, the Compact Muon Solenoid : technical proposal.

[84] CMS Collaboration, "The CMS experiment at the CERN LHC", *J. Instrum.* **3** (August, 2008) S08004–S08004. doi:10.1088/1748-0221/3/08/S08004.

[85] LHCb Collaboration, "LHCb : Technical Proposal". Tech. Proposal. CERN, Geneva, 1998.

[86] O. Adriani, L. Bonechi, M. Bongi et al., "LHCf experiment: Technical Design Report". Technical Design Report LHCf. CERN, Geneva, 2006.

[87] V. Berardi, M. G. Catanesi, E. Radicioni et al., "Total cross-section, elastic scattering and diffraction dissociation at the Large Hadron Collider at CERN: TOTEM Technical Design Report". Technical Design Report TOTEM. CERN, Geneva, 2004.

[88] J.-L. Caron, "The LHC injection complex.. L'ensemble d'injection du LHC.", (May, 1993). AC Collection. Legacy of AC. Pictures from 1992 to 2002.

[89] CMS Collaboration, "CMS tracking performance results from early LHC operation", *Eur. Phys. J. C* **70** (December, 2010) 1165–1192, arXiv:1007.1988. doi:10.1140/epjc/s10052-010-1491-3.

[90] CMS Collaboration, "Performance and Operation of the CMS Electromagnetic Calorimeter", *J. Instrum.* **5** (Oct, 2009) T03010. 39 p, arXiv:0910.3423. doi:10.1088/1748-0221/5/03/T03010.

[91] C. Sofiatti, "Study of the crystal transparency changes of the CMS ECAL", in *APS Division of Nuclear Physics Meeting Abstracts*. October, 2011.

[92] V. Timciuc and the CMS ECAL Group, "Database usage in the CMS ECAL laser monitoring system", *J. Phys. Conf. Ser.* **219** (2010), no. 2, 022045.

[93] CMS Collaboration, "Performance of the CMS Hadron Calorimeter with Cosmic

Ray Muons and LHC Beam Data", *J. Instrum.* **5** (Nov, 2009) T03012 . 35 p, arXiv:0911.4991. doi:10.1088/1748-0221/5/03/T03012.

[94] S. Abdullin, V. Abramov, B. Acharya et al., "Design, performance, and calibration of CMS hadron-barrel calorimeter wedges", *Eur. Phys. J. C* **55** (2008) 159–171. 10.1140/epjc/s10052-008-0573-y. doi:10.1140/epjc/s10052-008-0573-y.

[95] CMS Collaboration, "Performance of the CMS Drift Tube Chambers with Cosmic Rays", *J. Instrum.* **5** (Nov, 2009) T03015 . 47 p, arXiv:0911.4855. doi:10.1088/1748-0221/5/03/T03015.

[96] CMS Collaboration, "Performance of the CMS Cathode Strip Chambers with Cosmic Rays", *J. Instrum.* **5** (Nov, 2009) T03018 . 39 p, arXiv:0911.4992. doi:10.1088/1748-0221/5/03/T03018.

[97] CMS Collaboration, "Performance Study of the CMS Barrel Resistive Plate Chambers with Cosmic Rays", *J. Instrum.* **5** (Nov, 2009) T03017. 33 p, arXiv:0911.4045. doi:10.1088/1748-0221/5/03/T03017.

[98] CMS Collaboration, "CMS TriDAS project: Technical Design Report; 1, the trigger systems". Technical Design Report CMS. CERN, 2000.

[99] J. A. Jones and G. Hall, "Development of Trigger and Control Systems for CMS". PhD thesis, Univ. London, London, UK, 2007. Presented on 05 Mar 2007.

[100] C. Eck, J. Knobloch, L. Robertson et al., "LHC computing Grid: Technical Design Report. Version 1.06 (20 Jun 2005)". Technical Design Report LCG. CERN, Geneva, 2005.

[101] S. Agostinelli, J. Allison, K. Amako et al., "Geant4 – a simulation toolkit", *Nucl. Instrum. Meth. A* **506** (2003), no. 3, 250 – 303. doi:10.1016/S0168-9002(03)01368-8.

[102] CMS Collaboration, "Tau identification in CMS", Physics Analysis Summary TAU-11-001, CMS, 2011.

[103] G. Bagliesi, "Reconstruction and identification of tau decays at CMS", *J. Phys. Conf. Ser.* **119** (2008), no. 3, 032005. doi:10.1088/1742-6596/119/3/032005.

[104] CMS Collaboration, "Performance of CMS muon reconstruction in cosmic-ray events", *J. Instrum.* **5** (2010), no. 03, T03022, arXiv:0911.4994. doi:10.1088/1748-0221/5/03/T03022.

[105] CMS Collaboration, "Performance of muon identification in pp collisions at $\sqrt{s} = 7$ TeV", Physics Analysis Summary MUON-10-002, CMS, 2010.

[106] CMS Collaboration, "Measurement of Momentum Scale and Resolution of the CMS Detector using Low-mass Resonances and Cosmic Ray Muons", Physics Analysis Summary TRK-10-004, CMS, 2010.

[107] R. E. Kalman, "A New Approach to Linear Filtering and Prediction Problems", *J. Basic Eng. - T. ASME* **82** (1960), no. Series D, 35–45.

[108] C. Liu, N. Neumeister, N. Amapane et al., "Reconstruction of cosmic and beam-halo muons with the CMS detector", *Eur. Phys. J. C* **56** (2008) 449–460, arXiv:0810.3726. doi:10.1140/epjc/s10052-008-0674-7.

[109] S. Baffioni, C. Charlot, F. Ferri et al., "Electron reconstruction in CMS", *Eur. Phys. J. C* **49** (2007) 1099–1116. doi:10.1140/epjc/s10052-006-0175-5.

[110] CMS Collaboration, "Commissioning of the Particle-flow Event Reconstruction with the first LHC collisions recorded in the CMS detector", Technical Report PFT-10-001, CMS, 2010.

[111] CMS Collaboration, "Electron reconstruction and identification at $\sqrt{s} = 7$ TeV", Physics Analysis Summary EGM-10-004, CMS, 2010.

[112] W. Adam, R. Frhwirth, A. Strandlie et al., "Reconstruction of electrons with the Gaussian-sum filter in the CMS tracker at the LHC", *J. Phys. G Nucl. Partic.* **31** (2005), no. 9, N9. doi:10.1088/0954-3899/31/9/N01.

[113] CMS Collaboration, "Measurement of the W and Z inclusive production cross sections at $\sqrt{s} = 7$ TeV with the CMS experiment at the LHC", Physics Analysis Summary EWK-10-002, CMS, 2010.

[114] CMS Collaboration, "Simple Cut-Based Electron ID web page". https://twiki.cern.ch/twiki/bin/viewauth/CMS/SimpleCutBasedEleID.

[115] A. P. Vartak, M. LeBourgeois, and V. Sharma, "Lepton Isolation in the CMS Tracker, ECAL and HCAL", Technical Report AN-2010-106, CMS, 2010.

[116] D. Barge, C. Campagnari, G. S. et al., "Study of photon conversion rejection at CMS", Analysis Note AN-2009-159, CMS, 2009.

[117] CMS Collaboration, "Jet Performance in pp Collisions at 7 TeV", Physics

Analysis Summary JME-10-003, CMS, 2010.

[118] M. Cacciari, G. P. Salam, and G. Soyez, "The anti-k_t jet clustering algorithm", *J. High Energy Phys.* **2008** (2008), no. 04, 063.

[119] CMS Collaboration, "Determination of jet energy calibration and transverse momentum resolution in CMS", *J. Instrum.* **6** (November, 2011) 11002, arXiv:1107.4277. doi:10.1088/1748-0221/6/11/P11002.

[120] CMS Collaboration, "Jet Energy Corrections determination at 7 TeV", Technical Report JME-10-010, CMS, 2010.

[121] CMS Collaboration, "Particle-Flow Event Reconstruction in CMS and Performance for Jets, Taus, and MET", Physics Analysis Summary PFT-09-001, CMS, Apr, 2009.

[122] CMS Collaboration, "Commissioning of the Particle-Flow reconstruction in Minimum-Bias and Jet Events from pp Collisions at 7 TeV", Physics Analysis Summary PFT-10-002, CMS, Jul, 2010.

[123] J. Alwall, P. Demin, S. de Visscher et al., "MadGraph/MadEvent v4: the new web generation", *J. High Energy Phys.* **2007** (2007), no. 09, 028, arXiv:0706.2334. doi:10.1088/1126-6708/2007/09/028.

[124] T. Sjstrand, S. Mrenna, and P. Skands, "PYTHIA 6.4 physics and manual", *J. High Energy Phys.* **2006** (2006), no. 05, 026, arXiv:hep-ph/0603175. doi:10.1088/1126-6708/2006/05/026.

[125] M. R. Whalley, D. Bourilkov, and R. C. Group, "The Les Houches Accord PDFs (LHAPDF) and Lhaglue", arXiv:hep-ph/0508110.

[126] M. Whalley and A. Buckley, "LHAPDF web page". http://hepforge.cedar.ac.uk/lhapdf/.

[127] J. Marrouche and C. Foudas, "Triggering and W-Polarisation Studies with CMS at the LHC". PhD thesis, London, Imperial College London, London, 2010. Presented 14 Dec 2010.

[128] CMS Collaboration, "Electromagnetic physics objects commissioning with first LHC data", Physics Analysis Summary EGM-10-001, CMS, 2010.

[129] CMS Collaboration, "Measurement of the electron charge asymmetry in inclusive

W production in pp collisions at $\sqrt{s} = 7$ TeV", Physics Analysis Summary SMP-12-001, CMS, 2012.

[130] A. Ghezzi, "e/γ HLT twiki page". https://twiki.cern.ch/twiki/bin/view/CMSPublic/SWGuideEgammaHLT.

[131] W. Verkerke and D. Kirkby, "The RooFit toolkit for data modeling", *ArXiv Physics e-prints* (June, 2003) arXiv:arXiv:physics/0306116.

[132] W. Verkerke and D. Kirkby, "RooFit web page". http://roofit.sourceforge.net.

[133] F. James and M. Roos, "Minuit: A System for Function Minimization and Analysis of the Parameter Errors and Correlations", *Comp. Phys. Commun.* **10** (1975) 343–367. doi:10.1016/0010-4655(75)90039-9.

[134] P. Nason, S. Dawson, and R. Ellis, "The total cross section for the production of heavy quarks in hadronic collisions", *Nucl. Phys. B* **303** (1988), no. 4, 607 – 633. doi:10.1016/0550-3213(88)90422-1.

[135] W. Bernreuther, A. Brandenburg, Z. Si et al., "Top quark pair production and decay at hadron colliders", *Nucl. Phys. B* **690** (2004) 81–137, arXiv:hep-ph/0403035. doi:10.1016/j.nuclphysb.2004.04.019.

[136] R. Hamberg, W. van Neerven, and T. Matsuura, "A complete calculation of the order ${\alpha_s}^2$ correction to the Drell-Yan K-factor", *Nucl. Phys. B* **359** (1991), no. 23, 343 – 405. doi:10.1016/0550-3213(91)90064-5.

[137] CMS Collaboration, "Search for new physics with single-leptons at the LHC", Physics Analysis Summary SUS-11-015, CMS, 2011.

[138] CMS Collaboration, "Missing transverse energy performance of the CMS detector", *J. Instrum.* **6** (September, 2011) 9001, arXiv:1106.5048. doi:10.1088/1748-0221/6/09/P09001.

[139] CMS Collaboration, "CMS MET Performance in Events Containing Electroweak Bosons from pp Collisions at $\sqrt{s} = 7$ TeV", Physics Analysis Summary JME-10-005, CMS, 2010.

[140] M. H. Edelhoff, "Track Selection for the Alignment of the CMS Tracker". PhD thesis, RWTH Aachen, 2008.

[141] Bauer, G. et al., "Lepton Charge Asymmetry in the $pp \longrightarrow W \longrightarrow e\nu$ channel at $\sqrt{s} = 7$ TeV", Analysis Note AN-2010/469, CMS, 2010.

[142] J. Pumplin, D. R. Stump, J. Huston et al., "New Generation of Parton Distributions with Uncertainties from Global QCD Analysis", *J. High Energy Phys.* **7** (July, 2002) 12, arXiv:hep-ph/0201195. doi:10.1088/1126-6708/2002/07/012.

[143] CMS Collaboration, "First measurement of the cross section for top-quark pair production in protonproton collisions at", *Phys. Lett. B* **695** (2011), no. 5, 424 – 443. doi:10.1016/j.physletb.2010.11.058.

[144] CMS Collaboration, "Measurement of the Polarization of W Bosons with Large Transverse Momenta in W+Jets Events at the LHC", *Phys. Rev. Lett.* **107** (2011) 021802, arXiv:1104.3829. doi:10.1103/PhysRevLett.107.021802.

[145] W. Adam, C. Adleff, O. Buchmueller et al., "Preselection and sample properties for SUSY searches in the single lepton channel in 2011", Analysis Note AN-2011-315, CMS, 2011.

[146] A.-C. L. Bihan, "Expectations for first measurements of top-antitop pair production using early CMS data", *Nucl. Phys. B - Proc. Sup.* **210211** (2011), no. 0, 45 – 48. doi:10.1016/j.nuclphysbps.2010.12.043.

[147] O. Buchmueller, L. Gouskos, G. Karapostoli et al., "W-Boson Polarization based leptonic SUSY search", Analysis Note AN-2011-205, CMS, 2011.

[148] CMS Collaboration, "Measurement of the $t\bar{t}$ production cross section and the top quark mass in the dilepton channel in pp collisions at $\sqrt{s} = 7$ TeV", *J. High Energy Phys.* **2011** (2011) 1–49, arXiv:0901.2137. 10.1007/JHEP07(2011)049. doi:10.1007/JHEP07(2011)049.

[149] P. M. Nadolsky, H.-L. Lai, Q.-H. Cao et al., "Implications of CTEQ global analysis for collider observables", *Phys. Rev. D* **78** (July, 2008) 013004, arXiv:0802.0007. doi:10.1103/PhysRevD.78.013004.

[150] A. D. Martin, W. J. Stirling, R. S. Thorne et al., "Parton distributions for the LHC", *Eur. Phys. J. C* **63** (September, 2009) 189–285, arXiv:0901.0002. doi:10.1140/epjc/s10052-009-1072-5.

[151] A. D. Martin, W. J. Stirling, R. S. Thorne et al., "Uncertainties on α_S in global

PDF analyses and implications for predicted hadronic cross sections", *Eur. Phys. J. C* **64** (December, 2009) 653–680, arXiv:0905.3531. doi:10.1140/epjc/s10052-009-1164-2.

[152] A. D. Martin, W. J. Stirling, R. S. Thorne et al., "Heavy-quark mass dependence in global PDF analyses and 3- and 4-flavour parton distributions", *Eur. Phys. J. C* **70** (November, 2010) 51–72, arXiv:1007.2624. doi:10.1140/epjc/s10052-010-1462-8.

[153] F. E. James, "Statistical Methods in Experimental Physics; 2nd ed.". World Scientific, Singapore, 2006.

[154] L. Lyons, "Statistics for Nuclear and Particle Physicists". Cambridge University Press, 1989.

[155] S. S. Wilks, "The Large-Sample Distribution of the Likelihood Ratio for Testing Composite Hypotheses", *Ann. Math. Stat.* **9** (1938), no. 1, 60–62. doi:10.2307/2957648.

[156] A. Van den Bos, "Parameter Estimation for Scientists and Engineers". Wiley, New York, NY, 2007.

[157] A. L. Read, "Presentation of search results: the CL_s technique", *J. Phys. G Nucl. Partic.* **28** (2002), no. 10, 2693. doi:10.1088/0954-3899/28/10/313.

[158] T. Junk, "Confidence level computation for combining searches with small statistics", *Nucl. Instrum. Meth. A* **434** (1999), no. 23, 435 – 443. doi:10.1016/S0168-9002(99)00498-2.

[159] T. Junk, "Confidence level computation for combining searches with small statistics", *Nucl. Instrum. Meth. A* **A434** (1999) 435–443, arXiv:hep-ex/9902006. doi:10.1016/S0168-9002(99)00498-2.

[160] A. L. Read, "Modified frequentist analysis of search results (the CL_s method)", in *1st Workshop on Confidence Limits*, number CERN-OPEN-2000-205, pp. 81–101, CERN. Geneva, Switzerland, 2000.

[161] ATLAS Collaboration and CMS Collaboration, "Procedure for the LHC Higgs boson search combination in Summer 2011", Note 2011-005, CERN, Geneva, Aug, 2011.

[162] G. Cowan, K. Cranmer, E. Gross et al., "Asymptotic formulae for likelihood-based

tests of new physics", *Eur. Phys. J. C* **71** (February, 2011) 1554, arXiv:1007.1727. doi:10.1140/epjc/s10052-011-1554-0.

[163] L. Moneta, K. Cranmer, G. Schott et al., "The RooStats project", in *Proceedings of the 13th International Workshop on Advanced Computing and Analysis Techniques in Physics Research. February 22-27, 2010, Jaipur, India. p.57.* 2010. arXiv:1009.1003.

[164] K. Cranmer, G. Schott, L. Moneta et al., "RooStats web page". https://twiki.cern.ch/twiki/bin/view/RooStats/WebHome.

[165] W. Beenakker, R. Hopker, and M. Spira, "PROSPINO: A Program for the production of supersymmetric particles in next-to-leading order QCD", arXiv:hep-ph/9611232.

[166] B. Allanach, "SOFTSUSY: a program for calculating supersymmetric spectra", *Comp. Phys. Commun.* **143** (2002) 305–331, arXiv:hep-ph/0104145. doi:10.1016/S0010-4655(01)00460-X.

[167] CMS Collaboration, "Measurement of CMS Luminosity", Physics Analysis Summary EWK-10-004, CMS, 2010.

[168] P. Hudak, J. Hughes, S. Peyton Jones et al., "A history of Haskell: being lazy with class", in *Proceedings of the third ACM SIGPLAN conference on History of programming languages*, HOPL III, pp. 12–1–12–55. ACM, New York, NY, USA, 2007.

Colophon

A number of software tools were vital to the production of this thesis. The author is extremely grateful to the many individuals responsible. Without such high-quality tools, this work would simply not have been possible.

The thesis was written using the Emacs text-editor and typeset with TEX/LATEXusing the HEPThesis package. The `git` version control system was invaluable for maintaining backups and managing changes.

All work was performed using the GNU/Linux operating system, primarily the variant assembled by the volunteers of the Arch Linux project. Much of the code was written using the Python programming language. Whilst some plots were produced using the ROOT framework, the author recommends `matplotlib` for its superior API and powerful features.